Effects of Pressure Gradient on Two-Dimensional Separated and Reattached Turbulent Flows

by

Mohammad Khalid Shah

A Thesis Submitted to the Faculty of Graduate Studies of
The University of Manitoba
In Partial Fulfillment of the Requirements of the Degree of

Doctor of Philosophy
In
Mechanical Engineering

Department of Mechanical and Manufacturing Engineering
University of Manitoba
Winnipeg, Manitoba
Canada

ABSTRACT

An experimental program is designed to study the salient features of separated and reattached flows in pressure gradients generated in asymmetric diverging and converging channels. The channels comprised a straight flat floor and a curved roof that was preceded and followed by straight parallel walls. Reference measurements were also made in a parallel-wall channel to facilitate the interpretation of the pressure gradient flows. A transverse square rib located at the start of convergence/divergence was used to create separation inside the channels. In order to simplify the interpretation of the relatively complex separated and reattached flows in the asymmetric converging and diverging channels, measurements were made in the plain converging and diverging channel without the rib on the channel wall. All the measurements were obtained using a high resolution particle image velocimetry technique.

The experiments without the ribs were conducted in the diverging channel at Reynolds number based on half channel depth (Re_h) of 27050 and 12450 and in the converging channel at Re_h = 19280. For each of these three test conditions, a high resolution particle image velocimetry technique (PIV) was used to conduct detailed velocity measurements in the upstream parallel section, within the converging and diverging section, and downstream of the converging and diverging sections. From these measurements, the boundary layer parameters and profiles of the mean velocities, turbulent quantities as well as terms in the transport equations for turbulent kinetic energy and Reynolds stresses were obtained to document the effects of pressure gradient on the flow. In the adverse pressure gradient case, the turbulent quantities were enhanced more significantly in the lower boundary layer than the upper boundary layer. On the other

hand, favorable pressure gradient attenuated the turbulence levels and the effect was found to be similar on both the upper and the lower boundary layers.

For the separated and reattached flows in the converging, diverging and parallel-wall channels at Re_h = 19450, 12420 and 15350, respectively. The Reynolds number based on the approach velocity and rib height was $Re_k \approx 2700$. From these measurements, profiles of the mean velocities, turbulent quantities and the various terms in the transport equations for turbulent kinetic energy and Reynolds stresses were also obtained. The flow dynamics in the upper boundary layer in the separated region and the early stages of flow redevelopment were observed to be insensitive to the pressure gradients. In the lower boundary layer, however, the flow dynamics were entirely dominated by the separated shear layer in the separated region as well as the early region of flow redevelopment. The effects of the separated shear layer diminished in the redevelopment region so that the dynamics of the flow were dictated by the pressure gradients.

The proper orthogonal decomposition (POD) was applied to educe the dominant large scale structures in the separated and reattached flows. These dominant scales were used to document structural differences between the canonical upstream flow and the flow field within the separated and redeveloping region. The contributions of these dominant structures to the dynamics of the Reynolds normal and shear stresses are also presented and discussed. It was observed that the POD recovers Reynolds shear stress more efficiently than the turbulent kinetic energy. The reconstruction reveals that large scales contribute more to the Reynolds shear stress than the turbulent kinetic energy.

ACKNOWLEDGEMENTS

Praise be to Allah Almighty for bringing me this far in life. I would like to express my sincere appreciation and gratitude to my supervisor, Dr. Mark Francis Tachie for giving me the opportunity to work in this challenging field of research and for his patience and constant encouragement. His invaluable help with various aspects of my research and this document are greatly appreciated.

I would like to thank my family for their moral and financial support that enabled me to finish my thesis. I am also grateful to Dr. Maher Abou Al-Sood, Mr. Kofi Adane, Martin Agelinchaab and Dr. Samuel Paul for their support during the course of my study. Technical assistance provided by Mr. John Finken is gratefully acknowledged.

The financial support provided by the University of Manitoba in the form of conference travel award is gratefully acknowledged.

DEDICATION

This thesis is dedicated to:

My Wife, Aysha Bukhari,

My Daughter, Mariam,

and

Shah Families.

TABLE OF CONTENTS

LIST OF FIGURES

LIST OF TABLES

NOMENCLATURE

ENGLISH SYMBOLS

C : Additive constant in log law

C_f : Skin friction coefficient

C_i : Power law multiplicative factor

C_o : Power law multiplicative factor

Diff : Diffusion term in the transport equation of turbulent kinetic energy [m2/s3]

d_{image} : Particle image diameter [μm]

d_p : Particle diameter [μm]

d_{pitch} : Pitch diameter [μm]

$f_{\#}$: *f*-number of the lens

g : Acceleration due to gravity [m/s^2]

G : Clauser shape factor (= $(H\text{-}1)/(H(0.5C_f)^{0.5})$)

h : Half channel height [mm]

H : Shape factor (= δ^*/θ)

k : Step height [mm]

K : Pressure gradient parameter (= $(\nu/U_e^2)\partial U_e/\partial x$)

l_m : Mixing length [m]

M : Magnification factor

N : Interrogation area side [pixel]

P : Pressure

P_k	:	Production of turbulent kinetic energy
P_k	:	Production of Reynolds shear stress
Re_h	:	Reynolds number based on maximum streamwise velocity and half channel height (= $U_e h / \nu$)
Re_k	:	Reynolds number based on maximum streamwise velocity and step height (= $U_e k / \nu$)
Re_θ	:	Reynolds number based on maximum streamwise velocity and momentum thickness (= $U_e \theta / \nu$)
S	:	Skewness factor
F	:	Flatness factor
U	:	Streamwise component of mean velocity [m/s]
U_b	:	Bulk velocity [m/s]
U_e	:	Maximum streamwise velocity [m/s]
U_τ	:	Friction velocity [m/s]
U^+	:	Mean velocity in inner coordinates (= U/U_τ)
u	:	Streamwise velocity fluctuation [m/s]
V	:	Transverse component of mean velocity [m/s]
v	:	Transverse velocity fluctuation [m/s]
v_s	:	Settling velocity [m/s]
v_t	:	Eddy viscosity
$-uv$	:	Reynolds shear stress [m^2/s^2]
u^3, u^2v, uv^2, v^3,	:	Triple correlations of fluctuating velocity components [m^3/s^3]

u^2w, uw^2,

w^3

W : Spanwise component of mean velocity [m/s]

w : Spanwise turbulent intensity [m/s]

x : Streamwise coordinate (zero taken at the inlet to variable section) [mm]

x_r : Reattachment length [mm]

y : Transverse coordinate [mm]

y^+ : Transverse coordinate in inner coordinates ($= yU_\tau/\nu$)

z : Spanwise coordinate [mm]

GREEK SYMBOLS

β : Clauser pressure gradient parameter ($= (\delta^*/\tau_w)(\partial P/\partial x)$)

ε : Turbulent dissipation rate [m^2/s^3]

δ : Boundary layer thickness, defined as the location where local velocity is 99% of the maximum streamwise velocity [mm]

ΔU^+_{max} : Maximum deviation from the log law line

δ^* : Boundary layer displacement thickness [mm]

δ^+ : Reynolds number based on boundary layer thickness and friction velocity ($= \delta U_\tau/\nu$)

δ_z : Camera's depth-of-field [mm]

$\Delta_{z,req'd}$: Laser sheet thickness required for a Stereo-PIV system [mm]

λ : Wavelength of laser light source [nm]

Ω_z : Mean spanwise vorticity [s^{-1}]

θ : Boundary layer momentum thickness [mm]

κ : Von Karman constant

μ : Absolute viscosity [$N.s/m^2$]

ν : Kinematic viscosity [m^2/s]

Π : The wake parameter

ρ : Density [kg/m^3]

τ_w : Wall shear stress [N/m^2]

τ_r : Particle response time [s]

SUPERSCRIPTS

+ : Normalized by wall variables

ACRONYMS

APG : Adverse pressure gradient

FPG : Favorable pressure gradient

FISF : Fringe Imaging Skin Friction Technique

LDA : Laser Doppler anemometry

LOI : Laser Oil Interferometry

Nd: YAG : Neodymium: Yttrium Aluminum Garnet

PIV : Particle image velocimetry

ZPG : Zero pressure gradient

CHAPTER 1: INTRODUCTION

Ludwig Prandtl, a German aerodynamicist, first introduced the concept of a boundary layer in 1904. Prandtl showed that in the inner region, viscous effects at the wall bring the fluid to a halt, and then slowly moving particles retard their neighbors above, so that a distance away from the leading edge of the plate, there is a significantly retarded shear layer, or a boundary layer of thickness δ. In the region outside of the boundary layer, the effect of viscosity is negligible and the fluid may be treated as inviscid. In this thesis, the streamwise, transverse and spanwise directions will be denoted by x, y and z, respectively. The mean velocities along the x, y and z axes will be represented by U, V and W. The corresponding fluctuating components along the x, y and z will be denoted by u, v and w.

Boundary layers may be either laminar or turbulent depending on the value of the Reynolds number. At relatively low Reynolds numbers, the boundary layer is laminar and there is relatively little mixing. Consequently, the velocity gradient, $\partial U/\partial y$, is small and the wall shear stress, $\tau_w = \mu \partial U/\partial y$, is low. At high Reynolds numbers, the flow becomes very sensitive to perturbations. For a turbulent boundary layer, the velocity profile changes rapidly in the vicinity of the wall so that the velocity gradient, $\partial U/\partial y$, close to the wall and hence the wall shear stress, τ_w, is substantially higher than for a laminar boundary layer. In a turbulent boundary layer, the flow field is also much more complicated than in a laminar boundary layer. Flow quantities such as velocity, pressure and temperature have randomly fluctuating components which are irregular in space and

time. This makes it impossible to describe turbulence deterministically; instead it must be described statistically.

1.1 Pressure Gradients in Turbulent Flows

Turbulent flows with pressure gradient are often encountered in diverse engineering and technological applications. A considerable amount of research has been dedicated to such flows since the early works of Dönch (1926) and Nikuradse (1929) in diverging and converging channel flows. The motivation for these studies is to advance the understanding of the significant impact that pressure gradient has on the performance of engineering designs. A pressure gradient also greatly affects the structure of the turbulent boundary layers. Decelerating flows subjected to an adverse pressure gradient thicken the boundary layer and complicate the flow characteristics whereas accelerating flows stabilize the boundary layer (Kim *et al.*, 1999). For these reasons, pressure gradient driven turbulent boundary layers are also often used as prototypical flows to advance physical understanding of fluid flows of engineering importance.

1.1.1 Favorable Pressure Gradient

In a favorable pressure gradient (FPG) flow, the mean pressure decreases in the flow direction (i.e., $\partial P/\partial x < 0$) and the maximum streamwise velocity, U_e, increases with x, for example in a converging channel. In the presence of large enough FPG, reverse transition or laminarization occurs. FPG is encountered in many engineering applications, for example, at the leading edge of high lift systems. If a sufficiently strong FPG exists at the leading edge of an airfoil, the turbulent boundary layer may relaminarize which can affect the maximum lift coefficient (Bourassa *et al.*, 2000).

1.1.2 Adverse Pressure Gradient

Adverse pressure gradient (APG) in which pressure increases in the flow direction (i.e., $\partial P/\partial x > 0$), arises when the maximum streamwise velocity, U_e, is decreasing with x, for example in a diverging channel. APG exists at the termination of streamlined bodies such as submarines or ships, and often plays critical role in the performance of these devices. For a large enough pressure increase, the fluid may slow to zero velocity or even become reversed. When flow reversal occurs, the flow is said to be separated from the surface. This may have practical consequences in aerodynamics since flow separation significantly modifies the pressure distribution along the surface and hence the lift and drag.

1.2 Separation Induced by a Sharp Corner

Flow separation and recirculation caused by blunt obstacles or sudden constriction/expansion flow geometry also play an important role in many engineering applications. Whenever there is a sudden expansion of the flow geometry, an abrupt increase of the static pressure in the flow takes place. As a consequence, the flow close to the surface is retarded dramatically and separation occurs. The slope of the velocity profile $U(y)$ close to the surface becomes zero. This phenomenon, which gives rise to a vanishing wall shear stress at the separation position, makes the boundary layer thicken considerably. Beyond this point, the mean flow close to the surface in the separated region runs against the freestream direction. The main flow will reattach on to the surface again, so that a bounded area of back-flow or separation bubble is formed. While a sharp edge keeps the front end of the separated region fixed, the position of flow

reattachment may move up and down the surface that follows the sudden expansion/contraction.

A number of laboratory geometries have been devised to generate two-dimensional separated and reattached flows, and to study their transport and mixing properties. A backward facing step (see for example, Bradshaw and Wong, 1972) is commonly used to study separated and reattached flows. It is formed when two channels with different cross-sectional areas are connected as shown in Figure 1.1a. The sudden area change causes the flow to separate at the corner and forms a recirculation zone at high Reynolds number. The flow reattaches downstream of the step. Some other simple geometries that have been studied include a forward facing step (Abu Mulaweh, 2005), a transverse square rib (Tillman, 1945), a fence normal to the flow (Cutler and Johnston, 1989), a splitter plate (Ruderich and Fernholz, 1986), and a blunt plate (Kiya and Sasaki, 1983). These geometries are shown in Figure 1.1b - 1.1f. In all these cases the separation line is fixed by the geometry.

The significant impact of separation and reattachment on the efficiency and performance of engineering designs has fuelled a considerable amount of research. Pipe systems, for example, in chemical reactors or food-processing devices often exhibit abrupt changes in tube diameter, or may be furnished with baffles or ribs that obstruct the flow path. Similarly, flows over and around wall mounted obstacles or through orifices are frequently encountered in practice, examples being heat exchangers, combustors or flow meters. Separated flows determine, to a large extent, the drag of road vehicles and are the dominant feature of atmospheric flows over buildings, fences and hills. For example, on airfoils, separation results in a dramatically reduced lift also known as stall.

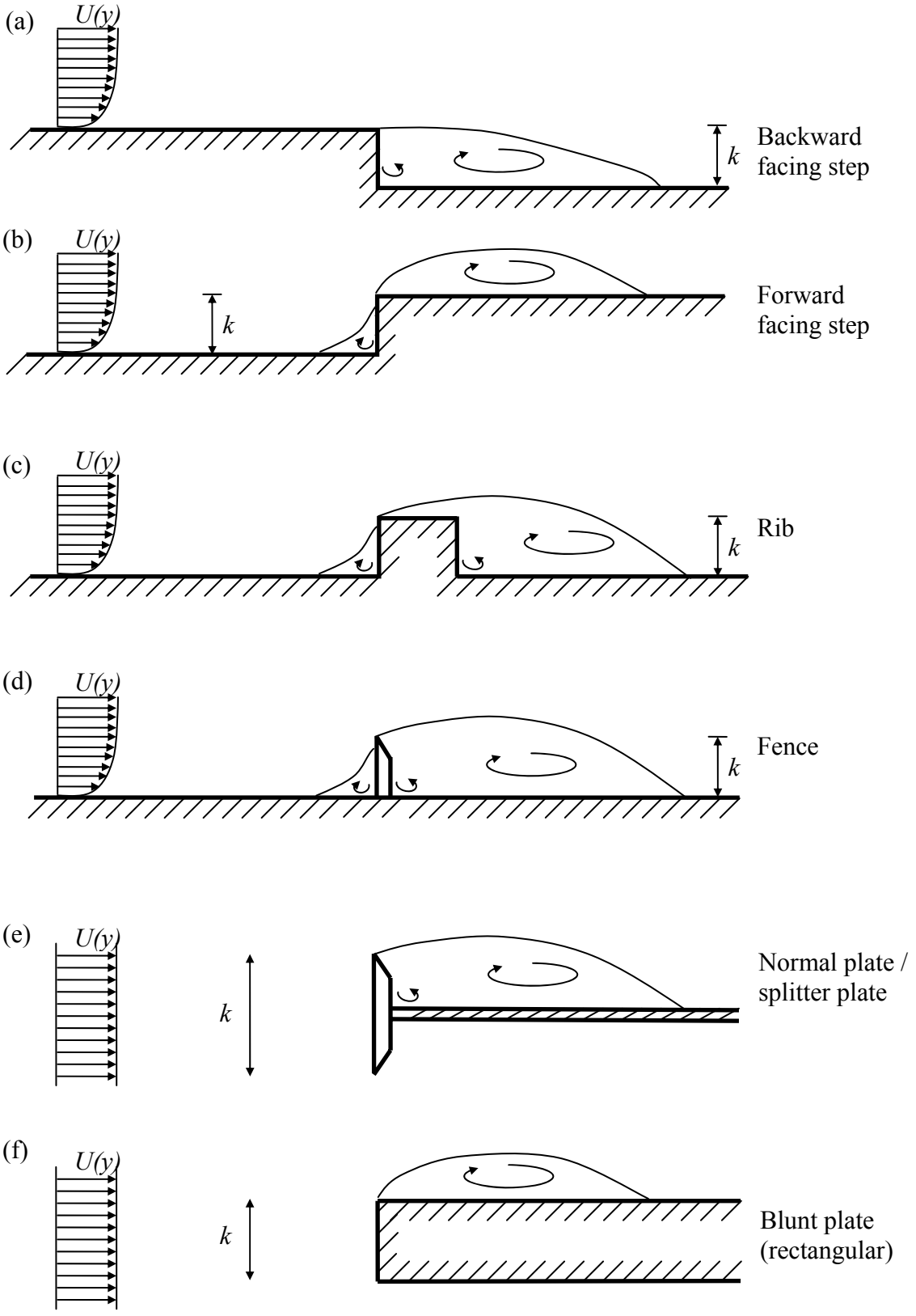

Figure 1.1: Various geometries used to induce flow separation.

1.3 Coherent Structures

It is generally accepted that turbulent shear flows are characterized by organized motions called coherent structures or eddies. Since the coherent structures are characteristic features of turbulent flows, understanding the physics of these structures is very important. The essential flow physics is believed to be buried within these coherent structures. It is generally accepted that a better understanding of coherent structures is the key to understanding turbulence and its control (Kostas *et al.*, 2005). An in-depth knowledge of coherent structures would also offer the possibility of clarifying the physical mechanism through which turbulent energy is produced and dissipated into heat. In spite of concerted research on coherent structures over the past decades, they are relatively less understood compared with one-point turbulent statistics. As rightly noted by Moin and Moser (1989), the present knowledge of organized motions has seldom been used in turbulence theories or quantitative models of turbulence. This was attributed to lack of quantitative definition of organized structures and an objective means for assessing their contribution to turbulence stresses, and their importance in the production of turbulence.

The process of identifying and describing coherent structures has been a very challenging undertaking since they are, more often than not, hidden amongst the incoherent turbulent motions (Kostas *et al.*, 2005). With the advent of increasing computing power, large volume of flow data can now be collected to study turbulence in its full complexity. Hence, to extract the most useful structural information about the physical processes, this large volume of data must be summarized in a concise manner. A variety of techniques such as Fourier transforms, conditional sampling and wavelet

transforms have been used to study coherent structures (Moin and Moser, 1989). The proper orthogonal decomposition (POD) has emerged as one of the most powerful statistical technique for extracting dominant features and identifying coherent structures. The POD technique was first introduced in turbulence research by Lumley (1967) in an attempt to systematically identify coherent structures in the turbulent flows and subsequently by Sirovich (1987) and Berkooz *et al.* (1993).

One of the most attractive features of the POD is that it can effectively compress and summarize large quantities of data so that the most useful information about the physical processes occurring maybe extracted (Kostas *et al.*, 2002). The POD captures the most energetic and hence largest structures of the flow in the first modes. In other words, if the dynamics of the flow is dominated by a few large flow structures the data can be represented satisfactorily using only a few of the first modes. More importantly, the contribution of the extracted eddies to turbulence stresses and their importance of turbulence production can be determined.

1.4 Research Motivation and Objectives

As discussed above, there are both practical and fundamental motivations to understand the dynamics of separated and reattached turbulent flows, and turbulent flows subjected to adverse or favorable pressure gradients. Numerous numerical and experimental studies have been conducted to investigate the characteristics of separated and reattached flows in zero pressure gradient (ZPG). The effects of adverse and favorable pressure gradients on attached turbulent flows have also been studied quite extensively. However, only a few studies have explored the separated and reattached flows in the presence of adverse and favorable pressure gradients. The combined effects of separation and pressure

gradient become far more complicated than either separation in ZPG or attached turbulent shear flows subjected to adverse or favorable pressure gradients. There is a need, therefore, to conduct extensive and detailed experiments to explore the effects of pressure gradients on separation and reattachment. A better understanding and comprehensive data from these types of flows will not only provide ground work for numerical studies but will also lead to the design of more efficient engineering systems.

The objectives and scope of this research are as follows:

(a) To study the effects of adverse and favorable pressure gradients on the characteristics of separated and reattached turbulent flows.

(b) To accomplish the primary objective by employing particle image velocimetry (PIV) as the measurement technique to obtain detailed instantaneous whole flow field measurements for mean velocity, Reynolds stresses, triple correlations and various terms in the transport equations for turbulent kinetic energy and Reynolds stresses.

(c) To apply the proper orthogonal decomposition technique (POD) to document the salient features of the large scale structures and to study the contributions of these large scales to the Reynolds normal and shear stresses.

1.5 Outline of the Thesis

In this thesis, an experimental study of separated and reattached turbulent flows in variable pressure gradients using PIV will be presented. In Chapter 2, a brief literature review of previous studies pertaining to canonical near-wall turbulent flows will be presented at first to simplify the complexity of the present study. Then, the relevant

studies pertaining to attached flows under pressure gradients, and separated and reattached flows in zero pressure gradients will be summarized. Subsequently, a review of previous studies on separated and reattached turbulent flows subjected to pressure gradients will be presented. Finally, the application of the POD technique to study coherent structures will be reviewed. Chapter 3 will provide an overview of the principles of PIV. The experimental setup and measurement procedure will be reported in Chapter 4. Results obtained in the converging and diverging channels without a rib on the channel floor will be presented in Chapter 5. Discussion of results on separated and reattached flows obtained in the converging and diverging channels will be presented in Chapter 6. Chapter 7 will report on the implementation of the POD, POD analysis of the experimental data and the reconstruction of the Reynolds stresses. Conclusions and an outline for future work will be presented in Chapter 8.

CHAPTER 2: Literature Review

A review of previous studies pertaining to turbulent flow separation and reattachment in pressure gradients is presented in this chapter. To gradually build understanding and simplify the complexity of the present study, at first a brief review of the canonical near-wall turbulent flows will be presented. Then, the effects of pressure gradients, and the phenomena of separation and reattachment will be treated separately. This will help develop the background understanding of the effects of separation and reattachment as well as the pressure gradient and better facilitate the review of the effects of the pressure gradients on separated and reattached flows. Finally, the application of the proper orthogonal decomposition to study coherent structures in wall bounded flows will be reviewed and the specific goals of the present study will be outlined.

2.1 Canonical Near-Wall Turbulent Flows and their Scaling Laws

The zero-pressure gradient turbulent boundary layers and two-dimensional fully developed channel flows are often referred to as canonical near-wall flows. They have been extensively researched because of their relatively simple geometry and flow physics. It is beyond the scope of this study to provide detailed review of previous studies. Therefore, only a brief summary of the main characteristics of canonical flows essential to the understanding of the more complex flow features in upcoming sections will be provided here.

According to classical theories, a typical boundary layer profile can be divided into two distinct layers; namely the inner region and the outer region. Viscosity plays an

important role in the inner region very close to the wall, while the outer region of the boundary layer is dominated by inertial effects. At sufficiently high Reynolds numbers, there exists an overlap region between the inner and outer regions. The flow dynamics in the overlap region are dependent on both viscous and inertial effects.

The extent of the various regions in terms of wall variables is illustrated in Figure 2.1. In the figure, $U^+ = U/U_\tau$, and $y^+ = yU_\tau/\nu$, where, U_τ (= $(\tau_w/\rho)^{0.5}$, τ_w is the wall shear stress and ρ is the density) is the friction velocity and ν is the kinematic viscosity. As shown in Figure 2.1, the inner region consists of the viscous sublayer, the buffer region and the overlap region. The velocity profile varies linearly with distance from the wall (i.e., $U^+ = y^+$) in the viscous sublayer. The viscous sublayer is also known as the linear region and may extend from $0 \le y^+ \le 5$ while the buffer region extends from $5 \le y^+ \le 30$. The outer region of the boundary layer extends from $30 \le y^+ \le \delta^+$, where δ is the boundary layer thickness. In this thesis, the boundary layer thickness is defined as the y-distance from the wall where local streamwise velocity is 99% of the maximum streamwise velocity. The overlap region extends from $30 \le y^+ \le 0.2\delta^+$.

Prandtl first proposed the boundary layer equations by simplifying the two dimensional incompressible Navier-Stokes equations for steady flows. For a boundary layer, it is assumed that $\delta << L$ (δ is the boundary layer thickness and L is the characteristic length of the plate). It follows from order of magnitude analysis that $\partial/\partial x << \partial/\partial y$. Thus, for incompressible turbulent boundary layer, the governing equations become,

$$\frac{\partial U}{\partial x} + \frac{\partial V}{\partial y} = 0, \tag{2.1}$$

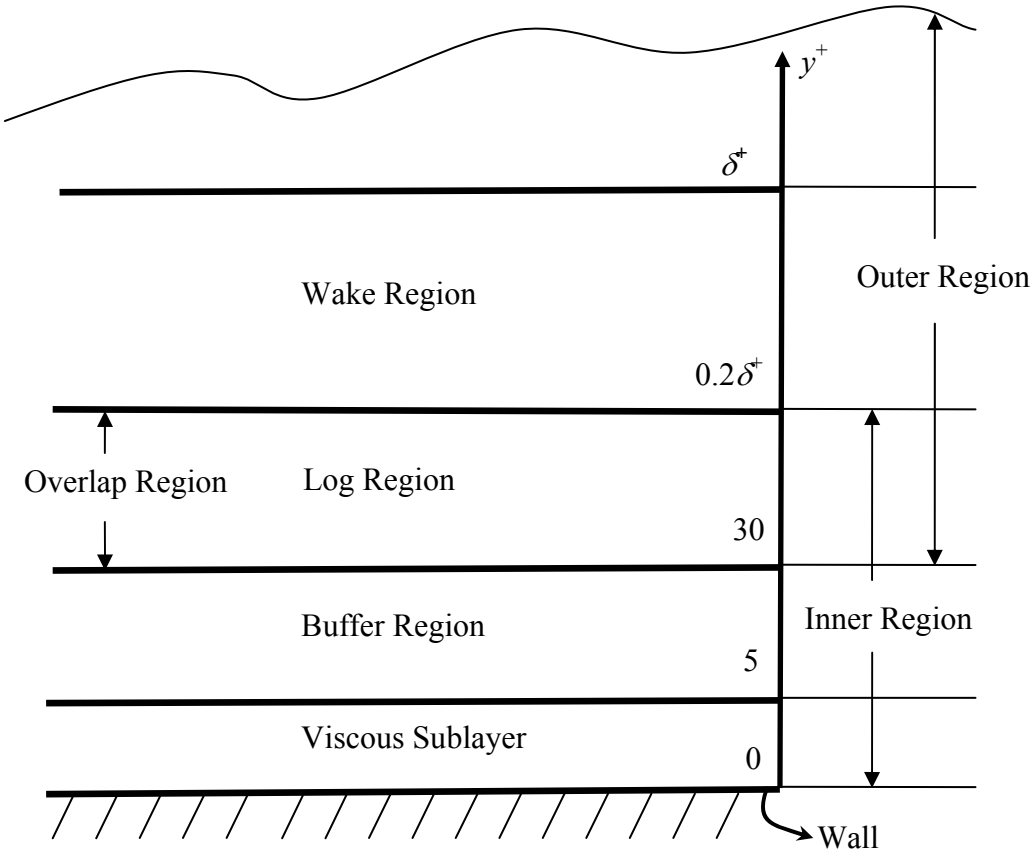

Figure 2.1: Schematic of different regions in a typical turbulent boundary layer profile.

$$U\frac{\partial U}{\partial x}+V\frac{\partial V}{\partial y}=-\frac{1}{\rho}\frac{\partial P}{\partial x}+\frac{\partial}{\partial y}\left[\nu\frac{\partial U}{\partial y}-uv\right], \tag{2.2}$$

where, P is the thermodynamic pressure, ρ is the density, ν is the kinematic viscosity and $-uv$ is the Reynolds shear stress. At the wall, where the turbulent shear stress is zero, the wall shear stress is given by,

$$\tau_w=\mu\left.\frac{\partial U}{\partial y}\right|_{y=0}. \tag{2.3}$$

The displacement thickness, δ^*, is the distance the plate would have to be moved into the flow so that the loss of the mass flux (due to the reduction in the uniform flow

area) is equivalent to the loss the boundary layer causes. For an incompressible flow the displacement thickness is given by,

$$\delta^* = \int_0^{\delta} (1 - \frac{U}{U_e}) dy \cdot \tag{2.4}$$

Similarly, the momentum thickness, θ, is the distance the plate would be moved into the flow so that the loss of momentum flux is equivalent to the loss the boundary layer actually causes. For an incompressible flow, the momentum thickness is given by,

$$\theta = \int_0^{\delta} \frac{U}{U_e} \left(1 - \frac{U}{U_e} \right) dy \, . \tag{2.5}$$

Therefore, the displacement thickness and momentum thickness provide measure of mass and momentum deficit associated with the boundary layer. The displacement and momentum thickness are appreciably easier to evaluate accurately from experimental data than the boundary layer thickness, δ. This fact, combined with their more physical significance accounts for their common use as characteristic boundary layer parameters. The ratio of displacement thickness to momentum thickness gives the dimensionless profile shape factor:

$$H = \frac{\delta^*}{\theta} \cdot \tag{2.6}$$

2.1.1 The Inner Layer

In the inner region, the flow is presumed to depend only on the wall shear stress (τ_w), the density (ρ), the dynamic viscosity (μ), and the distance from the wall (y). From dimensional considerations, the following dimensionless functional relationship is obtained for the mean velocity,

$$U^+ = f_i[y^+, \delta^+], \tag{2.7}$$

where, δ^+ is the Reynolds number based on the boundary layer thickness (δ) and the friction velocity and indicates the ratio of the outer to inner length scales. If the dimensionless functional relationship f_i is independent of Reynolds number, i.e.,

$$U^+ = f_i[y^+], \tag{2.8}$$

it implies that complete similarity exists in the inner region. Equation 2.8 is commonly referred to as the universal law of the wall.

2.1.2 The Outer Layer

In the outer region, the local velocity is independent of viscosity (ν) but dependent on the distance from the wall (y), the boundary layer thickness (δ) and a velocity scale (U_o). Unlike the inner layer, no equivalent theory has been proposed by the classical theories for the outer layer. Instead, classical theories (Clauser, 1954; Millikan, 1938) assumed that the friction velocity is the appropriate velocity scale (i.e., $U_o = U_\tau$) and the velocity distribution is given by

$$\frac{U_e - U}{U_\tau} = f_o\left[\frac{y}{\delta}, \delta^+\right]. \tag{2.9}$$

However, an alternate theory for a zero pressure gradient turbulent boundary layer proposed by George and Castillo (1997) showed that the appropriate scale for the outer region is the freestream velocity (i.e., $U_o = U_e$). In this case, the velocity distribution is given by:

$$\frac{U_e - U}{U_e} = f_o\left[\frac{y}{\delta}, \delta^+\right]. \tag{2.10}$$

In the above two equations, f_o expresses the dimensionless functional relationship. If f_o is independent of Reynolds number, complete similarity exists in the outer region, i.e.,

$$\frac{U_e - U}{U_o} = f_o\left[\frac{y}{\delta}\right]. \tag{2.11}$$

The following mixed scaling was more recently proposed by Zagarola and Smits (1998) for the mean velocity profile:

$$\frac{U_e - U}{U_e(\delta^* / \delta)} = f_o\left[\frac{y}{\delta}\right]. \tag{2.12}$$

Besides the scaling arguments summarized above, a number of alternative theories have been proposed. These are discussed in detail in the recent article by Buschmann and Gad-el-Hak (2007).

2.1.3 The Overlap Region

The scaling law for the overlap region is often used to determine the friction velocity and is therefore of considerable importance in near-wall turbulence research. It should be noted that in the overlap region, the inner length scale (ν/U_τ) is presumably too small to control the dynamics of the flow and the outer length scale (δ) is presumably too large to be effective (Tennekes and Lumley, 1972). Hence, the dynamics of the flow are dependent on the distance from the wall (y).

2.1.3.1 The Log Law

According to the classical theory (Clauser, 1954; Millikan, 1938) the inner and outer layers can be matched in the limit of infinite Reynolds number (i.e., assuming complete similarity) to obtain the classical log law:

$$U^+ = \frac{1}{\kappa}\ln(y^+) + C \tag{2.13}$$

where, $\kappa = 0.41$ is von-Kármán constant and $C = 5.0$ is an additive constant.

The friction velocity (U_τ) can be determined by fitting the logarithmic profile (Equation. 2.13) to the mean velocity data. This is known as the Clauser plot technique which is well established for canonical near-wall turbulent flows and flows with mild pressure gradients. Since the log law parameters are assumed to be universal, U_τ is the only adjustable parameter in the log law. Once the friction velocity is obtained from this technique, the skin friction can be calculated using the following relationship:

$$C_f = 2\left(\frac{U_\tau}{U_e}\right)^2. \tag{2.14}$$

2.1.4 Turbulence Quantity Scaling

Most of the earlier boundary layer analyses adopted U_τ^2 and U_τ^3 as the appropriate velocity scale for Reynolds stresses and various energy budget terms respectively, (see, Krogstad and Antonia, 1999), as suggested by classical theories. However, George and Castillo (1997) suggested U_e^2 as the appropriate velocity scale for the Reynolds normal stresses and $U_e^2 d\delta/dx$ as the appropriate scale for the Reynolds shear stress. They also showed that a mixed velocity scale, $U_\tau^2 U_e$, is the correct velocity scale for the triple velocity correlations, production and dissipation terms in the energy budget.

2.1.5 Reynolds Number Effects

The behavior of fluid flows is primarily governed by Reynolds number. In near-wall turbulence research, variations of Reynolds numbers are used. These include Reynolds

number based on momentum thickness Re_θ (= $U_e\theta/\nu$); Reynolds number based on step height Re_k (= $U_e k/\nu$); Reynolds number based on half channel height Re_h (= $U_e h/\nu$); and Reynolds number based on boundary layer thickness and friction velocity δ^+ (= $U_\tau\delta/\nu$).

Numerous studies have been conducted in the past to study how the mean flow characteristics and turbulent quantities vary with Reynolds number (Spalart 1988; Purtell *et al*., 1981; Degraaff, 1999; Österlund *et al*., 1999). The studies on wall bounded flows prior to 1994 were critically reviewed by Gad-el-Hak and Bandyopadhyay (1994). They showed that even at the highest Reynolds number flows available in the literature, turbulence quantities scaled using inner variables show Reynolds number effects. The results obtained from prior studies demonstrate that as Re_θ increases, the mean velocity profile becomes fuller and the shape factor, H, decreases accordingly.

Purtell *et al.* (1981) investigated turbulent boundary layers in the range $485 \leq Re_\theta \leq 5100$. It was found that even at the lowest Reynolds number, the log region does not disappear. The wake function showed strong Reynolds number effects for $Re_\theta < 2000$. An increase in the Reynolds number is accompanied by a decrease in the skin friction. A much larger extent of similarity was observed for the streamwise turbulent intensity when boundary layer thickness was used as length scale compared to inner variables.

Wie and Willmarth (1989) conducted experiments in a fully developed channel using a laser Doppler anemometry (LDA). The Reynolds number based on half channel height and centerline velocity, Re_h, varied from 6000-80000. The streamwise turbulent intensity profiles show similarity up to $y^+ = 12$ when scaled with inner variable but the transverse turbulent intensity and Reynolds shear stress profiles did not. Durst *et al.* (1998) studied Reynolds number effects in fully developed channel flows using a very

high resolution LDA. The Reynolds number, Re_h, varied from 1550-5650. They reported that the streamwise turbulent intensity scaled on inner variables for $y^+ \leq 50$. A peak value of $u_{max}^+ = 2.55$, independent of Reynolds number, was observed inside the buffer region, at $y^+ = 12$, for all the profiles. Ching *et al.* (1995) reported experiments in turbulent boundary layers at Re_θ ranging from 400 to 1320. The correlation coefficient displays a plateau with a value of about 0.4 in the region $y^+ \geq 10$. The streamwise and transverse turbulent intensity show Reynolds number effects well in to the viscous sublayer. The peak magnitude and location of transverse turbulent intensity and Reynolds shear stress increase with increasing Re_θ. A number of DNS results (i.e., Kim *et al.*, 1987 and Spalart 1988) also showed that Reynolds number effects penetrate down to the near-wall region.

2.2 Boundary Layer and Channel Flows with Pressure Gradient

Pressure gradients greatly complicate the flow characteristics, and as a result, pressure gradient boundary layers have offered a tremendous challenge both in theory and experiment. The pressure gradient parameter (K) is a non-dimensional parameter commonly used to characterize the pressure gradient,

$$K = \frac{\nu}{U_e^2}\frac{dU_e}{dx}, \tag{2.15}$$

where ν is the kinematic viscosity and U_e is the local maximum streamwise velocity. The Clauser pressure gradient parameter (β) is another non-dimensional parameter frequently used to characterize the pressure gradient and is given by,

$$\beta = \frac{\delta^*}{\tau_w}\frac{dP}{dx}, \tag{2.16}$$

where δ^* is the displacement thickness and τ_w is the wall shear stress. When dP/dx is varying in such a way that β is constant, then the skin friction (C_f) and shape factor (H) are also constant and the boundary layer is said to be in equilibrium. However, it should be noted that in case of separation, τ_w approaches zero and β tends to infinity. The pressure coefficient, c_p, and its gradient dc_p/dx are other useful parameters used to characterize the pressure gradient. The pressure coefficient is given by,

$$c_p = \frac{P - P_{ref}}{P_0 - P_{ref}}. \tag{2.17}$$

P is the static pressure, P_{ref} is pressure at a reference location and P_0 is the stagnation pressure. The relationship between C_f and H is also given by Clauser, and known as the Clauser shape factor,

$$G = \frac{H - 1}{H\left(0.5C_f\right)^{0.5}}. \tag{2.18}$$

A considerable amount of research has also been dedicated to attached boundary layer flows in pressure gradients. A summary of some selected previous experimental and numerical studies is provided in Table 2.1. The table provides a summary of the type of pressure gradient that was investigated, the value of the dimensionless pressure gradient parameter, the measurement technique and the flow quantities measured. In the table, TKE is the turbulent kinetic energy, P_k, *Diff* and ε are, respectively, the production, diffusion and the dissipation rate terms in the transport equation for the turbulent kinetic energy, l_m is the mixing length, S and F are, respectively, the skewness and flatness factors. Blackwelder and Kovasznay (1970, 1972) obtained detailed measurements in a converging channel with curved lower wall. They found that the absolute values of the

Table 2.1: Summary of previous attached boundary layer and channel flow studies in pressure gradients.

Authors	**Flow**	**Technique**	**Relevant Quantities**	***K* or β or dc_p/dx**
Abertine & Eaton (2005, 2006)	APG, FPG	LDA, FISF	*U, u, v, P_k, TKE*	$-1.4 < \beta < 2.31$
Angele & M.-Klingmann (2006)*	APG	PIV, LDA	*U, C_f, u, v, uv*	$0.1 < dc_p/dx < 0.7$
Ruetenik &Corrison (1955)	APG	Hot-wire	*U, u, v, w, uv*	
Samuel & Joubert (1974)*	APG	Hot-wire, Pitot Tube	*U, u, v, w, uv*	$0.06 < dc_p/dx < 0.3$
Skåre & Krogstad (1994)*	APG	Hot-wire, Pitot Tube	*U, u, v, w, uv, l_m, P_k, Diff, ε*	$12 < \beta < 21.4$
Spalart & Watmuff (1993)*	APG, FPG	Hot-wire, DNS, Preston Tube	*U, u, v, w, C_f, ε*	$-0.30 < \beta < 2$
Kline *et at.* (1967)*	ZPG, FPG, APG	Hot-wire,	*U*, others	$0.21 < K\times10^6 < 3.85$ $-2 < K\times10^6 < -0.25$
Cardoso *et al.* (1991)	FPG	Hot-wire	*U, C_f, u*	$-3.73 < \beta < -0.35$
Finnicum & Hanratty (1998)	FPG	DNS	*U, C_f, u, v, w, uv, TKE, P_k*	$K\times10^6 = 2.8, 2.03$
Ichimiya *et al.* (1998)*	FPG	Hot-wire	*U, u, S, F*	$0 < K\times10^6 < 3$
Blackwelder & Kovasznay (1972)*	FPG	Hot-wire	*U, u, v, uv*	$0 < K\times10^6 < 4.8$

* Curved wall used to create the pressure gradient.
DNS: Direct Numerical Simulation, LDA: Laser Doppler Anemometry, FISF: Fringe Imaging Skin Friction Technique.

mean velocities and stresses were approximately constant along a mean streamline except in the immediate vicinity of the wall. However, the relative values of u/U_e, v/U_e and $-uv/U_e^2$ decrease as the flow accelerates along the channel. Their results also indicate that the displacement and momentum thicknesses and the Reynolds number based on momentum thickness decrease in the region prior to laminarization. They found that the log region disappeared in the region of maximum acceleration ($K = 4.8\times10^{-6}$). However, at the location of lower acceleration ($K = 1.0\times10^{-6}$), friction velocity obtained from log

law was within 1% of the corresponding values obtained by measuring the velocity gradient in the viscous sublayer. The skin friction was observed to decrease in the converging section followed by an increase in the section outside convergence.

Ichimiya *et al.* (1998) studied relaminarization of turbulent boundary layers under strong FPG. The pressure gradient was created by a curved plate, preceded and followed by parallel plates. In the curved wall section, the acceleration parameter ranged from $0 \leq K \leq 3.0\times10^{-6}$. The maximum value of turbulent intensity (u) decreased in the converging section and then increased in the parallel downstream section. Escudier *et al.* (1998) reported experimental study of the response of an initially turbulent boundary layer to a variable FPG. The flow experienced a peak acceleration of $K = 4.8\times10^{-6}$. Integral parameters such as the displacement thickness (δ^*) and momentum thickness (θ) start to decay upstream of the contraction when K approaches 1.0×10^{-6}. The minimum values of the boundary layer thickness (δ) and the two integral thicknesses are observed at the point where K has decreased from its peak value to 3.0×10^{-6}. The shape parameter (H) increases abruptly when K exceeds 3.0×10^{-6}. H continues to increase and attains a peak value of 2.4 as K falls back to near zero. The mean velocity profiles become progressively "fuller" and the streamwise turbulent intensity decreases in the mid boundary layer with increasing value of K. Both the mean velocity and streamwise turbulent intensity profiles show an abrupt change where K increases to 3.0×10^{-6} which is consistent with the shape factor increase. They suggested that this critical value of K is likely dependent upon the initial value of Re_θ.

Kline *et al.* (1967) reported measurements in ZPG, APG and FPG flows. Their qualitative and quantitative measurements were focused on the regions closest to the

wall. They obtained wall shear stress in ZPG and in mild and strong APG and FPG using the Clauser plot technique. They also obtained wall shear stress from the slope of the mean velocity in the viscous sublayer ($y^+ \leq 5$) where the velocity profile is linear. On average, the two values differed by 10% for ZPG flow. For mild adverse and favorable pressure gradients, the maximum deviation was as much as 14% and 22%, respectively. They remarked that the wall shear stress obtained from the wall-slope method is more accurate than values from the log law. Qualitative measurements of ZPG in the viscous sublayer showed that the region is three dimensional and unsteady.

Samuel and Joubert (1974) studied boundary layer developing in an increasingly APG. They obtained skin friction values from the log law that were in good agreement with values obtained from Preston tubes and floating point element meter. Spalart and Watmuff (1993) reported experimental and numerical studies of turbulent boundary layer in APG preceded by FPG. Skin friction measurements were obtained using Preston tubes. The DNS results showed that the velocity profile in the buffer and lower log layer shifts up in FPG (β = -0.3), and down in APG ($0 < \beta < 2$). Similar but weaker trend in the same direction is also reported for the experimental data. Skåre and Krogstad (1994) conducted measurements in an equilibrium boundary layer in a strong APG ($12 < \beta < 22$). The log law and Preston tubes were found to produce the same values of skin friction. Due to the strong APG, the Reynolds shear stress ($-uv$) attained values considerably higher than the wall shear stress (τ_w). The measurements showed that the stress ratios are similar to those measured in ZPG turbulent boundary layers, indicating that the distribution of kinetic energy between the different stresses is unaffected by pressure gradient.

Turbulent boundary layers subjected to mild APG created over a 4° ramp, preceded by FPG, was studied by Aubertine and Eaton (2005). The mean velocity profiles become 'less full' in the diverging section. The velocity profiles exhibit a substantial log region but as the flow evolves downstream, the wake occupies an increasing portion of the boundary layer thickness. In this flow, the dimensionless pressure gradient parameter ranged from $-1.40 < \beta < 2.31$. Their results also indicate that the displacement and momentum thicknesses and the Reynolds number based on momentum thickness increase in the diverging section. The Reynolds stresses were found to be similar in the inner layer to ZPG profiles but higher in the outer layer.

Angele and Muhammad-Klingmann (2006) reported PIV and LDA measurements in APG with weak separation. The mean velocity profiles demonstrated an overlap with the log law for the flow where $\beta \leq 4.9$. The log law region vanished near the separation bubble.

2.3 Geometry Induced Separation

As mentioned earlier, a number of laboratory geometries have been devised to generate two-dimensional separated and reattached flows, and to study their transport and mixing properties. Backward facing steps, fences and blunt plates are among the most extensively studied and reported geometries in the literature. Figure 2.2 demonstrates various regions of a separated and reattached flow. Irrespective of the specific geometry, the flow field can be divided into two regions: (i) the separated region and (ii) the recovery/redevelopment region. The separated region spans from the point of separation at the upstream edge of the step to the location where the flow reattaches while the region

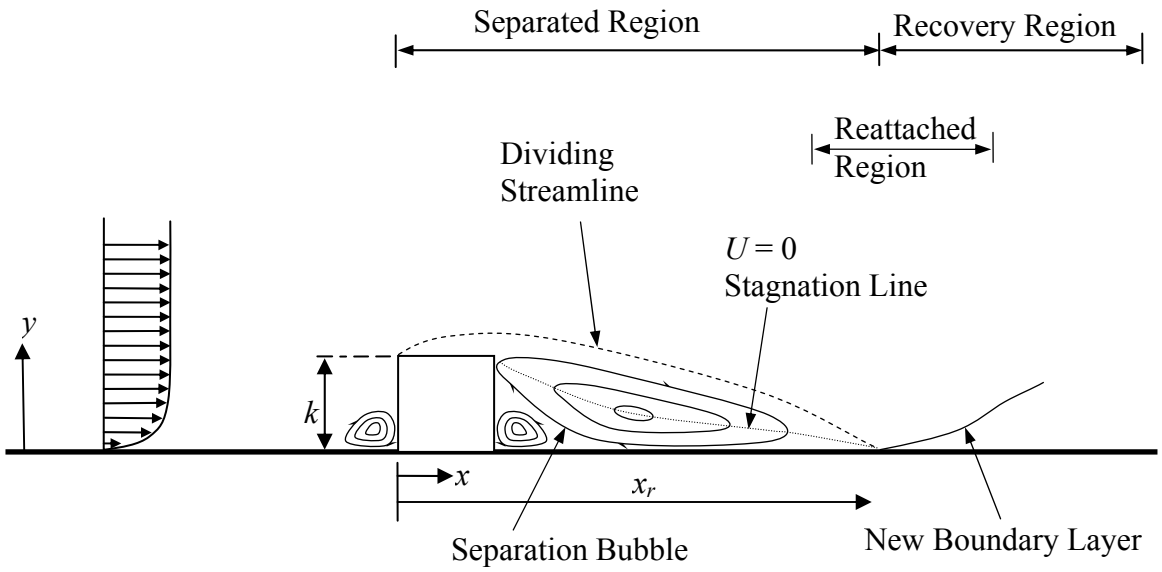

Figure 2.2: Flow regions downstream of a rib.

downstream of the reattachment region is called the recovery/redevelopment region. In a turbulent flow, the instantaneous location of reattachment fluctuates. The separated flow downstream of the step causes recirculation which is referred to as the separation bubble. The reattachment length, x_r, corresponds to the distance between the location of separation and the mean reattachment point.

2.3.1 Geometry Induced Separation without Pressure Gradients

A significant amount of research has been dedicated to studying the separated and reattached flows using various geometries without pressure gradients. A summary of some selected previous experimental and numerical studies is provided in Table 2.2. The table provides a summary of the type of geometry used, the Reynolds number based on the step height and the approach velocity, blockage ratio ($k/2h$), perturbation strength (k/δ), and the flow quantities measured. In this table, ν_t and Ω_z are, respectively, the eddy viscosity and the spanwise mean vorticity. Backward facing step has been

Table 2.2: Summary of previous boundary layer and channel studies in separated and reattached flows with zero pressure gradient.

Authors	Block	Technique	Re_k	$k/(2h)$	k/δ	Relevant Quantities
Castro (1998)*	Rib	Pitot tube, hot-wire	7500, 15000		0.069, 0.157, 0.169	c_p, U, u^2, $-uv$, ε, l_m, ν_t,
Bergeles & Athanassiadis (1981)*	Rib, Block	Hot-wire	27000	0.08	2.08	U, x_r
Abu-Mulaweh (2005)†	FFS	LDA	373.5-746.9	0.02, 0.03		U, V, u, v
Tachie *et al.* (2001) †	FFS	LDA	960-1890	0.03-0.06	0.07-0.09	H, G, U, u, C_f
Castro & Epik (1998) *	Blunt Plate	Hot-wire, Preston	6500		0.48, 0.42	U, u^2, v^2, w^2, $-uv$, u^3, u^2v, uv^2, v^3, uw^2, u^2w, w^3, TKE
Djilali & Gartshore (1991)†	Blunt Plate	Hot-wire	50000	0.06		c_p, C_f, U, u
Bradshaw & Wong (1972)*	BFS	Pitot-tube, Hot-wire	41000	0.20		G, U, u^2, v^2, $-uv$
Jović (1998) †	BFS	Hot-wire, LOI	6800-37200	0.04, 0.09	0.50-1.22	c_p, C_f, u, k, ν_t,
Kostas *et al.* (2002)†	BFS	PIV	4660	0.02	0.19	U, P, Ω_z, u^2, v^2, $-uv$
Piirto *et al.* (2003)†	BFS	PIV	15000	0.33	1.67	U, u^2, v^2, w^2, $-uv$, TKE

† Measurements have been reported in separated as well as redevelopment region.
*Measurements have been reported in redevelopment region only.
LOI: Laser Oil Interferometry

investigated quite extensively using experimental and numerical techniques. Detailed investigation of turbulent flow of BFS was conducted by Le *et al*. (1997) using direct numerical simulation (DNS) at Reynolds number based on step height Re_k = 5100 with

an expansion ratio (ER = outlet height/inlet height) of 1.20. A large negative skin friction peak ($\approx 3\times10^{-3}$) was observed in the reattachment region and the peak production of kinetic energy and dissipation were found at x/k = 1. Kostas *et al.* (2002) performed experiments over BFS at Re_k = 4660 using PIV and flow visualizations. The streamlines showed a recirculation region as well as a secondary recirculation region at the corner of the step. The largest values of Reynolds stresses are found upstream of reattachment (x_r/k = 6.28) followed by a rapid decline.

Djilali and Gartshore (1991) conducted measurements over a blunt plate of aspect ratio (AR = length/height) of 11.1 using a pulsed-wire surface shear stress probe, hot-wire and pulsed-wire anemometry at Re_k = 50000. They reported a decrease in reattachment length with increasing solid blockage defined as the ratio of the obstacle height to the channel or wind tunnel height. Backflow flow velocities were observed to be as large as $0.3U_e$ in the recirculation region. Similar to BFS, the peak streamwise turbulent intensity occurs upstream of reattachment.

Castro and Epik (1998) reported experimental and numerical results for a blunt plate of k = 9.6 mm at Re_k = 6500 using hot-wire and Preston tubes and CFX-4 (commercial CFD code). The transverse turbulent intensity and Reynolds shear stress retain peaks at reattachment much further downstream compared to the streamwise turbulent intensity. They reported that the redevelopment process is slow and non-monotonic in nature.

Tachie *et al.* (2001) performed LDA measurements of mean velocity and turbulence intensity upstream and at various locations downstream of a 3 mm forward facing step (FFS) in a shallow open channel flow at Reynolds number ranging from 960

$\leq Re_k \leq 1890$. Their results indicate that far downstream of the step i.e., $x/k \geq 50$, the mean velocity field is reasonably similar to the one obtained upstream of the FFS. However, turbulent intensity profiles do not collapse satisfactorily onto the corresponding upstream profiles even at $x/k \geq 100$. They also observed two peaks downstream of the reattachment location in the streamwise turbulent intensity profile which had not been reported in many of the earlier measurements.

A study of the forward facing step flow was conducted by Abu-Mulaweh (2005). He studied the effect of step heights by conducting experiments for 0, 11 and 22 mm step heights. Measurements of flow and thermal fields were obtained using LDA and a cold wire anemometry. It was found that, within the separation bubble, the mean turbulent intensity rises rapidly especially near the center of the bubble due to high mixing and large-scale unsteadiness, and it reduces as one moves to the reattachment point and over the boundary layer development region. As the FFS height increases, the velocity and temperature fluctuations are observed to increase. Furthermore, the reattachment length was found to decrease from 6.45k to 4.41k as the FFS height increased from 11 mm to 22 mm.

2.3.2 Geometry Induced Separation with Pressure Gradients

Most of the previous studies in separated and reattached flows have been performed in zero pressure gradient. In the presence of pressure gradient, the separated and reattached flow becomes much more complex. The following is a review of the previous studies of separated and reattached flows under the influence of pressure gradients. The pertinent information and measurement techniques used in these studies are summarized in Table 2.3.

Table 2.3: Summary of relevant previous studies involving separated and reattached flow with nonzero pressure gradient.

Authors	Flow	Geometry	Technique	Re_k	$k/(2h)$	Quantities
Kuehn (1980)	APG, FPG & ZPG	BFS	*	37400, 78600	0.12, 0.25	U, x_r
Driver & Seegmiller (1985)	APG & ZPG	BFS	LDA	37400	0.11	x_r, C_p, C_f, δ^*, θ, U, u^2, v^2, $-uv$, uv^2, v^3, P_k, ε, ν_t
Ra & Chang (1990)	APG, FPG & ZPG	BFS	Manometer	17000 - 72000	0.12, 0.23	C_p, x_r
Cutler & Johnston (1989)	APG	Fence	Hotwire, Pitot Tube	19000	0.07	U, V, u^2, v^2, $-uv$, P_k, ε

* The short technical note does not specify the type of instrumentation used.

Kuehn (1980) reported reattaching flow over a backward facing step in an adverse pressure gradient at $Re_\theta = 4950$. The step heights of 12.7 mm and 25.4 mm were used, and the corresponding Reynolds numbers based on step height were $Re_k \approx 37400$ and 78600. The roof immediately downstream of the backward facing step was tilted at several angles in the range $-10° \leq \alpha \leq 6°$. They observed that increasing the strength of the adverse pressure gradient caused the reattachment length to increase from $x_r/k = 6.75$ ($\alpha = 0°$) to $x_r/k = 9.5$ ($\alpha = 6°$) for $k = 12.7$ mm. For $k = 25.4$ mm a much more dramatic increase was observed and the reattachment length increased from $x_r/k = 7$ ($\alpha = 0°$) to $x_r/k = 19$ ($\alpha = 6°$). The opposite was observed when favorable pressure gradient was imposed. In this case, the reattachment length decreased to $x_r/k = 4.5$ ($\alpha = -10°$) for $k = 12.7$ mm. It should be noted that no turbulent quantities were reported in that study.

Driver and Seegmiller (1985) conducted measurements over a backward facing step in diverging channel flows using a LDA at $Re_\theta = 5000$. In their study, 12.7 mm step

was used to produce the flow separation. Immediately downstream of the step, the top wall was linearly deflected at several angles ranging from $-2° \leq \alpha \leq 10°$. The reattachment length was found to increase monotonically from $x_r/k = 6$ ($\alpha = -2°$) to $x_r/k = 10$ ($\alpha = 10°$). Detailed measurements of mean velocities, Reynolds stresses, triple correlation and turbulent kinetic energy balance were reported as far downstream as 32 step heights for $\alpha = 0°$ and 6°. The Reynolds stresses were found to be similar in both cases of wall divergence (i.e., $\alpha = 0°$ and 6°). However, the Reynolds stresses downstream of reattachment decayed more slowly when $\alpha = 6°$ than in the zero pressure gradient case. The triple velocity correlations were observed to diminish rapidly on the lower wall upon approaching reattachment while production of turbulent kinetic energy was found to decrease in case of adverse pressure gradient downstream of the step.

Ra and Chang (1990) investigated reattached flow downstream of a backward facing step at Reynolds number ranging between $530 \leq Re_\theta \leq 1100$. For the two step heights, $k = 20$ mm and $h = 45$ mm, the Re_k was in the range of $17000 \leq Re_k \leq 72000$. Downstream of the step, the top wall was curved to create several different configurations of adverse, favorable and zero pressure gradients for the two steps. They found that the reattachment length increased with increase in streamwise pressure gradient. They also found that the reattachment length of the consistently increasing streamwise pressure gradient is larger and its growth became more rapid with increase of the pressure gradient compared with that of the constant pressure gradient. In that study no detailed turbulent quantities were reported.

Cutler and Johnston (1989) reported the relaxation of a reattached turbulent boundary layer downstream of a wall fence, $k = 7.37$ mm, in an adverse pressure gradient

at Re_k = 19000. The adverse pressure gradient imposed on the turbulent boundary layer was adjusted by means of a nonlinear curved roof to keep the boundary layer in equilibrium. In their study, the flow separated and reattached upstream of the divergence. The measurements were conducted only in the redevelopment region up to 83 step heights. They indicated that the results downstream of reattachment were qualitatively similar to those downstream of a zero-pressure gradient reattachment data of Driver and Seegmiller (1985) and Kim *et al.* (1980). All the mean velocity profiles in the diverging section exhibit an extensive log region. The Reynolds stresses fall monotonically downstream of reattachment while the mixing length, l_m, and eddy viscosity, ν_t, peak close to reattachment and subsequently decay. The Clauser shape parameter (G) rapidly falls to 11.4 at about $x = 61k$ downstream of reattachment and remains constant.

2.4 POD and Coherent Structures

Many turbulent flows are characterized by structures and in particular by characteristic recurrent forms that are called coherent structures (Holmes *et al.* 1998). As mentioned earlier, a thorough understanding of their dynamics and interactions is very important to understanding turbulence and its control (Kostas *et al.* 2005). The proper orthogonal decomposition (POD) was first introduced in the context of fluid mechanics by Lumley (1967) to identify and study the dynamics of the large-scale structures in turbulent fields with finite total energy. The POD decomposes a series of experimental or numerical measurements into a number of modes which make up an orthonormal basis spanning the entire data set. The POD provides an optimal set of basis functions for an ensemble of data to reconstruct the coherent structures as mixtures of POD modes. The basis functions it yields are called empirical eigenfunctions, empirical basis functions, or empirical

orthogonal functions (Holmes *et al*. 1998). The POD captures the most energetic and hence largest structures of the flow in the first modes. In other words, if the dynamics of the flow is dominated by a few large flow structures the data can be represented satisfactorily using only a few of the first modes.

The POD analysis is based on correlation functions. The need to input the correlation functions also makes implementation of the POD difficult when applied to PIV data. This is because the high spatial resolution of the PIV data makes the direct computation of the correlation matrix difficult due to storage requirements (Shinneeb 2006). In contrast to the direct POD method, however, a popular method called the snapshot suggested by Sirovich (1987) is more relevant in this situation and gives equivalent results. In this case, each instantaneous PIV measurement is considered to be a snapshot, N, of the flow while, M is the total number of vectors in the field. Graftieaux *et al*. (2001) tested these two methods and found no significant differences, apart from the fact that greater computation time and memory are required for the direct method. The snapshot method usually requires $O(N^3 + N^2M)$ operations for completion while the direct method requires $O(M^3 + M^2N)$ operations (Robbins, 1998). In the present PIV measurements, for example, $M = 32385$ and $N = 2040$. Based on these values, the snapshot method would require 0.14×10^{12} operations compared with 36×10^{12} operations for the direct method. Detailed reviews and discussions on POD can be found, for example, in Berkooz *et al*. (1993) and Holmes *et al*. (1998).

The POD has been implemented in many types of flows, such as jets, boundary layers, backward facing step flows. In most of the studies the fluctuating velocity fields were analyzed, assuming that the large-scale coherent structures contain the main fraction

of the turbulent kinetic energy. For example, Reichert *et al.* (1994) observed that, for turbulent flow in a square channel, the first 100 POD modes contain over 95% of the turbulent kinetic energy while the first 10 modes captured over 50% of the total energy. Sub-domain modes were able to capture more of their domains total energy. In other words, the sub-domain decomposition was found to be more effective than full domain decomposition. The relatively small scale structures were only captured when the number of modes was increased to about 100. It was found that the first mode contributed more to $-uv$ than to kinetic energy. The more recent DNS study reported by Alfonsi and Primavera (2007) showed that the first 16 modes contribute about 20% of the total energy while 6.9% of the energy resides in the first three modes.

Moin and Moser (1989) applied DNS and POD to study fully developed channel flow. It was found that the contribution of the dominant modes to Reynolds shear stress is significantly higher than to turbulent kinetic energy. They reported that the convergence to the energy and the turbulent intensities is monotonic however; there is no such guarantee for the Reynolds shear stress. It was expected that the convergence of the POD expansion in the subdomain is better than the whole domain. However, it was found that the expansion converges faster in the wall layer than in a subdomian of the same size away from the wall, despite the fact that turbulent quantities vary most rapidly in the wall region.

Sen *et al.* (2007) carried out POD analysis of DNS data obtained over a smooth surface and for flow over egg carton roughness using 6000 realizations. The contribution of the first few modes to total energy is higher in smooth than in rough walls. Slow convergence of POD modes obtained for a rough wall indicates an increase in the range

of length scales. Profiles of turbulent intensities and Reynolds shear stress converge towards the time-average statistics faster in the inner region than in the outer region.

Kostas *et al*. (2002, 2005) performed POD analysis on both the fluctuating velocity and vorticity fields of a backward facing step at two Reynolds numbers (Re_k = 580 and 4660). They used 1024 PIV realizations in the *x*-*y* plane to perform the POD analysis. Large scale structures seem to be largely responsible for the persistence of u^2 and $-uv$ in the flow downstream of the reattachment while v^2 is governed predominantly by the fine scale structures. For this reason, both the spatial distribution and the peak $-uv$ were recovered by using approximately 50 modes but v^2 requires modes in excess of 50 to recover the peak value.

Orellano and Wengle (2001) reported POD analysis of the LES data at Re_h = 3000 over a fence in forced and unforced flow using 6000 realizations. They reported that 2000 POD modes represented 99% of turbulent kinetic energy while 20 modes represent about 25% of the turbulent kinetic energy for the unforced flow. The POD analysis of the transverse velocity component indicated the formation of a mainly 2-D vortex shedding from recirculation zone. The results reveal that the shedding of large-scale structures from the recirculation bubble behind the obstacle is the dominant process downstream of fence in the unforced flow.

2.5 Summary of the Literature and Problem Definition

Canonical flows and separated and reattached flows with and without pressure gradients have been reviewed. In the light of previous studies, the following observations can be made:

a) Attached flows under adverse and favorable pressure gradients and separated flows in zero pressure gradients have been investigated extensively. The majority of the previous pressure gradient studies have been conducted using point-wise measurement techniques such as LDA and hotwire. In general, the effect of APG on the flow is to enhance the mass and momentum transport while FPG attenuates it. Even though the agreement among the research community is not unanimous, log law remains a useful technique for obtaining friction velocity. These flows appear to be relatively well understood.

b) A wide variety of two-dimensional geometries have been used to study the phenomena of separation and reattachment in zero pressure gradients. The reattachment length of a separated flow is a sensitive parameter with dependence on freestream turbulence, perturbation strength, blockage ratio as well the pressure gradient. The turbulence levels are significantly enhanced in the separated shear layer and the peak values for the profiles of the turbulent quantities are attained about one step height upstream of reattachment. Downstream of the reattachment, the turbulence levels decay rapidly. In separated and reattached flows, most of the previous studies were conducted using point-wise measurement techniques as well. Moreover, only a few studies to date have investigated separated and reattached flows under the influence of pressure gradients. Given the complex nature of the separated and reattached turbulent flows, a whole-field technique (such as a PIV) that would allow accurate measurements of quantities such as the vorticity, various terms in the transport

equations for mean momentum, turbulent kinetic energy and Reynolds stresses is desirable.

c) The proper orthogonal decomposition is an effective statistical tool that has been applied to a range of turbulent flows to study the characteristics of coherent structures. Given the importance of coherent structures in turbulent flows, it is worthwhile to study the flow structure in separated and reattached flows. Such a study would provide a more in depth understanding of the flow.

In this research, a PIV technique will be used to conduct detailed velocity measurements in separated and reattached turbulent flow in a channel under the influence of variable pressure gradients. A transverse square rib will be used to create the separated and reattached flow. The data reported will include the iso-contours and profiles of the mean velocity, turbulent intensities, Reynolds shear stress, and triple velocity correlations. The budget terms, mixing length and the eddy viscosity will also be presented. Finally, the POD technique will be applied to the experimental data to provide an insight into the role and contributions of the structures to the Reynolds stresses of these flows. This research will contribute to the understanding of the complex flow dynamics and provide useful data for the validation of turbulence models.

CHAPTER 3: PRINCIPLES OF PARTICLE IMAGE VELOCIMETRY

Particle image velocimetry (PIV) is a non-intrusive optical measurement technique that provides simultaneous whole-field velocity measurement. PIV is well suited for estimating velocity gradients and derived quantities such as vorticity and the various terms in the transport equations for turbulent kinetic energy and Reynolds stresses. Due to these attractive features, PIV has been applied in many areas of fluid mechanics and aerodynamics research in the recent past. In this chapter, the basic principle of the PIV is outlined and the various components of PIV are described.

3.1 Planar PIV

A typical experimental setup using a planar PIV is shown in Figure 3.1. The setup consists of an optically transparent test-section, flow seeded with light reflecting particles, a pulsed light source (laser) to illuminate the area of interest, a film or CCD camera to record the illuminated particles, a synchronizer to control the camera and laser, and a computer with suitable software to record, store and process the recorded images.

The basic principle of the PIV involves a flow field seeded with small light scattering particles that are presumed to faithfully follow the fluid motion. These seeding particles are then illuminated by two pulses of laser sheet separated by a time delay, Δt. The light scattered by the seeding particles is recorded and two successive images are captured. The images are divided into a grid of small so-called interrogation areas. For each interrogation area, a numerical correlation algorithm (auto-correlation or cross-correlation) is applied to statistically determine the local displacement vector (Δs) of

particles between the first and the second illuminations. The velocity, V, for a particular interrogation area is then obtained from the expression $V = \Delta s/\Delta t$. A velocity vector map over the whole target area is obtained by repeating the correlation for each interrogation area over the two image frames captured. Since the entire flow field can be analyzed at once, PIV provides simultaneous whole field measurement in contrast to point measurement techniques such as laser Doppler anemometry (LDA) and hot-wire anemometry. The description of the basic components of a PIV is presented in detail in the following sections.

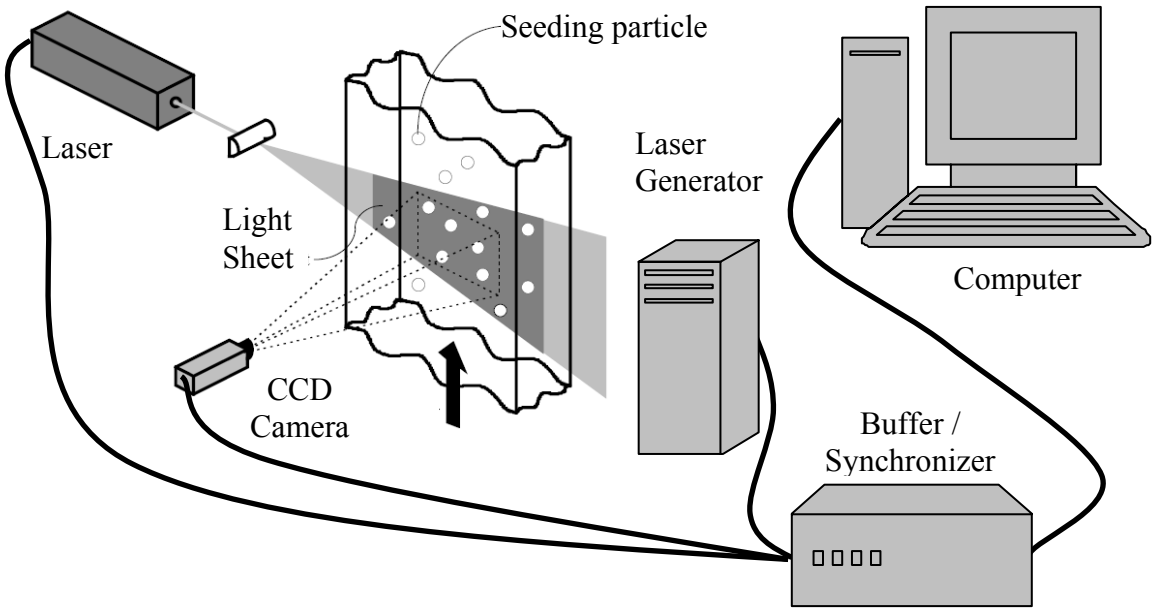

Figure 3.1: A typical experimental set-up of a planar PIV system.

3.1.1 Light Source

For PIV measurements, a high intensity laser is required to freeze the motion of the particles during image capturing. The fact that the whole field is illuminated and the camera captures the sidewards scattered light by the particles makes a high power laser necessary. Frequency doubled neodymium-yttrium-aluminum-garnet (Nd:YAG) lasers

are commonly used for PIV measurements because these lasers provide monochromatic light with high intensity illumination. Laser-emitted light is passed through a lens system to create a plane sheet of light to illuminate the region of interest. The length and width of the light sheet can be adjusted to the field of view required.

3.1.2 Seeding Particles

The seeding particles should be small enough to follow the flow faithfully but large enough to scatter sufficient light for them to be detected by the camera. Also, the seeding particles should be distributed homogeneously (Westerweel *et al.*, 1996). Since PIV measures the velocity of the particle but not the fluid velocity, it is essential that the particles have certain hydrodynamic properties to ensure that they faithfully follow the flow. Particles that have negligible settling velocity are desirable. The settling velocity can be estimated from Stokes drag law for flow around a sphere under gravity and is given by (Mei *et al.*, 1991),

$$v_s = \frac{(\rho_p - \rho_f) g d_p^2}{18 \mu_f}, \tag{3.1}$$

where ρ_p is the particle density, ρ_f is the fluid density, g is the acceleration due to gravity, d_p is the diameter of the particle and μ_f is the viscosity of the fluid. Hence, the settling velocity can be minimized by using small particles and/or particles whose density is similar to that of the working fluid.

The ability of a particle to follow the flow is characterized by its response time. The response time is a measure of the tendency of the particles to attain velocity

equilibrium with the fluid. The response time, τ_r, for the particle (for Stokes' flow) is (Raffel *et al*., 1998):

$$\tau_r = \rho_p \frac{d_p^2}{18\mu_f}. \tag{3.2}$$

The particles must also be good at scattering light to ensure that they are visible to the CCD sensor (Willert and Gharib, 1991). The particle size and shape, the refractive index and the wavelength of radiation are the factors that affect the light scatter by a particle. A variety of seeding particles are commercially available ranging from few microns to hundreds of microns. Some of the widely used particles for liquids are polyamide seeding particles, silver-coated hollow glass spheres, hollow glass spheres, polystyrene latex and fluorescent polymer particles, to mention a few.

3.1.3 Recording Medium

The CCD camera is the most widely employed recording device for PIV. CCD cameras have several advantages over the photographic film cameras. These advantages include higher frame rates and possibility of on-line image analysis. However, photographic film cameras do offer higher resolution. The major component of a CCD camera is the CCD sensor which consists of an array of detectors called pixels. The CCD camera employed in the PIV studies generally uses high-performance progressive scan interline CCD chips. The chip consists of an array of photosensitive cells and an equal number of storage cells. After the first laser pulse is triggered, the first image is acquired and immediately transferred from the photosensitive cells to the storage cells. Later, when the second laser pulse is triggered, the photosensitive cells are available to store the second image. In this case, the storage cells contain the first image and the photosensitive cells contain the

second image. Then both images are transferred sequentially from the camera to the computer for storage. This allows the exposure interval Δt to be reduced to less than 1 microsecond.

3.1.4 Methods of Correlation in PIV

The images recorded by the CCD camera are sub-divided into smaller regions called interrogation areas. For each of the interrogation areas, the images at the first and second frames are correlated to obtain an average displacement vector. The end result is a vector map of average displacements for all the interrogation areas. Auto-correlation and the cross-correlation/adaptive-correlation are the most commonly used correlation methods.

In auto-correlation, the particles in an interrogation area are correlated with themselves. This results in a large central peak (the self-correlation peak) in the correlation plane along with two displacement peaks, one on each side of the central peak. The distance from the central peak to either of the displacement peaks corresponds to the average particle displacement in the interrogation area. Because of the presence of the self-correlation peak, particle displacements less than 2-3 pixels cannot be detected. This reduces the dynamic range of the auto-correlation technique. Furthermore, 180-degree directional ambiguity of the correlation method is a major drawback.

In cross-correlation, on the other hand, particles in two different interrogation areas belonging to two different images at the first and second frames are correlated. Since the order of the image recording is known, directional ambiguity is no longer a concern. With the cross-correlation method, two sequential images of flow field with a specific time between them are considered as two spatial signals. The spatial shift can be represented by using a linear digital signal image process as shown in Figure 3.2. The

function f(m, n) describes the light intensity within the interrogation area at time t and the function g(m, n) describes the intensity recorded at time Δt later. The function f(m, n) is considered as the input signal and g(m, n) is the output of the transfer function s(m, n) in the presence of noise function d(m, n). The capitalized function shown in Figure 3.2 represents the Fourier transforms of the respective functions, and u, v are the coordinates of the spatial frequency domain. The challenge of this technique is to estimate the spatial shift function s(m, n) on the basis of known functional values of f(m, n) and g(m, n) in the presence of noise function d(m, n). A commonly used method in finding spatial shift function s(m, n) is the statistical technique of spatial cross-correlation. The detail of this method and the computational implementation are given in Willert and Gharib (1991) and Raffel *et al.* (1998).

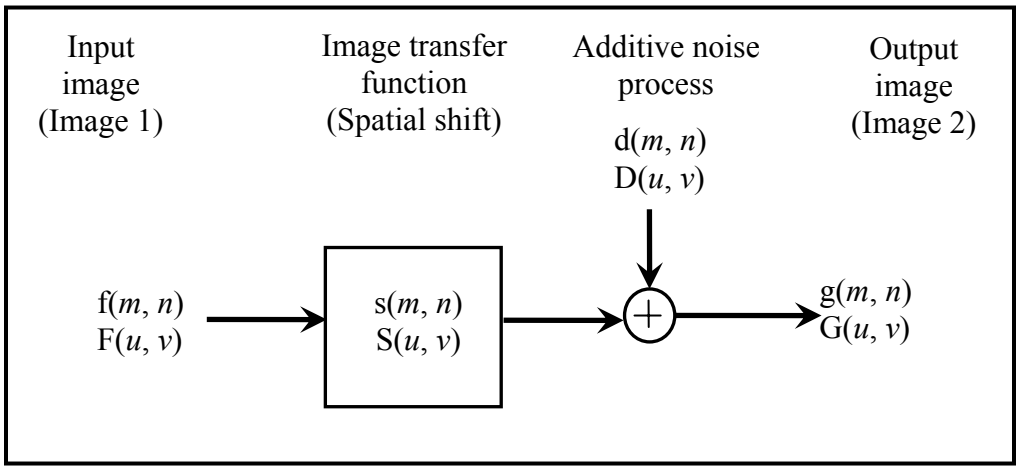

Figure 3.2: Image displacement function.

The adaptive-correlation algorithm is an advanced type of cross-correlation. It is an iterative method which relies on the knowledge of the actual velocity spatial distribution (which is not known *a priori*) and is the objective of the measurement procedure itself. Therefore, an initial guessed offset value is used to introduce an offset

from the first window (the interrogation area in the image frame from laser pulse one) to the second window. The result of each single interrogation is used as an input to evaluate the interrogation parameters for the subsequent iteration. The process terminates when a convergence criterion is fulfilled or after a prescribed number of iterations. The use of adaptive correlation helps in two major ways. First, the signal strength is raised due to the capture of the in-plane dropout. In-plane dropout occurs because during the time between the two light pulses some of the particle images leave the interrogation area and are lost. This loss of particles reduces signal strength and the number of successful vectors that can be obtained. Secondly, a refinement of the interrogation area is possible because an adaptive window offset may be applied, again producing a successful signal.

3.2 Optimizing PIV Measurements

The combination of laser energy, camera magnification and light sheet dimension needs to be optimized in order to obtain results from a PIV system with high accuracy. Even under ideal experimental conditions, a PIV vector map may contain spurious vectors. These spurious vectors emanate from interrogation spots where signal-to-noise ratio is less than unity. That is, a noise peak is higher than the signal peak. Keane and Adrian (1990) focused their study on the detection probability (i.e., the percentage of valid vectors). To improve the signal-to-noise ratio, they recommended the interrogation areas be large enough to accommodate a sufficient number of particles, but small enough so that one vector describes the flow. The particle size should be selected such that the particle image size is approximately two pixels when imaged by the digital camera (Raffel *et al.*, 1998). The particle image diameter, d_{image} , is given by:

$$d_{image} \approx [d_p^2 M^2 + (2.44(1+M)f_\#)\lambda] \quad (3.3)$$

where d_p is particle diameter, $f_\#$ is the *f*-number of the lens, λ is the wavelength of the laser light, and M is the magnification factor of the camera. Raffel *et al.* (1998) suggested that when the image diameter becomes too small there is insufficient information to make effective use of sub pixel interpolation because there is a likelihood of biasing data towards integer pixel values. Sub pixel interpolation is used to increase the resolution or accuracy when detecting the position of the correlation peak which makes it possible to determine displacements with an accuracy of fractions of a pixel.

The seeding density is dependent on the type of PIV method used. For the two-frame cross-correlation method, Willert and Gharib (1991) showed that to obtain a high valid detection probability the particle image density should be larger than 6. Using very high particle image densities, large particle image diameters, and small interrogation cell sizes will reduce the error due to gradients. The movement of the particles can only be tracked as long as they remain within the same interrogation area during both exposures. Also, the particles should not traverse more than a quarter of the side length of the interrogation areas between exposures to keep the number of particles that leave the interrogation area down.

The thickness of a laser sheet, Δ_z, is usually chosen to be smaller than the depth-of-field of the recording system, δ_z. Consequently, all particles illuminated by the light sheet produce in-focus images, reducing background noise in the image field (Adrian 1991). The depth-of-field of the lens is given by,

$$\delta_z = 4(1+M^{-1})^2 f_\#^2 \lambda. \quad (3.4)$$

It should be noted that for a given magnification, a large depth-of-field can only be obtained at the cost of increasing the $f_{\#}$ implying that a smaller fraction of the light scattered by the particles will reach the sensor.

The components of the PIV system (the camera, laser, seeding particles and software to process the PIV images) used in the present study will be described in detail in Chapter 4.

CHAPTER 4: EXPERIMENTAL SETUP AND MEASUREMENT PROCEDURE

In this chapter, the water tunnel test facility where the expereiments were performed is described. The design and specifications of the variable pressure gradient channels and the parallel-wall channel that were inserted into the water tunnel test section to conduct experiments is presented. The test conditions for pressure gradient flows with and without separation and their measurement procedure are outlined. Convergence tests and the effect of spatial resolution on mean and turbulent statistics are also presented. Finally, the effect of rib location inside the diverging channel is explored and a brief discussion is presented.

4.1 The Water Tunnel

The water tunnel was designed and constructed by Engineering Laboratory Design, Inc., Minnesota, USA. The system, which is shown in Figure 4.1, consists of a flow conditioning section, test section, circulating pump, variable speed drive, piping, supporting framework and filtering station. The overall dimensions of the unit are: 5370 mm in length, 1822 mm in height and 1435 mm in width. The settling chamber upstream of the contraction is fitted with perforated steel plates and honeycomb. A settling chamber is designed to ensure quality flow transition from high speed pipe velocities to low speed test section velocities, while reducing turbulence and providing flow uniformity. The perforated plates and honeycomb installed in the settling chamber are used to straighten the flow. A 6:1 contraction, with a symmetrical cross section, is used prior to the working section to further reduce the turbulence intensity by accelerating the

mean flow. The test section was fabricated using Super Abrasion Resistant® (SAR) clear acrylic to facilitate optical access and flow visualization. The interior dimensions of the test section are 200 mm wide by 200 mm high by 2500 mm long. A 25 hp transistor inverter type variable speed controller regulates the speed of the motor that drives the pump. A filter system is furnished as a means of removing dye concentrations and other contaminants from the system's water. The filtration can be activated at any time, but it is not operated during experiments.

Figure 4.1: The water tunnel facility.

4.1.1 Variable Pressure Gradient Channels

A variable pressure gradient channel made of 3 mm thick acrylic plates was inserted into the main channel. For FPG, the flow encounters an asymmetric converging channel (Figure 4.2a) while an asymmetric diverging channel (Figure 4.2b) is used to create an APG flow. It can be seen from both figures that the first 1000 mm of the channel (*OA*)

and the last 500 mm of the channel (*BC*) have straight parallel walls. The 1000 mm section of the channel (*AB*) located between these parallel sections diverges non-linearly from a height of 54 mm to 84 mm for the APG case, and converges from 84 mm to 54 mm for the FPG case. The zero location for x is taken at the start of convergence/ divergence (*A*) and $y = 0$ on the lower wall. The heights of the variable channel for APG and FPG are, respectively given by:

$$2h(x) = 54 - 7.39\times10^{-4}(x) + 5.73\times10^{-5}(x)^2 - 3.12\times10^{-9}(x)^3 - 5.09\times10^{-11}(x)^4 + 2.78\times10^{-14}(x)^5, \quad (4.1)$$

$$2h(x) = 84 - 4.01\times10^{-2}(x) + 2.09\times10^{-5}(x)^2 - 7.17\times10^{-8}(x)^3 + 8.83\times10^{-11}(x)^4 - 2.78\times10^{-14}(x)^5, \quad (4.2)$$

where x is measured in millimeters and the relationship is valid between $0 \leq x \leq 1000$.

The choice of above profiles was partly constrained by the test section of the existing main water channel and the need to obtain two-dimensional mean flow at the mid-span of the converging and diverging channels. A number of curved profiles were tried and the pressure gradient along the channel was analytically calculated assuming an inviscid flow. The profiles described above (Equations. 4.1 and 4.2) were chosen because they produced pressure gradients that were not so severe as to cause flow separation (in the diverging channel) or relaminarization (in the converging channel), yet high enough to noticeably modify the flow field compared with that in the channel with parallel walls. The velocity and pressure distributions obtained from the inviscid assumption in these converging and diverging channels will be presented later in Chapters 5 and 6.

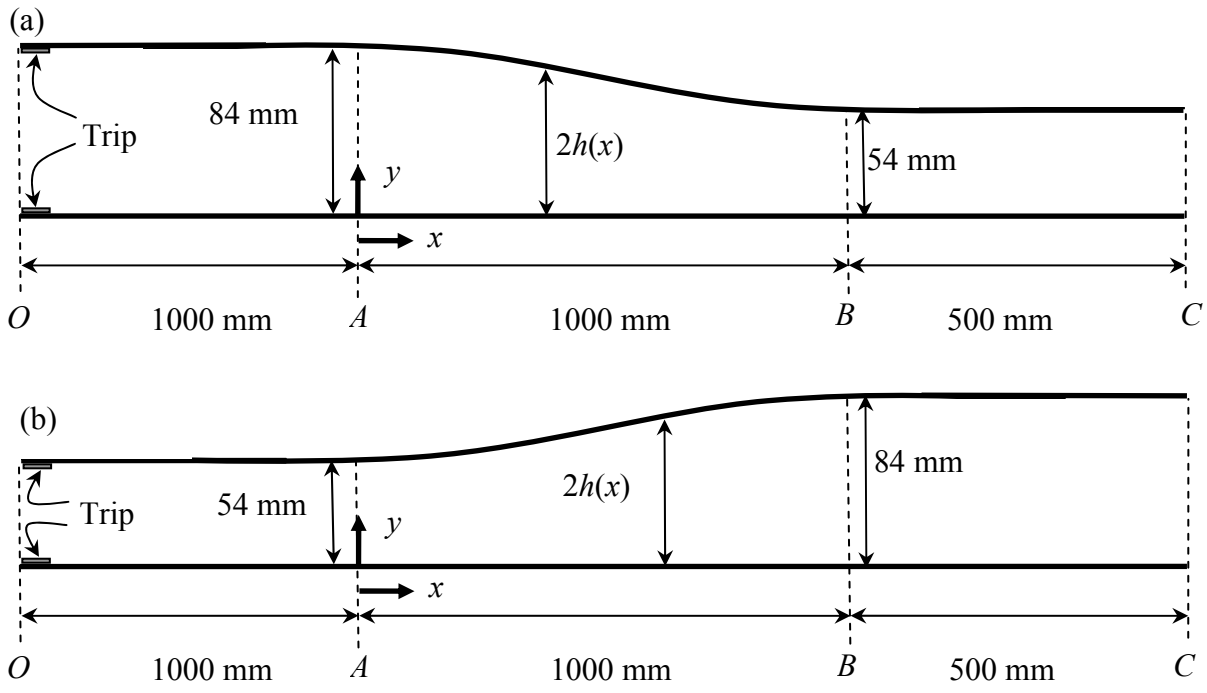

Figure 4.2: Schematic side view of test sections: (a) converging channel, (b) diverging channel (not to scale).

4.1.2 Geometry Induced Separation

In the present study, a transverse square rib was used to create separation in the diverging, converging as well as parallel wall channels. A schematic of a transverse square rib inside these channels is shown in Figure 4.3. As shown in Figure 4.3a, the parallel-wall channel is also 2500 mm long channel while the half-channel height, h = 34.5 mm. It should be noted that the height of the parallel-wall was chosen as the average of the heights of inlet section (or the upstream parallel sections) of the converging and diverging channels. The separated and reattached flows in the parallel-wall channel will serve as a reference case for the separated and reattached flows in the pressure gradients. The rib was made of clear acrylic bar of height, k = 6 mm and width, w = 6 mm. The rib spanned across the entire width of the channel. The rib was secured at the bottom wall of the channel at a particular location with double sided tape. The

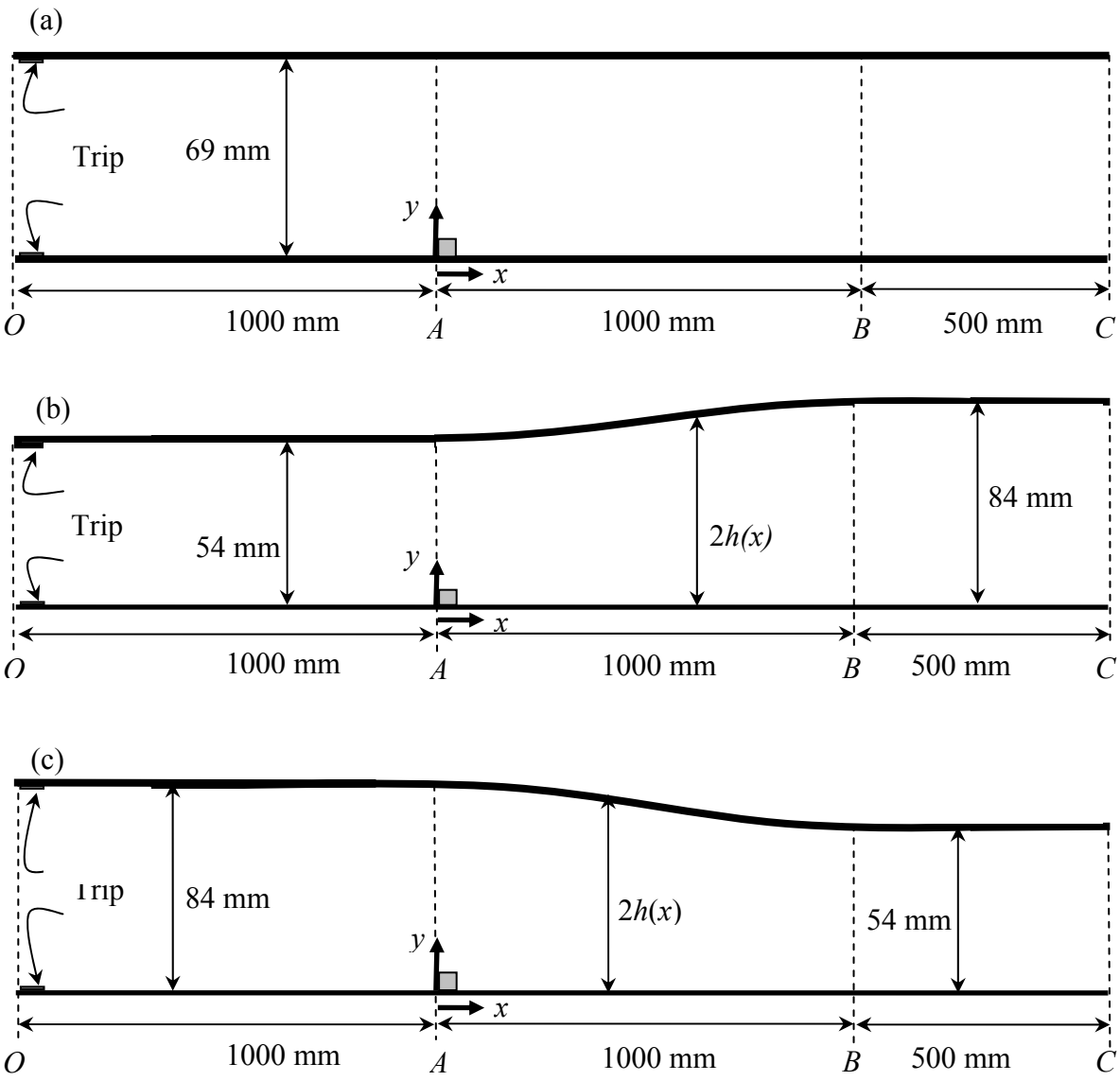

Figure 4.3: Schematic of the transverse square rib in the various channels: a) parallel-walled channel, (b) diverging channel and (c) converging channel. (not to scale).

upstream edge of the rib was used as the reference where $x = 0$ and $y = 0$ at the lower wall of the channel.

4.2 PIV System

The flow was seeded with 5 μm polyamide seeding particles having a specific gravity of approximately 1.03. The settling velocity and response time of the particles calculated

from Equations 3.1 and 3.2 were v_s = 0.41 μm/s and t_r = 1.43 μs, respectively (for all the experiments). The settling velocity is insignificant compared to the streamwise mean velocity measured. Similarly, the response time is very small compared to the sampling time employed in this study. These imply that the particles follow the fluid flow faithfully. An Nd-YAG laser (120 mJ/pulse) of 532 nm wavelength was employed to illuminate the flow field. The laser sheet was located at the mid-span of the channel. A 12-bit HiSense 4M camera (2048 pixel × 2048 pixel CCD array size and a 7.4 μm-pixel pitch) was coupled to a 60 mm AF Micro Nikkor lens.

The instantaneous digital images were post-processed by the adaptive-correlation option of the commercial software developed by Dantec Dynamics (FlowManager 4.50.17). As mentioned in Chapter 3, the adaptive-correlation algorithm is an advanced type of the standard cross-correlation. The adaptive correlation uses a multi-pass FFT cross-correlation algorithm to determine the average particle displacement within the interrogation area (IA). A three-point Gaussian curve fit was used to determine particle displacement with sub-pixel accuracy. A moving average validation was used during processing. The moving average validation validates or rejects vectors based on a comparison between neighboring vectors. The rejected vectors are then replaced by vectors estimated from surrounding values. For all the test conditions in each measurement plane, 2040 pairs of instantaneous images were recorded and an interrogation area of 32 pixels x 16 pixels with 50% overlap were used to compute the mean velocity and turbulent statistics. The rationale for using 32 pixels x 16 pixels with 50% overlap will be explained in section 4.6.

4.3 Measurement Procedure

The CCD digital camera was positioned perpendicular to the plane of the light sheet for all the test conditions. The laser pulse separation time Δt was found based on the estimation that the particle displacement should be less than one quarter of the interrogation area, using the following expression,

$$\Delta t = \frac{N \times d_{pitch}}{4MU_{\max}}, \tag{4.3}$$

where, N is the interrogation window size, d_{pitch} is the pixel pitch, M is the magnification factor and U_{max} is the maximum velocity of the flow. In addition to the condition stated above, particle displacement of at least 2 times the pixel pitch was satisfied (see Equation. 3.3) in order to ensure high signal-to-noise ratio and high quality data. Before acquiring the 2040 image pairs at any test location, an on-line validation of the velocity vectors was performed to ensure that the PIV parameters were correctly chosen and yielded high quality velocity vectors. In all cases, the number of substituted velocity vectors in the main flow domain was always less than 2% percent.

4.3.1 Variable Pressure Gradient Channels

As stated earlier, prior to measurements in the converging and diverging channels with the square rib installed on the channel floor, experiments were conducted in these channels without the square rib. The rationale was to understand the effects of adverse and favorable pressure gradients on the mean velocities and turbulent statistics in the plane channel, i.e. without the ribs. For a given test condition, the volume flow rate was kept constant during all the measurements to maintain the upstream conditions as similar as possible. A 42 mm wide trip made of four 6 mm wide rectangular bars, 6 mm apart,

were used at the upper and lower walls of the channel entrance to ensure a rapid development of the turbulent boundary layer.

The measurements in the APG or diverging channel were made at Reynolds number based on the upstream half channel height $h(x)$ (at $x < 0$) and approach velocity, Re_h = 27050 and 12450. These tests would be denoted subsequently as Test D1 and Test D2, respectively. The measurements in the FPG were obtained at Re_h = 19280 and would be denoted as Test C. Table 4.1 provides a summary of these test conditions. In this table, x is the corresponding location where the approach flow condition in the upstream parallel section was specified, U_e is the maximum streamwise velocity and U_b is the bulk velocity. As shown in the table, the ratio U_e/U_b varied from 1.08 to 1.10. These values are not significantly different from a value of 1.16 reported in the DNS study by Kim *et al.* (1987) in a fully developed channel. The relatively high value in the DNS study is likely due to the fact that the Reynolds number is lower in the DNS study than in the present study.

Table 4.1: Summary of test conditions for variable pressure gradient channels.

Test	***Location***	***x* (mm)**	**U_e (m/s)**	**U_b (m/s)**	**U_e/U_b**
D1 Re_h = 27050	*L1*	-85	1.002	0.928	1.08
D2 Re_h = 12450	*L1*	-39	0.461	0.427	1.08
C Re_h = 19280	*L1*	-98	0.459	0.417	1.10

As shown in Figure 4.4, for each test condition (Test D1, Test D2 and Test C), measurements were obtained in five *x-y* planes: upstream of the convergence/divergence (denoted as *P1*), three planes (*P2, P3* and *P4*) within the converging/diverging section

and a plane (*P5*) downstream of convergence/divergence. The data set extracted from *P1* is referred to as *L1*, from *P2* as *L2* and so on (see Figure 4.4). The specific x locations corresponding to *L2*, *L3*, *L4* and *L5* for each test condition will be provided in Chapter 5. The measurement plane preceding the convergence/divergence section will hereafter be referred to as upstream section, the planes in the converging/diverging section will be referred to as the variable section and the measurement plane downstream of the convergence/divergence section will be referred to as the downstream section.

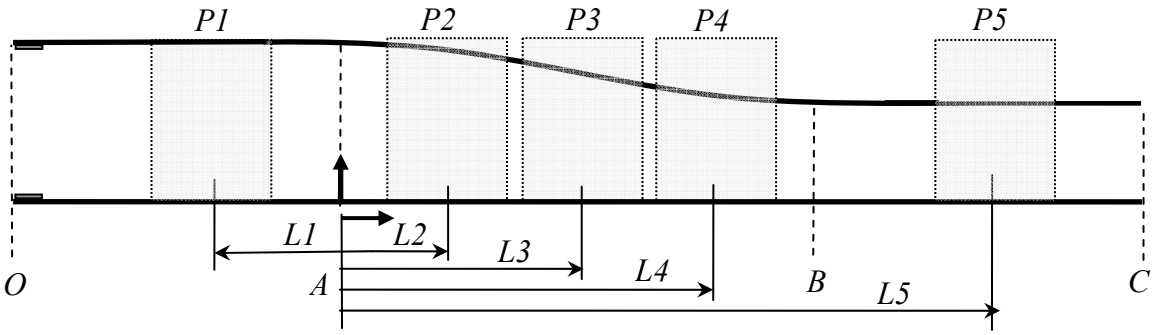

Figure 4.4: Experimental setup: *L1* to *L5* correspond to locations where detailed data analysis was performed (not to scale).

4.3.2 Geometry Induced Separation

The two-dimensional square rib of height k = 6 mm was glued to the bottom of the channel at x = 0 (1000 mm from the inlet of a given channel) for the parallel-wall channel (Test CC), diverging channel (Test APG) and the converging channel (Test FPG) to cause flow separation at Re_h = 15350, 12420 and 19450 respectively. These Reynolds numbers are based on the approach or upstream velocity obtained at x/k = -30. A summary of test conditions at the upstream parallel sections is presented in Table 4.2. It should be noted that the upstream velocities (U_e) for these test cases were chosen to

mimic those for Test D2 and Test C described above in Section 4.3.1. As in the previous section, the ratio U_e/U_b varied from 1.08 to 1.10. It should be remarked that the Reynolds number based on the approach velocity and step height was kept nearly constant ($Re_k = U_e k/\nu$) for all the three tests.

Table 4.2: Summary of test conditions for the separated and reattached flows.

Test	***PG***	***Location of Geometry***	U_e **(m/s)**	U_b **(m/s)**	U_e/U_b	Re_k
CC Re_h =15350	ZPG*	$x/k = 0$	0.445	0.408	1.09	2640
FPG Re_h =19450	FPG	$x/k = 0$	0.463	0.429	1.08	2760
APG-I **APG-II** **APG-III** Re_h =12420	APG	$x/k = 0$ $x/k = -25$ $x/k = +25$	0.460	0.416	1.10	2760

* Note that the flow in parallel-wall channel (Test CC) is nearly zero pressure gradient.

For the APG channel, in addition to placing the rib at $x/k = 0$ (Test APG-I), measurements were also made with the ribs placed at an upstream section of the diverging section ($x/k = -25$: Test APG-II) and within the diverging section ($x/k = 25$: Test APG-III). The goal was to study how rib location, relative to the start of divergence, would modify the flow field. These results will be presented and discussed in Section 4.7. As will be shown in that section, no significant effects of rib location on the flow characteristics were observed. Therefore, only data obtained at $x = 0$ for the APG channel will be discussed in detail in Chapter 6.

As shown in Figure 4.5, for each test condition (i.e., Tests CC, APG and FPG), reference measurements were made in an x-y plane upstream of the rib (denoted as P_0) to characterize the approach flow and then in five other planes ($P_1 - P_5$) located around and

downstream of the rib. From these measurement planes, profiles were extracted at x/k = -30 in P_0, x/k = 1, 2, 4, 9, 13 in P_1, x/k = 21, 30 in P_2, x/k = 50 in P_3, x/k = 120 in P_4 and x/k = 200 in P_5. It should be noted that the location x/k = 200 is within the downstream parallel section (BC) for the variable pressure gradient channels.

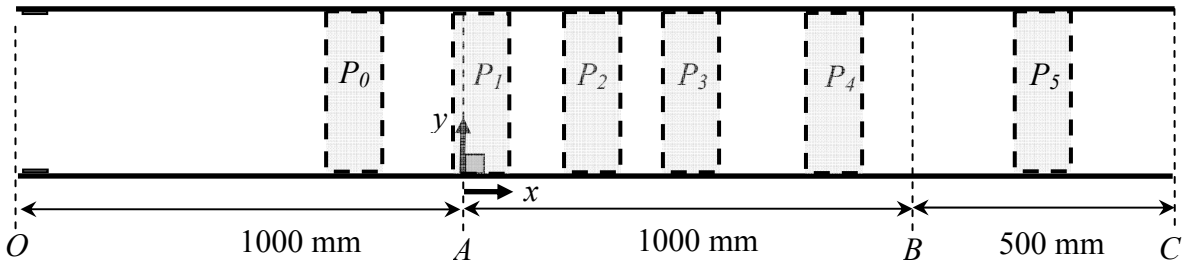

Figure 4.5: Experimental Setup: P_0 to P_5 correspond to locations where detailed data analysis was performed for a given channel (not to scale).

4.4 Two-Dimensionality of the Mean Flow

The two-dimensionality of the flow field upstream of the converging and diverging sections, and also in the separated shear layer and redevelopment region is presented and discussed in Appendix A. The results show that the mean flow at the upstream section and in the separated and redevelopment regions is fairly two-dimensional.

4.5 Measurement Uncertainty

Measurement uncertainty analysis was made following the AIAA standard derived and explained by Coleman and Steele (1995) in Appendix A. In general, a complete uncertainty analysis involves identifying and quantifying both the bias and precision errors in each part of the measurement chain. In PIV technique, the accuracy of velocity measurement is limited by the accuracy of the sub-pixel interpolation of the displacement

correlation peak. According to studies such as Forliti *et al.* (2000), a Gaussian peak-fitting algorithm (algorithm used in the present study) is found to have the lowest bias and precision errors. Particle response to fluid motion, light sheet positioning, light pulse timing and size of interrogation area are among the other sources of measurement uncertainties. On basis of the size of interrogation area and curve fitting algorithm used to calculate the instantaneous vector maps, and the large number of instantaneous vector maps used to calculate the mean velocity and turbulent quantities, the uncertainty in the mean velocity at 95% confidence level is estimated to be ± 2%, and those for the mean momentum flux and vorticity are estimated to be ± 5%. The uncertainties in turbulence intensities, Reynolds shear stress and triple velocity correlations are estimated to be ± 5%, ± 10% and ± 15%, respectively. The uncertainties in the mixing length, eddy viscosity and budget terms are estimated to be within ± 15%. Error bars are used in the figures to denote the measurement uncertainty at 95% confidence interval.

4.6 Convergence Test

The sample size required for statistical convergence in turbulent flows depends on the local turbulence level and the statistics being measured. Moreover, the measurement uncertainty in a given quantity also depends on the sample size and turbulence level. To determine the sample size required to accurately compute the mean and turbulent statistics, a set of 2040 image pairs were acquired. A sample size of N = 510, 1020 and 2040 were used to calculate the mean velocity, turbulent intensities, Reynolds shear stress and triple velocity correlations. As shown in Figure 4.6, for each quantity, a comparison is made for a typical profile obtained in the separated region (x/k = 4) and in the

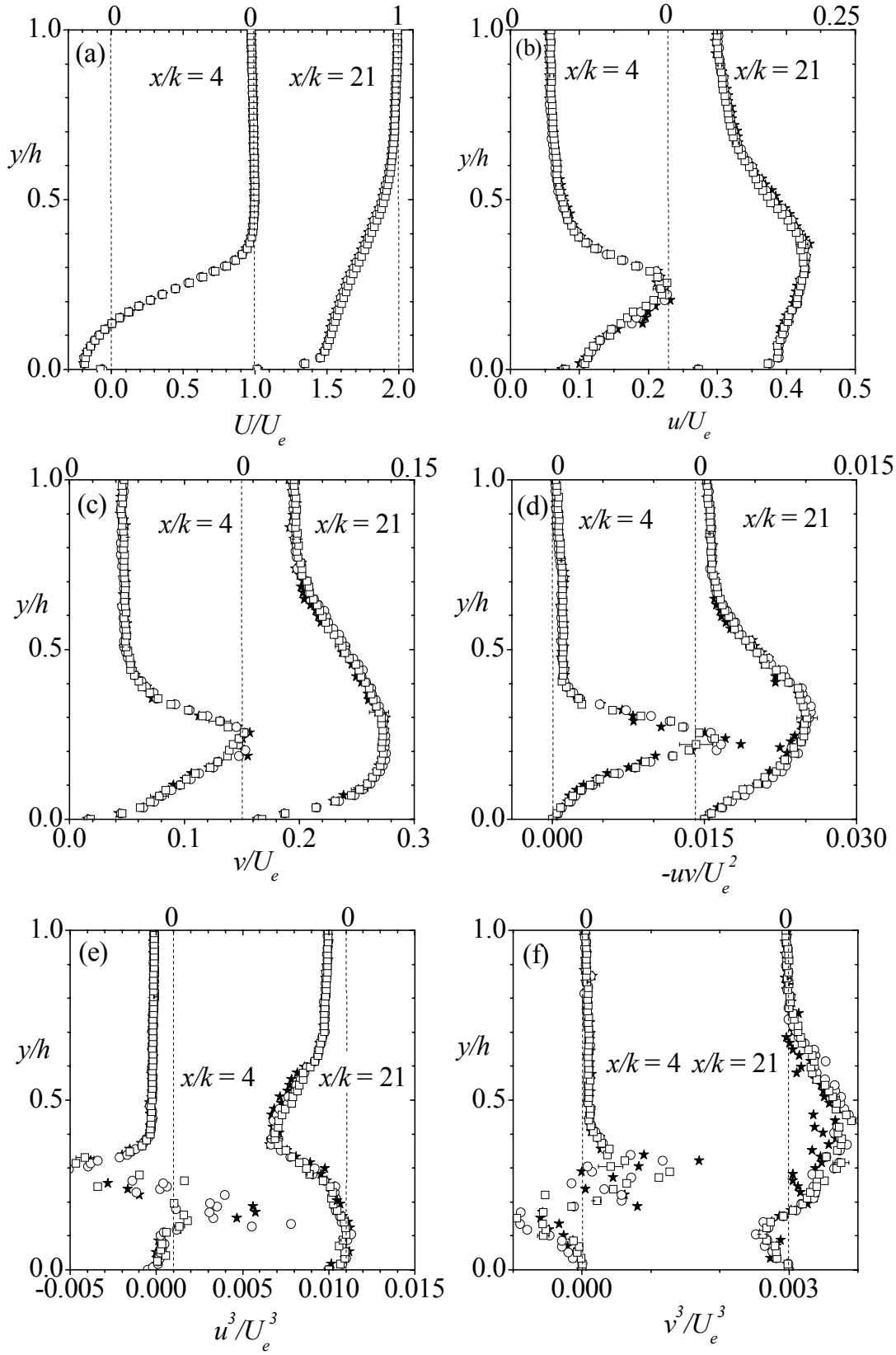

Figure 4.6: Profiles of the mean velocity and turbulent quantities obtained using N = 510 (ξ), 1020 (–) and 2040 (∀): (a) U, (b) u, (c) v, (d) $-uv$, (e) u^3 (f) v^3.

redevelopment region (x/k = 21) for Test FPG. It can be seen that for a sample size of 510, the mean velocity, turbulent intensities and Reynolds shear stress collapse reasonably well while the triple velocity correlations show some scatter. However, the profiles obtained from sample size of either 1020 or 2040 collapse reasonably well for all the statistics. These results are in good agreement with those reported by Tachie *et al.* (2007) and Shah *et al.* (2008). Therefore, a sample size of 2040 was used for the computation of the mean velocity and turbulent quantities reported subsequently.

Similar results (not shown) were obtained for the other test conditions and locations summarized in Tables 4.1 and 4.2. It should be noted that the sample size of 2040 used in the present study is substantially larger than those used to compute the mean and turbulent statistics in previous studies. For example, Piirto *et al.* (2003) used 510 images to compute the mean velocity, Reynolds stresses and the various transport terms in turbulent kinetic energy equation in separated and reattached flow downstream of a backward facing step.

4.7 Spatial Resolution Test

Previous studies demonstrate that low spatial resolution can underestimate the true values of the turbulent quantities (see for example, Piirto *et al.*, 2003). In a recent study (Shah *et al.,* 2008), a detailed investigation was undertaken to study the effect of spatial resolution on the mean velocity and higher order terms (up to fourth moments) over smooth and rough wall surfaces. For the smooth wall, the interrogation area sizes in wall units varied from 2.9 to 33.6. A marginal reduction in u_{max} and v_{max} values was observed as the IA sizes were increased. However, the mean velocity, Reynolds shear stress, the triple

correlations, skewness, flatness factors (except F_v) and production term were found to be nearly independent of IA sizes. It was found that the dissipation rate was the most sensitive to spatial resolution and the spatial resolution effects were observed to persist across the entire channel height. Based on those results, it was concluded that an IA of $\Delta y^+ = 16.8$ was adequate to resolve the mean and the turbulent quantities except the dissipation rate. It should also be noted that the Reynolds number of one of the smooth wall tests was chosen to mimic that of DNS of Kim *et al.* (1987). A very good agreement between the previous DNS study and the experimental results was observed, providing confidence in the accuracy of the PIV results.

Saikrishnan *et al.* (2006) also studied the effects of spatial resolution on turbulent intensity and Reynolds shear stress by comparing measurements obtained from various PIV interrogation area sides with DNS results. They found that the near-wall or buffer region was most sensitive to the size of the interrogation area, and as the resolution increased, the PIV values approached the DNS values. Their results show that in the buffer region, PIV interrogation area of $\Delta y^+ = 20$ gave values of u^+, v^+ and $-u^+v^+$ that are, respectively, 96%, 92% and 95% of the corresponding DNS values.

4.7.1 Variable Pressure Gradient Channel

In the present study of the flow in the variable pressure gradient channels without the rib, the PIV images were processed using two interrogation areas (IAs), 32 pixels × 32 pixels with 50% overlap (Δx = 0.750 mm × Δy = 0.750 mm) and 32 pixels × 16 pixels with 50% overlap (Δx = 0.750 mm × Δy = 0.375 mm) to evaluate any effects of spatial resolution on flow statistics. Figure 4.7 shows profiles of the mean velocity and turbulent quantities obtained using the two IAs at *L2* of Test D2. It is clear that the profiles of the mean

velocity, turbulent intensities and Reynolds shear stress obtained from the two IAs are nearly indistinguishable. This implies that both IAs provide spatial resolutions that are adequate for these quantities.

Similar results were obtained for all the other test conditions summarized in Table 4.1. In fact, based on maximum friction velocity for a given test, Δy^+_{max} = 18.6, 9.1 and 13.2, respectively, for Tests D1, D2 and C. As noted above, the studies

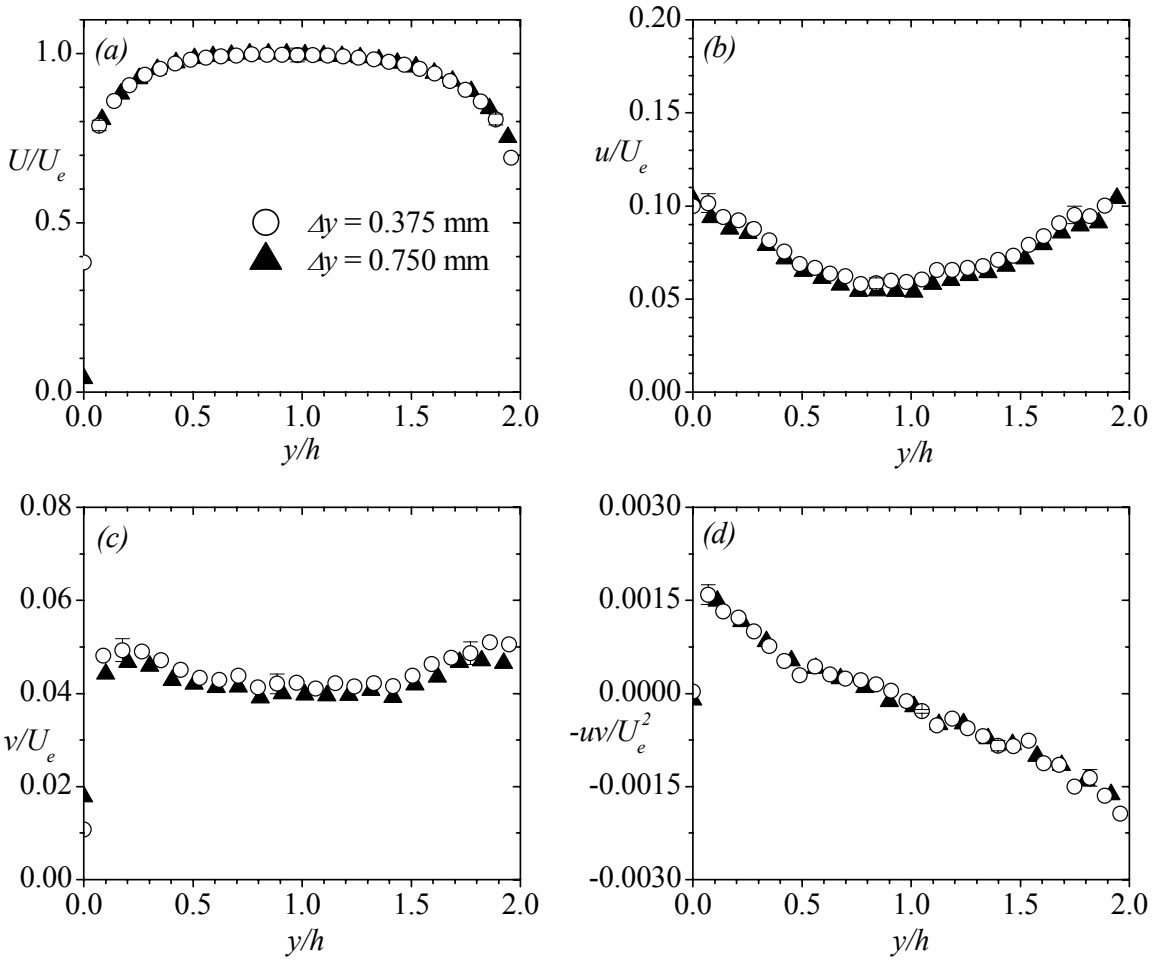

Figure 4.7: Profiles of the mean velocity and turbulent quantities obtained using the two IAs at the *L2* of Test D2: (a) *U*, (b) *u*, (c) *v*, (d) *-uv*. Note, appropriate number of data points is skipped to avoid data congestion.

conducted by Shah *et al.* (2008) and Saikrishnan *et al.* (2006) revealed that PIV resolution of $\Delta y^+ \approx 20$ is adequate to provide accurate data across the boundary layer. Hence, even in the case of lowest resolution of $\Delta y^+_{max} = 18.6$ for Test D1, the current resolution will yield reasonably accurate results. Based on these results, subsequent profiles reported for Test D1, D2 and C are those obtained from an IA of 32 pixels × 16 pixels with 50% overlap. It should also be noted that these resolutions are better than in many previous PIV studies. For example, recent PIV measurements in APG by Angele and Muhammad-Klingmann (2006) were performed with a spatial resolution of 2.2 mm × 2.2 mm corresponding to $\Delta y^+ = 149$.

4.7.2 Geometry Induced Separation

In case of the separated and reattached flows under the influence of pressure gradients, the profiles at $x/k = 4$ and 21 for Test FPG were also used to study the effect of spatial resolution on flow statistics in the separated and the redevelopment regions, respectively. The location $x/k = 4$ was chosen because of the spatial resolution effects would be most extreme in the separated region. Figure 4.8 shows the data obtained from IAs of 32 pixels × 32 pixels with 50% overlap ($\Delta x = 0.70$ mm × $\Delta y = 0.70$ mm) and 32 pixels × 16 pixels with 50% overlap ($\Delta x = 0.70$ mm × $\Delta y = 0.35$ mm). In the redevelopment region no significant effects of spatial resolution on the mean or turbulent quantities are observed. In the separated region, however, the effect of a larger IA size is to decrease the values of a given quantity, and these effects are most pronounced for the triple velocity correlations. For example, the maximum difference in $(u/U_e)_{max}$ and $(-uv/U_e^2)_{max}$ in the recirculation region is 7% and 5% while those in u^3_{max} and v^3_{max} are, respectively,

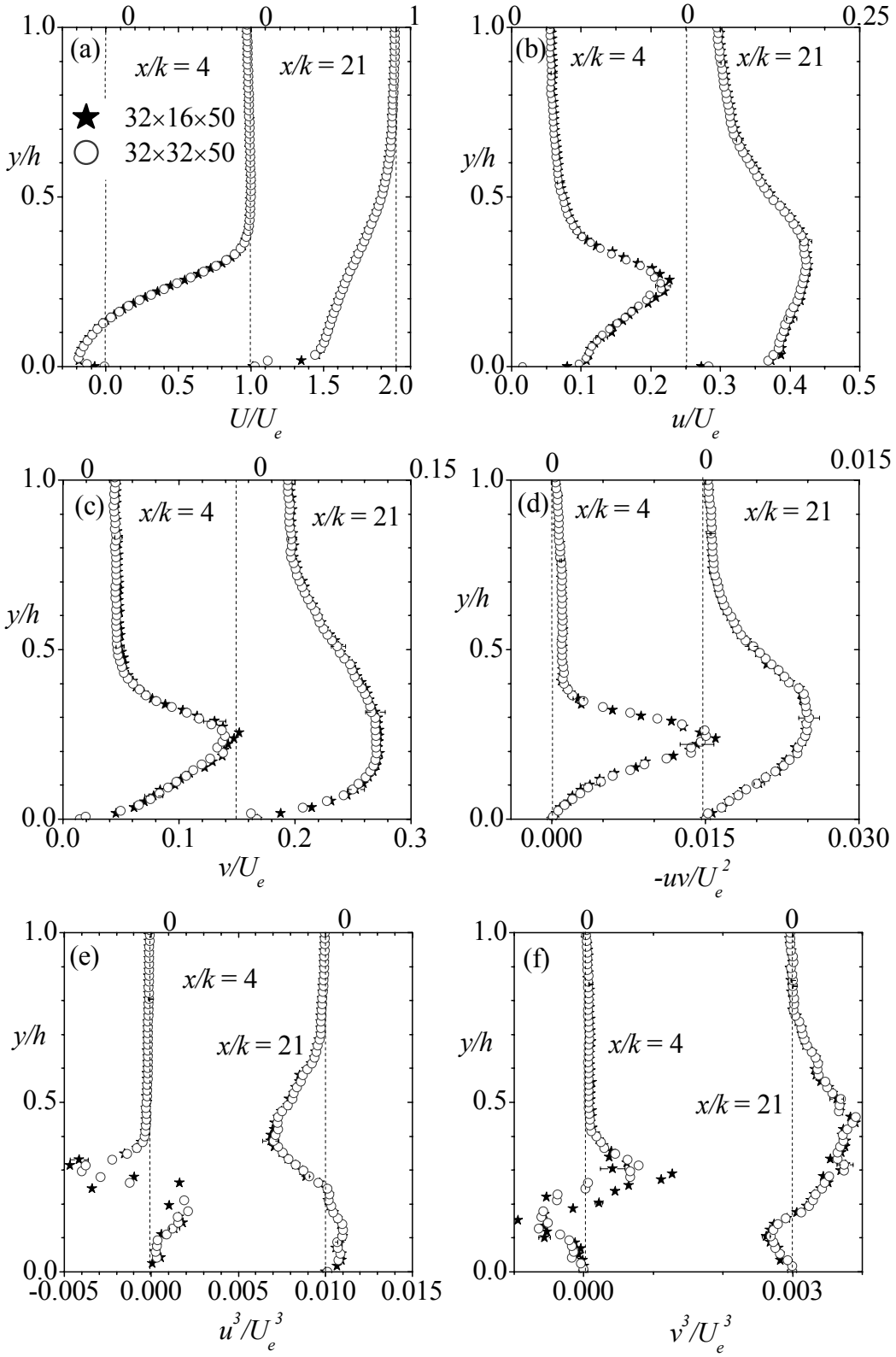

Figure 4.8: Profiles of the mean velocity and turbulent quantities obtained using IA of 32 pixels × 32 pixels and 32 pixels × 16 pixels: (g) U, (h) u, (i) v, (j) $-uv$, (k) u^3 (l) v^3.

15% and 35%. The data reported subsequently were those obtained from the 32 pixels × 16 pixels with a 50% overlap. This resulted in a spatial resolution of $\Delta y = 0.056h$, $0.065h$, and $0.059h$, respectively, for Tests CC, APG and FPG. Based on the friction velocity for the approach boundary layer, the resolution in wall variables was, respectively, $\Delta y^+ = 7.9$, 9.0 and 8.3 for Tests CC, APG and FPG. As will be shown subsequently, the friction velocities obtained downstream of the ribs are either similar or smaller than the corresponding upstream values. Therefore, the values of Δy^+ computed based on local viscous length scale in the redevelopment region would be either similar or smaller than those stated above. Based on these results and discussion provided previously, the spatial resolution is expected to be sufficient to adequately resolve mean and the turbulent quantities.

4.8 Effect of the Rib Location

As stated earlier, three test cases were performed in the diverging channel by varying the location of the rib within the test section. For the first test case (Test APG-I), the rib was located at $x/k = 0$. The rib was then moved to $x/k = -25$ (Test APG-II) and finally to $x/k = 25$ (Test APG-III). The goal was to examine how the flow field is affected by separation taking place at the inlet to divergence (Test APG-I), and compare the results to those for which separation occurred in the absence (Test APG-II) and presence of pressure gradient (Test APG-III). The profiles obtained $x/k = 1$, 2, 4, 9, 13, 20 and 30 for each of these three test conditions (Test APG-I, Test APG-II and Test APG-III) are presented and discussed in this section.

4.8.1 Iso-Contours and Streamlines of Mean Velocity

The iso-contours of the mean velocity and the streamlines obtained downstream of the rib for Test APG-I, Test APG-II and Test APG-III are shown in Figure 4.9. It is observed that these streamlines are qualitatively similar. In each case, the flow separates at the leading edge of the rib and is deflected upward from the rib. As expected, recirculation bubble is formed downstream of the rib and subsequently the flow reattaches. The reattachment length x_r is defined as the distance between the upstream edge of the rib (x/k = 0) and the reattachment point. From the streamlines of the three test cases, the reattachment length was estimated to be x_r/k = 10.3, 10 and 12 for Test APG-I, Test APG-II and Test APG-III, respectively. The observation that the reattachment length increases in adverse pressure gradient has also been reported by with increasing is similar to that reported by Kuehn (1980) and Ra and Chang (1990).

4.8.2 Profiles of the Mean Velocity and Turbulent Statistics

The mean velocity profiles are shown in Figure 4.10a. Notwithstanding the different reattachment lengths, the profiles for the three test cases at a given x-location are similar. In all the three test cases the presence of the rib greatly altered the profiles by decreasing the velocities at the lower wall. The negative velocities near the lower wall at x/k = 2, 4 and 9 indicates that the profiles are in the recirculation region. At x/k = 2, the negative velocities are as high as 20% of the maximum streamwise velocity.

For the turbulent intensities plotted in Figure 4.10b and 4.10c, no significant effect of rib location can be observed. The streamwise turbulent intensity (Figure 4.10b) increases significantly downstream of the separation i.e., at x/h = 1 and subsequently decays in the region x/k > 13. Downstream of the separation, the location of maximum

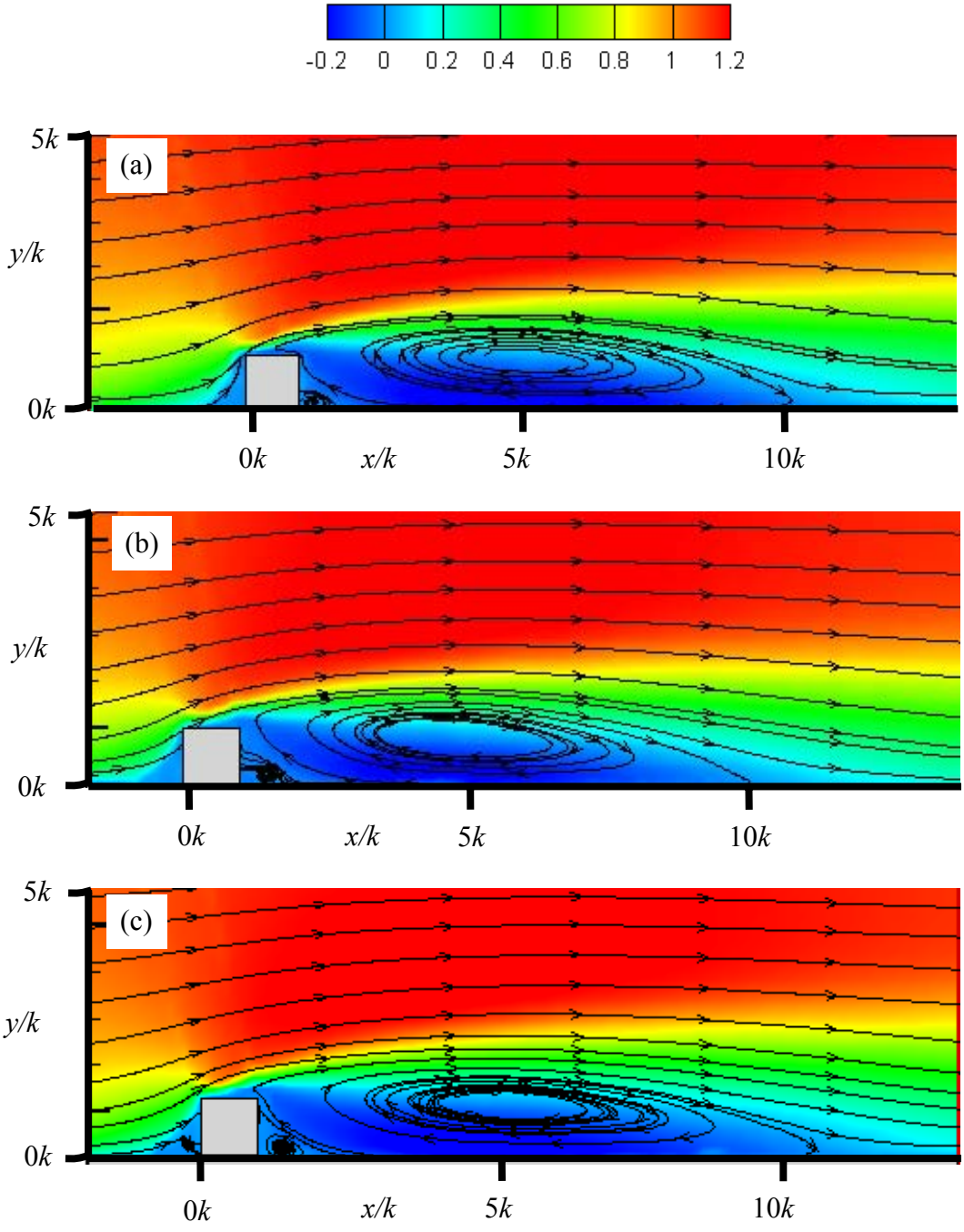

Figure 4.9: Iso-contours of mean velocity and streamlines: (a) Test APG-I, (b) Test APG-II and (c) Test APG-III.

turbulent intensity consistently moves away from the wall. The transverse turbulent intensity (Figure 4.10c) also rises in the recirculation region and gradually decays after $x/k = 13$. The rapid growth and subsequent decay of the turbulent intensities downstream

of x/k = 13 indicates that the effect of the rib on turbulent intensities is much stronger than the effect caused by the wall divergence. This may explain why all the three profiles are nearly similar at all the locations. Similarly, the Reynolds shear stress (Figure 4.10d) and the triple velocity correlations (Figure 4.11) do not show any significant variation with different rib locations. Based on these results, only Test APG-I (hereafter denoted by Test APG) will be presented and discussed in detail in Chapter 6.

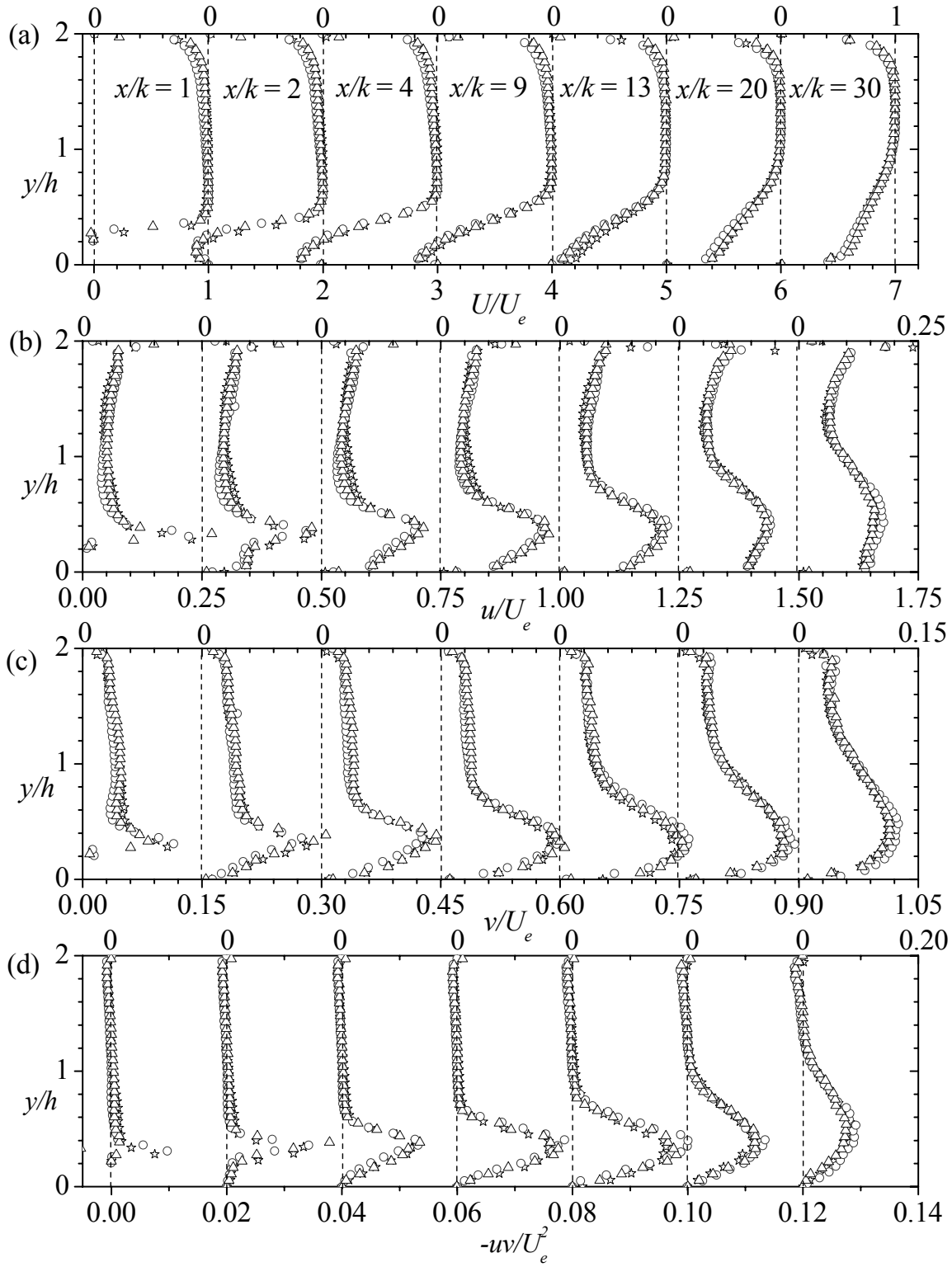

Figure 4.10: Profiles of mean velocity and turbulent quantities: (a) Mean streamwise velocity, (b) Streamwise turbulent intensity, (c) Transverse turbulent intensity and (d) Reynolds shear stress profiles. (ψ, APG-I; –, APG-II; 8, APG-III).

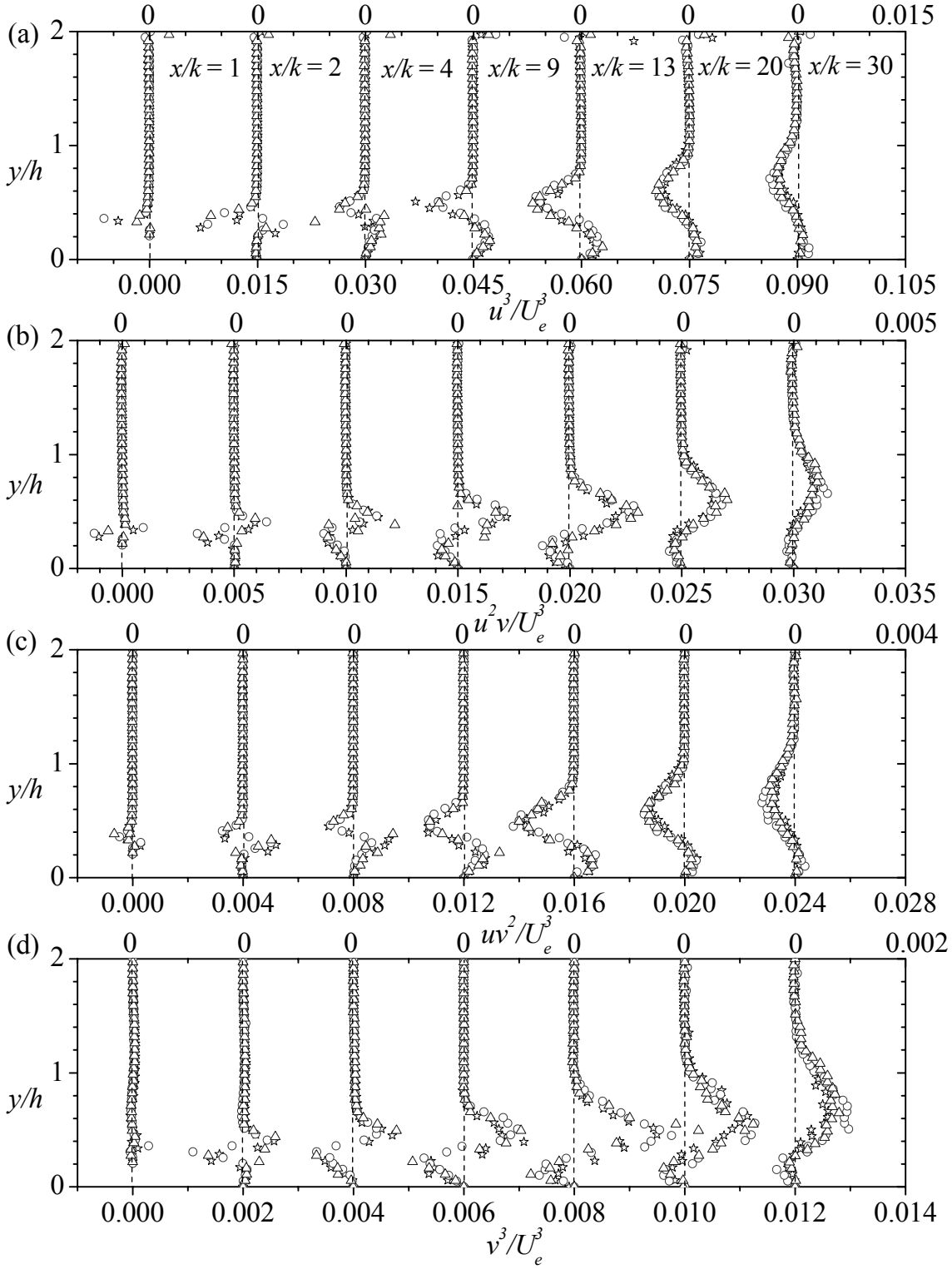

Figure 4.11: Profiles of triple correlations: (a) u^3/U_e^3 (b) u^2v/U_e^3 (c) uv^2/U_e^3 (d) v^3/U_e^3. (ψ, APG-I; –, APG-II; 8, APG-III).

CHAPTER 5: ATTACHED FLOW IN CONVERGING AND DIVERGING CHANNELS

As noted in Section 4.3.1, experiments were conducted in the converging and diverging channels without the transverse rib attached to the channel floor. The rationale is to understand the effects of variable pressure gradient on the relatively simple generic turbulent flow before moving on to the more complex separated and reattached flows. Measurements of mean velocities and turbulent quantities on the curved upper wall and flat lower wall of the channels are used to document the interaction between the lower and upper boundary layers under the influence of the variable adverse and favorable pressure gradient.

5.1 Boundary Layer Characteristics

The complete test conditions and various streamwise locations for which detailed data sets will be presented in this chapter are summarized in Table 5.1. For a given test condition (Tests D1, D2 and C), at each location (*L1*, *L2*, *L3*, *L4* and *L5*), x is the corresponding streamwise distance from the beginning of the variable section, U_e is the local maximum velocity, y_{max} is the wall normal distance from the lower wall to the location of maximum streamwise velocity U_e, Re_θ is the Reynolds number based on local maximum streamwise velocity, U_e, and momentum thickness, θ, and U_τ is the friction velocity obtained from the log law. Because of the asymmetric nature of the channels, the boundary layer on the upper wall develops at a different rate compared to the boundary layer on the lower wall. Therefore, both the upper and lower wall parameters are reported. The term "lower boundary layer" is used to describe the profile formed on

the lower wall up to the y_{max} location while "upper boundary layer" is from the upper wall to y_{max} location. Subscripts '*U*' and '*L*' are used, respectively, for a parameter obtained from the upper and lower boundary layers. The values of friction velocity and their accuracy are discussed in Section 5.3.

Table 5.1: Summary of test conditions and boundary layer parameters.

Test	***Location***	***x*** **(mm)**	U_e **(m/s)**	y_{max}/h	$Re_{\theta,L}$	$Re_{\theta,U}$	$U_{\tau,L}$	$U_{\tau,U}$
D1	*L1*	-85	1.002	0.46	1150	1070	0.0480	0.0495
Re_h = 27050	*L2*	310	0.950	0.58	2270	1360	0.0415	0.0448
	L3	580	0.843	0.65	3930	1930	0.0329	0.0370
	L4	840	0.738	0.60	4150	2100	0.0283	0.0330
	L5	1190	0.735	0.65	4170	1780	0.0300	0.0343
D2	*L1*	-39	0.461	0.45	550	740	0.0242	0.0235
Re_h = 12450	*L2*	324	0.427	0.51	960	850	0.0207	0.0211
	L3	585	0.389	0.59	1540	1040	0.0175	0.0185
	L4	845	0.308	0.69	2080	670	0.0127	0.0156
	L5	1228	0.300	0.67	1840	560	0.0132	0.0158
C	*L1*	-98	0.459	0.40	750	1630	0.0238	0.0218
Re_h = 19280	*L2*	205	0.476	0.47	720	990	0.0252	0.0242
	L3	526	0.630	0.64	680	640	0.0323	0.0328
	L4	738	0.694	0.49	700	720	0.0352	0.0358
	L5	1342	0.731	0.48	1150	1380	0.0347	0.0344

The local maximum streamwise velocity U_e obtained at selected x locations within the various planes of measurement are shown in Figure 5.1a. In this figure, the dashed vertical lines at x = 0 and x = 1000 represent the start and end of the variable section. For APG case (Test D1 and Test D2), the maximum streamwise velocity decreases monotonically and plateaus outside the diverging section, that is, where the top and bottom walls of the channel become parallel. Downstream of the divergence section the freestream velocities are 25% and 35% lower for the case Test D1 and Test D2, respectively, than the corresponding upstream value. As expected, for the FPG case (Test C), the maximum streamwise velocity increases monotonically and remains constant

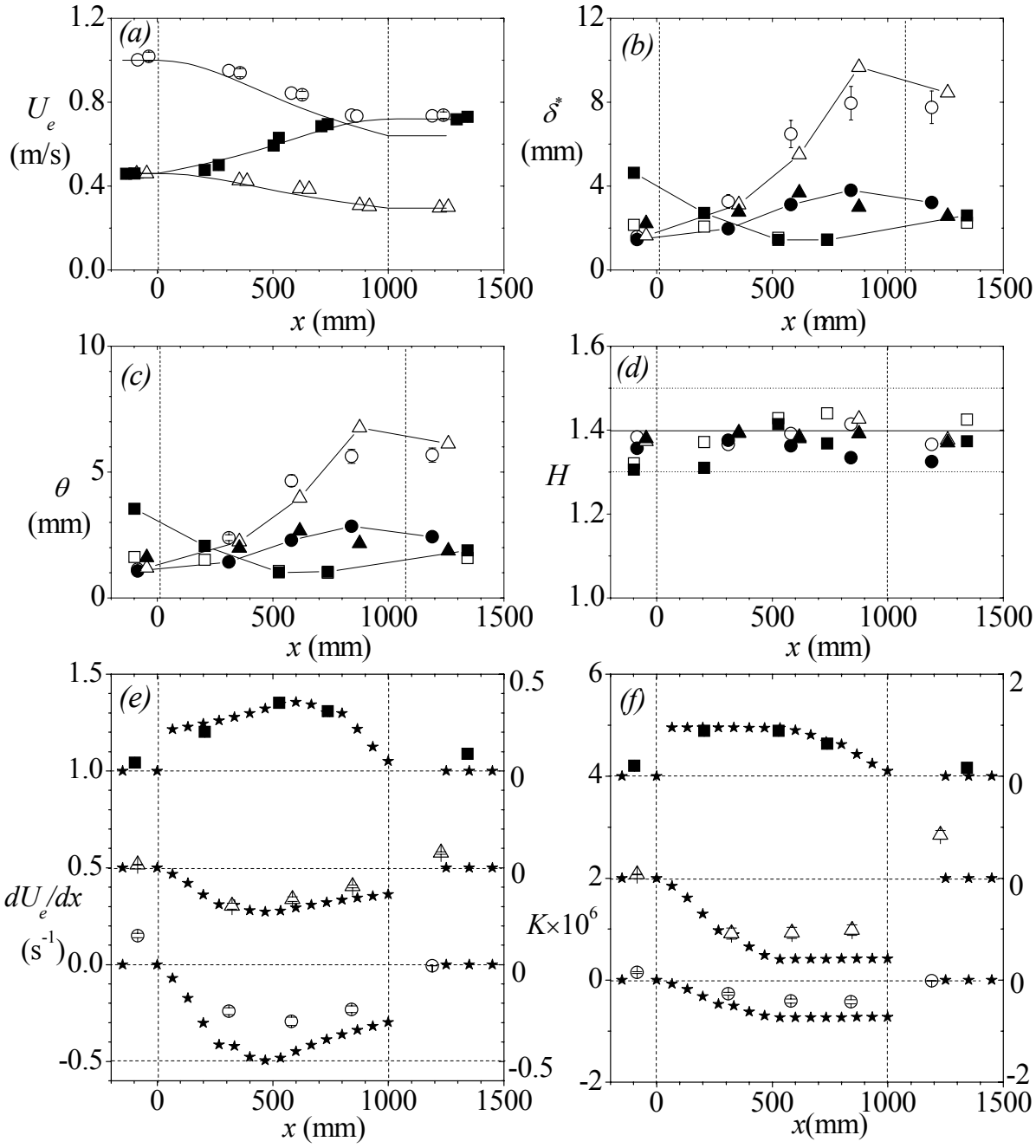

Figure 5.1: Various mean flow parameters: (a) local freestream velocity, (b) displacement thickness, (c) momentum thickness, (d) shape factor, (e) velocity gradient (f) acceleration parameter. Symbols in (a) D1: –; D2: 8; C: !; in (b), (c) and (d) $D1_L$: –; $D2_L$: 8; C_L: ∀; $D1_U$: ,; $D2_U$: 7; C_U: !; in (e) and (f) Inviscid: ξ; D1: –; D2: 8; C: !.

outside the converging section. Downstream of the converging section, the maximum streamwise velocity is almost 60% higher than the upstream value. As mentioned in

Chapter 4, the converging and diverging channels were designed assuming the flow through them was inviscid. The solid lines in Figure 5.1a show how the mean velocity would have varied in the converging and diverging sections if the flow was inviscid. In spite of the boundary layer growth on the walls of the channel, the experimental values (symbols) are only ± 7% different from the inviscid values (lines) except at the last measurement plane of Test D1 where the difference is about 13%.

The displacement thickness, δ^*, and momentum thickness, θ, for the upper and lower boundary layers are plotted in Figures 5.1b and 5.1c, respectively. In case of APG (Tests D1 and Test D2) values of δ^* and θ obtained from the lower and upper boundary layers increase monotonically in the diverging section and decrease slightly at downstream location *L5*. The increase in δ^* and θ within the diverging section is indicative of the characteristic higher mass and momentum flux deficit associated with APG. A similar trend was observed in previous studies, for example, by Spalart and Watmuff (1993) and Aubertine and Eaton (2005) in their study of APG turbulent flows. It can also be observed that values of δ^* and θ obtained from the lower boundary layer are higher than those from the upper boundary layer, an indication that the impact of the APG is greater on the lower boundary layer than on the upper boundary layer. The maximum increase in δ^* (the lower boundary layer) when compared to the upstream value is approximately 500% for Test D1 and Test D2. Corresponding increase in θ is about 450% for Test D1 and Test D2. Spalart and Watmuff (1993) observed an increase of 250% in δ^* and 190% in θ for their boundary layer flow in APG.

Boundary layer thinning associated with FPG resulted in a decrease of δ^* and θ in the converging section. For Test C, a decrease of 50% in δ^* and 57% in θ is observed.

The shape parameter, $H = \delta^*/\theta$, for the three test cases is plotted in Figure 5.1d. In spite of the large differences found among values of δ^* and θ for the various test conditions and measurement locations, the values of H remains nearly constant at 1.4 ± 0.1. The present H values are in good agreement with H = 1.3 - 1.4 reported by Escudier *et al.* (1998) in FPG flows where the acceleration parameter $K < 3\times10^6$.

The increase in U_e along the variable section is not exactly linear. However, in estimating the gradient dU_e/dx from the measured data in each measurement plane, a linear variation of U_e with x was assumed and dU_e/dx was evaluated as the slope of a least square linear fit to U_e versus x. The coefficient of determination was 0.999, an indication of an excellent curve fit. The values of dU_e/dx and $K = (\nu/U_e^2)(dU_e/dx)$ calculated from measured values are plotted in Figures 5.1e and 5.1f. Corresponding values of dU_e/dx and K obtained from the inviscid flow velocity distributions shown in Figure 5.1a are denoted by star symbols in Figures 5.1e and 5.1f. Note that values of dU_e/dx and K vary from 0 to 0.5 and 0 to 2×10^{-6}, respectively, and the vertical axis is staggered. It should be noted that K is negative and positive, respectively, in the variable section of the diverging and converging channels, and becomes nearly zero at the downstream parallel section of each channel. The absolute value of the K increases dramatically from *L1* to *L2*, remains nearly constant up to *L4* and then decreases downstream of the variable section. The absolute values of K for Test D2 are generally higher than those obtained in Test D1.

5.2 Profiles of the Mean Velocities, Momentum Flux and Spanwise Vorticity

The development of the mean streamwise velocity profiles in the APG and FPG are shown in Figure 5.2a using outer scaling (U_e and $h(x)$). The profiles in Figure 5.2a and those to be presented subsequently contain 255 data points. However, appropriate

number of data points is skipped to minimize data congestion. In Figure 5.2a, the five profiles obtained in the upstream (*L1*), variable (*L2, L3* and *L4*) and downstream sections (*L5*) are plotted together for each of the three test cases. The pressure gradient effects are more pronounced close to the walls. Smits and Wood (1985) suggested that the major influence of pressure gradient is felt in the near wall region and its effect decreases away from the wall.

In case of the APG, the rapid deceleration has substantially slowed the flow close to the wall and increased the thickness of the boundary layer. It can be seen that at the walls, the deviation from the upstream profile increases progressively up to *L4* and then begin to recover back to the upstream profile at *L5*. The profiles at *L1* and *L5* (which correspond to the upstream and downstream parallel sections) nearly collapsed for the upper boundary layer in case of Test D2. Aubertine and Eaton (2005) also observed a similar increase in deviation from the upstream profiles in APG. Their profile at the last measurement location in the parallel section (at $x/L_r = 1.67$, L_r = length of the ramp) was significantly less full compared to the upstream profile. One of the important observations is that APG produced in asymmetric channel has more profound effects on the mean flow on the flat wall than on the curved wall. This causes greater deviation among the profiles of the lower boundary layer for Test D1 and Test D2.

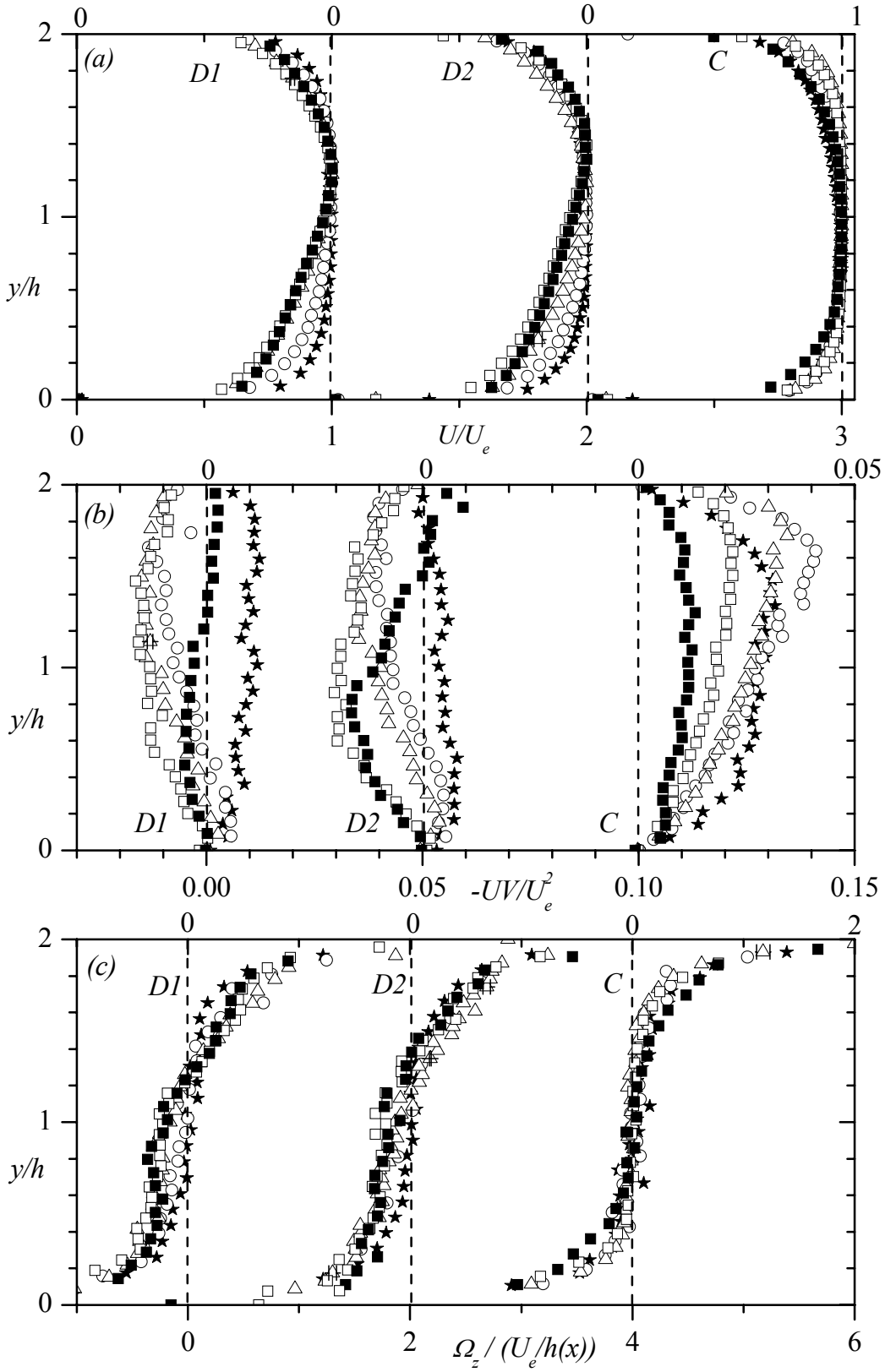

Figure 5.2: Mean quantities in outer coordinates: (a) mean velocity (b) mean momentum flux, (c) mean vorticity. Symbols are: *L1*, ξ; *L2*, –; *L3*, 8; *L4*, ∀; *L5*, !.

As for the FPG, the upper boundary layer is affected slightly more than the lower boundary layer. In the upper boundary layer, the profiles for FPG become 'more full' from *L1* to *L3* and those obtained at *L4* and *L5* appear to be recovering back to *L1*. The mean velocity deviation from the upstream profile in FPG and subsequent recovery towards upstream profile is also reported by Ichimiya *et al.* (1998). They observed that their profiles in the region of $0.4 < y/\delta < 1.5$ were indistinguishable.

The mean momentum flux ($-UV$) is related to the momentum transport across the channel. Typically, in fully developed channel, V and $-UV$ is zero. Figure 5.2b shows the variation of $-UV$ at all five locations for the three tests. Values of $-UV$ are positive at *L1* because the flow upstream of the diverging or converging section developed under a slight FPG. For Test D1 and Test D2, the profiles are predominantly negative. The minimum values, $(-UV/U_e^2)_{min}$, occurs at the centre of the channel and is about -0.015 and -0.021 for Test D1 and Test D2, respectively. At *L5*, the recovery towards the upstream profiles is much faster for the upper boundary layer compared to the lower boundary layer for Test D1 and Test D2. In case of Test C, at *L2*, the profile increases for the upper boundary layer compared to the upstream profile and subsequently decay falling below the upstream profile but remains positive. The maximum peak occurs closer to the upper wall. At *L4*, $(-UV/U_e^2)_{max}$ is about 0.023 and occurs at $y/h = 1.6$.

The mean spanwise vorticity ($\Omega_z = \partial V/\partial x - \partial U/\partial y$) profiles are shown in Figure 5.2c. In all three cases, the vorticity is negative at the lower wall indicating that $\partial U/\partial y > \partial V/\partial x$. For Test D1 and Test D2, the profiles exhibit a mild increase in magnitude across the channel whereas at *L5*, the profile is returning towards the upstream profile. The upstream profile exhibits nearly zero Ω_z in the region of $0.6 < y/h < 1.2$. However, under

the influence of APG, the location where $\Omega_z = 0$ shifts to y/h = 1.2 and 1.4 at *L4* for Test D1 and Test D2, respectively. For Test C, a slight decreasing trend is observed under the influence of FPG for profiles *L1* to *L4*. It should be noted that in FPG, Ω_z is nearly zero in the region, $0.4 < y/h < 1.6$, which is substantially wider compared to APG.

5.3 Friction Velocity and Mean Velocity Profiles in Inner Coordinates

The friction velocity U_τ was determined using the Clauser chart technique, that is, by fitting the measured mean velocity to the classical log law:

$$U^+ = 2.44 \ln y^+ + 5.0. \qquad (5.1)$$

As mentioned earlier, previous studies (Samuel and Joubert, 1974; Cutler and Johnston, 1989; and Aubertine and Eaton, 2005, 2006) showed that the log law is valid for mild and moderate APG. As the APG increases so does the strength of the wake and in case of strong APG the logarithmic region disappears. The log law has also been applied to moderate and mild FPG (Fernholz and Warnack, 1998) but disappeared as the acceleration becomes strong (Blackwelder and Kovasznay, 1972), i.e., at $K = 4.8 \times 10^{-6}$.

The velocity profiles obtained from the upper and lower boundary layers are plotted in Figures 5.3a to 5.3e using inner coordinates. The profiles exhibit a substantial log law region in all cases. It should be noted that most of the profiles have data points below $y^+ = 10$. The strength of the wake is varying as the flow develops along the converging and diverging channels. The variation of the wake parameter, Π, can be seen in Figure 5.3f. The values of Π were estimated from the relation: $\Delta U^+_{max} = 2\Pi / \kappa$, where ΔU^+_{max} is the maximum deviation of the experimental data in Figure 5.3 from the log law.

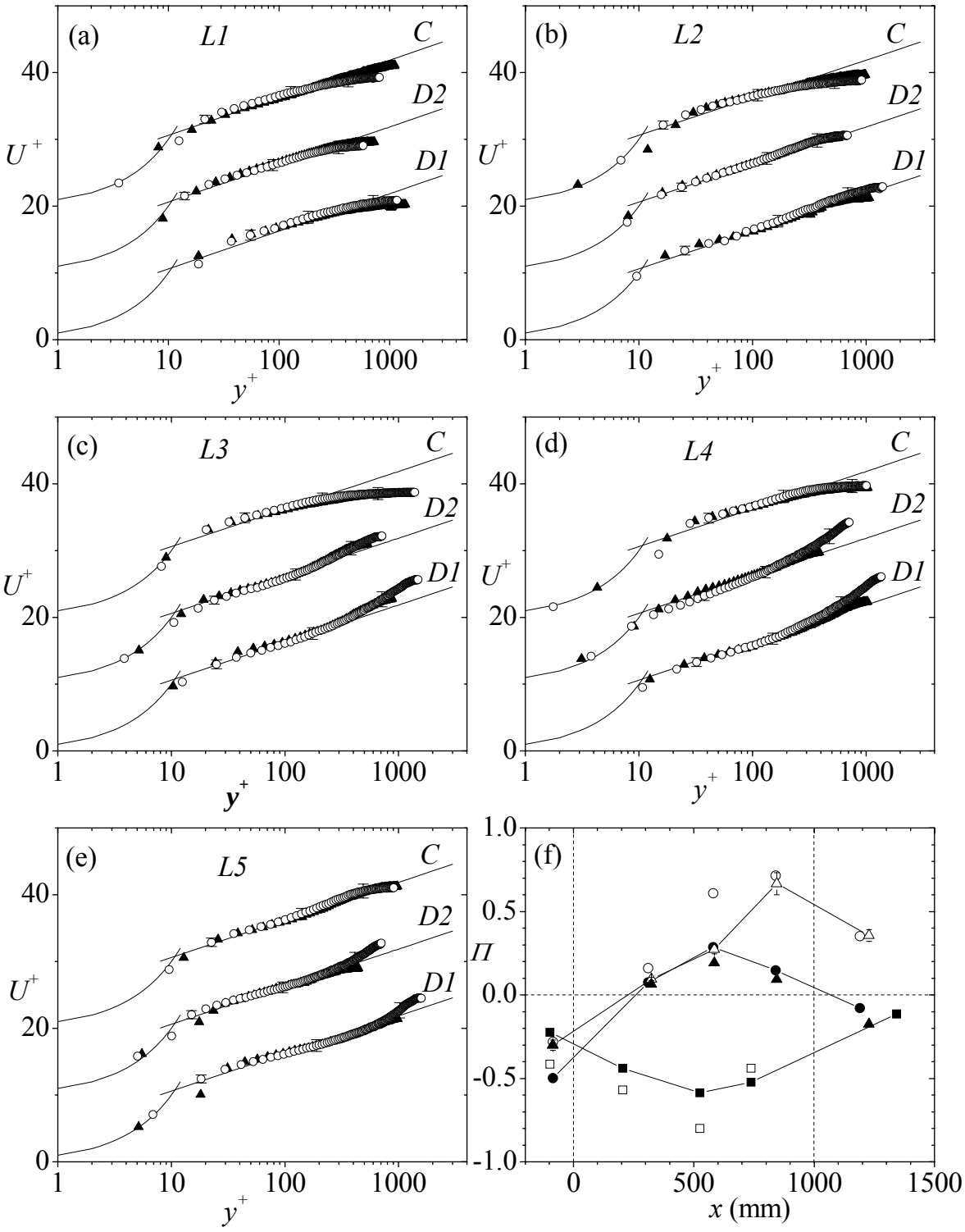

Figure 5.3: Mean velocity profiles in inner coordinates: (a) *L1*, (b) *L2*, (c) *L3*, (d) *L4*, (e) *L5*, (f) Wake parameter. Symbols in (a) - (e) Lower: –; Upper: 7; in (f) $D1_L$: –; $D2_L$: 8; C_L: ∀; $D1_U$: ,; $D2_U$: 7; C_U: !.

The wake parameter is known to depend on pressure gradient and is also affected by Reynolds number. It increases in APG and decreases in FPG (White, 1974). At *L1*, Π is negative because of the low Reynolds number, the high background turbulence levels, and the fact that the flow is developing under a slight favorable pressure gradient. The strength of wake increases for Test D1 and Test D2 in the variable section and subsequently decreases in the downstream section. On the other hand, the wake strength decreases for the FPG and recovers as the flow moves to the downstream section. This confirms the finding of Perry *et al.* (1966) that pressure gradient does not distort the logarithmic profile but simply controls its y-range of applicability.

The optimized U_τ values obtained from the log law are summarized in Table 5.1. The skin friction coefficient ($C_f = 2[U_\tau / U_e]^2$) distribution for the lower and the upper boundary layers is plotted in Figure 5.4. The measurement uncertainty in C_f is estimated to be ±7%. For Test D1 and Test D2, the skin friction values in the diverging section decreased compared to *L1* and then began to increase at *L5* for the lower boundary layer and at *L4* for the upper boundary layer. The maximum reduction was found to be approximately 40% for Test D1 and Test D2. In both cases, the maximum reduction was attained in the lower boundary layer. A decrease in skin friction values has been reported in many studies (Aubertine and Eaton, 2005; and Skåre and Krogstad, 1994). As for the FPG, the skin friction in the lower boundary layer increases at *L2* and then decreases from there on. However, for the upper boundary layer, the skin friction continues to increase until *L3* and then starts to decrease at *L4* and *L5*. Blackwelder and Kovasznay (1972) observed an increase in skin friction value in FPG upstream of the convergence but decreased towards its laminar value as it entered the converging channel.

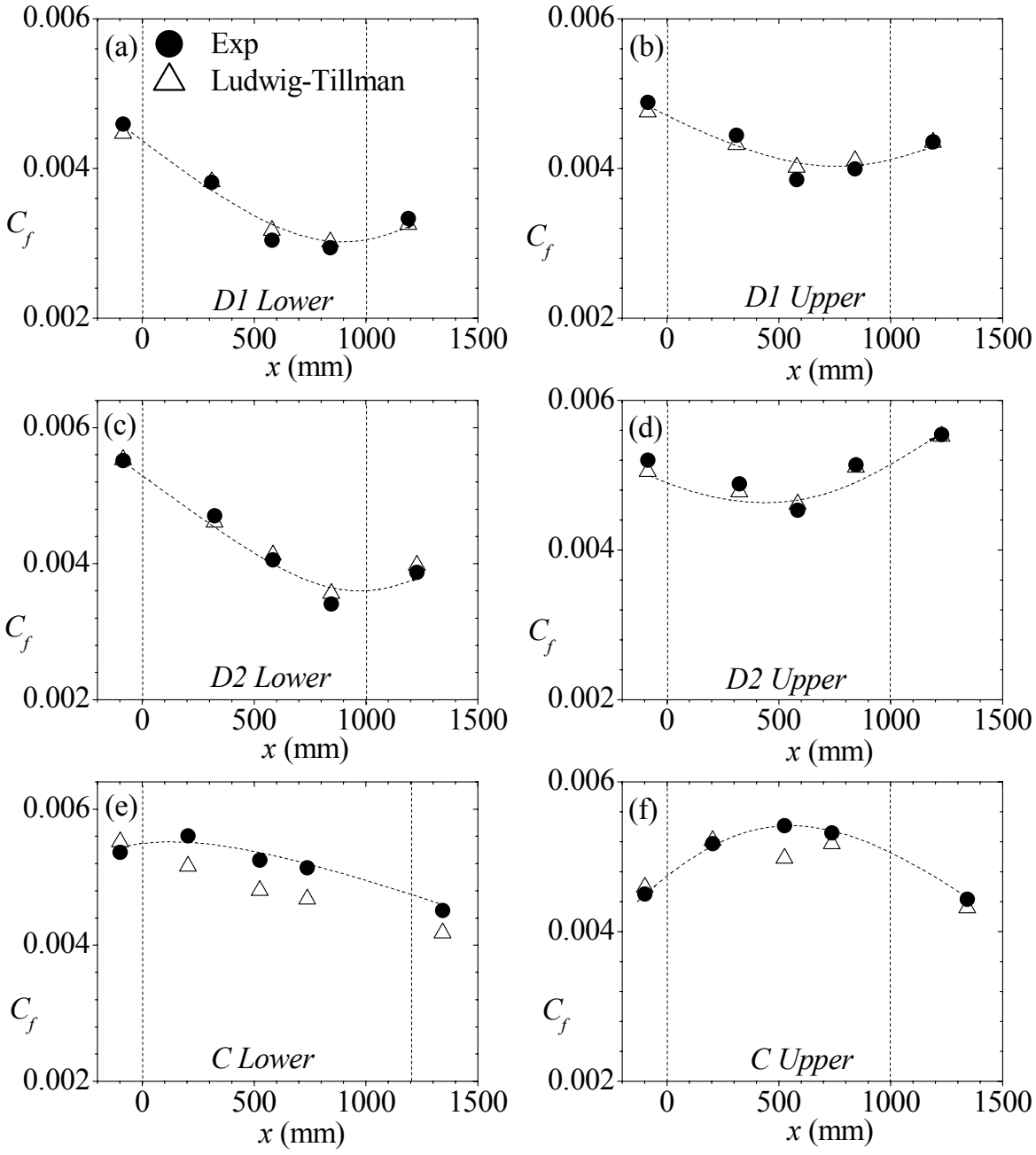

Figure 5.4: Skin friction distribution: (a) Test D1: lower, (b) Test D1: upper, (c) Test D2: lower, (d) Test D2: upper, (e) Test C: lower, (f) Test C: upper. Trend lines are for visual aid only. Symbols are: Clauser Plot Technique: ,; Correlation in Equation 5.2: 8.

The skin friction values were also estimated using the Ludweig-Tillman correlation (White, 1974):

$$C_f = 0.256 Re_\theta^{-0.268} 10^{-0.678H}. \quad (5.2)$$

This correlation has been previously used in channel flows and flows with pressure gradients (Bradshaw and Wong, 1972; and Cutler and Johnston, 1989) to estimate skin friction. The correlation depends on the values of δ^* and θ for its accuracy. The measurements of δ^* and θ are expected to be reliable since almost all data sets have measurements starting in the region, $2 \leq y^+ \leq 10$. In determining the displacement and momentum thicknesses, the measured data were extrapolated to the wall using $U = 0$ at $y = 0$. For APG case (Test D1 and Test D2), the values are found to be within ± 5% of skin friction values obtained by log law. For the FPG case (Test C), the difference between the two values is found to be within ± 10%.

5.4 Mean Velocity Defect Profiles

As mentioned in Chapter 2, different velocity and length scales have been proposed to interpret the mean velocity defect profiles. Therefore, a comparison of different velocity and length scales to analyze the mean velocity defect profiles is provided in the present study. The velocity scales include U_τ proposed by classical theory, and the mixed velocity scale ($U_e\delta^*/\delta$) proposed by Zagarola and Smits (1998) for the zero pressure gradient turbulent boundary layer flows. The mixed velocity scale ($U_e\delta^*/\delta$) was later extended to turbulent boundary layers with pressure gradients by Castillo (2000). The boundary layer thickness δ is commonly used to normalize y but a more useful characteristic length scale for pressure gradient turbulent boundary layers is the defect thickness ($\Delta = \delta^* U_e/U_\tau$) proposed by Clauser (1954).

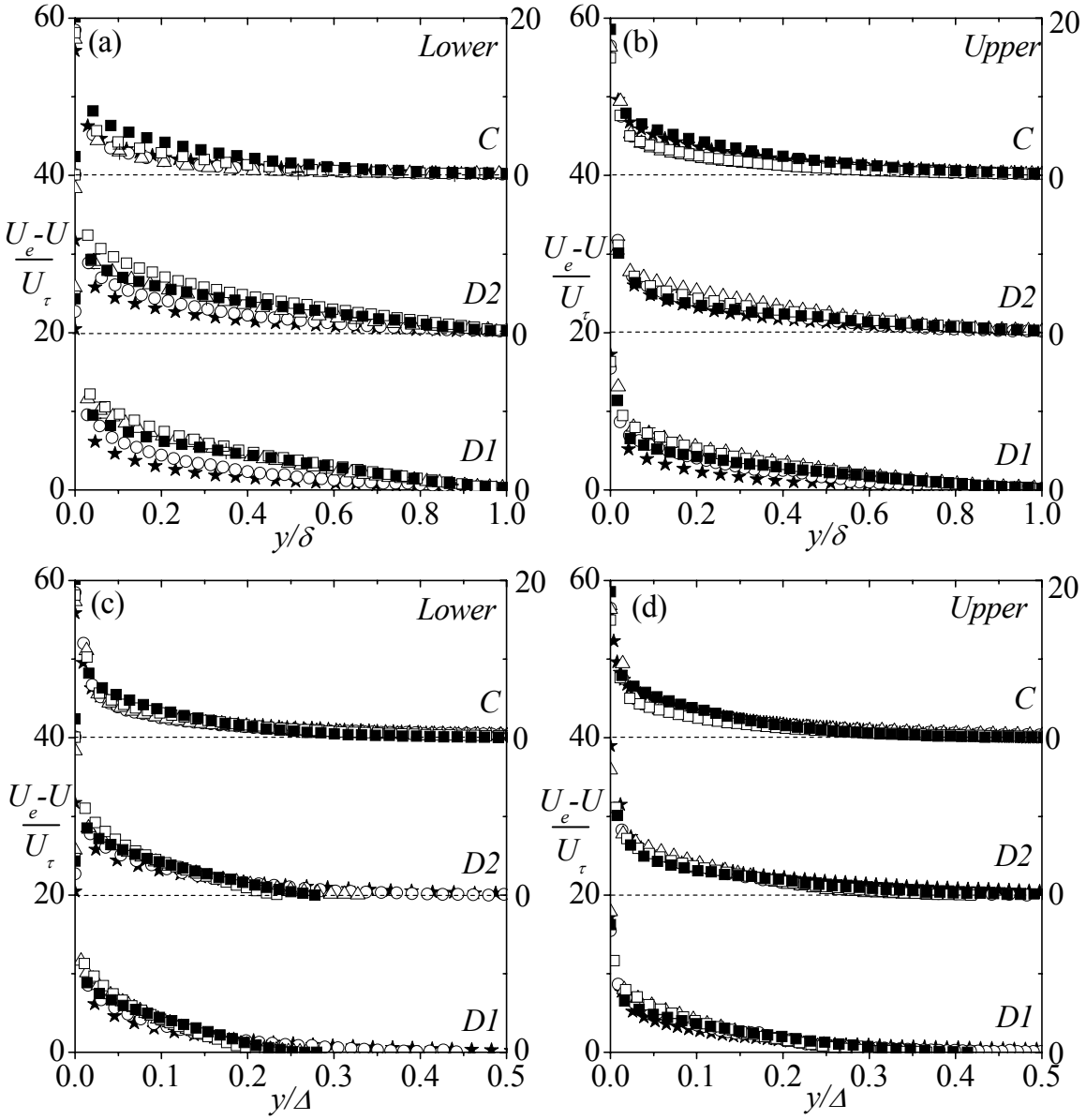

Figure 5.5: Mean velocity defect profiles normalized by friction velocity. Note that in (a) and (b) y by δ; in (c) and (d) y by Δ. Symbols are: *L1*: ξ; *L2*, –; *L3*, 8; *L4*, ∀; *L5*, !.

The mean velocity defect profiles normalized by U_τ are plotted in Figure 5.5. The values of y are normalized by δ in Figures 5.5a and 5.5b while Δ is used to normalize y in Figures 5.5c and 5.5d. A distinct pressure gradient effect can be seen among the defect profiles at various locations for a given test when δ is used to normalize y. For APG, increasing upward deviation from the *L1* profile is observed in the diverging section and

profile at *L5* returning towards upstream profile. Similar to the mean velocity profiles (Figure 5.2a), the pressure gradient effect is greater for the lower boundary layer. For FPG, profiles move downwards and subsequently return towards the upstream profile at *L5*. It can be seen from Figures 5.5c and 5.5d that for $y/\Delta > 0.1$, profiles are nearly indistinguishable at all the locations for a given test.

In Figure 5.6, $U_e\delta^*/\delta$ is used to plot the defect profiles. The boundary layer thickness, δ, is used to normalize y in Figures 5.6a and 5.6b while y is normalized by Δ in Figures 5.6c and 5.6d. It can be seen that the mixed scaling does a better job in collapsing the profiles onto a single curve compared to U_τ (Figures 5.5a and 5.5b). Figures 5.6c and 5.6d also show that Δ provides a good collapse among profiles of a given test and for $y/\Delta > 0.1$, the profiles are nearly indistinguishable. In Figure 5.6, both length scales (δ and Δ) provide a reasonable collapse among the profiles. However, comparing all the combinations of velocity and length scales used in Figures 5.5 and 5.6, it can be concluded that when mean velocity defect profiles are normalized by $U_e\delta^*/\delta$ and y by δ the best overall collapse among the profiles is achieved for a given test.

5.5 Turbulence Intensities and Reynolds Shear Stress

The streamwise turbulent intensity, u, normalized by U_e and y by $h(x)$ is shown in Figure 5.7a. It should be recalled that $h(x)$ is local half channel height. For APG, the peak value $(u/U_e)_{max}$ occurs very close to the wall and the profile decays rapidly away from the wall. As the flow develops through the diverging section, the peak value $(u/U_e)_{max}$ increases. The location of $(u/U_e)_{max}$ moves away from the wall and the location of local minimum moves closer to the upper wall. The peak values for the upper and lower boundary layers

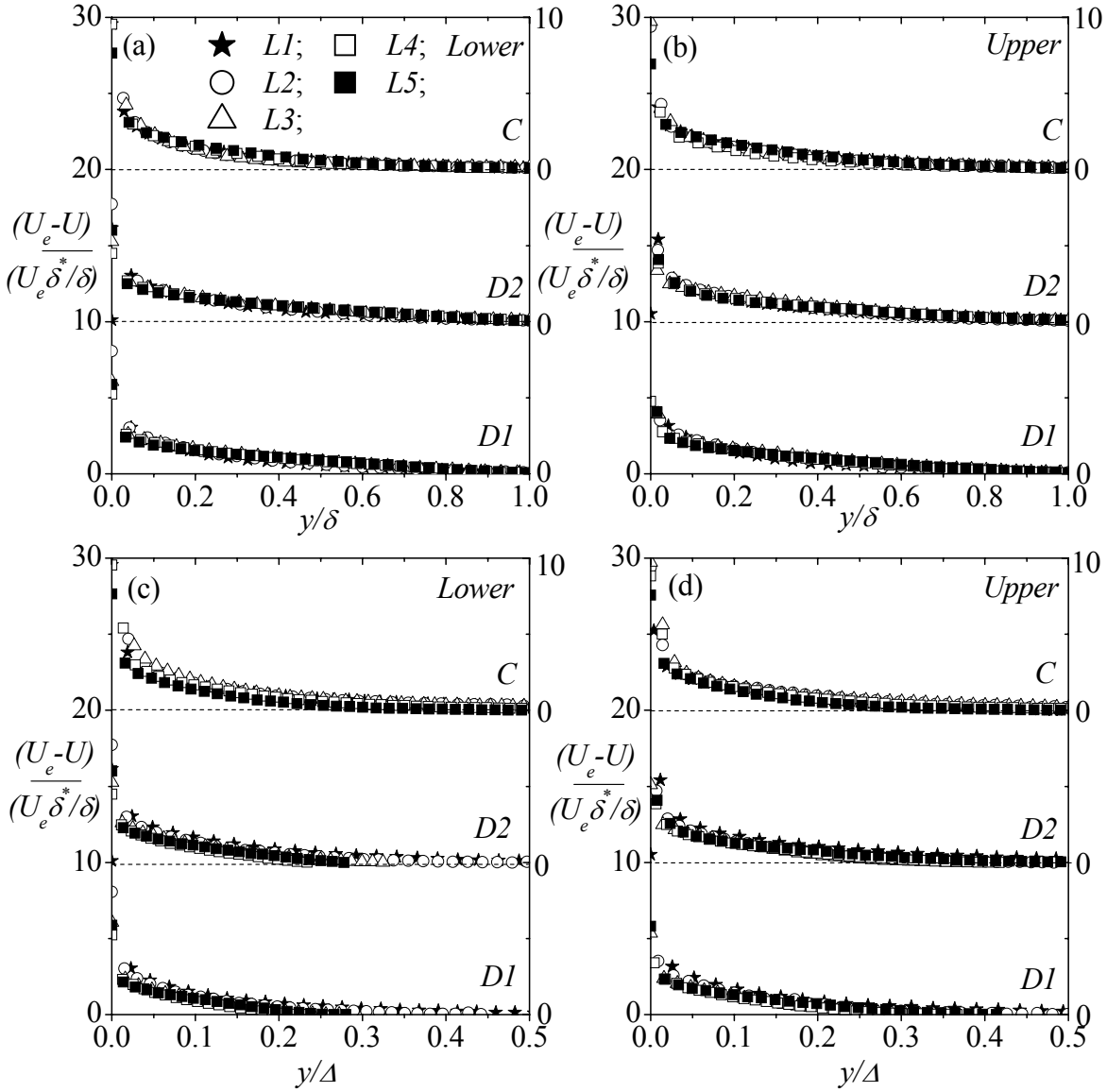

Figure 5.6: Mean velocity defect profiles normalized by mixed scaling proposed by Zagarola and Smits (1998). Note that in (a) and (b) y by δ; in (c) and (d) y by Δ. Symbols are: *L1*: ξ; *L2*, –; *L3*, 8; *L4*, ∀; *L5*, !.

are similar. The effect of APG is more dramatic in Test D2 which has greater magnitude of K. For this test, $(u/U_e)_{max}$ at *L4* occurred at $y/h = 0.23$. This corresponds to $y/\delta = 0.18$ compared to $y/\delta = 0.45$ for the data reported by Skåre and Krogstad (1994). As the flow returns to the parallel plates, *L5*, the turbulent intensity begins to decay but it is still high compared to the upstream profile.

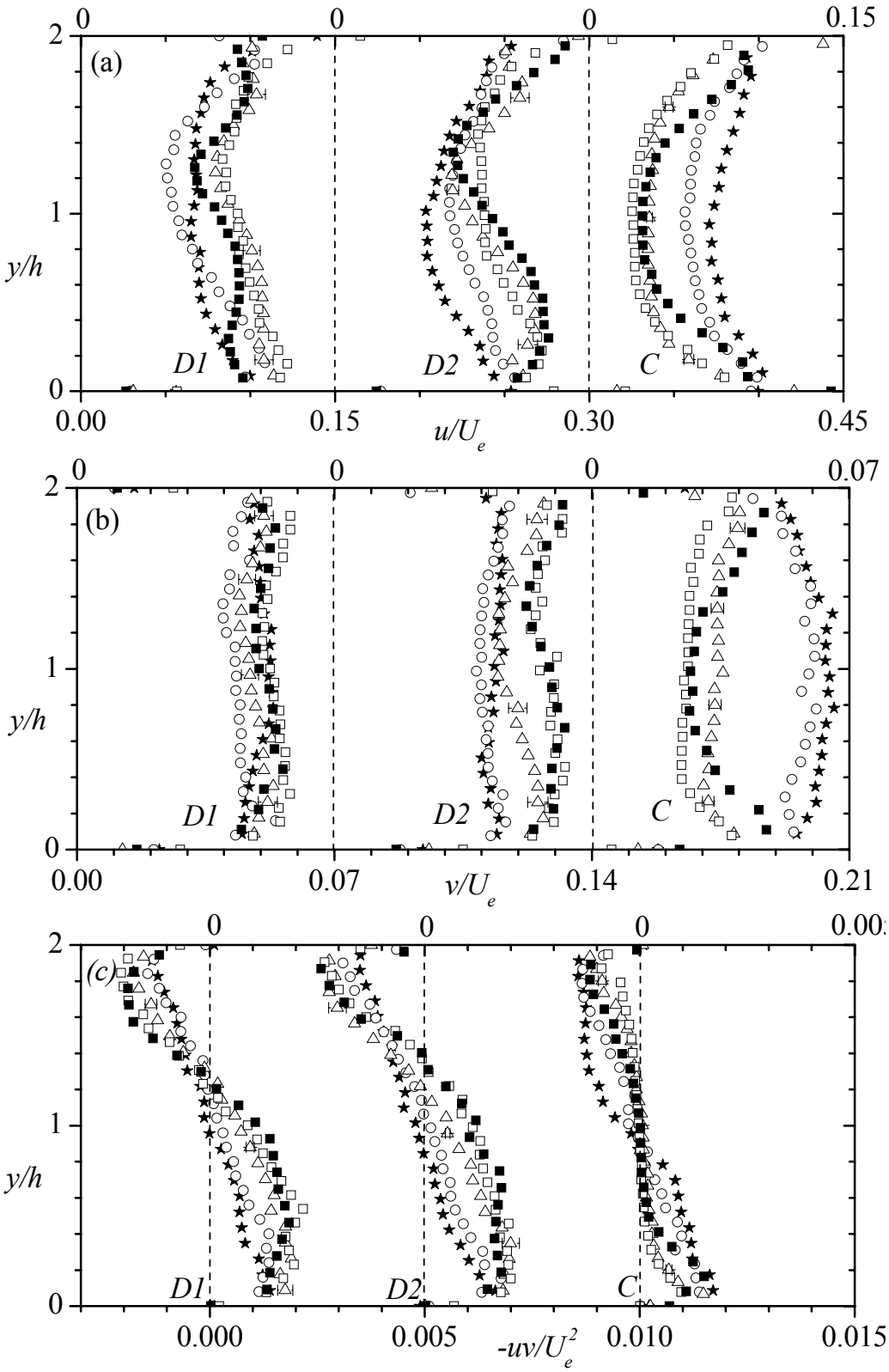

Figure 5.7: Profiles of turbulent intensities and Reynolds shear stress in outer coordinates: (a) streamwise turbulent intensity, (b) transverse turbulent intensity, (c) Reynolds shear stress. Symbols are: *L1*: ξ; *L2*, –; *L3*, 8; *L4*, ∀; *L5*, !.

The acceleration of the flow produces a progressive decay of the streamwise turbulent intensity for Test C, an opposite trend compared to the APG. Here, $(u/U_e)_{max}$ at *L4* decreased by 64% compared to the upstream value. Unlike, the APG profiles, these profiles remain nearly symmetric at all locations.

Figures 5.7b and 5.7c show that the development of transverse turbulent intensity, v, and Reynolds shear stress are qualitatively similar to the streamwise turbulent intensity. It should be noted that the Reynolds shear stress is positive in the lower boundary layer and negative in the upper boundary layer. This is in accordance with the orientation of the mean shear layer. The most significant effects of pressure gradient on the transverse turbulent intensity can be seen in Test C where $(v/U_e)_{max}$ at *L4* is 61% lower than at *L1*. The values of the Reynolds shear stress are increasing in the APG and the location of $(-uv/U_e^2)_{max}$ is moving away from the walls. Compared to the upstream profile at the lower wall, the value of $(-uv/U_e^2)_{max}$ at *L4* is 45% and 30%, respectively, higher for Test D1 and Test D2 On the contrary, the shear stress is decaying in magnitude under the effect of FPG. In the region $0.5 < y/h < 1.25$, the shear stress is nearly zero at *L3* and *L4*. For a two-dimensional flow, positive $\partial U/\partial x$ (FPG) is associated with negative $\partial V/\partial y$ and Townsend (1961) suggested that negative $\partial V/\partial y$ tends to flatten the large eddies and reduces their contribution to Reynolds stresses.

According to Townsend (1976), the simplest index of turbulence structure is the relative values of the components of the Reynolds stress tensor. These stress ratios v^2/u^2, $-uv/u^2$ and $-uv/v^2$ are shown in Figure 5.8. The distribution of the stress ratios also provides insight into large-scale anisotropy (Krogstad *et al.* 2005). Standard two-equation turbulence models (e.g., k-ε and k-ω) implicitly assume local isotropy (i.e., v^2/u^2

is unity), the information presented herein will be invaluable to turbulence modelers. Near the upper and lower walls, no systematic pressure gradient effects are observed for both the APG and FPG profiles. However, away from the walls, there is a considerable decay and flattening of the stress ratio within the diverging section. For Test D2, for example, the maximum value of v^2/u^2 in the diverging section is about 0.3 to 0.4 compared to 0.65 at the upstream location. This can be attributed to more rapid increase in u^2 due to APG compared to v^2. Skåre and Krogstad (1994) reported that the mechanism for redistributing the turbulent energy between the different normal stresses is independent of the mean flow pressure gradient. Their stress ratio profiles were similar throughout the whole boundary layer. Their finding may be attributed to the APG turbulent boundary being maintained in equilibrium.

For FPG, on the other hand, away from the walls, profiles of v^2/u^2 in the converging section are higher in comparison to the upstream profile. This implies that FPG attenuates u^2 more significantly than v^2 does. It is also evident that v^2/u^2 profiles are significantly higher in FPG than in APG. The peak values at *L2* to *L4* for the FPG case, for example, are about twice as high as in the APG case. This is an indication that, in principle, Second Moment Closures which solve the transport equations for the Reynolds stresses would be more suitable for predicting pressure gradient turbulent flows than the two-equation turbulence models. Figures 5.8b and 5.8c show that pressure gradient does not have any significant effects on $-uv/u^2$ and $-uv/v^2$ in the near-wall region. However, in APG $-uv/u^2$ and $-uv/v^2$ show an increasing trend away from the walls which can be attributed to a greater rate of increase of $-uv$ compared to u^2 and v^2. The location where $-uv/u^2$ and $-uv/v^2$ changes sign moves closer to the upper wall. In FPG case, $-uv/u^2$ shows

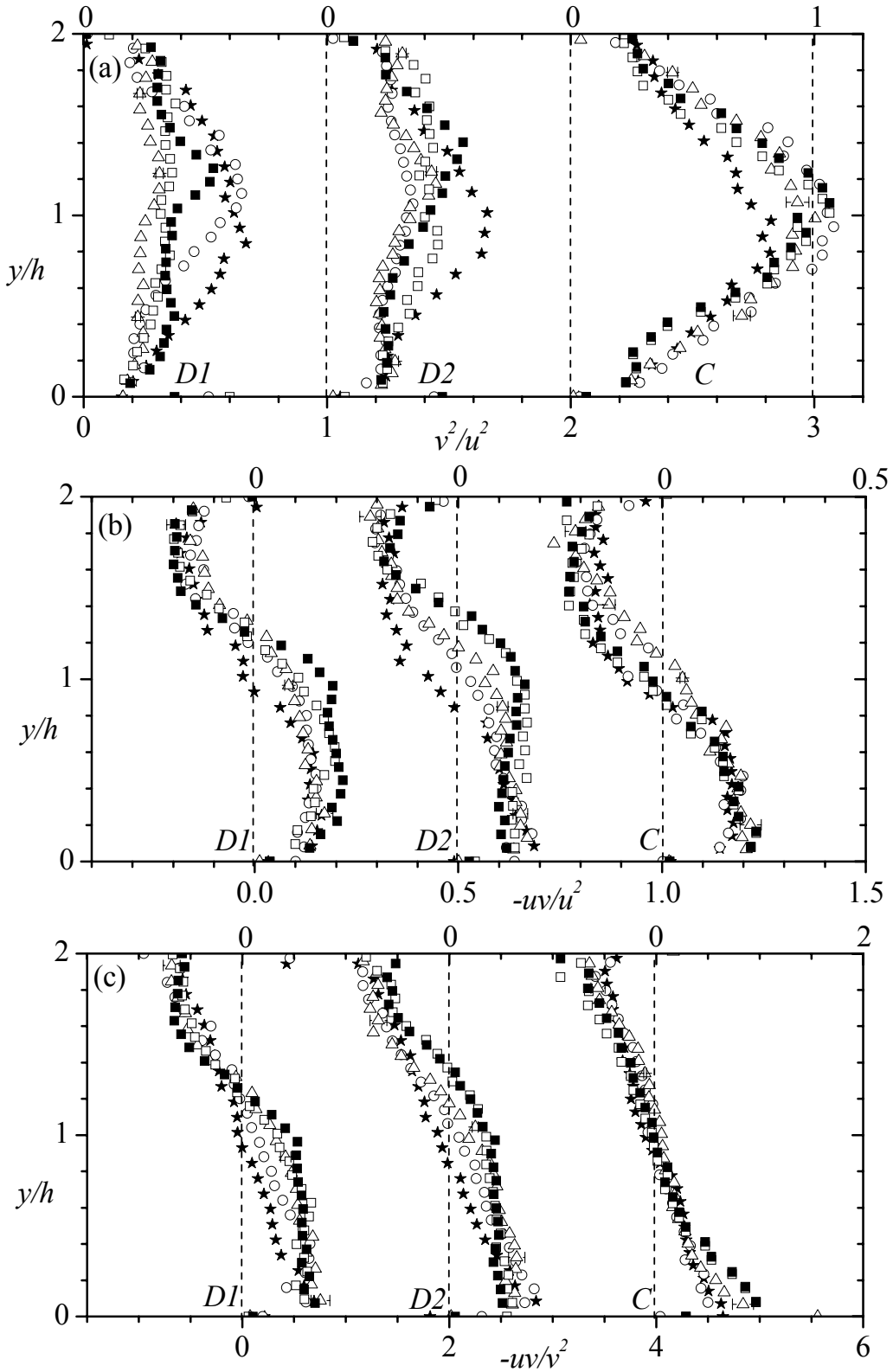

Figure 5.8: Stress ratio profiles: (a) v^2/u^2, (b) $-uv/u^2$, (c) $-uv/v^2$. Symbols are: *L1*: ξ; *L2*, –; *L3*, 8; *L4*, ∀; *L5*, !.

a decreasing trend implying that u^2 is decaying slower than $-uv$ but no systematic effects of FPG are observed in case of $-uv/v^2$.

The streamwise and transverse turbulent intensities normalized by the friction velocity are shown in Figures 5.9-5.11. Durst *et al.* (1998) compiled values of u^+_{max} from sixteen different studies in boundary layer and fully developed channel flows over a large range of Reynolds number ($Re_h = 10^3$ to 10^6) and reported that $u^+_{max} = 2.55 \pm 0.25$. These values are in excellent agreement with present value of $u^+_{max} \approx 2.6$. Similarly, values of $v^+_{max} = 0.90$ - 1.1 obtained in the present study are comparable to those reported by Wei and Willmarth (1989) in the range $Re_h = 14914$ - 39582. Close to the walls, the values of u^+ and v^+ are significantly higher at all the locations compared to *L1* for APG (Figures 5.9 and 5.10) and remain high up to the edge of the boundary layer. For FPG, *L1* profiles are higher than the rest of turbulent intensity profiles.

The Reynolds shear stress in inner coordinates can be seen in Figure 5.11a and 5.11b. To facilitate visual comparison, the negative Reynolds shear stress in the upper boundary layer is plotted as positive values in Figure 5.11b. A value of $-u^+v^+_{max} = 0.65$ was obtained at *L1*. Even though this value is smaller than the expected value of $-u^+v^+_{max} = 1$ at high Reynolds numbers, they are not significantly different from a value of $-u^+v^+_{max} = 0.7$ reported in the DNS study by Kim *et al.* (1987). The lower values (less than unity) are likely due to low Reynolds number effects. The variation of shear stress is essentially the same as in the case of turbulent intensities. An increasing deviation compared to *L1* is observed for APG while a decreasing trend is seen for FPG. Again, more pronounced effects of pressure gradient are observed at the lower wall. In the lower boundary layer at *L4*, $(-u^+v^+)_{max}$ increases to 1.45 and 1.30 for Test D1 and Test D2

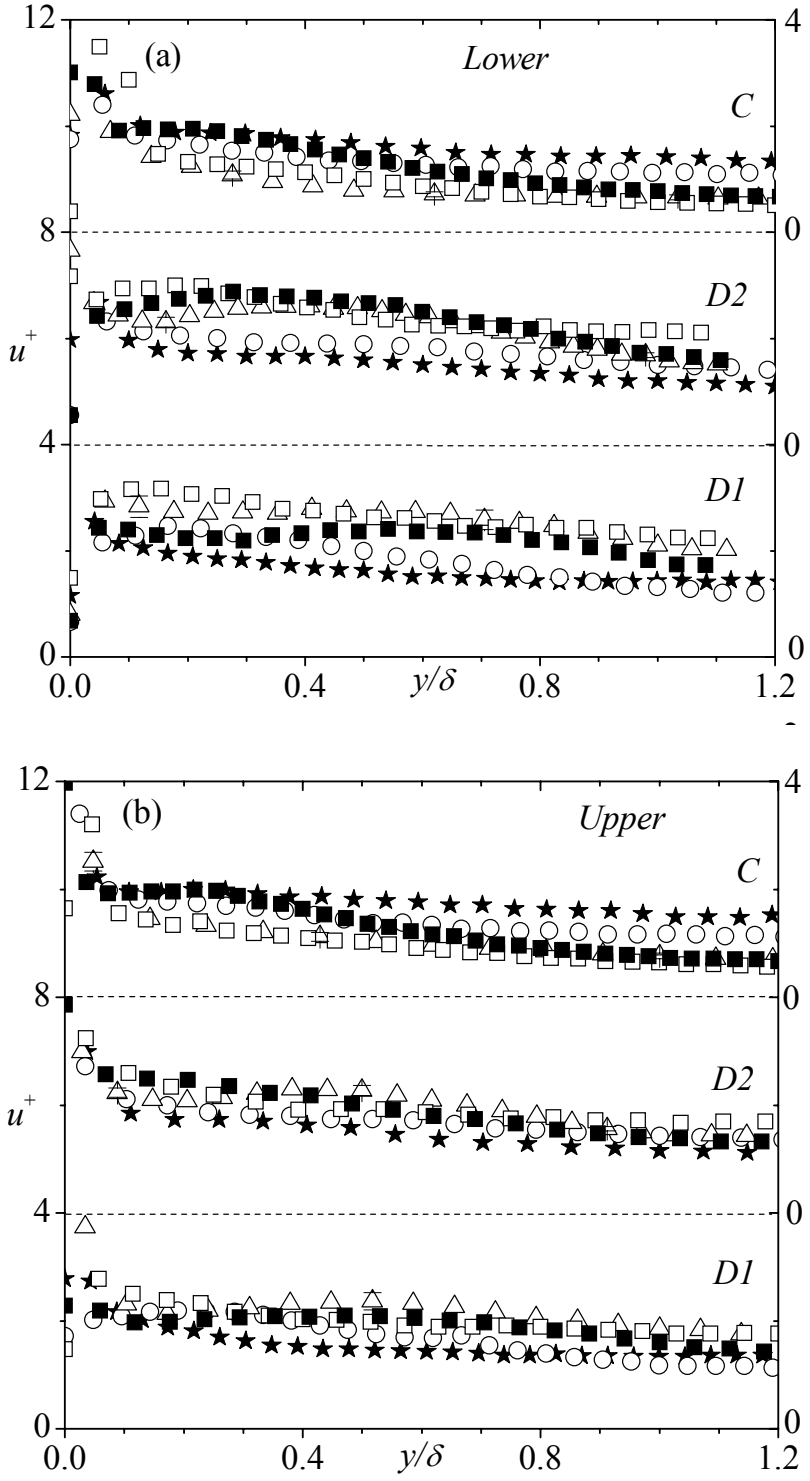

Figure 5.9: Profiles of streamwise turbulent normalized by friction velocity: (a) lower and (b) upper. Symbols are: *L1*: ξ; *L2*, –; *L3*, 8; *L4*, ∀; *L5*, !.

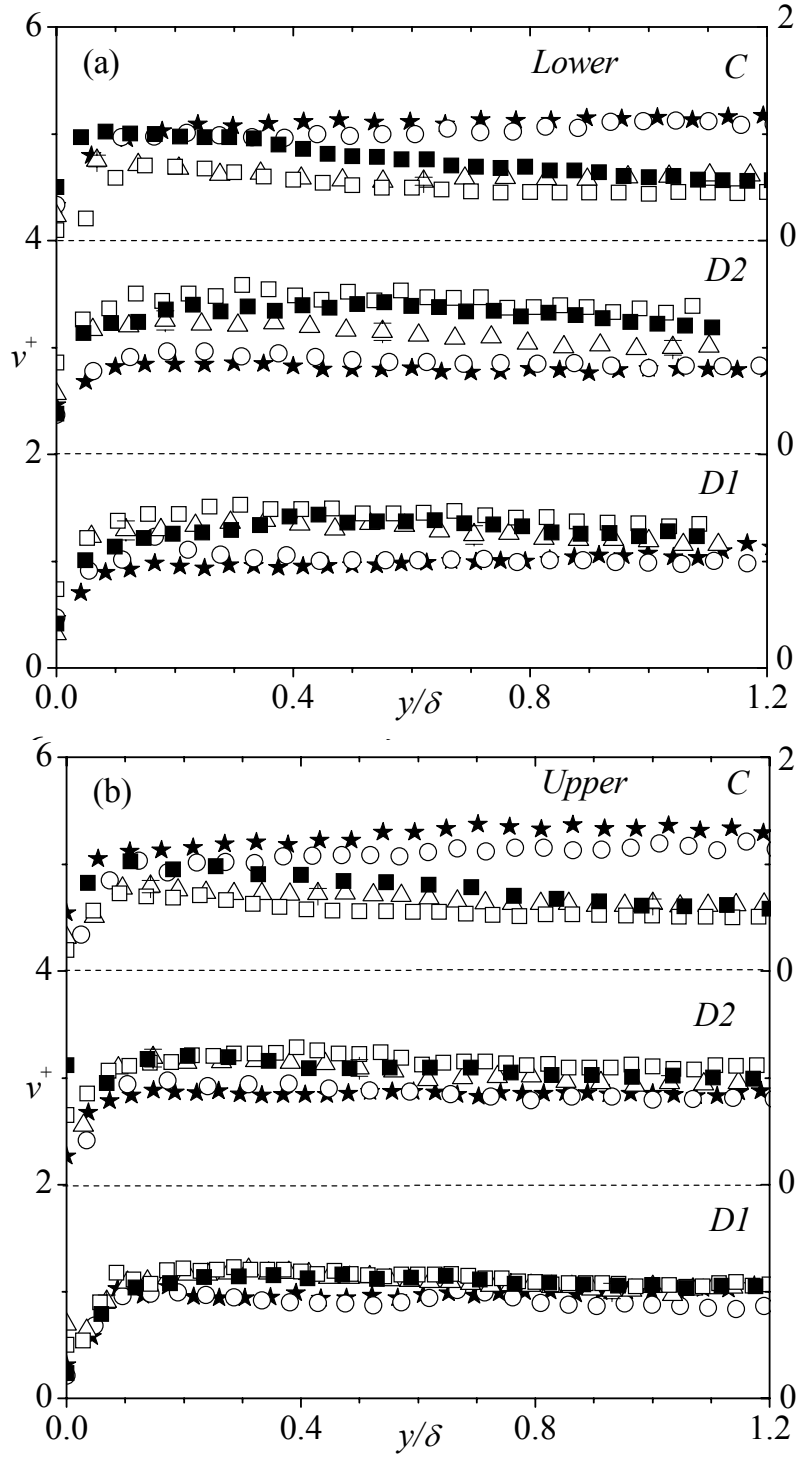

Figure 5.10: Profiles of transverse turbulent intensities normalized by friction velocity: (a) lower and (b) upper. Symbols are: *L1*: ξ; *L2*, –; *L3*, 8; *L4*, ∀; *L5*, !.

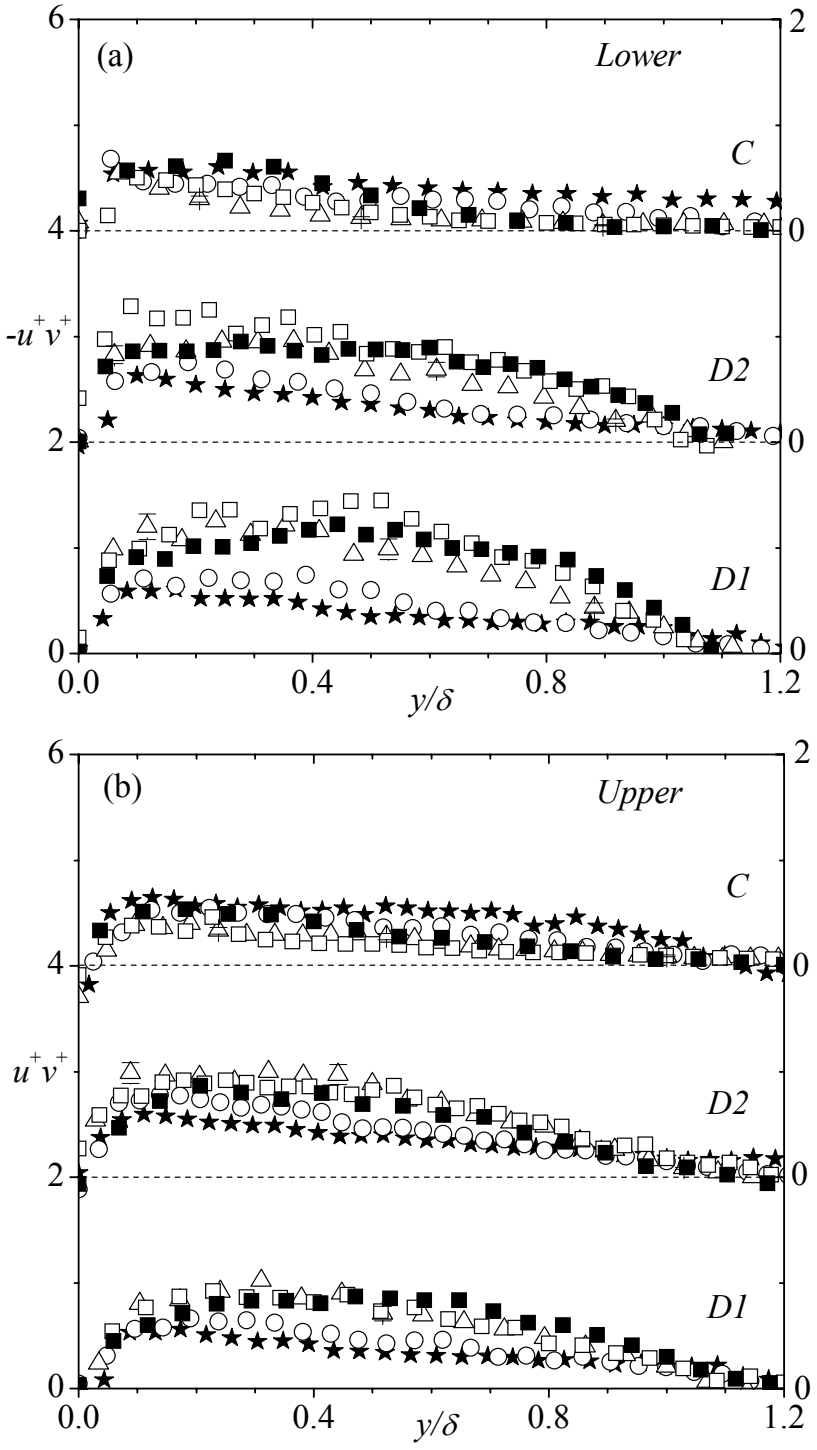

Figure 5.11: Profiles of Reynolds shear stress normalized by friction velocity: (a) lower and (b) upper. Symbols are: *L1*: ξ; *L2*, –; *L3*, 8; *L4*, ∀; *L5*, !.

respectively. Under the influence of FPG, in lower boundary layer of *L4*, $(-u^+v^+)_{max}$ remains at 0.65**.**

5.6 Turbulence Production

The production terms in the transport equations for the Reynolds stresses and turbulent kinetic energy are, respectively, given by $Pu_iu_j = -[u_iu_k\partial U_j/\partial x_k + u_ju_k\partial U_i/\partial x_k]$ and $P_k = [-u_iu_j\partial U_j/\partial x_i]$. For a two dimensional turbulent flow, the production terms in u^2 and $-uv$ are, respectively, $P_{uu} = [-u^2\partial U/\partial x - uv\partial U/\partial y]$ and $P_{uv} = [-u^2\partial V/\partial x - v^2\partial U/\partial y]$. Similarly, the production term in turbulent kinetic energy is $P_k = [-uv\,(\partial U/\partial y + \partial V/\partial x)] - [(u^2\partial U/\partial x + v^2\partial V/\partial y]$. It was found that $\partial U/\partial y >> \partial V/\partial x$ so that $-uv\partial U/\partial y$ becomes the dominant production term in P_{uu} and P_k while $-v^2\partial U/\partial y$ is the major contributor to P_{uv}.

Typical profiles of $-uv\partial U/\partial y$ and $-v^2\partial U/\partial y$ for the various tests at *L3* and *L4* are compared with upstream profile in Figures 5.12a and 5.12b, respectively. The effect of the APG is to enhance the production term, $-uv\partial U/\partial y$, (Figure 5.12a). The term remains high away from the wall due to high magnitude of $-uv$ and $\partial U/\partial y$ over most of the channel. In FPG, the production term peaks very close to the wall and rapidly decays. The term is nearly zero in the region $0.5 < y/h < 1.4$. The magnitude of the production term, $-v^2\partial U/\partial y$, (Figure 5.12b) behaves in qualitatively similar manner as the $-uv^2\partial U/\partial y$ term. This production term is also enhanced in APG and attenuated in FPG.

5.7 Summary of Results

An experimental study has been conducted in variable adverse and favorable pressure gradient channel flow. The results show that the mean velocity profiles become

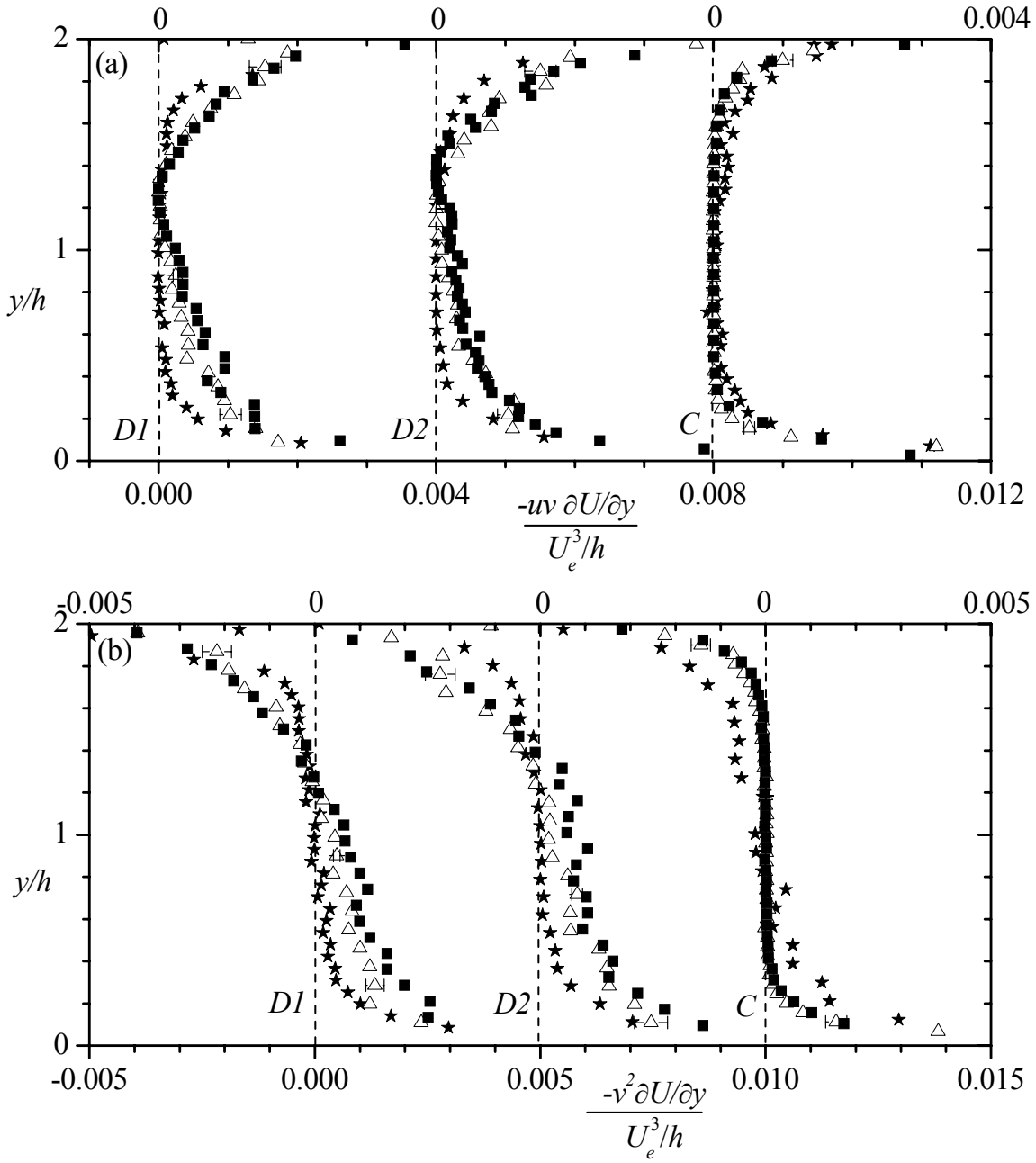

Figure 5.12: Profiles of turbulence production: (a) $-uv\partial U/\partial y$, (b) $-v^2\partial U/\partial y$. Symbols are: *L1*: ξ; *L3*, 8; *L4*, ∀.

'more full' in favorable pressure gradient and 'less full' in adverse pressure gradient. The APG is observed to affect the lower boundary layer more significantly compared to the upper boundary layer. However, the effect of FPG on the upper and the lower

boundary layers was found to be nearly similar. Momentum flux is predominantly negative in APG and positive in FPG. The APG enhances production of turbulent kinetic and Reynolds shear stress, while these quantities are attenuated by FPG. As a result, the turbulent intensities and Reynolds shear stress are increased in APG and decreased in FPG. For turbulent intensities the location of the minimum peak and for Reynolds shear stress, the location where $-uv = 0$, was observed to shift towards the upper wall under the influence of APG. However, in FPG, turbulent intensities and Reynolds shear stress remained fairly symmetric. Different velocity and length scales were used to plot the mean velocity defect profiles. The scale ($U_e\delta^*/\delta$, δ) is the most successful in collapsing the profiles onto a single curve.

The stress ratios are plotted to provide insight into large-scale anisotropy. The effect of pressure gradients is observed only away from the wall. Away from the wall, the FPG was observed to promote isotropy while APG reduces it. On the other hand, $-uv/v^2$ and $-uv/u^2$ increase in APG away from the wall but no systematic trend was observed for FPG.

CHAPTER 6: GEOMETRY INDUCED SEPARATION IN PRESSURE GRADIENTS

The results of the separated and reattached experiments conducted in the parallel-wall (Test CC), diverging (Test APG) and converging (Test FPG) channels are presented and discussed in this chapter. In this chapter, only tests for which the rib was located at x/k = 0 will be considered. That is, results Tests APG-II and APG-III for which the rib was, respectively, located at x/k = -25 and 25 will not be reported. The data sets presented in this chapter include the mean velocities, Reynolds stresses, triple velocity correlations, terms in the transport equations for the turbulent kinetic energy and Reynolds shear stress as well as distributions of eddy viscosity and mixing length in the separated and redevelopment regions. Selected data sets reported in the previous chapter for the generic asymmetric converging and diverging channels without a rib attached to the lower wall are also included and serve as a reference for interpreting the separated and reattached flows. The results obtained in this section for Test CC are compared with previous studies obtained downstream of a transverse square rib. The open channel flow measurements of Agelinchaab and Tachie (2008) and the wind tunnel measurements by Antoniou and Bergeles (1988) downstream of a rib are compared and discussed in Appendix C. The present results show reasonable agreement with the previous data.

6.1 Upstream Flow and Boundary Layer Parameters

A summary of some of the pertinent upstream flow and boundary layer parameters for each test condition is presented in Table 6.1. These parameters at the upstream location include the maximum streamwise velocity (U_e), the boundary layer thickness (δ) defined

Table 6.1: Summary of upstream flow parameters.

Test	U_e (m/s)	U_e/U_b	δ (mm)	δ^* (mm)	θ (mm)	H	Re_k	Re_θ	k/δ	$k/(2h)$	$k^+ = kU_\tau/\nu$
CC	0.445	1.09	19	2.2	1.4	1.57	2640	620	0.31	0.09	140
APG	0.460	1.10	21	2.8	1.8	1.55	2760	830	0.29	0.11	140
FPG	0.464	1.08	39	3.6	2.5	1.44	2760	1150	0.15	0.07	140

as the y location where the local velocity is 99% of U_e, the displacement thickness (δ^*), the momentum thickness (θ), the Reynolds number based on upstream U_e and k (Re_k), the Reynolds number based on upstream U_e and θ (Re_θ) and the perturbation strength (k/δ). As noted in Chapter 4, the ratio of U_e/U_b is approximately 1.1 for the three test conditions. This value is in good agreement with prior experiments (Shah *et al.*, 2008) and DNS study (Kim *et al.*, 1987) conducted at similar Reynolds number. The boundary layer thickness of the approach flow is nearly the same for Test CC and APG but higher for Test FPG likely due to the larger physical flow domain of the converging channel. The shape factors obtained for the three test cases are not significantly different. These values also compare reasonably well with prior data at similar Re_θ (Purtell *et al.*, 1981). The perturbation strength k/δ of 0.31, 0.29, and 0.15, respectively, in Tests CC, APG and FPG implies a weak perturbation according to the classification proposed by Bradshaw and Wong (1972). The blockage ratio, $k/(2h)$, where $2h$ is the channel height at $x = 0$ and the ratio of the rib height to the viscous length scale of the approach flow ($k^+ = kU_\tau/\nu$, where U_τ is the friction velocity) are also reported in Table 6.1. The value of $k^+ = 140$ indicates that the crest of the rib is well beyond the buffer region ($y^+ \leq 30$) but within the logarithmic layer in all the tests. This would imply that the rib distorts the viscous region

of the approach boundary layer, and the distortion of the inner region of the approach boundary layer by the rib is identical in all the tests.

6.2 Iso-Contours of Mean Flow and Turbulent Quantities

The iso-contours of the mean velocity (U), mean spanwise vorticity ($\Omega_z = \partial V/\partial x - \partial U/\partial y$) and Reynolds shear stress ($-uv$) were obtained to reveal some qualitative features of the flow pattern in the vicinity and downstream of the rib (Figure 6.1). The data are made dimensionless using the approach maximum streamwise velocity (U_e) and rib height (k). The corresponding streamlines are superimposed on each plot to show the extent of the recirculation region and to relate the turbulent quantities to the mean flow pattern. The vertical axis is shown up to $y = 6k$, which is above the half channel height in Test APG ($h = 4.5k$) near the half channel height of Test CC ($h = 5.75k$) and below that of Test FPG ($h = 7k$). In each case, the flow separates at the leading edge of the rib and is deflected upward from the rib. As expected, a recirculation bubble is formed downstream of the rib and subsequently the flow reattaches. A counter clockwise rotating vortex at the downstream edge of the rib can also be observed. The lower half of the recirculation bubble is dominated by reverse flow with a maximum magnitude of $0.2U_e$ located at $x/k \approx 4$ to 5 and adjacent to the floor. The reattachment length (x_r) was estimated as the x-location where the separated streamline reattached on the floor. It was found that $x_r/k = 10.4$, 10.3 and 9.8, respectively, in Tests CC, APG and FPG. The x_r/k values in Tests CC and APG are almost identical and the value for FPG is only 5% smaller than those in Tests CC and APG.

As is well known, the reattachment length is a sensitive parameter that depends on various parameters. For example, it would increase with increasing k/δ (Eaton and

CC	APG	FPG

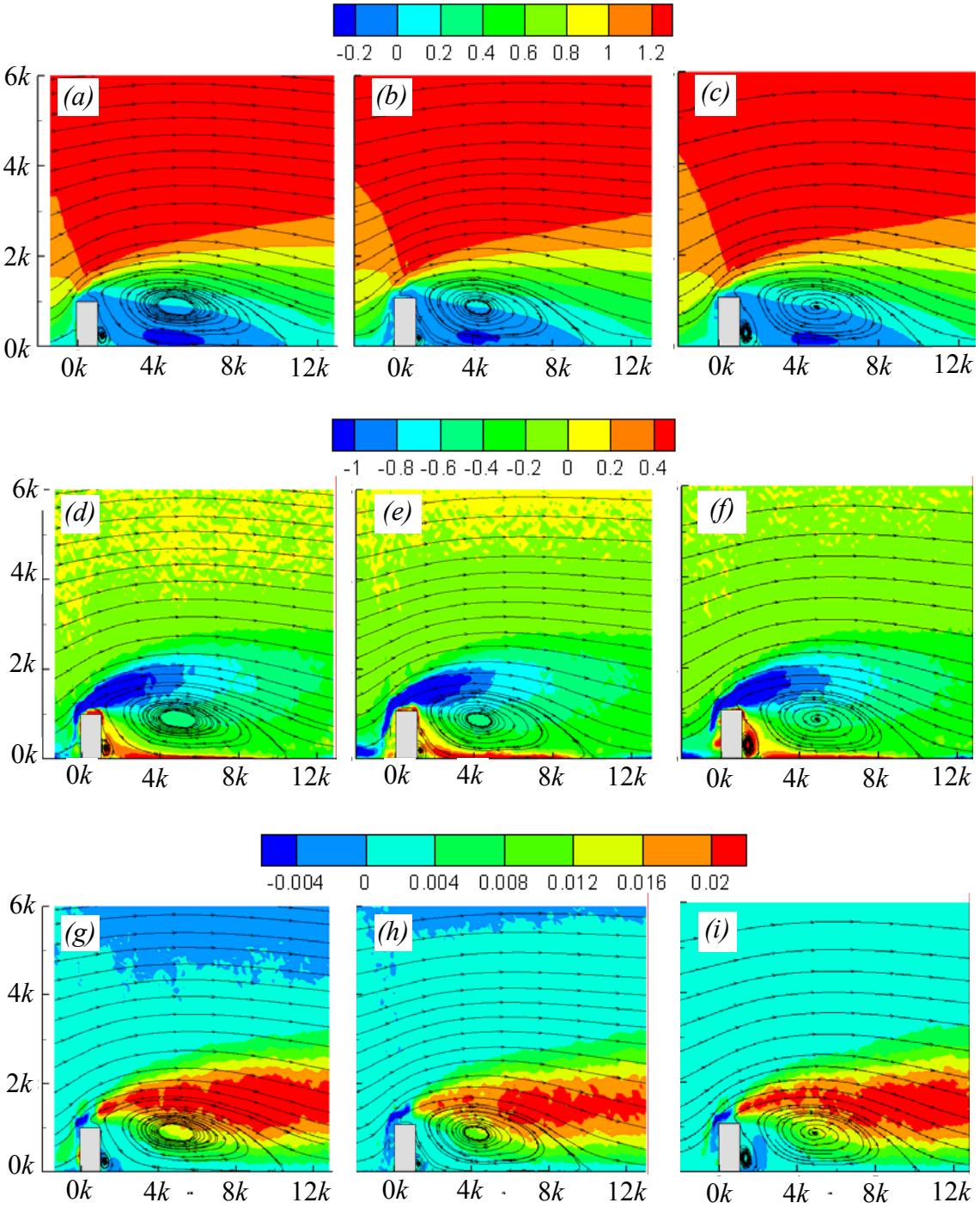

Figure 6.1: Iso-contours of mean velocity, vorticity and Reynolds shear stress: (a), (b) and (c) U; (d), (e) and (f) Ω_z; (g), (h) and (i) $-uv$.

Johnston, 1981) and is negatively correlated with freestream turbulence (Castro, 1979). Castro (1979) reported a value of x_r that ranged from $x_r/k = 9$ to 11 for a boundary layer of thickness $0.069k$ to $0.169k$. The closeness of x_r/k values in the present study may be partly due to the notion that the inner layer of the approach boundary layer was equally distorted in all the tests. Furthermore, (and as will be shown in Figure 6.2a and 6.2b), the distributions of the maximum velocity and the acceleration/deceleration parameter in the separated region ($0 < x/k < 12$) do not vary significantly from test to test.

The present value of $x_r/k = 10.4$ for Test CC ($k/\delta = 0.31$) is 10% lower than $x_r/k = 11.5$ reported by Bergeles and Athanassiadis (1981). However, it should be noted that in their study, the perturbation strength was higher ($k/\delta = 2.08$) and the background freestream turbulence was lower (0.5% compared with background turbulence of 5% in the present study). Both effects (higher k/δ and lower turbulence level) would increase the reattachment length. Agelinchaab and Tachie (2008) reported a value of $x_r/k = 8.5$ in their open channel flow over a square rib ($k/\delta = 0.11$). The lower value reported by Agelinchaab and Tachie (2008) may be partly attributed to the lower perturbation strength (i.e., $k/\delta = 0.11$ in their study compared with $k/\delta = 0.15$ to 0.31 in the present study).

The mean flow patterns are qualitatively similar for the three cases but the rib affects a greater portion of channel height in Test APG than Test FPG. The iso-contours of the mean spanwise vorticity reveal regions of intense shear layer close to the rib. Since, $\partial V/\partial x << \partial U/\partial y$, values of Ω_z are negative everywhere expect in the very near wall region inside the separation bubble. It is apparent from the plots that the bulk vorticity is generated at the top plane of the rib and convected downstream. The Reynolds shear

stress also reveals regions of high turbulence levels in the vicinity of the separated shear layer. This should be expected because a strong shear layer ($\partial U/\partial y$) or intense mean vorticity is associated with enhanced production of turbulent kinetic energy and Reynolds shear stress.

6.3 Boundary Layer Parameters

The boundary layer parameters shown in Figure 6.2 can provide insight into the characteristics of the separated shear layer and its subsequent redevelopment. Due to the asymmetric nature of the flow, these parameters were evaluated in both the lower and upper boundary layers which are, respectively, defined as the flow region from the lower wall up to the location of U_e, and from the upper wall to the location of U_e. The values of $U_e/U_{e,ref}$ at selected x locations within the various planes of measurement are plotted in Figure 6.2a; $U_{e,ref}$ is the maximum streamwise velcoity at the corresponding upstream locations. Except for the plane containing the rib, P_1, a linear variation of U_e with x was assumed and dU_e/dx was evaluated as the slope of a least square linear fit to U_e versus x. Because U_e varied non-linearly with x within the separated region, P_1, a fifth order polynomial was fitted to the measured data and the curve fit was differentiated to estimate dU_e/dx. For each test condition, the coefficient of determination was 0.994 or higher indicating the excellent fit with the experimental data.

The values of the dimensionless acceleration/deceleration parameter, $K = (\nu/U_e^2)(dU_e/dx)$ are plotted in Figure 6.2b. In the upstream parallel section (not shown), the acceleration parameter was $K = 0.13\times10^{-6}$. For comparison, selected data obtained in the same channels (but with no rib attached to the channel floor) and at identical upstream U_e (= 0.460±0.010 m/s) are shown. As discussed in Chapter 5, the data obtained

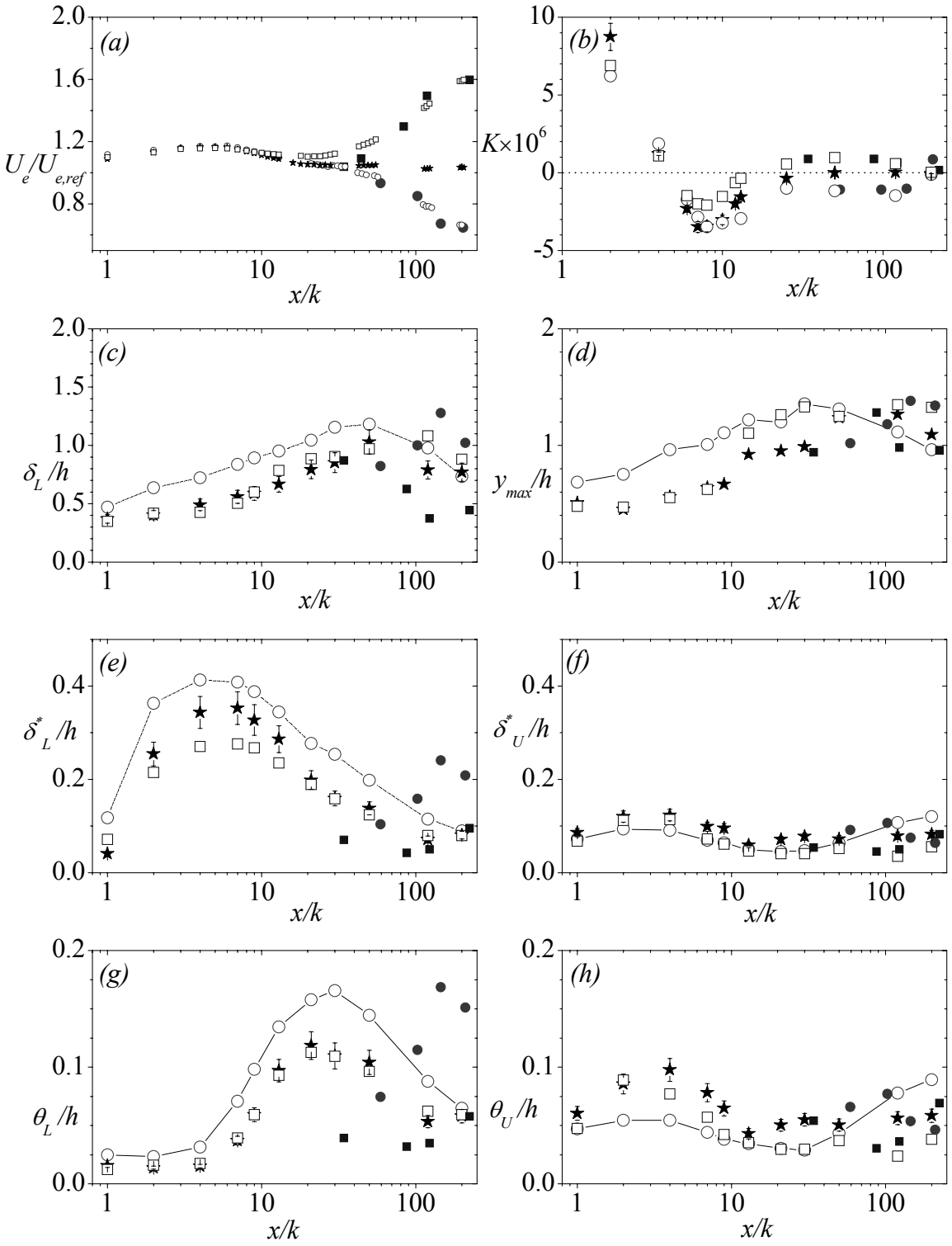

Figure 6.2: Boundary layer parameters: (a) $U_e/U_{e,ref}$, (b) K, (c) δ_L/h, (d) y_{max}/h, (e) δ^*_L/h, (f) δ^*_U/h, (g) θ_L/h and (h) θ_U/h. Symbols: CC: ξ; APG: –; FPG: ∀. Reference Test D2: , and Test C: ! are from the flow in pressure gradient channels without the rib on the channel wall. Note $U_{e,ref}$ is the maximum streamwise velocity at the upstream location.

in the channels without the rib installed on the channel floor show the expected trend within the variable section and downstream parallel section of the channel.

Regardless of the pressure gradient, it is evident that the blockage produced by the rib caused the flow to accelerate up to $x/k = 4$ (which corresponds approximately to the center of the recirculation bubble) followed by a region of flow deceleration down to $x/k = 13$. In this region, the magnitude of K in Test FPG is up to 50% of the values obtained in Test CC and Test APG. Beyond the reattachment location, the velocity variation remains nearly constant in Test CC whereas it decreases monotonically in Test APG and increases in Test FPG. At $x/k = 120$, for example, U_e is only 3% different from its upstream value in Test CC but it is 40% higher in Test FPG and 27% lower in Test APG. The pressure gradient distortion caused by the rib seems to disappear ($K \approx 0$) beyond $x/k = 20$ in Test CC but the combined effects of the rib and the pressure gradients persists up to $x/k = 120$ in Tests APG and FPG. It is important to note that the values of U_e and K with or without a square rib attached to the channel floor for a particular pressure gradient (e.g., FPG) are not significantly different in the region $x/k > 30$. This would imply that pressure gradient has stronger effects on the mean flow at these locations than the distortion produced by the ribs.

The values of δ, y_{max} (wall normal distance from the lower wall to the location of local U_e), δ^* and θ normalized by the local half channel height, are plotted in Figure 6.2c – 6.2h. In the absence of the ribs, APG increased the boundary layer parameters (and vice versa for FPG). The boundary layer thickness and y_{max} obtained in the channels with a rib installed on the channel floor exhibit a monotonic growth up to $x/k < 120$. On the other hand, δ^*_L and θ_L increase to a maximum value at $x/k = 7$ and $x/k = 21$ (except for θ in Test

APG which is at x/k = 30) and then begin to decrease monotonically. Even with the rib attached to the floor, APG thickened the lower boundary layer and produced significantly larger values of δ_L/h, δ^*_L/h and θ_L/h than in Test CC. On the other hand, the values obtained in Test FPG are either smaller than or similar to those obtained in Test CC. The trends observed for δ^*_L and θ_L are similar to those reported by Driver and Seegmiller (1985) for their wall divergence of $\alpha = 0°$ and 6°. This shows that even though mass and momentum deficit are enhanced downstream of the rib in the separated and early redevelopment region, APG tends to further increase and FPG tends to decrease the mass and momentum fluxes at the lower boundary layer. Although the values of δ^*_U/h and θ_U/h vary from one test to the other, these differences are significantly smaller than in the lower boundary layer.

6.4 Flow Development Downstream of the Rib

In this section, profiles of the mean velocities, turbulent quantities and terms in the transport equation for turbulent kinetic energy at selected streamwise locations in the separated region (x/k = 1, 2, 4, 9) and the redevelopment region (x/k = 13, 21, 30, 50, 120, 200) in Tests CC, APG and FPG are plotted together to document the effects of the pressure gradient on the flow development downstream of the rib. For comparison, the upstream profile is also plotted at each x/k location. Typical profiles obtained in the variable sections of the FPG channel (at x/k = 123) and APG channel (at x/k = 140) without the rib in Chapter 5 are compared with those obtained in the pressure gradient channels with the rib at x/k = 120. Similarly, profiles that were obtained at x/k = 224 in the FPG channel and at x/k = 205 in the APG channel without the rib in Chapter 5 are compared with those obtained at x/k = 200 in the pressure gradient channels with the rib.

Although the *x/k* locations are not identical in the pressure gradient channels with and without the rib, the comparison is still invaluable. The local maximum velocity (U_e) and half channel height (h) are used as the appropriate velocity and length scales.

6.4.1 Mean Velocity Profiles

The mean streamwise velocity profiles are shown in Figure 6.3a and 6.3b. The upper boundary layers of the upstream profile and those obtained downstream of the ribs at x/k = 1 to 50 are nearly similar. This observation suggests that the upper boundary layer is not significantly affected by the separated shear layer produced by the rib or the pressure gradient. Further downstream (at x/k = 120 and 200), however, the profiles in Test APG are 'less full' than the upstream profile and those in Test CC and Test FPG. This would imply that any effects resulting from the differences in blockage ratio in the various tests should be confined to the lower boundary layer.

As expected, the presence of the rib reduced the values of U close to the lower wall considerably. Consequently, the lower boundary layer profiles downstream of the rib become 'less full' compared with the reference upstream profile. The maximum backflow is approximately $0.2U_e$ for all the test cases. This value is similar to those reported in previous separated and reattached flows downstream of a forward facing step (Tachie *et al.* 2001) and backward facing step (Eaton and Johnston, 1981). Similar to the observations made in Chapter 5, the profiles obtained in the APG are the most distorted and the variation of U with y from the lower wall is also more gradual in Test APG than in the other profiles. The implications of this observation to turbulence production will be discussed later. The mean velocity recovered back towards the upstream profile at x/k = 200. As expected, the recovery process is slowest in Test APG. The profiles obtained at

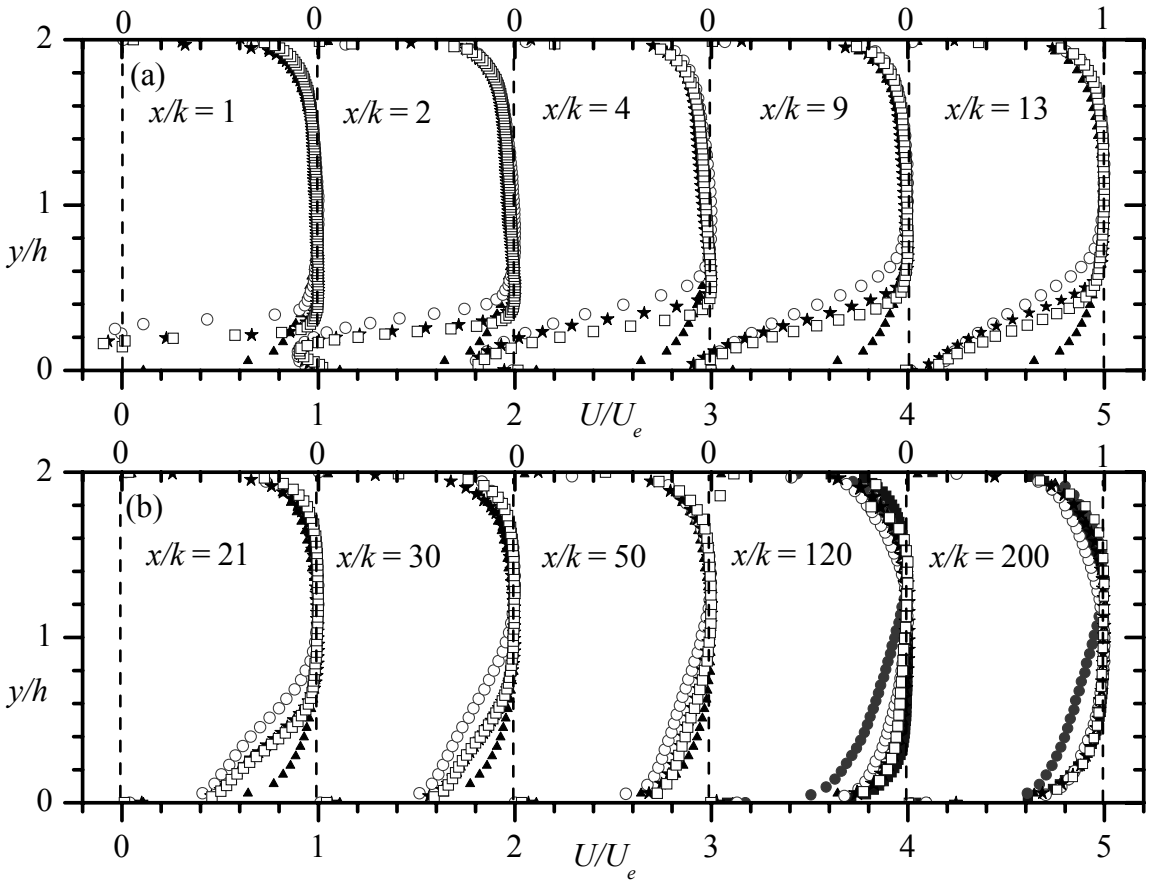

Figure 6.3: Streamwise mean velocity profiles at various streamwise locations. Symbols: Upstream:7; CC: ξ; APG: –; FPG: ∀. In (b) and (d) Test D2: ,, at x/k = 140 (*L4*) and 205 (*L5*), and Test C: !, profiles at x/k = 123 (*L4*) and 224 (*L5*).

x/k = 120 and 200 in the FPG (with or without ribs) are nearly indistinguishable. In APG, on the other hand, the present profiles are in better agreement with the reference upstream profile than if no rib was attached to the floor.

The mean transverse velocity, V, is nearly zero upstream of the rib but at x/k = 1 its value increased to about $0.2U_e$ to $0.25U_e$ (Figure 6.4a and 6.4b). The values of V are predominantly positive in the region $x/k \leq 4$ because, as shown in Figure 6.1a – 6.1c, the mean streamlines curve upwards as the rib is approached. Beyond x/k = 4, the streamlines curve downwards resulting in negative velocity. The transverse velocity

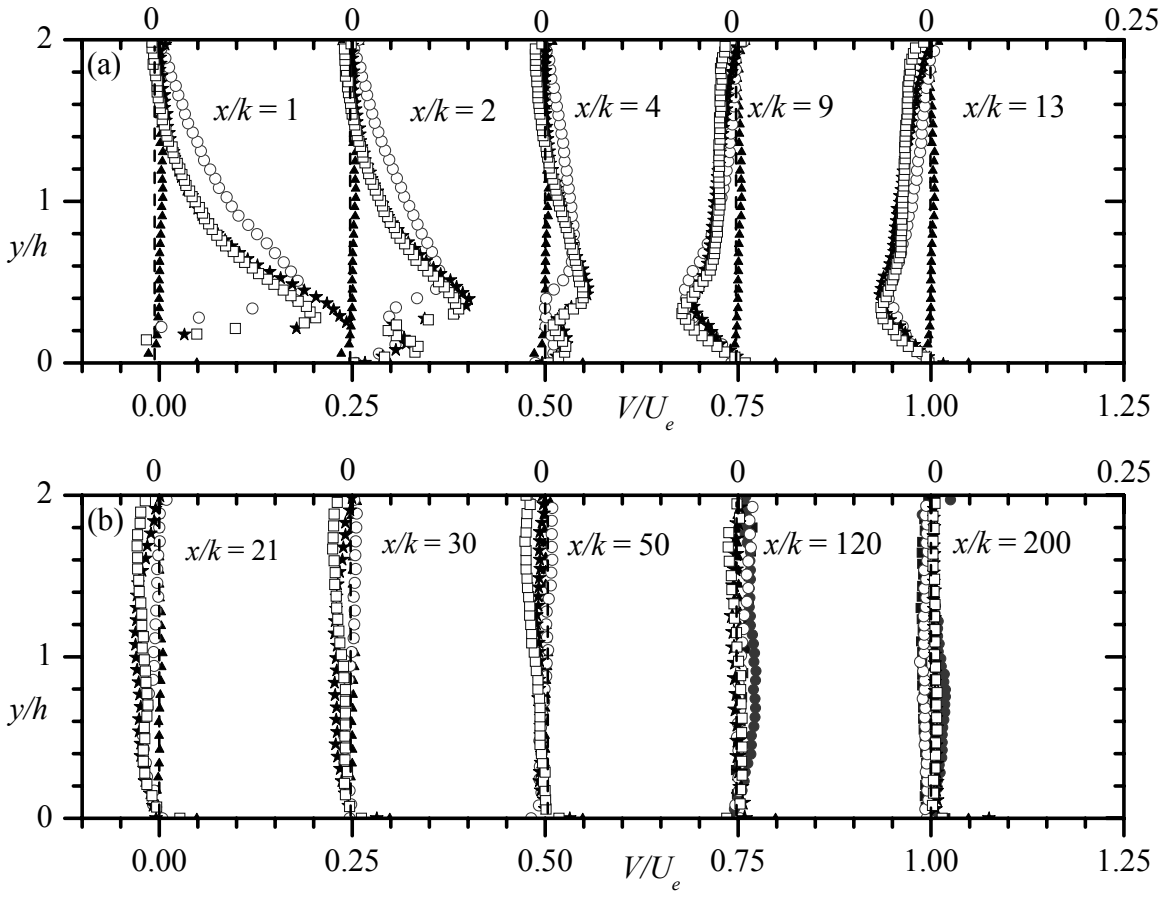

Figure 6.4: Transverse mean velocity profiles at various streamwise locations. Symbols: Upstream:7; CC: ξ; APG: –; FPG: ∀. In (b) and (d) Test D2: ,, at x/k = 140 (*L4*) and 205 (*L5*), and Test C: !, profiles at x/k = 123 (*L4*) and 224 (*L5*).

decays rapidly downstream of the recirculation. At x/k = 21 and 200, for example, the values of V/U_e are, respectively, less than 4% and 1% for all test cases.

Figure 6.4 also shows that the values of $\partial V/\partial y$ are also substantially larger in the separated region than in the upstream and redevelopment regions. Since $v^2\partial V/\partial y$ is the principal production term in the v^2 transport equation, the mechanism for the production of v^2 in the separated region would be different from that in the upstream and redevelopment regions where $\partial V/\partial y$ are small. In the absence of the ribs, V is predominantly positive in the diverging channel (Tests D1 and D2 in Chapter 5), and

negative in the converging channel (Test C). With the ribs on the lower wall however, the sign of V is independent of pressure gradient in the region $x/k \leq 21$. This observation implies that the effects of the separated shear layer on the mean flow outweigh any pressure gradient effects in this region.

6.4.2 Turbulent Intensities and Reynolds Shear Stress

The streamwise and transverse turbulent intensities are plotted in Figure 6.5 and 6.6. In the separated region and the early stage of flow redevelopment ($x/k \leq 50$), the profiles are asymmetric about the channel mid-plane ($y/h = 1$). At these streamwise locations, the values of u_{min}/U_e and v_{min}/U_e are nearly independent of pressure gradient. In the core region of the channel, the distributions of the turbulence intensities are also only marginally affected by pressure gradient. Although the background turbulence level in the present study (e.g. $u_{min}/U_e \approx 0.05$) is an order of magnitude higher than typical values reported in wind tunnel experiments, it is comparable to data reported in other two-dimensional channel flows. For example, Durst *et al.* (1998) compiled u_{min}/U_e values reported in 16 different experiments performed in a fully developed channel and concluded that $u_{min}/U_e = 0.04 \pm 10\%$. Irrespective of the pressure gradient, the turbulence level rises consistently until $x/k = 9$ (which is approximately one step height upstream of the reattachment point) and then begins to decay rapidly beyond $x/k = 13$. Eaton and Johnston (1981) compiled results obtained for previous studies on separated and reattached flows downstream of backward facing step. In that article, they also reported that maximum turbulence levels reach a peak value approximately one step height upstream of reattachment and then rapidly decays.

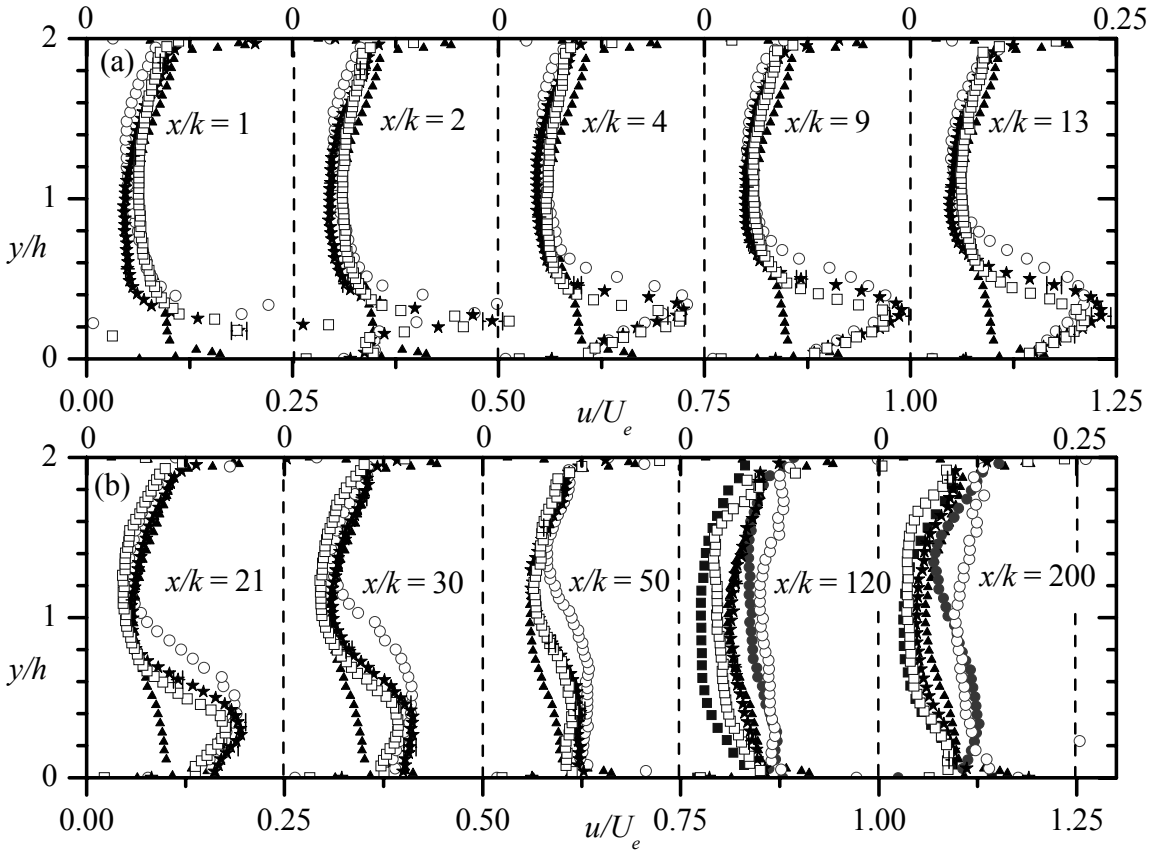

Figure 6.5: Streamwise turbulent intensity profiles at various streamwise locations. Symbols: Upstream:7; CC: ξ; APG: –; FPG: ∀. In (b) and (d) Test D2: „ at x/k = 140 (*L4*) and 205 (*L5*), and Test C: !, profiles at x/k = 123 (*L4*) and 224 (*L5*).

At x/k = 9, the peak values of the streamwise turbulent intensity in Test APG, Test FPG and Test CC are $(u/U_e)_{max}$ = 0.23±0.01 which are approximately 40% higher than the corresponding upstream value. At this location, $(v/U_e)_{max}$ = 0.15±0.01 which is three-times the corresponding upstream value. The region of enhanced turbulence levels coincides with the flow region of strong shear layer in Figure 6.3. As the flow evolves downstream of the rib and the shear layer propagates outwards from the lower wall so does the region of high turbulence levels. Similar to the mean flow, the region of elevated turbulence level represents a larger fraction of the local channel height in Test APG than in Test FPG and Test CC. At $x/k \geq 120$, all the profiles regain their symmetry with

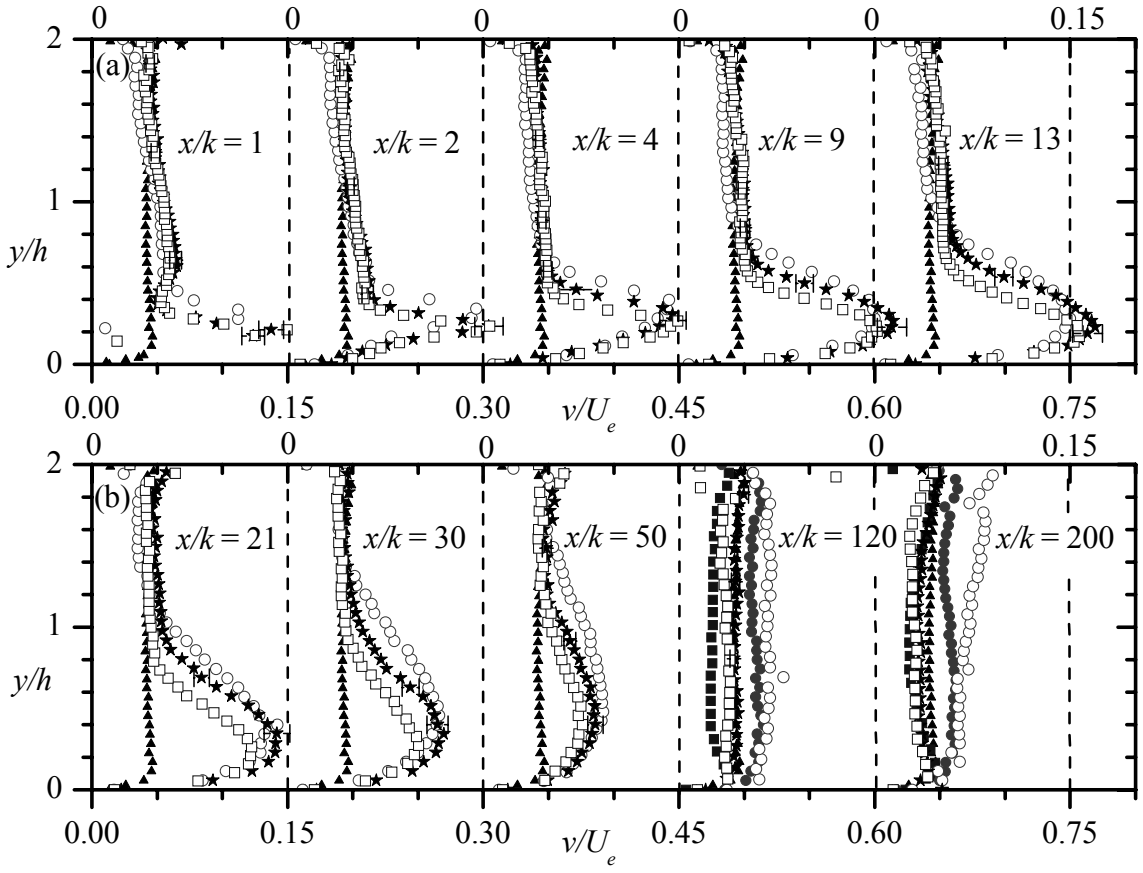

Figure 6.6: Transverse turbulent intensity profiles at various streamwise locations. Symbols: Upstream:7; CC: ξ; APG: –; FPG: ∀. In (b) and (d) Test D2: ,, at x/k = 140 (*L4*) and 205 (*L5*), and Test C: !, profiles at x/k = 123 (*L4*) and 224 (*L5*).

respect to the channel mid-plane. In this region, the profiles in Test CC collapsed reasonably well on to the corresponding upstream profile. On the other hand, profiles obtained in the FPG are lower than the upstream profiles whereas those obtained in APG are still higher than the upstream profiles. These observations are valid for the profiles for pressure gradient flows with and without the rib.

The Reynolds shear stress (Figure 6.7a and 6.7b) downstream of the rib exhibits a similar trend as the turbulent intensities. In these cases, the peak values of $(-uv/U_e^2)_{max}$ at x/k = 9 are about 10 times as high as the upstream value. In accordance with the shear

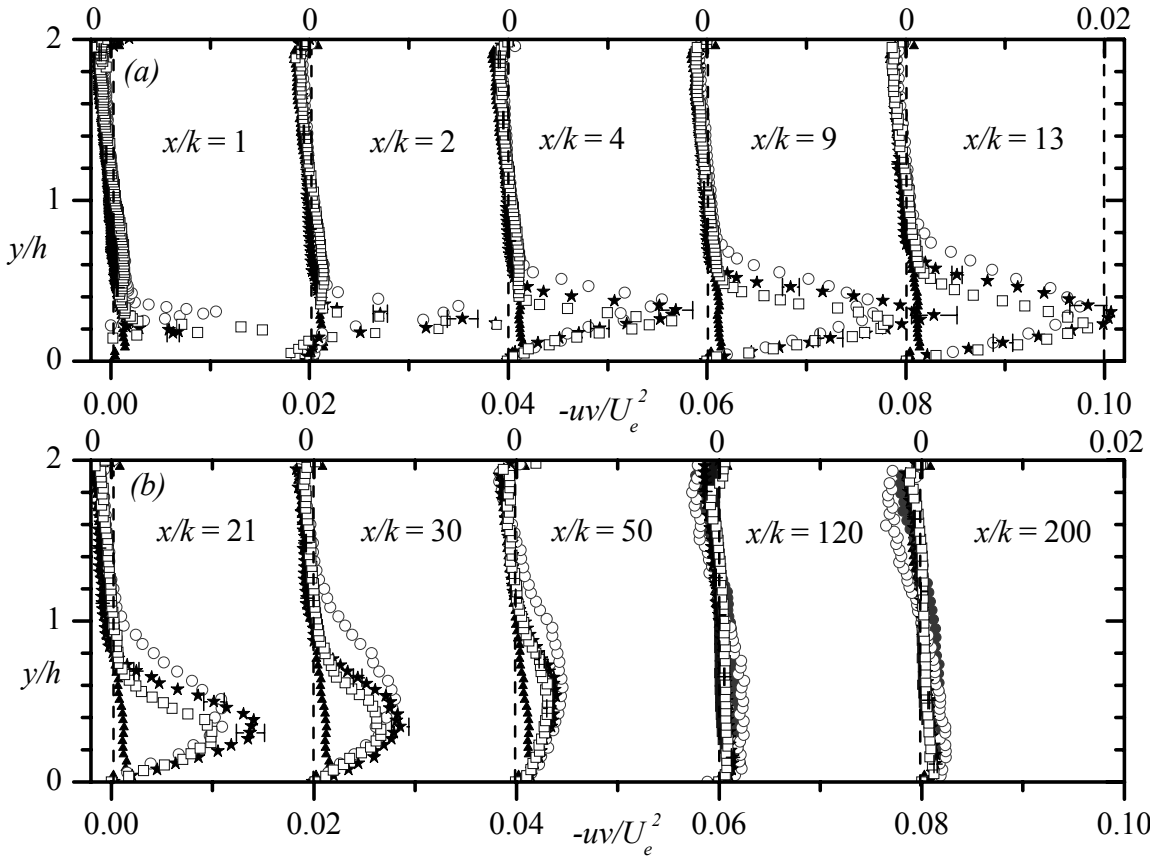

Figure 6.7: Reynolds shear stress profiles at various streamwise locations. Symbols: Upstream:7; CC: ξ; APG: –; FPG: ∀. In (b) and (d) Test *D2*: ,, at x/k = 140 (*L4*) and 205 (*L5*), and Test *C*: !, profiles at x/k = 123 (*L4*) and 224 (*L5*).

layer, the Reynolds shear stress is negative in the recirculation region adjacent to the lower wall.

Figure 6.8 shows the y-locations where $-uv$ changes sign ($y_{uv=0}$) and also where the maximum values of U (y_{Ue}), u ($y_{u,max}$), v ($y_{v,max}$) and $-uv$, ($y_{-uv,max}$), occurred at selected streamwise locations in the region $0 \leq x/k \leq 30$. The dividing streamline, which separates the core flow from the main recirculating flow, is also plotted for the FPG. The y_{Ue} location increases monotonically with x (Figure 6.8a). However, the increase is more dramatic in the separated region and in the vicinity of reattachment ($x/k \leq 12$) than downstream in the redevelopment region ($x/k \geq 20$). According to the eddy viscosity

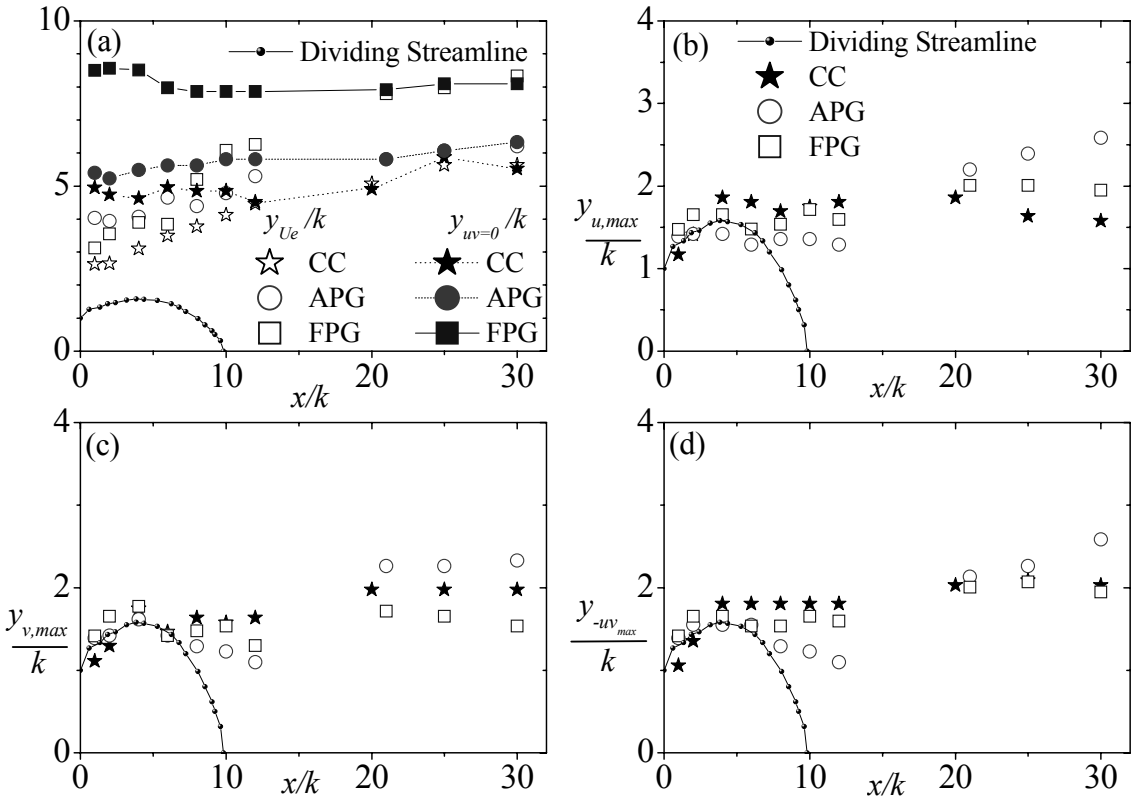

Figure 6.8: The y-locations corresponding to maximum mean and turbulent quantities at various streamwise locations: (e) y_{Ue} (b) $y_{u,max}$ (c) $y_{v,max}$ (d) $y_{-uv,max}$.

models, $-uv = \nu_t \partial U/\partial y$, hence $y_{Ue} \approx y_{uv=0}$. This condition is met downstream of reattachment but in the separated region, y_{Ue} is closer to the wall than $y_{uv=0}$ is.

Along the first half of the separation bubble, u_{max}, v_{max} and $-uv_{max}$ occur approximately along the dividing streamline (Figure 6.8b – 6.8d). However, near the reattachment location and beyond, the locations of the maximum values depart from the dividing streamline and move further away from the wall. Ruderich and Fernholz (1986) also reported that $y_{u,max}$, $y_{v,max}$ and $y_{-uv,max}$ fall on the dividing streamline in the range, $0 \leq x/x_r \leq 0.5$. In general, these values are higher in Test APG than in Tests CC and FPG downstream of the reattachment.

6.4.3 Reynolds Stress Ratios

As mentioned earlier, the distribution of the stress ratios provides insight into large-scale anisotropy. The ratio of the normal stresses is shown in Figure 6.9. The profiles show that the degree of anisotropy is certainly higher close to the upper wall irrespective of the pressure gradient and the flow regions. The inherent intense mixing within the separated region promotes local isotropy (i.e., v^2/u^2 is closer to unity), particularly in the vicinity of the lower wall, compared to the upstream profile. In other words, in the separated region, turbulent kinetic energy is more evenly distributed compared to the canonical upstream flow resulting more isotropic flow. This observation implies that the mechanism responsible for the production and redistributing turbulent kinetic energy into u^2 and v^2 in the separated region and the canonical upstream flow is different. As described earlier, in canonical near-wall turbulent flows (where $\partial V/\partial y$ is identically zero or nearly zero), the term $v^2\partial V/\partial y$ would not contribute to turbulence production. Instead, turbulent kinetic energy is produced almost entirely by the shear stress term, $-uv\partial U/\partial y$. This energy would then be transferred to the u^2 component of the Reynolds normal stresses and subsequently re-distributed into the v^2 and w^2 components via the pressure-strain correlation. Therefore, the relatively low values of v^2/u^2 at the upstream location may be due to the notion that v^2 only benefits from the energy redistribution process. On the other hand, the relatively higher values of v^2/u^2 in the separated region can be attributed to the large values of V (and $\partial V/\partial y$) in the separated shear layer than at the upstream location. This is because the large values of $\partial V/\partial y$ would generate large values of $v^2\partial V/\partial y$, which is the major production term in the v^2 transport equation, and hence larger values of v^2.

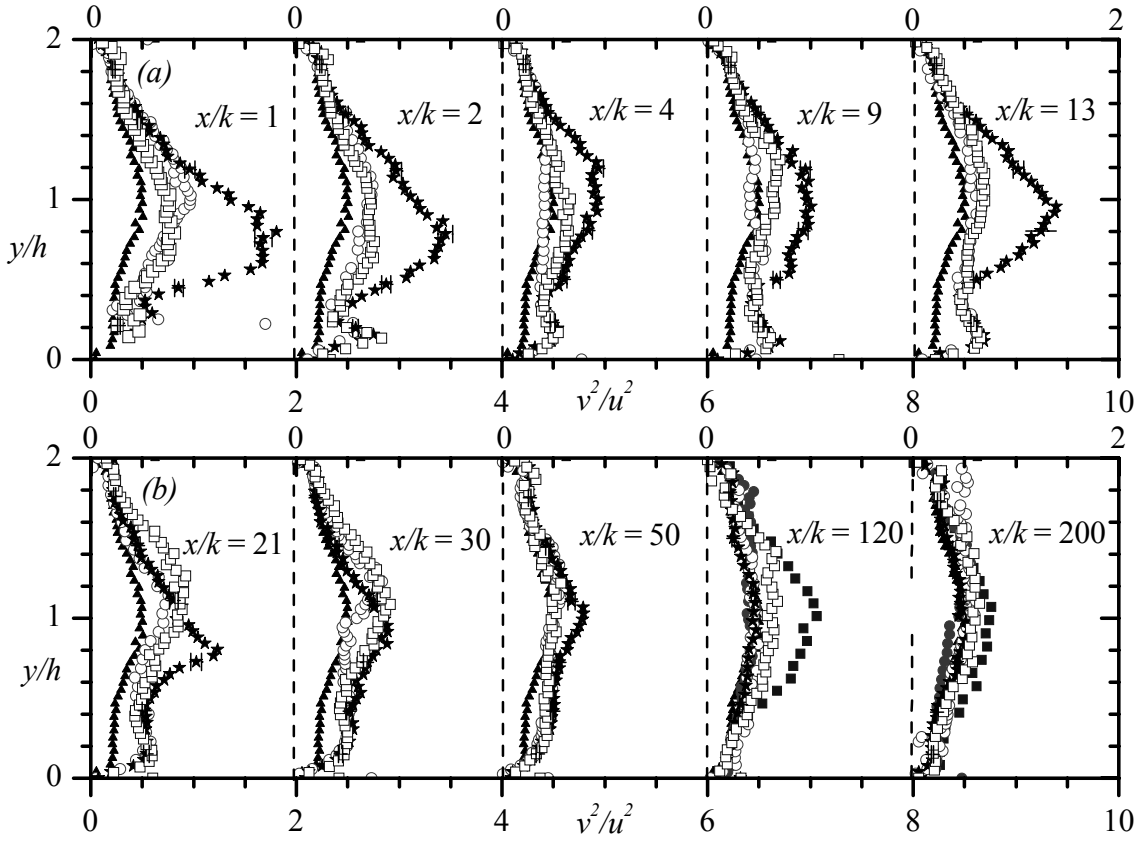

Figure 6.9: Reynolds stress ratios, v^2/u^2, at various streamwise locations. Symbols: Upstream:7; CC: ξ; APG: –; FPG: ∀. In (b) and (d) Test D2: ,, at x/k = 140 (*L4*) and 205 (*L5*), and Test C: !, profiles at x/k = 123 (*L4*) and 224 (*L5*).

The FPG flow without the rib is the most isotropic. In their APG equilibrium boundary layers, however, Skåre and Krogstad (1994) reported that the stress ratios are independent of pressure gradient. But it should be remarked that their study pertained to an equilibrium boundary layer.

Based on the observations outlined above, it is clear that turbulence models which cannot distinguish between the various Reynolds stresses would not be suitable for the flow field investigated in this work. Moreover, any suitable models for these flows would need to account for the non-negligible production term in the transport equation for v^2. This would imply that mixing length and standard two-equation isotropic

turbulence models cannot accurately reproduce the flow field in the separated region and early stage of flow redevelopment. More advanced models such as Second Moment Closures would be more appropriate for these flows.

The shear stress correlation coefficient, $-\rho_{uv} = -uv/[u^2v^2]^{0.5}$, and the stress ratios $-uv/u^2$ and $-uv/v^2$ are plotted in Figure 6.10 to Figure 6.12. Since these quantities express the ratio of the shear stress to the normal stresses, an increase in these ratios by an effect such as separation would imply that the particular effect is more effective in enhancing the shear stress than it augments the normal stresses. For the present smooth wall data,

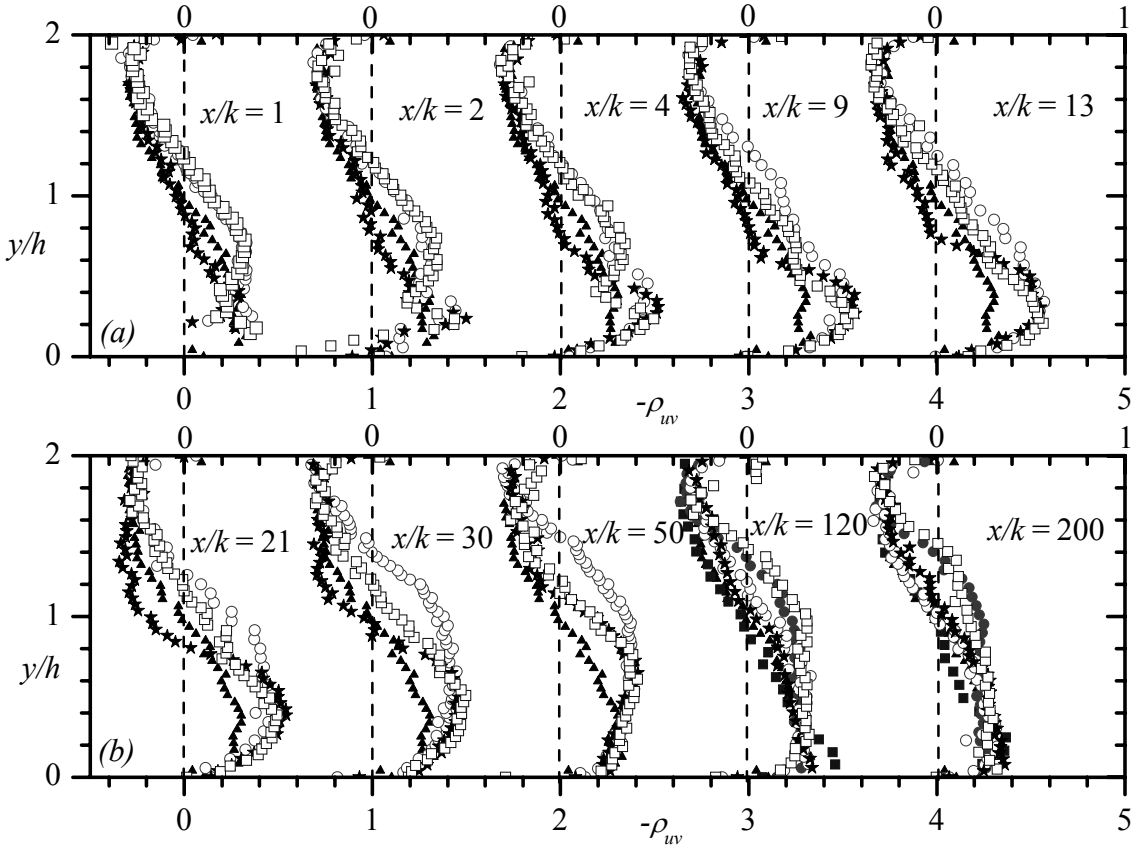

Figure 6.10: Reynolds shear stress correlation coefficient, $-\rho_{uv} = -uv/(v^2u^2)^{0.5}$, at various streamwise locations. Symbols: Upstream:7; CC: ξ; APG: –; FPG: ∀. In (b) and (d) Test *D2*: ,, at x/k = 140 (*L4*) and 205 (*L5*), and Test *C*: !, profiles at x/k = 123 (*L4*) and 224 (*L5*).

$-\rho_{uv,max} = 0.37$ which is not significantly different from $-\rho_{uv,max} \approx 0.4$ reported in the LDA study by Ching *et al*. (1995).

Close to the upper wall, no significant effect of pressure gradient or separated shear layer is observed on $-\rho_{uv}$ (Figure 6.10). However, an increased correlation between u and v is observed at the lower wall and at $x/k = 9$, $-\rho_{uv,max} = 0.6$. In the redevelopment region, the correlation peak at the lower wall decays to the upstream level. In the presence of pressure gradient, the zero location progressively moves upwards. Distributions of $-uv/v^2$ (Figure 6.11) are similar for the upstream location and downstream of the rib near the walls implying that the two stresses are increasing and

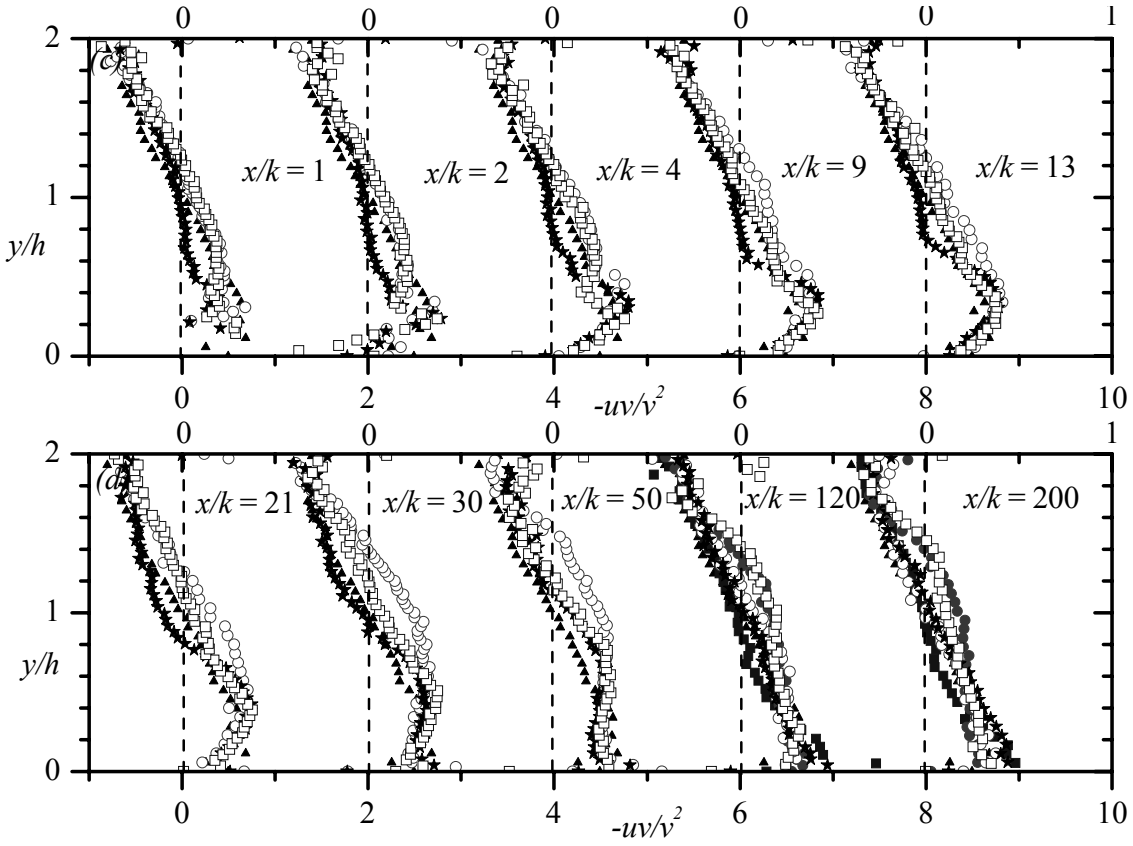

Figure 6.11: Reynolds stress ratios, $-uv/v^2$, at various streamwise locations. Symbols: Upstream:7; CC: ξ; APG: –; FPG: ∀. In (b) and (d) Test *D2*: ,, at $x/k = 140$ (*L4*) and 205 (*L5*), and Test *C*: !, profiles at $x/k = 123$ (*L4*) and 224 (*L5*).

attenuating proportionately. However, $-uv/u^2$ (Figure 6.12) at the lower wall increases progressively downstream of the rib up to x/k = 50. This increase is most pronounced around reattachment and extends away from the wall in the redevelopment region. These findings are noteworthy because they confirm the notion that the peak values v^2 and $-uv$ retain peaks they have around reattachment for much longer than u^2 as observed by Castro and Epik (1998) and Alving and Fernholz (1996). They suggested that this is a salient feature in flows developing subsequent to reattachment.

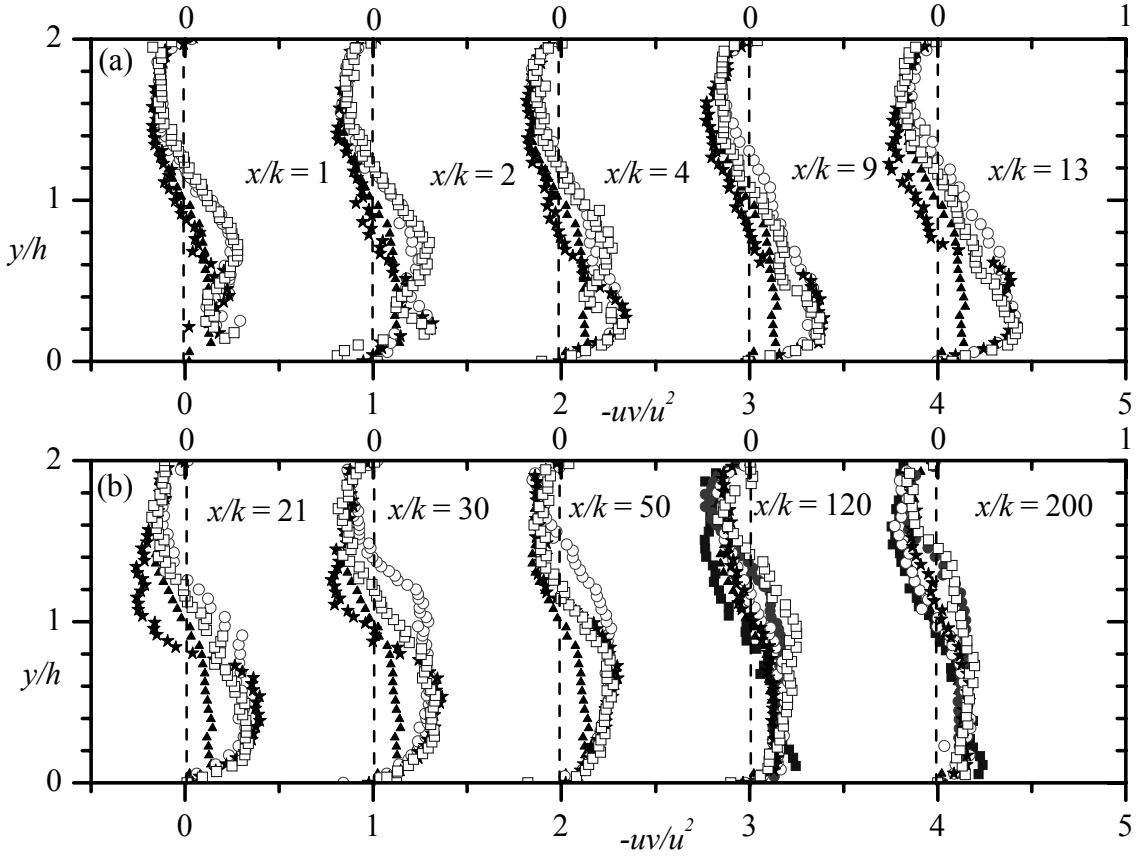

Figure 6.12: Reynolds stress ratios, $-uv/u^2$, at various streamwise locations. Symbols: Upstream:7; CC: ξ; APG: –; FPG: ∀. In (b) and (d) Test *D2*: ,, at x/k = 140 (*L4*) and 205 (*L5*), and Test *C*: !, profiles at x/k = 123 (*L4*) and 224 (*L5*).

The Townsend's structure parameter, $-uv/2k$, is an important parameter that is used for calibrating turbulence models. The structure parameter is typically taken as 0.15 in zero pressure gradient flows. For example, a value of $-uv/(2k) = 0.15$ has been specified by the turbulence model proposed by Harsha *et al.* (1970) while a value of $-uv/2k = 0.12$ is recommended in the model by Launder (1975). .

Since the mean velocity and fluctuating component in the spanwise direction were not measured in the present study, the turbulent kinetic energy was approximated from $k = 0.7[v^2 + u^2]$. The DNS study of backward facing step flow by Le *et al.* (1997) indicated that the coefficient value of 0.7 used in the present study provides a better approximation

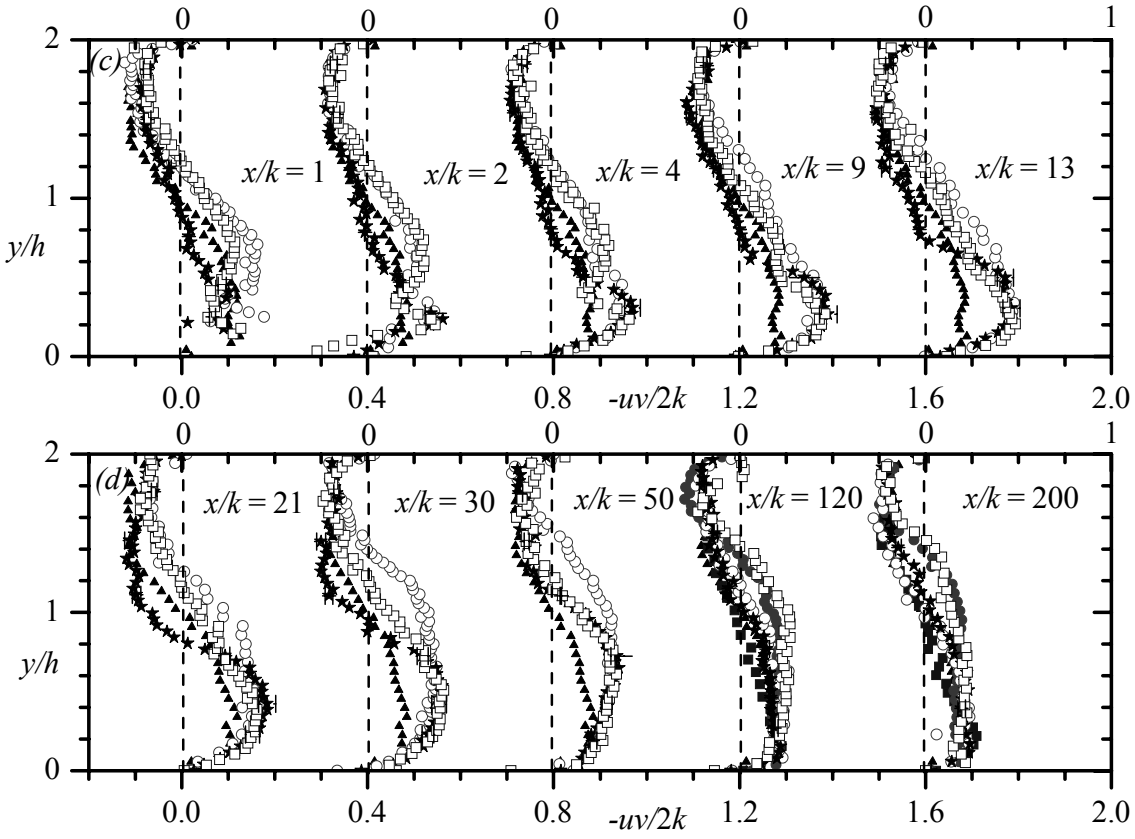

Figure 6.13: Reynolds stress ratios, $-uv/2k$, at various streamwise locations. Symbols: Upstream:7; CC: ξ; APG: –; FPG: ∀. In (b) and (d) Test *D2*: ,, at $x/k = 140$ (*L4*) and 205 (*L5*), and Test *C*: !, profiles at $x/k = 123$ (*L4*) and 224 (*L5*).

of the turbulent kinetic energy for the fast evolving flow in the separated region. A value of 0.7 has also been used in a previous study of backward facing step flow by Jović (1996). The relatively low values ($|-uv/2k|_{max} \approx 0.1$) obtained upstream of the ribs in the present study (Figure 6.13) may be partly due to low Reynolds number effects. Figure 6.13a and 6.13b shows that $|-uv/2k|$ is as high as 0.2 in the separated region and early stage of redevelopment ($4 \leq x/k \leq 21$), and reduces to 0.15 and 0.1, respectively, in the regions $30 \leq x/k \leq 50$ and $120 \leq x/k \leq 200$. The profiles are nearly independent of pressure gradient except that the y/h locations where $-uv/2k$ changes sign are different for the various test conditions.

6.4.4 Triple Velocity Correlations

The triple velocity correlations are important turbulence statistics because their gradients constitute the turbulent diffusion terms in the transport equations for the turbulent kinetic energy and Reynolds stresses. For example, $\partial uv^2/\partial y$ and $\partial[u^2v + v^3]/\partial y$ are associated with the transport of uv and $[u^2 + v^2]$, respectively, in the transverse direction. Therefore, the triple velocity correlations, u^3, u^2v, uv^2 and v^3 plotted in Figure 6.14 can provide guidance for modeling the turbulent diffusion term in the turbulent kinetic energy transport equation. Similar to the results presented by Driver and Seegmiller (1985) for separated and reattached flow downstream of a backward facing step, u^3 and uv^2 have opposite signs compared to u^2v and v^3.

As in previous canonical turbulent boundary layers as well as separated and reattached flows, the levels of u^3 are significantly higher than the other triple velocity correlations. The profiles exhibit the characteristic features of a free shear flow in the early stages of separation. For example, they are nearly antisymmetric about the centerline of the

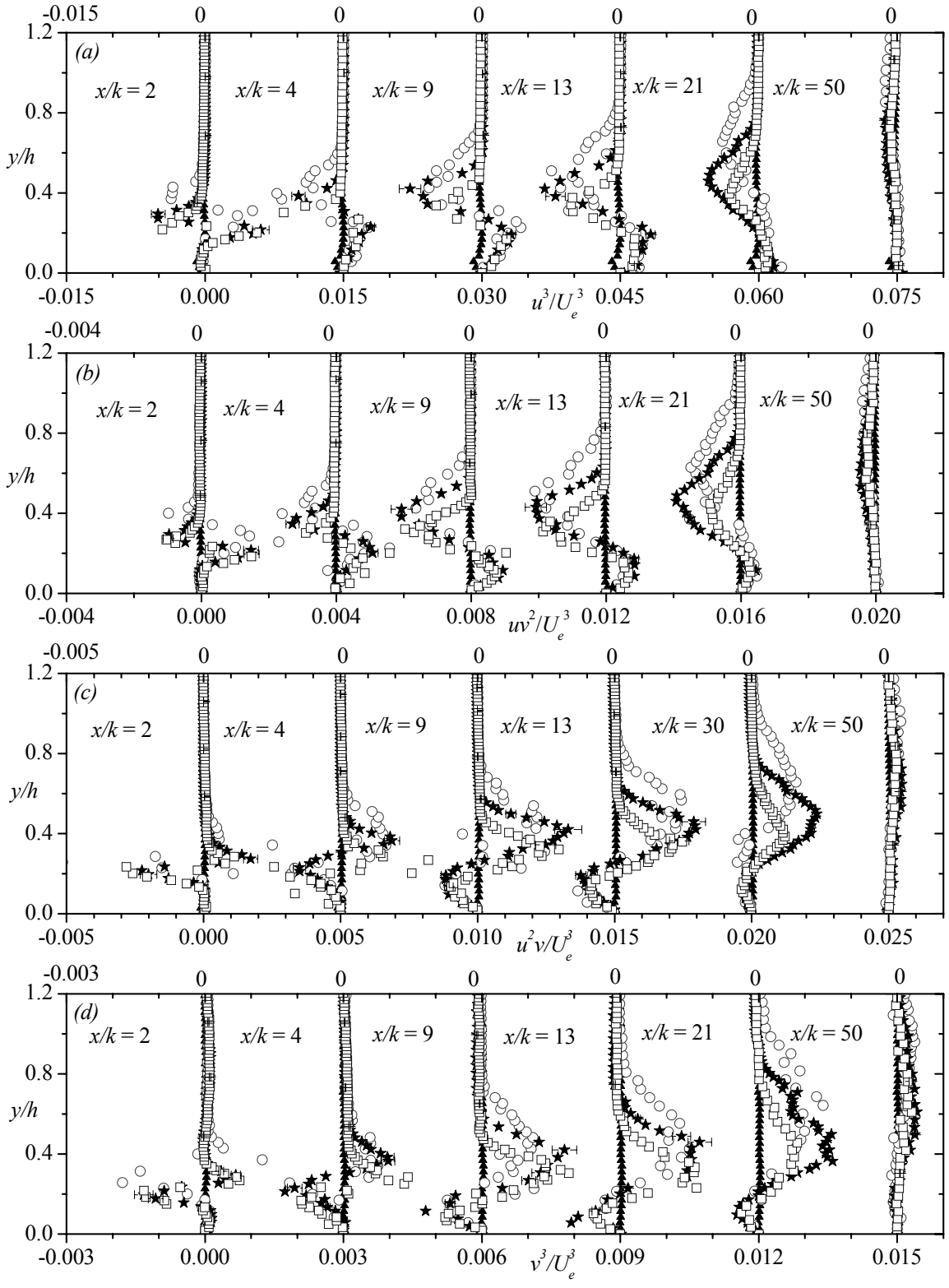

Figure 6.14: Triple correlations at various streamwise locations: (a) u^3, (b) uv^2, (c) u^2v and (d) v^3. Symbols: Upstream: 7; CC: ξ; APG: –; FPG: ∀.

separated shear layer, reaching peak values to either side of the centerline of the shear layer and tapering off to zero at the edges of the shear layer. The negative lobes of the u^2v and v^3 and positive lobes of u^3 and uv^2 close to the lower wall have disappeared in the region $x/k \geq 50$. The values of the triple velocity correlations have reduced significantly at $x/k = 50$. Hence, the levels of $[u^2v + v^3]$ (not shown) have also significantly reduced at $x/k = 50$ implying that their contribution of the turbulent transport (diffusion term) is diminished. Chandrsuda and Bradshaw (1981) and Jović (1996) also reported that the triple correlations on the wall side of the shear layer diminish rapidly upon approaching reattachment because the main contribution of the triple correlations come from the large eddies which are rapidly attenuated close to the wall near reattachment.

6.4.5 Turbulent Kinetic Energy Budget

As discussed in Chapter 5, for a two dimensional flow, the production (P_k) term in the transport equation for the turbulent kinetic energy is as follows:

$$P_k = [-uv(\partial U/\partial y + \partial V/\partial x) - (u^2\partial U/\partial x + v^2\partial V/\partial y)] \tag{6.1}$$

Similarly, the dissipation rate (ε_k) and convection (C_k) terms in the transport equation for the turbulent kinetic energy are as follows:

$$\varepsilon_k = \nu\left[2\overline{(\partial u/\partial y)(\partial v/\partial x)} + \overline{(\partial u/\partial y)^2} + \overline{(\partial v/\partial x)^2} + 2\overline{(\partial u/\partial x)^2} + 2\overline{(\partial v/\partial y)^2} + 2\overline{(\partial w/\partial z)^2}\right] \tag{6.2}$$

$$C_k = 0.5\,[U(\partial u^2/\partial x + \partial v^2/\partial x) + V(\partial u^2/\partial y + \partial v^2/\partial y)] \tag{6.3}$$

Because the spanwise velocity was not measured, the last term in the expression for Equation 6.2 was estimated from the continuity equation for the fluctuating velocity components as follows:

$$\overline{(\partial w/\partial z)^2} = \overline{(\partial u/\partial x + \partial v/\partial y)(\partial u/\partial x + \partial v/\partial y)}\,. \tag{6.4}$$

Equation 6.2 and 6.4 is identical to that employed by Piirto *et al.* (2003) in their PIV study of a backward facing step. The gradient terms in the energy budget equations were calculated using a second order central difference scheme. The diffusion term for the turbulent kinetic energy was also evaluated but those data are not shown because they showed scatter.

The budget terms in the turbulent kinetic energy at selected x-locations in the separated region and in the redevelopment region are shown in Figure 6.15a – 6.15c. It was observed that $\partial U/\partial y >> \partial V/\partial x$ everywhere irrespective of the pressure gradient and streamwise location. Although, $\partial U/\partial x$ and $\partial V/\partial y$ are smaller than $\partial U/\partial y$, they are generally not negligible in the separated region. The mean flow is approximately two-dimensional and $\partial U/\partial x \approx -\partial V/\partial y$ from continuity. As can be seen from Equation 6.1, the production of turbulent kinetic energy, P_k consists of contribution from the shear stresses ($-uv\partial U/\partial y$ and $-uv\partial V/\partial x$) and the normal stresses ($u^2\partial U/\partial x$ and $v^2\partial V/\partial y$). Unlike a fully developed channel flow, the magnitude of the production by the normal stresses is individually high in the separated region and early stage of flow development. However, because they are of opposite sign (and $\partial U/\partial x \approx -\partial V/\partial y$), their sum is much smaller than the individual normal stress terms ($u^2\partial U/\partial x$ and $v^2\partial V/\partial y$) and the shear stress term ($-uv\partial U/\partial y$). Since $\partial U/\partial y > \partial V/\partial x$ over most of the shear layer, $-uv\partial U/\partial y$ is the dominant term for production by the shear stress.

It should be noted that in Figure 6.15a, the region of enhanced production levels coincides with the flow region of strong shear layer in the separated region. The production peak is lower in Test APG than Tests CC and FPG but region of non-

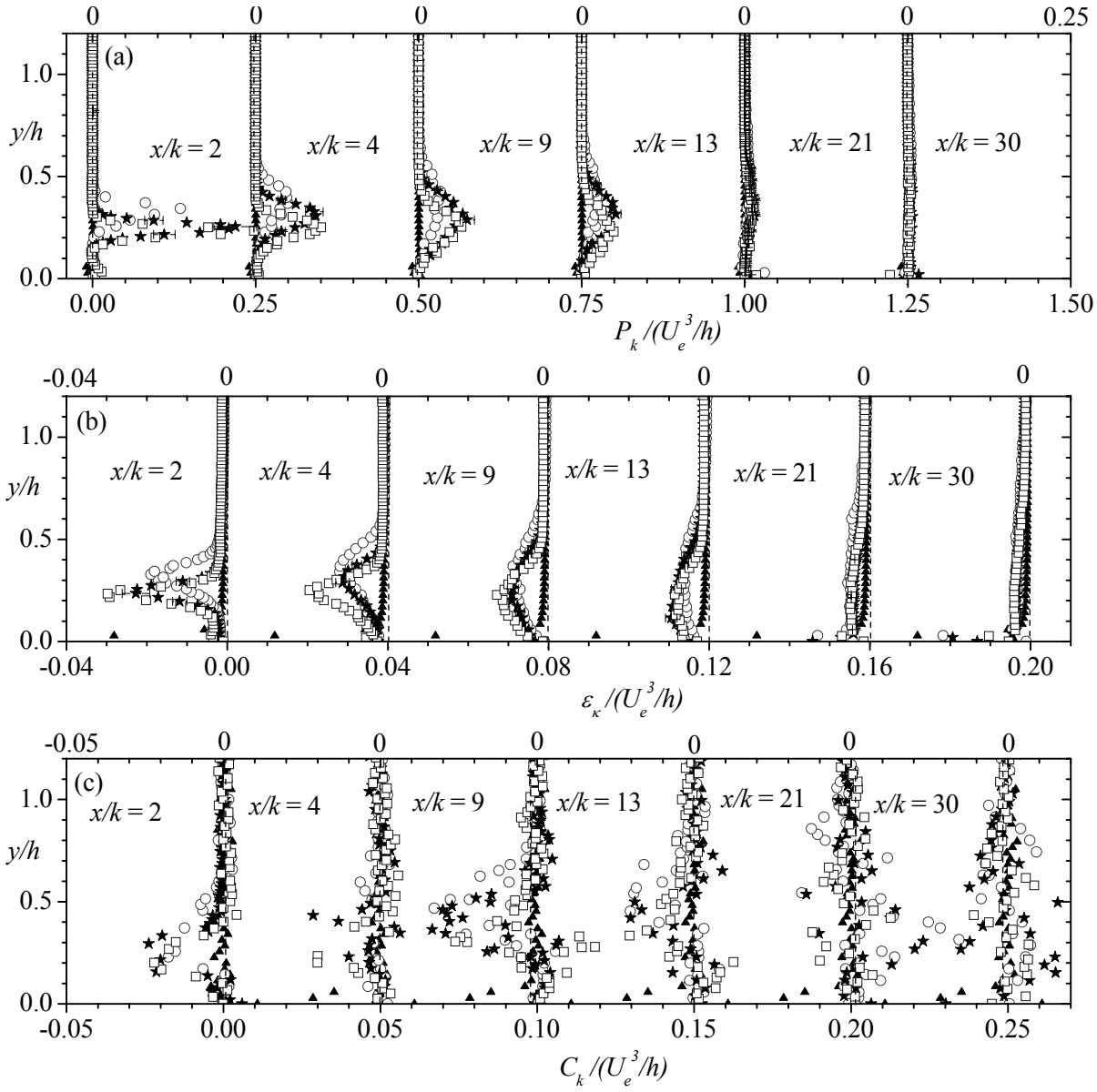

Figure 6.15: Triple correlations and various terms for turbulent kinetic energy budget at selected streamwise locations: (a) P_k (b) ε_k and (c) C_k. Symbols: Upstream: 7; CC: ξ; APG: –; FPG: ∀.

negligible production is largest for Test APG. This finding is similar to measured data obtained in the APG and FPG flows with no rib on the channel floor. It was observed from Figure 6.3a and 6.3b that the variation of U with y is slowest (implying lower values of $\partial U/\partial y$) in Test APG whereas the peak values for the Reynolds normal and shear

stresses are nearly similar for the three test conditions in the separated region. Since $-uv\partial U/\partial y$ is the major contributor to the production term, Figure 6.15a is consistent with observations made in Figure 6.3 and Figure 6.5.

The dissipation term (Figure 6.15b) is substantially less than production. The implication is that the flow is not in energy equilibrium state. The imbalance ($P_k \neq -\varepsilon_k$) is due to non-negligible transport of turbulent kinetic energy by the mean flow (convection) and turbulence diffusion (not shown) both of which are predominantly negative. Thus, Figure 6.15 implies that turbulent models based on equilibrium assumptions would not be able to accurately predict flow in the recirculation region and in the early stage of flow redevelopment. In general, only turbulence models that take into account all the transport terms (including diffusion and convective terms) can accurately predict these complex flows. At $x/k = 30$, the budget terms have significantly reduced. It is expected that as the flow evolves farther downstream, the diffusion and convection terms will eventually become negligible so that energy equilibrium will be established.

6.5 The Lower Boundary Layer in the Redevelopment Region

In this section, the lower boundary layer is used to provide a more detailed analysis and discussion of the effects of pressure gradient on the redevelopment of the reattached flow. As defined earlier, the lower boundary layer is the flow region that extends from the lower channel wall to the location of the local maximum streamwise velocity. It was shown in the previous sections of this chapter that the separated shear layer and pressure gradients modified the lower boundary layer of the mean velocity and turbulent statistics more than the upper boundary layer. For this reason, the upper boundary layer will not be considered in this section. The profiles of the mean velocity and Reynolds stresses as

well as distributions of the mixing length and eddy viscosity obtained in the lower boundary layer of the redevelopment region are interpreted using the friction velocity, U_τ. Although U_τ is traditionally used to interpret the mean velocity profile, various studies conducted in pressure gradient turbulent flows over smooth and rough surfaces showed that the mixed scaling, $U_e\delta^*/\delta$, proposed by Zagarola and Smits (1998) collapses the defect profiles better than U_τ. Therefore, the mean velocity defect profiles are also scaled using $U_e\delta^*/\delta$.

6.5.1 Mean Velocity Profiles

The log law has been used in the past to analyze the redevelopment region of separated and reattached turbulent flows. In the redevelopment region, for example, Bradshaw and Wong (1972) reported the presence of the log region for $(x-x_r)/k \geq 10$. In the present study, the friction velocity U_τ was determined by fitting the measured mean velocity to the following law of the wall in the viscous sublayer (Equation 6.5), the classical log law (Equation 6.6), and the empirical formula (Equation 6.7) proposed by Spalding to facilitate a smooth transition from the linear to log region:

$$U^+ = y^+ \tag{6.5}$$

$$U^+ = \kappa^{-1} \ln y^+ + 5.0 \tag{6.6}$$

$$y^+ = U^+ + e^{5\kappa}(e\kappa^{U^+}\text{-}1\text{-}\kappa U^+\text{-}0.5(\kappa U^+)^2 - 1/6(\kappa U^+)^3 - 1/24(\kappa U^+)^4) \tag{6.7}$$

where $U^+ = U/U_\tau$, $y^+ = yU_\tau/\nu$, κ (= 0.41) is the von Karman constant, and ν is the kinematic viscosity.

Figure 6.16 shows the measured mean velocity profiles in the region $x/k \geq 13$, as well as Equations 6.5, 6.6 and 6.7. Equations 6.5 and 6.7 describe the measured data

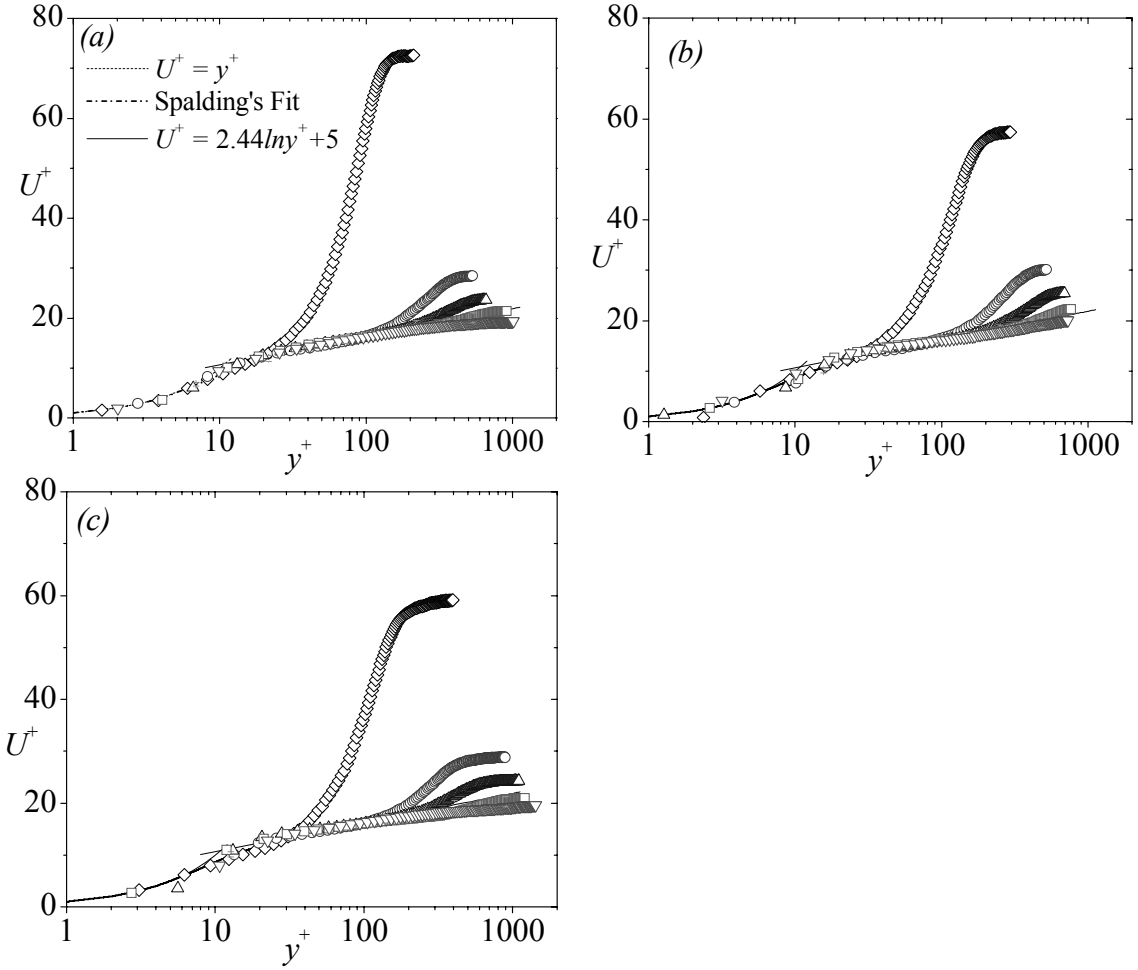

Figure 6.16: Mean velocity profiles in inner: (a) CC, (b) APG and (c) FPG. Symbols - Upstream: Upstream: –,– ; *x/k* = 13: M; *x/k* = 21: –; *x/k* = 30: 8; *x/k* = 50: ∀; *x/k* = 120:X.

reasonably well in the region $y^+ < 30$. In most cases, data points were obtained in the linear viscous sublayer. As expected, no substantial logarithmic region exists at *x/k* = 13 and the profiles immediately downstream of the reattachment are characterized by a large wake component. The log law region is limited to $y^+ \leq 150$ at *x/k* = 21 (Chandrsuda and Bradshaw, 1981), however, as the streamwise distance increases, so does the extent of overlap region between the measured data and the log law.

The skin friction values estimated from $C_f = 2(U_\tau/U_e)^2$, where U_τ is the friction velocity determined by fitting the measured mean velocity profiles to the log law are

plotted in Figure 6.17. Jović (1998) and Le *et al.* (1997) reported negative C_f values in the recirculation region and a value of $C_f = 0$ at the point of reattachment. Measurements of C_f in the recirculation region were, however, not made in the present study. The values of C_f rise rapidly from approximately 0.0006 at $x/k = 13$ to a value of about 0.005 at $x/k \geq 120$ (which is within 6% of the corresponding upstream value). The rapid rise of C_f downstream of reattachment is a common feature in the redevelopment region of separated and reattached flows (Ruderich and Fernholz, 1986; Le *et al.* 1997). The previous results demonstrate that the variations of C_f exhibit discernible pressure gradient effects. However, the values of C_f, are nearly independent of pressure gradient in the presence of the rib.

The C_f values were also estimated using the Ludweig-Tillman correlation:

$$C_f = 0.246 Re_\theta^{-0.268} 10^{-0.678H} \tag{6.8}$$

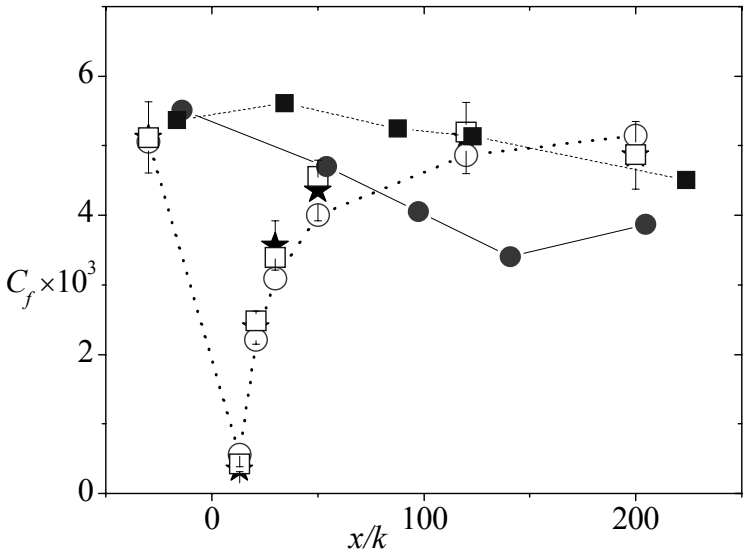

Figure 6.17: Variation of the skin friction coefficient. Symbols: CC: ξ; APG: –; FPG: ∀; Reference values; Test *D2*: ,; *C*: !.

This correlation has been previously used in separated and reattached flows without pressure gradient (Bradshaw and Wong, 1972) and with pressure gradients (Cutler and Johnston, 1989) to estimate C_f. The accuracy of the correlation depends on the values of δ^* and θ. An accurate determination of δ^* and θ would require measurement of the mean velocity close to the wall. As shown in Figure 6.16, almost all test cases and measurement locations have measured data sets starting in the region, $1 < y^+ \leq 10$. Therefore, the values of δ^* and θ (and hence C_f values determined from Equation 6.8) are expected to be reasonably accurate. It should be noted that in determining δ^* and θ, the measured data were extrapolated to the wall using $U = 0$ at $y = 0$. The differences between the C_f values obtained from the log law and Eqn. 6.8 are within ± 10%.

The mean defect profiles normalized by U_τ are shown in Figure 6.18a, 6.18b and 6.18c while those normalized by the mixed scaling, $U_e\delta^*/\delta$, are plotted in Figures 6.18d, 6.18e and 6.18f. The profiles in the region of $x/k < 120$ are distinctly different from the upstream profile. As the flow develops further downstream, the profiles relax back onto the upstream profile. It was observed that the profiles obtained at $x/k = 120$ and 200 (not shown) are similar to the upstream profiles. Although none of the velocity scales was able to collapse the profiles in the early region of redevelopment, the mixed scaling does a better job in collapsing the profiles than the friction velocity. This finding is similar to the observation made in Chapter 5 that, in pressure gradients without the rib on the channel wall, mixed scaling does a better job of collapsing the data.

6.5.2 The Reynolds Stresses

As shown in Figure 6.13, the skin friction coefficient, C_f, (and U_τ) at $x/k = 13$ which is immediately downstream of the reattachment point was very low. Because of the very

low values of U_τ and the very high peak values of the turbulent intensities and Reynolds shear stress (Figures 6.5 - 6.7) at x/k = 13, the peak values of u^+u^+, v^+v^+ and $-u^+v^+$ were extremely high. In Test CC, for example, $u^+u^+_{max}$ = 309, $v^+v^+_{max}$ = 165 and $-u^+v^+_{max}$ = 119 which are orders of magnitude higher than the corresponding values of $u^+u^+_{max} \approx 9$, $v^+v^+_{max} \approx 1$ and $-u^+v^+_{max}$ = 0.7 at the upstream section. Therefore, the profiles at x/k = 13 will not be shown.

One of the salient features of the Reynolds stress profiles in the redevelopment region is that they attain maxima in the outer layer as far downstream as x/k = 50 (Figure 6.19 and 6. 20). At x/k = 13 (not shown) and 21, u^+u^+ exhibits two peaks which is most distinct in Test APG. For example, in Test APG (Figure 6.19b) at x/k = 21, the values of the two peaks are u^+u^+ are 25 and 33 and they occurred at y^+ = 15 and 185, respectively. Note that the location of the inner peak (y^+ = 15) is in the buffer region, and identical to y^+ = 15 reported in canonical boundary layers. Previous studies (Tachie *et al.* 2001; Le *et al.*, 1997) also made a similar observation in the region $10 \leq x/k \leq 20$. Although the location of the inner peak in the early region of flow development is similar to those in canonical near-wall turbulent flows, the peak values ($u^+u^+_{\max}$) downstream of the reattachment region are substantially higher than typical values of $u^+u^+_{\max}$ = 8 to 9 reported for fully developed channel flows.

Irrespective of the pressure gradient, the Reynolds stresses are higher than the upstream profiles up to x/k = 50. The profiles have nearly recovered to the upstream profile in Test CC; however, the presence of the pressure gradient complicated the recovery process. For example, the profiles in Test APG and FPG at x/k = 120 and 200 (not shown) are self-similar. However, those in Test APG are still significantly higher

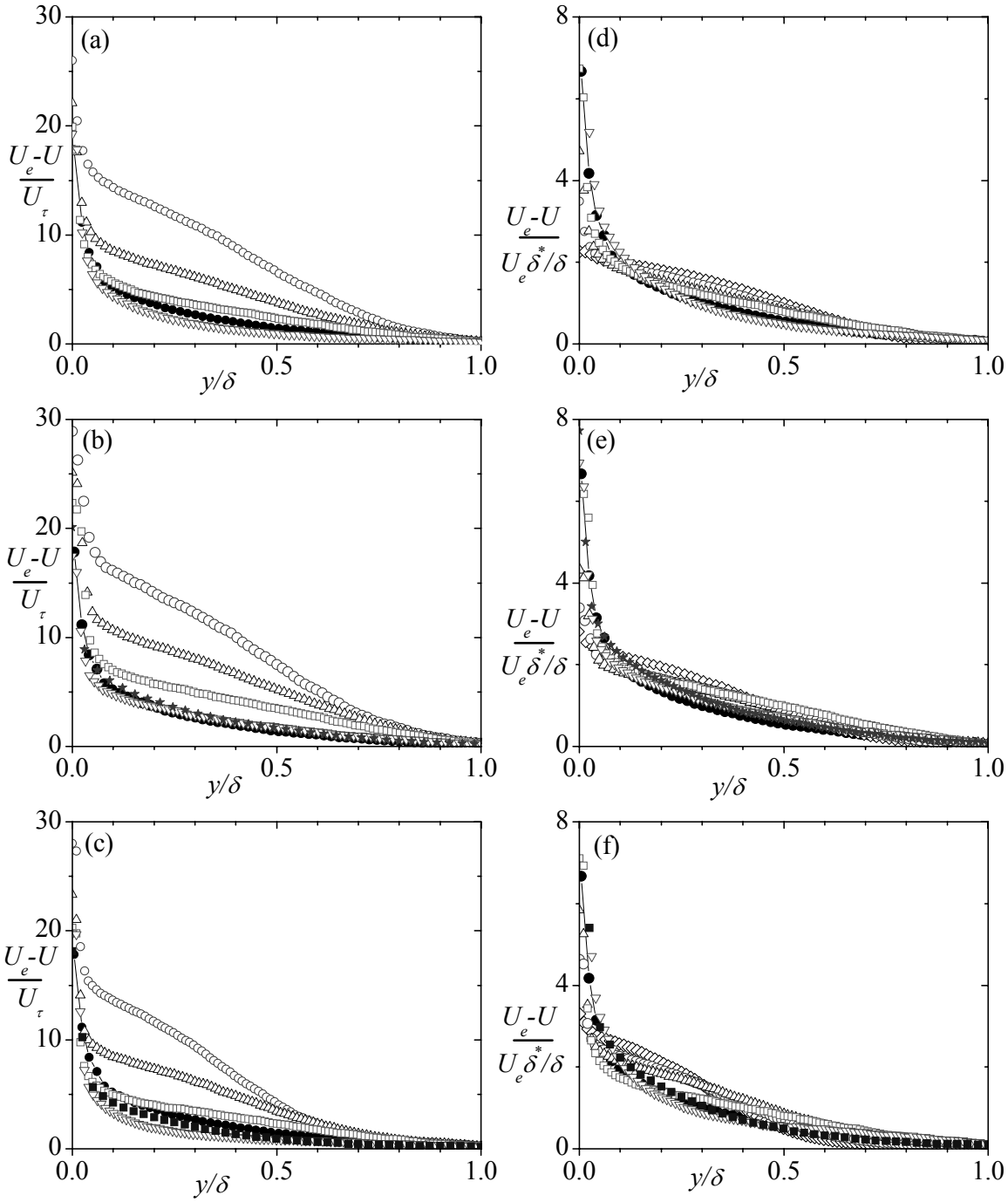

Figure 6.18: Mean velocity profiles in outer coordinates. CC: (a) & (d); APG (b) & (e); FPG (c) & (f). Symbols - Upstream: –,– ; *x/k* = 13: M; *x/k* = 21: –; *x/k* = 30: 8; *x/k* = 50: ∀; *x/k* = 120:X. In (b) and (e), reference Test *D2* profile at *x/k* = 140 (ξ: *L4*) and in (c) and (f) the Test *C* profile at *x/k* = 123 (!: *L4*).

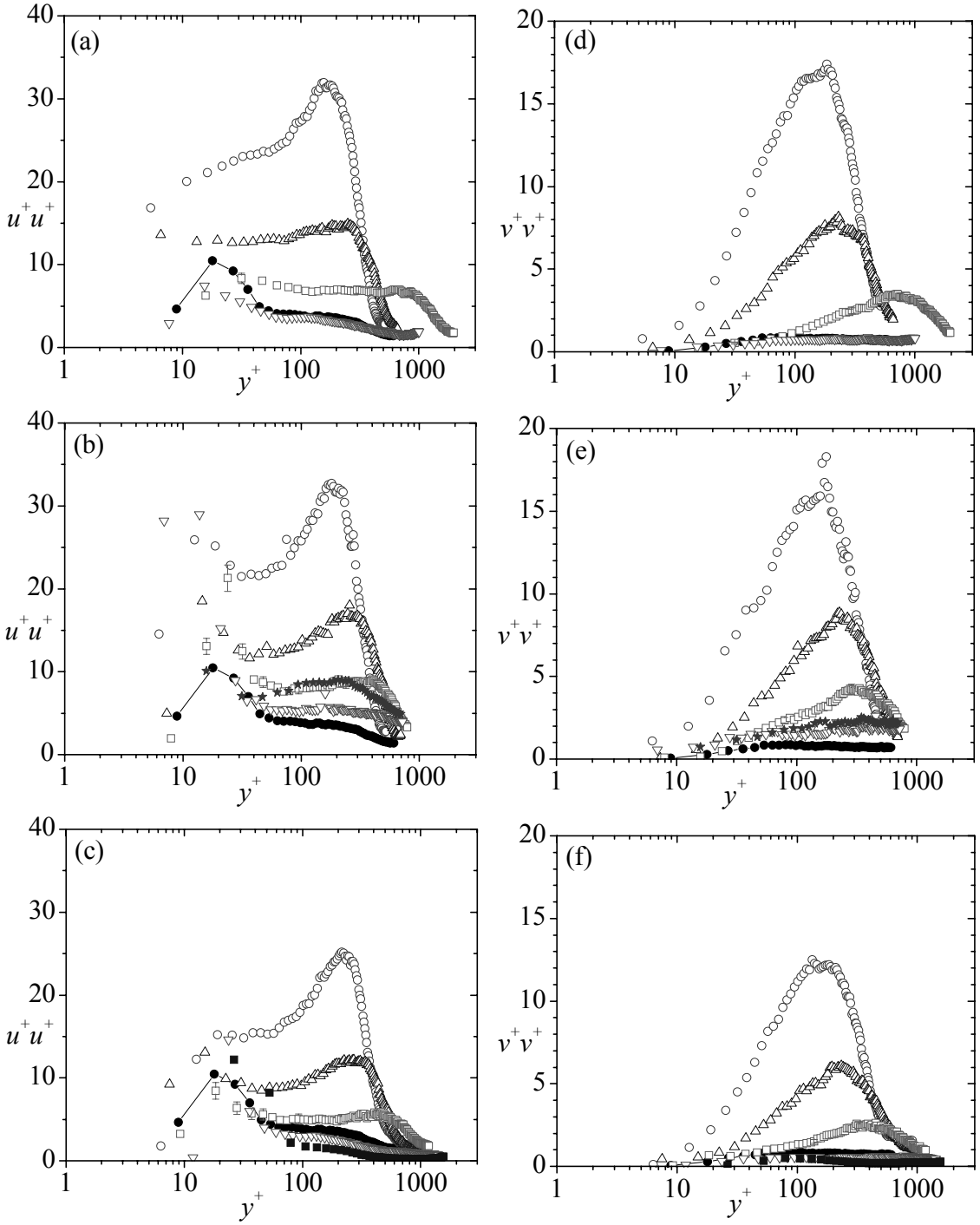

Figure 6.19: Reynolds stress profiles. CC: (a) & (d); APG: (b) & (e); FPG: (c) & (f). Symbols - Upstream: -,-; x/k = 21: –; x/k = 30: 8; x/k = 50: ∀; x/k = 120:X. In (b) and (e), reference Test *D2* profile at x/k = 140 (,: *L4*) and in (c) and (f) the Test *C* profile at x/k = 123 (!: *L4*).

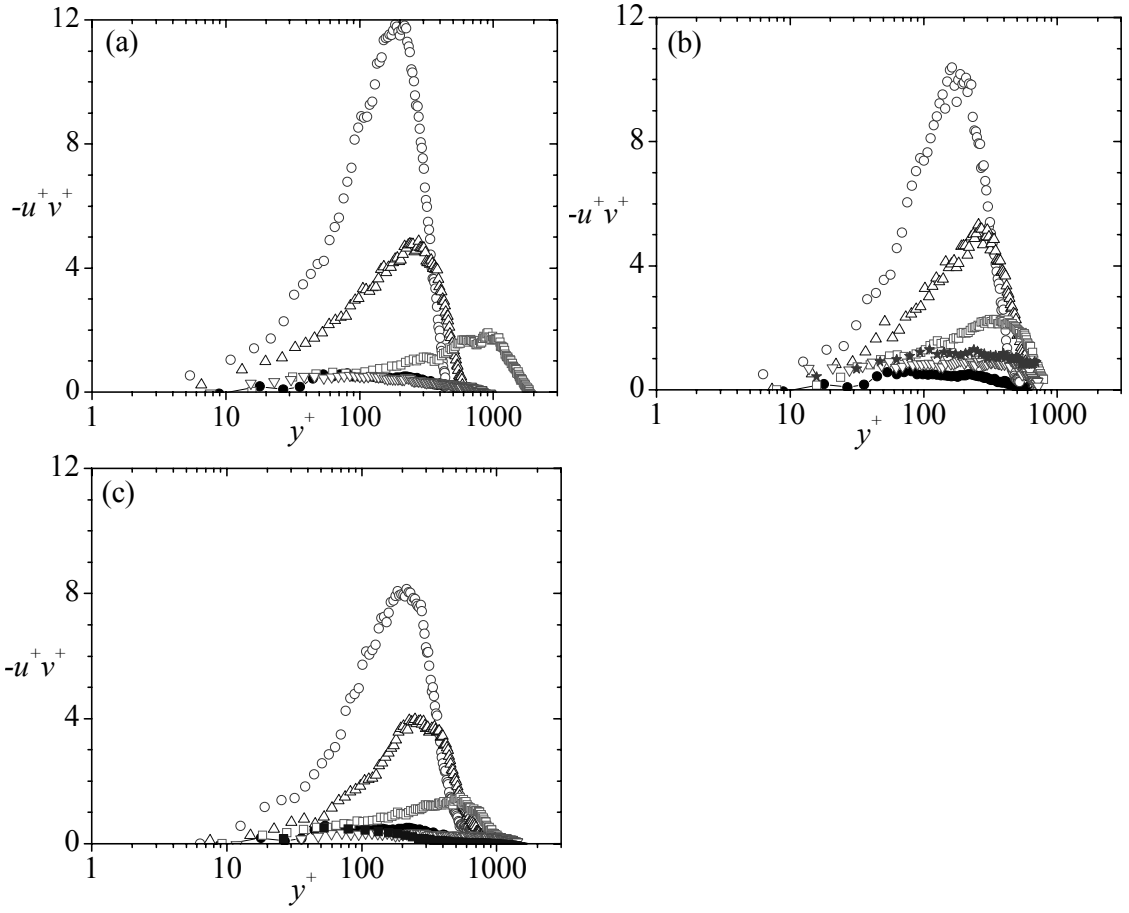

Figure 6.20: Reynolds shear stress profiles. (a) CC, (b) APG and (c) FPG. Symbols - Upstream: -,-; *x/k* = 21: –; *x/k* = 30: 8; *x/k* = 50: ∀; *x/k* = 120:X. In (b) reference APG profile at *x/k* = 140 (,: *L4*) and in (c) the FPG profile at *x/k* = 123 (!: *L4*).

than the corresponding upstream profile while those in Test FPG are lower. Since turbulence levels are generally attenuated by FPG and enhanced by APG, these observations imply that in the late stage of flow redevelopment, pressure gradient becomes the dominant effect. Similar to the findings by Jović (1998) in backward facing step flow, the Reynolds stresses recover faster in the inner region than in the outer region (which requires much longer distance). Furthermore, the profiles obtained in the APG and FPG experiments with the ribs are, respectively, higher and lower than the corresponding profiles obtained without a rib on the channel floor.

6.5.3 Profiles of Mixing Length and Eddy Viscosity

The methodology of modeling turbulent flows via mixing length, $l_m = (-\overline{uv})^{0.5}/(\partial U/\partial y)$, and eddy viscosity, $\nu_t = -\overline{uv}/(\partial U/\partial y)$ is one of the simplest and easiest to implement in all turbulence models (Wilcox, 2004). Even though they fail to incorporate the exact physical processes, they have been successful in predicting some of the flow characteristics in simple shear flows. In the inner region ($y/\delta < 0.2$) of canonical boundary layer and channel flows, the mixing length follows the universal relation $l_m = \kappa y$ (where $\kappa = 0.41$, is the von Kármán constant). A constant value of 0.09δ is normally used for canonical boundary layers in the outer region. This is also the value recommended, for example, in the turbulence model proposed by Johnson and King (1985).

The distributions of mixing length at selected locations in the separated and redevelopment regions are shown in Figure 6.21. The upstream profile follows the universal relation in the inner region. In the outer region, the upstream profile increases continuously likely because of the low Reynolds number effects as well as the depressed wake observed in the log law plots. In such a case, $\partial U/\partial y$ tends to zero more rapidly than $-\overline{uv}$ does, producing relatively higher l_m values than in canonical boundary layers at moderate and high Reynolds numbers.

Figure 6.21a and 6.21b show that, in the separated region (x/k = 4 and 9) the linear region observed in canonical near-wall turbulent flows does not exist. Furthermore, the profiles attain a near-constant value in the outer region but this value is lower than $l_m = 0.09\delta$ for canonical near-wall turbulent flows. These results imply that

turbulence models based on the mixing length approach would fail to accurately predict the flow characteristics in the separated region.

In the early stages of redevelopment (x/k = 13 and 21), a linear region is established in the inner region but the slope is about twice the value of $\kappa = 0.41$ observed in the upstream profile. In the outer region, the profiles begin to increase above the value of 0.09δ. The results also imply that the Reynolds shear stress is decaying slower than the mean shear ($\partial U/\partial y$). Further downstream, at x/k = 50 and 120, the slope in the inner region has reduced to 0.41 suggesting complete recovery in the inner region. Similar to the results obtained in the APG without a rib, the mixing length decays in the outer region compared to the upstream profile due to higher characteristic values of $\partial U/\partial y$.

The distributions of the eddy viscosity are shown in Figure 6.22. The profiles obtained downstream of the rib are higher than the upstream profile. It appears that the slope in the near wall region gradually increases downstream of the rib for locations $x/k <$ 50. It is observed that the eddy viscosity in the outer part of the flow also rises initially in the region $x/k < 50$ and subsequently begins to decay farther downstream. These high values of the eddy viscosity in the outer parts of the flow far downstream indicate that $\partial U/\partial y$ is decaying more rapidly than the shear stress.

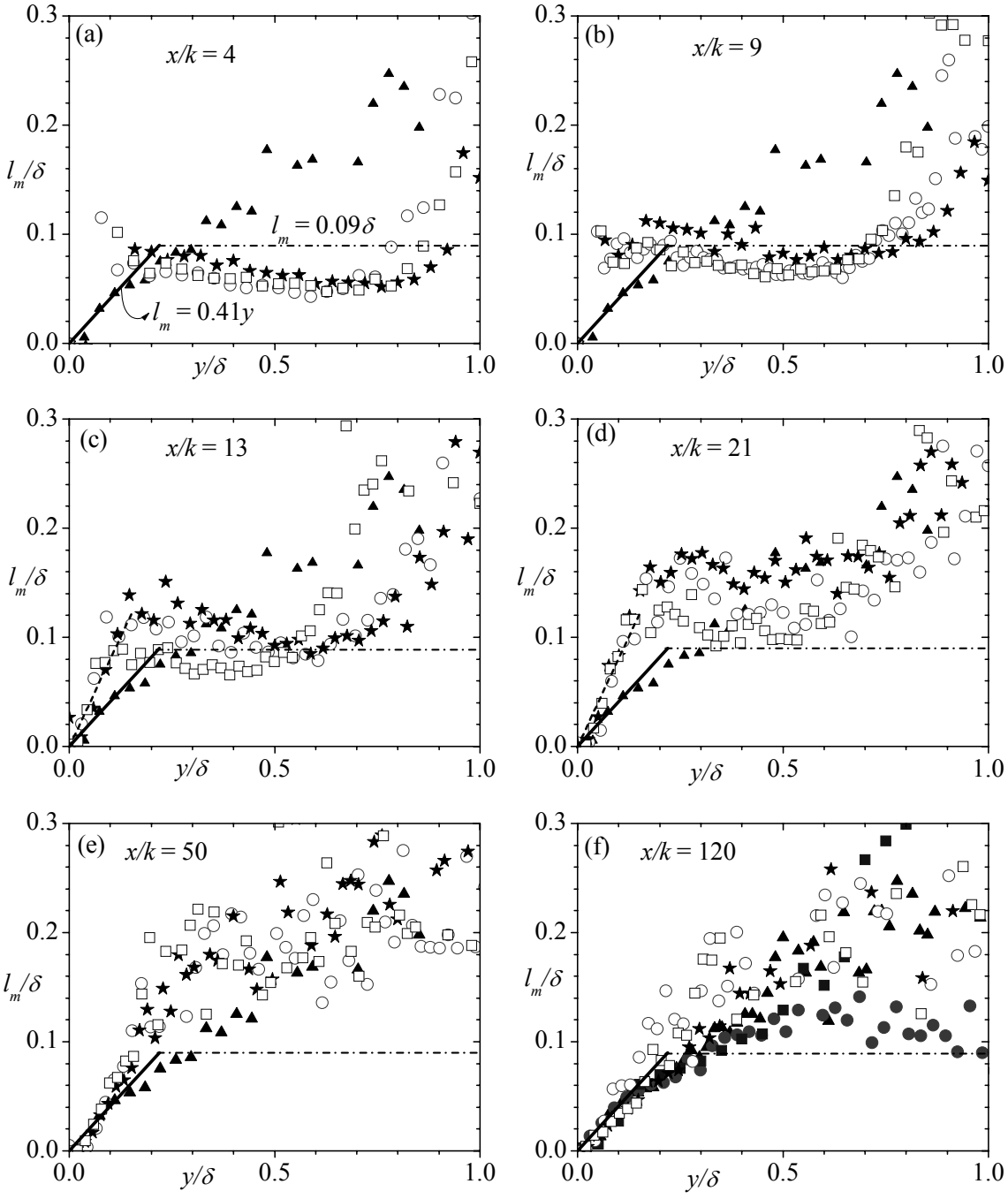

Figure 6.21: Profiles of mixing length at selected locations. Symbols: Upstream: 7; CC: ξ; APG: –; FPG: ∀. In (f) reference Test D2 (,) at *x/k* = 140 (*L4*) and 205 (*L5*), and Test *C*: (!) profiles at *x/k* = 123 (*L4*) and 224 (*L5*). Solid lines denote $l_m = \kappa y$ and dash-dot lines denote $l_m = 0.9$.

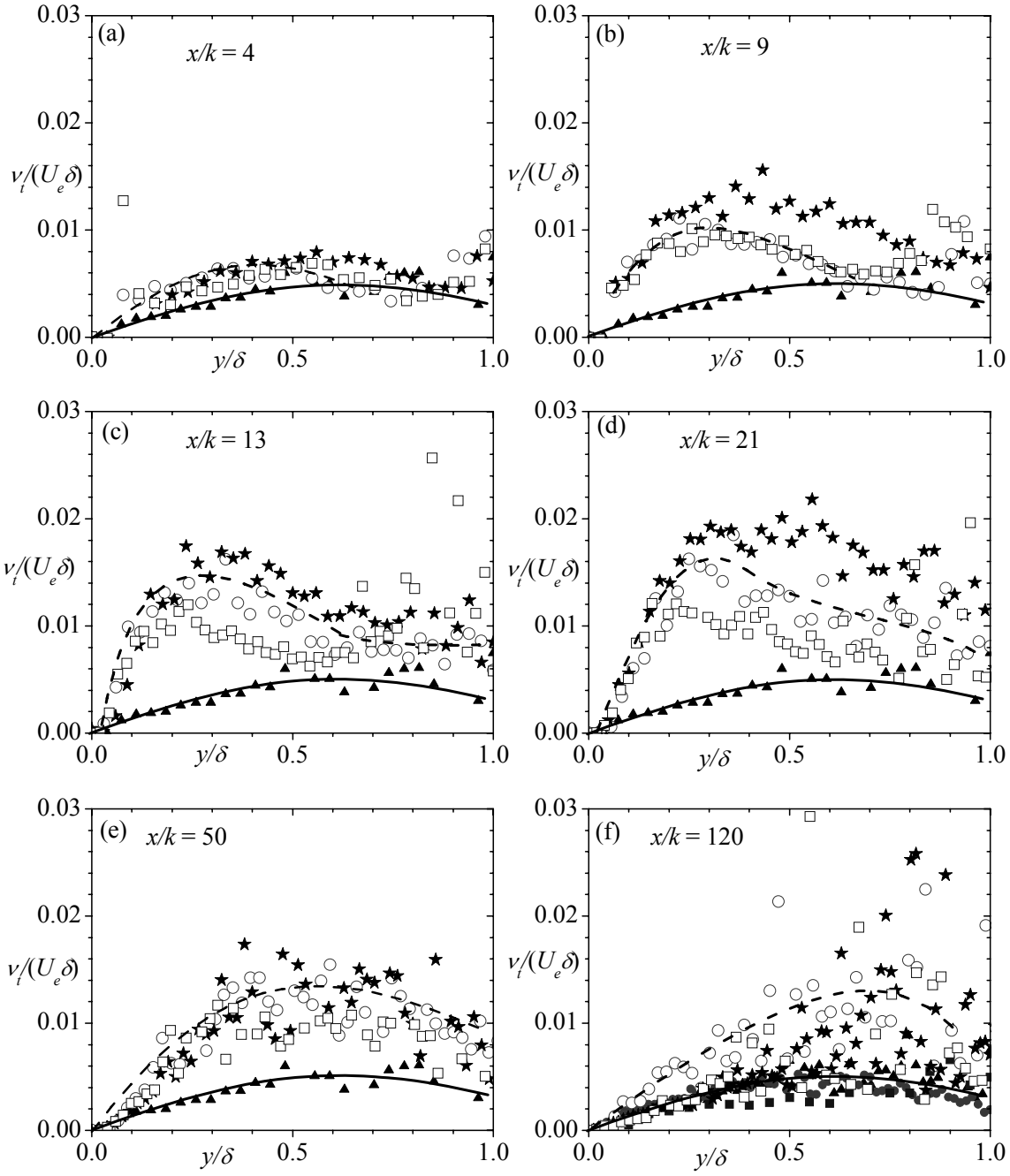

Figure 6.22: Profiles of eddy viscosity at selected locations. Symbols: Upstream: 7; CC: ξ; APG: –; FPG: ∀. In (f) reference Test *D2* (,) at *x/k* = 140 (*L4*) and 205(*L5*), and Test *C* (!) profiles at *x/k* = 123 (*L4*) and 224 (*L5*). Note, the lines are for visual aid only.

6.6 Summary of Results

An experimental study of turbulent flow over a transverse square rib in nearly zero, adverse and favorable pressure gradients has been conducted. The reattachment lengths of x_r/k = 10.4, 10.3 and 9.8 were found for the nearly zero, adverse and favorable pressure gradients, respectively. The mean velocity profiles were distorted substantially downstream of the rib. Similarly, turbulence production was significantly enhanced in the separated shear layer, and so were the turbulence intensities and Reynolds shear stress.

The flow dynamics in the upper boundary layer of the separated region and early stage of flow redevelopment were insensitive to pressure gradient. Significant differences were, however, found in the lower boundary layer. For example, APG modifies the mean velocity and turbulent quantities across a larger portion of the channel than in FPG. In this region, the mean profiles in APG increase more gradually from $U = 0$ at wall to U_{max} than those in FPG while the turbulence quantities decay more rapidly from its peak value compared with those in APG. Furthermore, APG produced higher mass and momentum deficits than if the pressure gradient were nearly zero or favorable. The results show that the mean defect profiles at various stages of redevelopment collapsed better when scaled with the mixed scaling $U_e\delta^*/\delta$ than with the friction velocity U_τ.

Unlike canonical near-wall turbulent flows (such as fully developed channel flow) the convective and diffusion terms in turbulent kinetic energy transport equation were not negligible in the separated region. Therefore, the production term is not exactly balanced by dissipation rate. This implies that turbulence models based on equilibrium assumption will not be able to reproduce the flow in the separated region.

In the nearly zero pressure gradient experiments, the profiles of the Reynolds stresses in wall variables became self-similar and collapsed onto the upstream profile at x/k = 120. Although the profiles in the adverse and favorable pressure gradients also became self-similar at x/k = 120, they fail to collapse onto the corresponding upstream profiles. In general, the Reynolds stresses in APG and FPG are, respectively, higher and lower than the upstream profile. Since these are the salient features of APG and FPG flows even without ribs attached to the channel floor, it is concluded that the late stage of flow redevelopment is dominated by the pressure gradient. The results also imply that a significantly longer distance would be required if APG and FPG flows should ever relax back to the upstream flow. Furthermore, the profiles obtained in the FPG channel with the rib, at $x/k \approx 120$, and those in the same channel but without the ribs collapsed reasonably well but significant differences exist between the results with and without the rib in the APG channel.

In the separated region, the distribution of mixing length in the inner region does not follow the well-documented linear profile reported for simple near-wall turbulent flows. This suggests that turbulence models making such assumptions may not be able to accurately model the complex nature of the flow. Even though a linear distribution of the mixing length is observed in the early stage of flow development, the slope was nearly twice as large as those in canonical turbulent flows. Based on the results presented in this chapter, it is apparent that advanced turbulence models such as Second Moment Closures that solve the Reynolds transport equations rather than the primitive mixing length or eddy viscosity models would be more suitable for predicting the separated shear layer and early region of flow redevelopment.

CHAPTER 7: IMPLEMENTATION AND APPLICATION OF POD

In this chapter the proper orthogonal decomposition is applied to the separated and reattached flows in pressure gradients. The first section of this chapter outlines the implementation of the POD. Subsequently, POD of the measured data is performed to investigate the contribution of the dominant structures to the turbulent kinetic energy and Reynolds shear stress. Further insight into the flow structures is gained by reconstructing the flow with increasing number of POD modes. A comparison between the reconstructed profiles and those obtained from the PIV image ensembles is also provided.

7.1 Implementation of POD

As mentioned earlier (Section 2.4)**,** the snapshot POD method proposed by Sirovich (1987) is employed in the present study. In this case, each instantaneous PIV data is considered a snapshot of the flow and the total number of snapshots is denoted by N. The total number of vectors in each velocity field (snapshot) is M. For a two-dimensional flow domain considered in this study, the snapshot POD analysis concerns the fluctuating parts of the velocity components (u_j^n, v_j^n) where u and v denote the fluctuating part of the velocity components in the streamwise and transverse directions, respectively. The index n runs through the N snapshots while j runs through the M positions of velocity vectors in a given snapshot (i.e. $u_j = u(x_j, y_j)$). The fluctuating velocity components were obtained by subtracting the ensemble-average snapshot from each member of the instantaneous velocity field. The ensemble-average snapshot is often considered the zeroth mode of the POD.

The present snapshot analysis follows the procedure outlined by (Meyer *et al.* 2007), and is described below. The time-average velocity ($\overline{\boldsymbol{u}}$) for a sequence of instantaneous velocity vectors $\hat{\boldsymbol{u}}^n$ (where $n = 1 \ldots N$) is given by:

$$\overline{\boldsymbol{u}} = \frac{1}{N}\sum_{i=1}^{N} \hat{\boldsymbol{u}}^n \tag{7.1}$$

The fluctuating part of the velocities is then obtained by subtracting the vectors in each instantaneous velocity field from the average (Equation 7.1) as follows

$$\boldsymbol{u} = \hat{\boldsymbol{u}} - \overline{\boldsymbol{u}}. \tag{7.2}$$

All fluctuating velocity components from the N snapshots are arranged in a matrix $\boldsymbol{U}$ as follows:

$$\boldsymbol{U} = [\boldsymbol{u}^1 \quad \boldsymbol{u}^2 \quad \cdots \quad \boldsymbol{u}^N] = \begin{bmatrix} u_1^1 & u_1^2 & \cdots & u_1^N \\ \vdots & \vdots & \vdots & \vdots \\ u_M^1 & u_M^2 & \cdots & u_M^N \\ v_1^1 & v_1^2 & \cdots & v_1^N \\ \vdots & \vdots & \vdots & \vdots \\ v_M^1 & v_M^2 & \cdots & v_M^N \end{bmatrix} \tag{7.3}$$

The $N \times N$ auto-covariance matrix is obtained from

$$\boldsymbol{C} = \boldsymbol{U}^T\boldsymbol{U} \tag{7.4}$$

A set of N eigenvalues, λ^i, and a corresponding set of orthonomal eigenvectors, ϕ_i which satisfy,

$$\boldsymbol{C}\boldsymbol{\phi}^i = \boldsymbol{\lambda}^i\boldsymbol{\phi}^i \tag{7.5}$$

can be evaluated from the auto-covariance matrix, where i spans the range from 1 to N. The functions ϕ are called empirical eigenfunctions, coherent structures, or POD modes. Here the eigenvalues are ordered by decreasing value:

$$\lambda^1 > \lambda^2 > \cdots > \lambda^N > 0 \tag{7.6}$$

The normalized POD modes ($\boldsymbol{\varphi}^i$) are constructed from the projection of the eigenvectors ($\boldsymbol{\phi}^i$) of Equation 7.5 on the original fields as follows:

$$\boldsymbol{\varphi}^i = \frac{\sum_{n=1}^{N} \boldsymbol{\phi}_n^i \, \boldsymbol{u}^n}{\left\| \sum_{n=1}^{N} \boldsymbol{\phi}_n^i \, \boldsymbol{u}^n \right\|} , \qquad i = 1, \ldots, N. \tag{7.7}$$

where $\phi_n{}^i$ is the nth component of the eigenvector corresponding to λ^i from Equation (7.5). Here $\| \, . \, \|$ is the L_2-norm defined as,

$$\|y\| = \sqrt{y_1^2 + y_2^2 + \cdots + y_M^2} \, . \tag{7.8}$$

The expansion or POD coefficients, a_i, of each mode were calculated by projecting the data set onto the calculated POD modes:

$$\boldsymbol{a}^n = \boldsymbol{\Psi}^T \boldsymbol{u}^n \tag{7.9}$$

where, $\boldsymbol{\Psi} = [\boldsymbol{\varphi}^1 \quad \boldsymbol{\varphi}^2 \quad \ldots \quad \boldsymbol{\varphi}^N]$.

The POD extracts time-independent orthonormal basis functions, $\boldsymbol{\varphi}^i$, and time-dependent orthonormal amplitude coefficients, $\boldsymbol{a}^n$, such that the expansion of any member of the ensemble using an arbitrary number of modes m was performed using:

$$\boldsymbol{u}^n = \sum_{i=1}^{m} \boldsymbol{a}_i^n \, \boldsymbol{\varphi}^i = \boldsymbol{\Psi} \boldsymbol{a}^n \tag{7.10}$$

Equation 7.10 is known as the proper orthogonal decomposition of u^n. This equation gives the best approximation of the data ensemble u^n in the sense that the average least-squares truncation error (Equation 7.11) is a minimum for any given number $m \leq N$ of basis functions over all possible sets of orthogonal basis functions (Cizmas *et al*. 2003).

$$\varepsilon_m = \overline{\left\| \boldsymbol{u}^n - \sum_{i=1}^{m} \boldsymbol{a}_i^n \boldsymbol{\varphi}^i \right\|^2} \tag{7.11}$$

Here $\|.\|$ is the L^2-norm and over-bar represents a spatial average of all M grid points in the velocity field. The value m specifies the number of basis modes included in the reconstruction.

The time averaged energy of the fluctuating component is given by the sum of all the eigenvalues (Kostas *et al.* 2002),

$$E = \sum_{i=1}^{N} \lambda_i \tag{7.12}$$

Meanwhile the energy fraction associated with i^{th} mode is given by $E_i = \frac{\lambda_i}{E}$.

7.2 Application of POD to the Experimental Data

In this section, the POD technique described above is used to analyze and interpret the dominant structures in the separated and reattached turbulent flows discussed in Chapter 6. As shown in that chapter, the effects on the mean and turbulent quantities in the separated as well as the early reattachment region were most significant in the lower half of the channel. Therefore, for all test cases considered in this section, the POD analysis was applied to the flow region $y/k \leq 6$ which encompass the lower boundary layer. The confinement of the analysis to the lower boundary layer also reduced the computational effort considerably.

7.2.1 Convergence and Energy from Dominant Mode

The number of snapshots required to adequately capture the energy content for a given mode depends on the nature or complexity of the flow. Moreover, the amount of energy

associated with a mode may not fully converge due to insufficient number of snapshots. For example, Cazemier *et al.* (1998) applied the POD to analyze the velocity field for a cavity flow at a Reynolds number (based on cavity height) of 22000. They reported that 700 snapshots were insufficient to obtain fully converged eigenvalue corresponding to the first mode. Sen *et al*. (2007) applied POD to their DNS results of fully developed channel flows over a smooth and a rough surface. For the smooth wall, the Reynolds number based on the friction velocity and channel half-height, Re_τ (= $U_\tau h/\nu$), was 180. In that study, N = 6000 realizations were used in the POD analysis.

To evaluate the sample size or number of snapshots necessary to perform the POD analysis in the present study, the fractional turbulent kinetic energy (TKE) associated with the most dominant mode, $\lambda_1/\Sigma\lambda$, was computed for an increasing number of snapshots. The results for Tests SM, CC-P1, FPG-P1, APG-P1, APG-P2 and APG-P3 are summarized in Table 7.1. It should be noted that Test SM corresponds to the measurement plane obtained in upstream section of Test APG. As described in Section 4.3.2, P1 is the measurement plane containing the rib whereas P2 and P3 correspond to measurement planes in the redevelopment region. As the number of snapshots increases, the relative contribution of the first mode to the total energy ($\lambda_1/\Sigma\lambda$) in the separated and reattachment region (Tests CC-P1, FPG-P1 and APG-P1) as well as in the early region of flow redevelopment (APG-P2) consistently decreases until a threshold number (N_{thr}) is reached beyond which no further significant reduction is observed. In the case of Test CC-P1, for example, $\lambda_1/\Sigma\lambda$ = 12.7±0.4% for N ≥ 50. At least 500 snapshots are required to reduce the percentage variation in $\lambda_1/\Sigma\lambda$ for Test FPG-P1 to 0.2% (that is, $\lambda_1/\Sigma\lambda$ = 11.9±0.2% for N ≥ 500). For Tests APG-P1 and APG-P2, a minimum of 50 and 250

snapshots, respectively, are necessary to reduce the percentage variation to a similar level.

Table 7.1: Energy convergence for increasing number of snapshots of the first mode.

Snapshots (N)	SM	CC-P1	FPG-P1	APG-P1	APG-P2	APG-P3
	$\lambda_1/\Sigma\lambda$ %	$\lambda_1/\Sigma\lambda$ %	$\lambda_1/\Sigma\lambda$ %	$\lambda_1/\Sigma\lambda$ %	$\lambda_1/\Sigma\lambda$ %	$\lambda_1/\Sigma\lambda$ %
10	23.39	20.21	27.63	23.50	34.12	30.88
20	24.21	14.46	19.56	16.95	28.04	23.21
50	19.16	13.03	18.36	11.12	23.06	17.81
100	19.91	13.50	16.59	9.95	18.77	18.17
250	20.29	12.94	13.68	10.89	16.86	20.71
500	23.05	12.58	12.27	10.99	16.65	18.81
1000	22.13	12.43	11.97	10.62	16.20	17.55
1500	22.62	12.36	11.70	11.05	15.89	17.53
1700	22.89	12.35	11.90	11.10	15.88	17.88
1800	23.16	--	11.89	11.09	15.94	17.79
2040	23.41	--	11.77	11.15	15.90	17.84

On the contrary, the values of $\lambda_1/\Sigma\lambda$ obtained from the first 250 snapshots for Test SM and Tests APG-P3 do not decrease consistently with increasing number of snapshots. In the case of Test SM the percentage differences for $10 \leq N \leq 2040$ is not particularly large, and for $N \geq 250$, $\lambda_1/\Sigma\lambda = 22.9 \pm 0.5\%$. One would conclude from Table 7.1 that, in all cases, the percentage contribution of the first mode to the total energy vary a little (less than 1%) when N = 500 snapshots are used. Therefore, the N = 1700 (Test CC-P1) and N = 2040 (Tests SM, FPG-P1, APG-P1, APG-P2 and APG-P3) used in the subsequent analysis are sufficient to achieve converged results.

The number of snapshots used in the present study is comparable to those used in previous POD studies. For example, Alfonsi and Primavera (2006) used 2000 snapshot for smooth wall channel flow while Kostas *et al.* (2005) used 1024 snapshots for the decomposition of their backward facing step flow. In the smooth wall data reported by

Sen *et al.* (2007), it was observed that the values of $\lambda_1/\Sigma\lambda$ vary less than 1% for $1000 \leq N \leq 6000$.

For the upstream test case (N = 2040), the first POD mode contributed 23.41% of the total turbulent kinetic energy. This value is only 7% less than the value of 28.58% reported by Sen *et al*. (2007). It should be noted that $Re_\tau = 780$ in the present case compared with $Re_\tau = 180$ in the study by Sen *et al*. (2007). It has been suggested that as the Reynolds number increases (and the flow becomes increasingly turbulent) there is a more even or uniform distribution of energy among the various modes. As a result, the value of $\lambda_1/\Sigma\lambda$ would decrease with increasing Re_τ as noted above. Similarly, in the DNS analysis of a fully developed channel flow at $Re_h = 3200$, Moin and Moser (1989) reported $\lambda_1/\Sigma\lambda = 32\%$. Their Re_h is a quarter of the value for Test SM, and may explain the relatively higher value of $\lambda_1/\Sigma\lambda$ reported by Moin and Moser (1989). In their PIV study of backward facing flow, Kostas *et al.* (2005) also reported higher value of $\lambda_1/\Sigma\lambda = 47\%$ for $Re_k = 580$ than a value of $\lambda_1/\Sigma\lambda = 13\%$ for $Re_k = 4660$. It should be noted that the flow field studied by Kostas *et al.* (2005) is not exactly the same as that studied in the present study. In the present Test CC, for example, $Re_k = 2640$ and the reattached length was 10.4 compared with 4.8*k* and 6.8*k* for $Re_k = 580$ and 4660, respectively, in the study by Kostas *et al.* (2005). However, $\lambda_1/\Sigma\lambda = 12.4\%$ for Test CC is not significantly different from $\lambda_1/\Sigma\lambda = 13\%$ for $Re_k = 4660$.

The value of $\lambda_1/\Sigma\lambda$ for the upstream flow (Test SM) is nearly twice as large as those obtained in the separated and reattached region (Tests CC-P1, FPG-P1 and APG-P1). This observation is also consistent with the results presented downstream of a backward facing step by Kostas *et al.* (2005). It was argued that the reduced $\lambda_1/\Sigma\lambda$ in the

separated region is associated with the more complex flow features in the separated region which produced a more uniform distribution of energy among the various modes. In other word, the increased level of flow complexity in the separated region results in a less efficient decomposition and would more evenly distribute the energy across the modes.

The energy level associated with the first mode as well as the energy convergence is similar for the three test cases in the recirculation region i.e., Tests CC-P1, APG-P1 and FPG-P1. This is not surprising because, as observed in Chapter 6, the flow dynamics in the recirculation region was dominated primarily by the separated shear layer and nearly independent of pressure gradient.

The results also show that as the flow evolves downstream of the separated and reattached region, the flow becomes structurally less complex so that the energy content in mode 1 becomes substantially larger than those in the separated shear layer. For example, there are 40% and 60% increase in $\lambda_1/\Sigma\lambda$ as the flow evolved from APG-P1 to APG-P2 and APG-P3, respectively. It should also be noted that the $\lambda_1/\Sigma\lambda$ values in the redevelopment region are in closer agreement with the upstream value than those in the separated shear layer.

7.2.2 Spectra of Turbulent Kinetic Energy

The energy associated with each mode as well as cumulative sum for the first 50 modes is plotted in Figure 7.1a and 7.1b, respectively, to illustrate the effectiveness of the decomposition to capture energy in the upstream section (Test SM), in the separated shear layer (Tests CC-P1, APG-P1 and FPG-P1) and in the development region of the Test APG (Test APG-P2 and APG-P3). An efficient decomposition will capture nearly

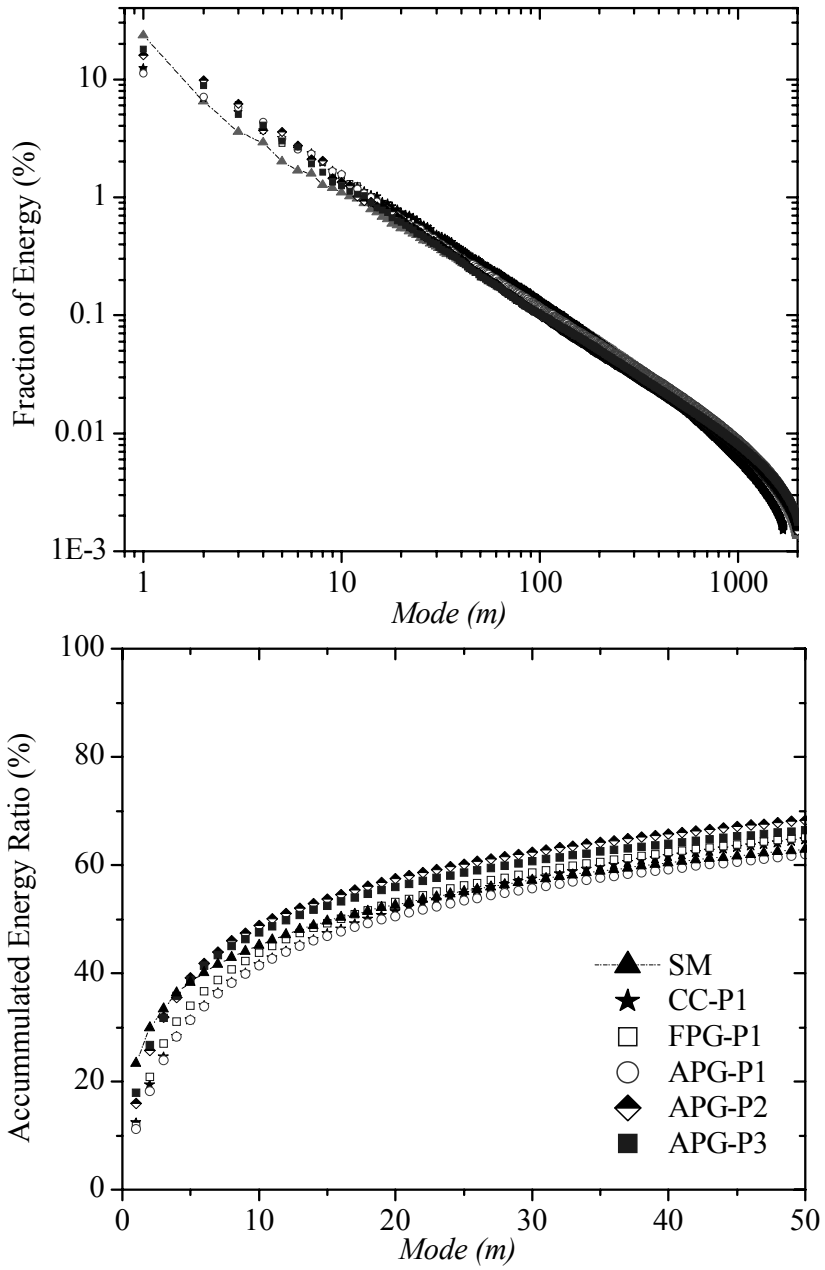

Figure 7.1: Eigenvalue spectra of various test cases: (a) Fractional contribution to the turbulent kinetic energy by the modes and (b) Accumulated energy ratio of modes as a function of mode number. Symbols are SM: 7; CC-P1: ξ; FPG-P1: ∀; APG-P1: –; APG-P2: Σ; APG-P3: !.

100% of the total energy with a relatively small number of modes. As expected, the energy associated with the modes decrease exponentially with increasing mode. Figure

7.1a reveals that the energy magnitude drops two orders within the first 100 modes. This implies that the first 100 modes contain most of the energy.

For the Test CC, the first 25 and 50 modes, respectively, contributed 50% and 65% of the total turbulent kinetic energy. This is comparable to the energy spectra for backward facing step reported by Kostas *et al.* (2005). They reported about 57% energy by mode 25 and 67% energy by mode 50 for their backward facing step at the higher Reynolds number (Re_k = 4660). Consistent with the data presented in Table 7.1, a noticeable increase is observed in the energy level of the first mode for Tests APG-P2 and APG-P3 which are downstream of the reattachment region. The convergence of the upstream flow is faster compared to the separated flow but beyond mode 20 the convergence is nearly similar for all the flows except for Tests APG-P2 and APG-P3.

7.2.3 Spectra of Reynolds shear Stress

Consideration is now turned to the contribution of the dominant modes to Reynolds shear stress. It should be recalled that the mean flow is represented by the zeroth mode. Therefore, $\partial U/\partial y$ is independent of the POD modes. Since the production of turbulent kinetic energy in quasi-two-dimensional turbulent flows is almost entirely given by $-uv\partial U/\partial y$, the contribution of the dominant modes to the Reynolds shear stress is equivalent to the fractional contribution to the total energy production. It should be noted that the formulation of the POD ensures that the characteristic eddies are those with maximal contribution to turbulent kinetic energy. In other words, the theory does not maximize the contribution of the dominant structures to the Reynolds shear stress and turbulence production.

Table 7.2 provides a summary of the relative contribution of the first mode to the total Reynolds shear stress for the various test cases analyzed in the previous section. The convergence of the Reynolds shear stress is observed to be qualitatively similar to that of turbulent kinetic energy. For snapshots $N \geq 500$, less than 2% variation is observed in the values of $uv_1/\Sigma uv$. Similar to the observations made in the previous sections, $uv_1/\Sigma uv$ for the upstream test condition is higher than those in the separated shear layer. Moreover, the values in the redevelopment region are higher than those in the separated layer but somewhat lower than the upstream value. These results suggest that the relative contribution of mode 1 to the total Reynolds shear stress (and turbulence production) also decreases with increasing complexity in flow structure.

A comparison between the data presented in Table 7.1 and Table 7.2 reveals that the contribution of the first mode to the Reynolds shear stress is much higher than the contribution to the turbulent kinetic energy. For Test SM, for example, $uv_1/\Sigma uv = 34\%$ compared with $\lambda_1/\Sigma\lambda = 23\%$. In general, the values of $uv_1/\Sigma uv$ are approximately 45% to 60% larger than the corresponding $\lambda_1/\Sigma\lambda$ values. The higher contribution of the Reynolds shear stress compared to the turbulent kinetic energy by the first mode is in agreement with the findings of Moin and Moser (1989). The implications of these observations are that the characteristic large scales contribute more efficiently to the Reynolds shear stress than they contribute to the normal stresses (or turbulent kinetic energy).

In Figure 7.2a, the cumulative sum of the Reynolds shear stress as a function of modes is plotted while the cumulative sum of the Reynolds shear stress and the turbulent kinetic energy is compared in Figure 7.2b. The shear stress appears to converge faster for

the first five modes at the upstream section than the other planes. Subsequently, (N > 5) the convergence rate becomes similar for all test cases (Figure 7.2a). No significant difference is observed between the three test cases in the separated shear layer.

Table 7.2: Reynolds shear stress convergence for increasing number of snapshots of the first mode.

Snapshots (*N*)	SM	CC-P1	FPG-P1	APG-P1	APG-P2	APG-P3
	$uv_1/\Sigma uv$ %	$uv_1/\Sigma uv$ %	$uv_1/\Sigma uv$ %	$uv_1/\Sigma uv$ %	$uv_1/\Sigma uv$ %	$uv_1/\Sigma uv$ %
10	31.89	33.52	46.06	34.59	52.26	55.71
20	19.98	19.24	31.97	24.58	36.35	33.75
50	19.78	18.87	26.26	15.92	31.13	22.73
100	24.67	21.41	21.92	13.98	27.74	28.09
250	30.00	19.74	18.41	15.80	25.59	32.16
500	35.40	19.31	17.60	16.08	24.46	29.50
1000	33.12	18.93	16.17	15.23	23.93	27.35
1500	33.20	18.98	15.75	16.16	23.51	27.61
1700	33.88	19.07	16.00	16.27	23.19	28.28
1800	34.02	--	16.14	16.17	23.22	28.33
2040	34.36	--	15.80	16.50	23.34	28.52

For all the test cases, the convergence of the Reynolds shear stress is faster than for the turbulent kinetic energy. At the upstream section, for example, 85% of the Reynolds shear stress (Σuv) is recovered by mode 50 while only 66% of turbulent kinetic energy ($\Sigma\lambda$) is recovered. It is interesting to note that this finding is similar to experimentally observed behavior of large eddies. Blackwelder and Kovasznay (1972) found that the largest eddies in a turbulent boundary layer contribute proportionately more to Reynolds shear stress than to the turbulent kinetic energy.

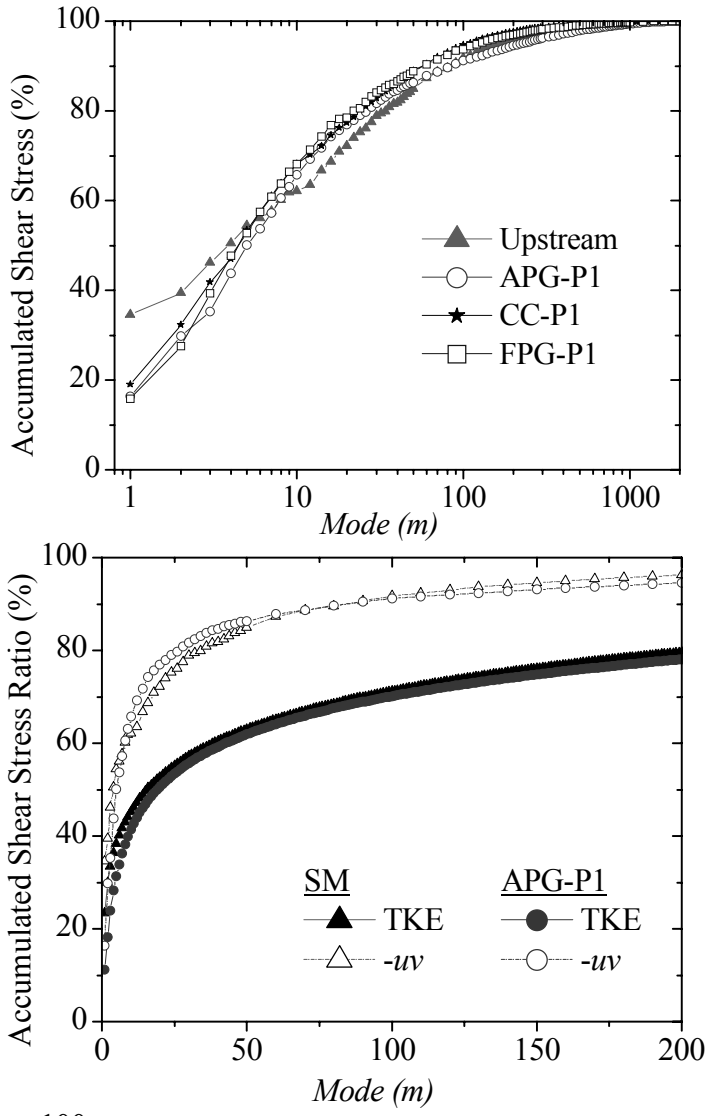

Figure 7.2: Shear stress spectra of various test cases: (a) Fractional contribution to the shear stress by the modes and (b) Accumulated shear stress ratio of modes as a function of mode number.

7.2.4 Reconstruction of the Turbulent Quantities

7.2.4.1 Iso-Contours of Turbulent Intensities and Reynolds Shear Stress

Low order representations of the instantaneous velocity fields were constructed from 1, 2, 5, 50, 100, 500 and 1000 POD modes. From the reconstructed velocity fields, the corresponding turbulent intensities and Reynolds shear stress distributions were

determined. The iso-contour plots of the reconstructed quantities for Tests CC-P1, APG-P1 and FPG-P1 exhibit a similar behavior. Therefore, only iso-contours for Test APG-P1 are shown and discussed in detail here. The iso-contours for Tests CC-P1 and FPG-P1 are presented in Appendix B.

The iso-contours of the streamwise turbulent intensity, transverse turbulent intensity and Reynolds shear stress for Test APG-P1 are plotted in Figures 7.3, 7.4 and 7.5, respectively. The corresponding iso-contour plots from the time averaged PIV data (hereafter referred to as PIV data) are also shown for comparison. The figures are plotted to qualitatively illustrate the cumulative effect of using increasingly more modes in the data reconstruction. As the number of the modes is increased, a consistent progression towards the contours obtained from PIV data is observed. The POD reconstruction shows that the first few modes capture the energy in the region near and downstream of the reattachment. This indicates that the flow dynamics in these regions are determined by large scale structures. The results also show that higher order modes or relatively small-scale structures contribute to the peak of turbulent intensity along the mean separation streamline in the separated region for $x/k \leq 5$. The contribution of various length scales to the reconstructed turbulent intensities and Reynolds shear stress is different. This will be discussed in the next section. It appears that relatively fewer POD modes are required to reconstruct the Reynolds shears stress than is needed for the transverse turbulent intensity. The implication is that the dominant scales are more relevant to the dynamics of the Reynolds shear stress when compared with the transverse turbulent intensity. This observation will be quantified in the subsequent sections.

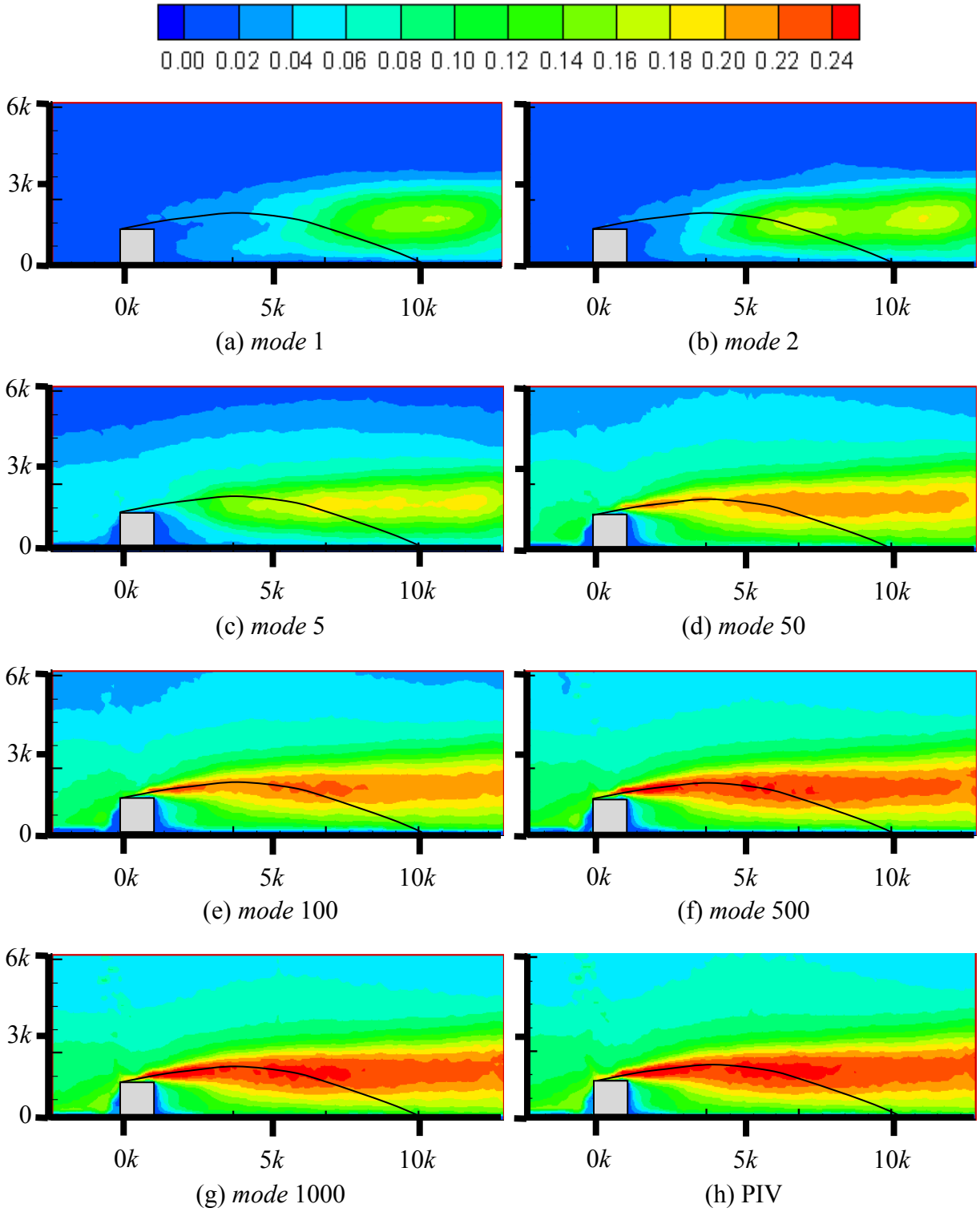

Figure 7.3: Iso-contours of streamwise turbulent intensity, u/U_e^2, obtained using (a) 1, (b) 2, (c) 5, (d) 50, (e) 100, (f) 500 and (g) 1000 modes in reconstruction and (h) from PIV data. Mean separation line is also shown.

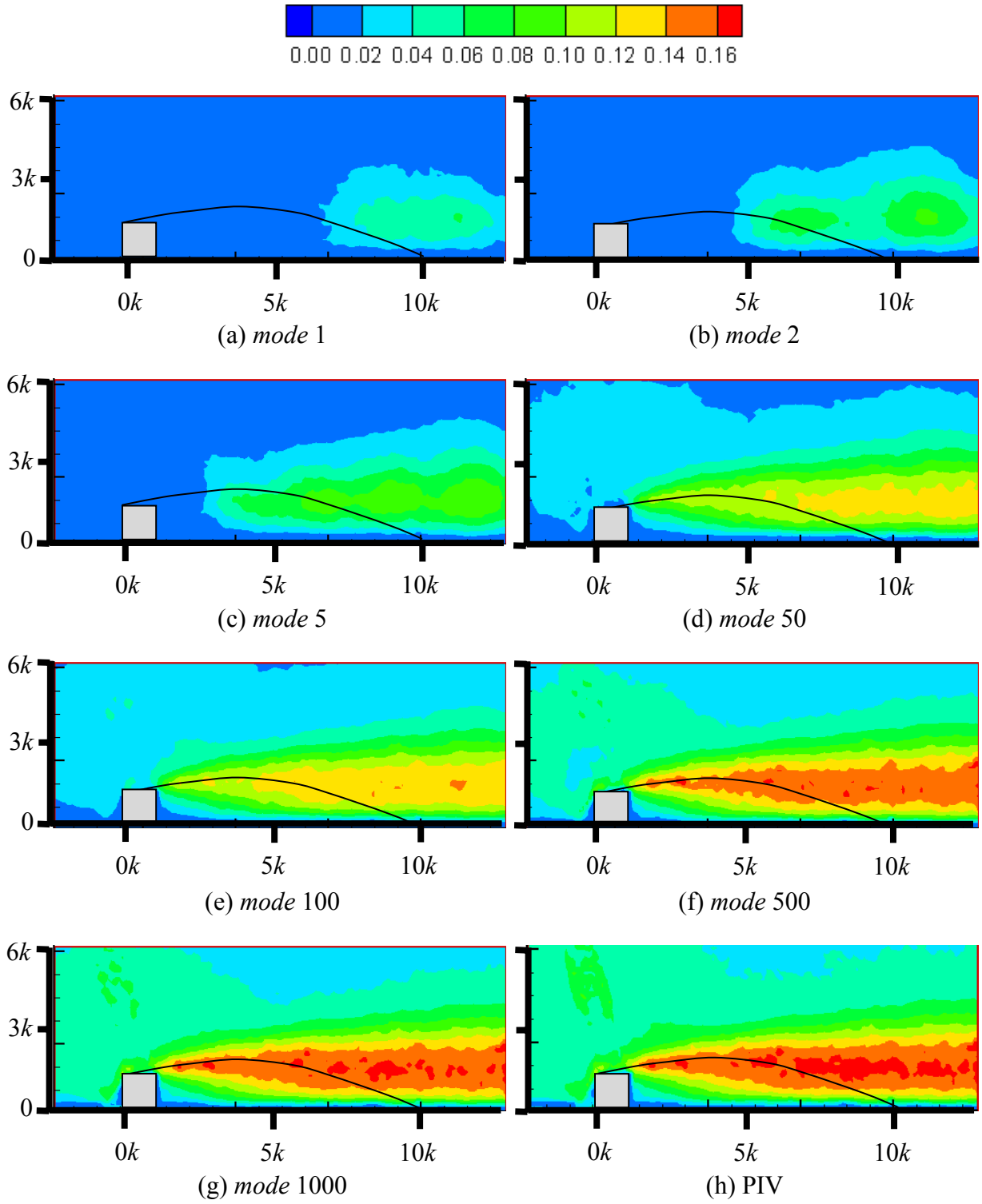

Figure 7.4: Iso-contours of transverse turbulent intensity, v/U_e^2, obtained using (a) 1, (b) 2, (c) 5, (d) 50, (e) 100, (f) 500 and (g) 1000 modes in reconstruction and (h) from PIV data. Mean separation line is also shown.

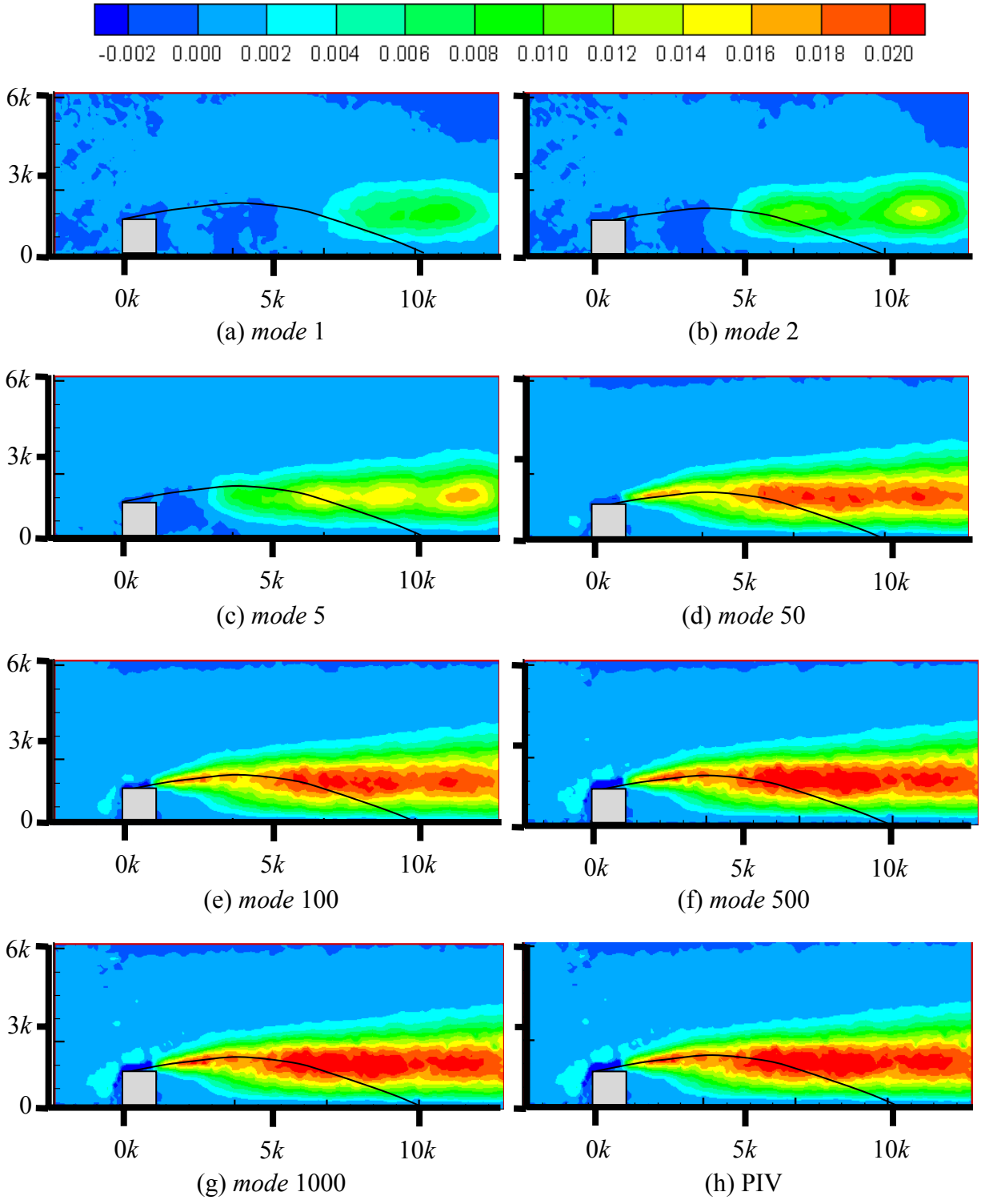

Figure 7.5: Iso-contours of Reynolds shear stress, $-uv/U_e^2$, obtained using (a) 1, (b) 2, (c) 5, (d) 50, (e) 100, (f) 500 and (g) 1000 modes in reconstruction and (h) from PIV data. Mean separation line is also shown.

7.2.5 Reconstructed Profiles of Turbulent Intensities and Reynolds Shear Stress

The profiles of turbulent intensities and Reynolds shear stress reconstructed from selected modes at selected streamwise locations are used to examine the number of modes necessary for the reconstructed profiles to collapse onto the corresponding profiles obtained from the PIV ensemble (or PIV profiles). The following selected locations and/or test cases will be used: upstream section (Test SM) and x/k = 4, 9 and 30 for Test APG. As mentioned earlier, the location x/k = 4 corresponds approximately to the centre of the separation bubble while x/k = 9 represents the location approximately one step height upstream of the reattachment point and x/k = 30 is in the redevelopment region.

For the upstream test condition (Test SM) shown in Figure 7.6, the first few modes ($m \leq 5$) were not able to capture the sharp peak observed in the streamwise intensity profile close to the wall. Moreover, at these lower modes, the y-location of $-uv_{max}$ is farther away from the wall than in the PIV profile. Overall, the agreement between the reconstructed profiles and the corresponding PIV profile improves as the number of mode (m) increases. For a given mode, the reconstructed profiles of the Reynolds shear stress and streamwise turbulent intensity are closer to the corresponding PIV profiles than observed for the transverse turbulent intensity. Furthermore, the collapse onto the PIV profiles is faster in the outer region than in the inner region. For example, the data presented in Figure 7.6 shows that, close to the channel centerline, nearly 80%, 62% and 100% of the u, v and $-uv$ obtained from the PIV were recovered by m = 50. Meanwhile, only 66%, 48% and 76% of u_{max}, v_{max} and $-uv_{max}$ from the PIV were recovered by m = 50. By 250 modes, the Reynolds shear stress collapsed very well onto the PIV data but the reconstructed values of v are still significantly smaller than the

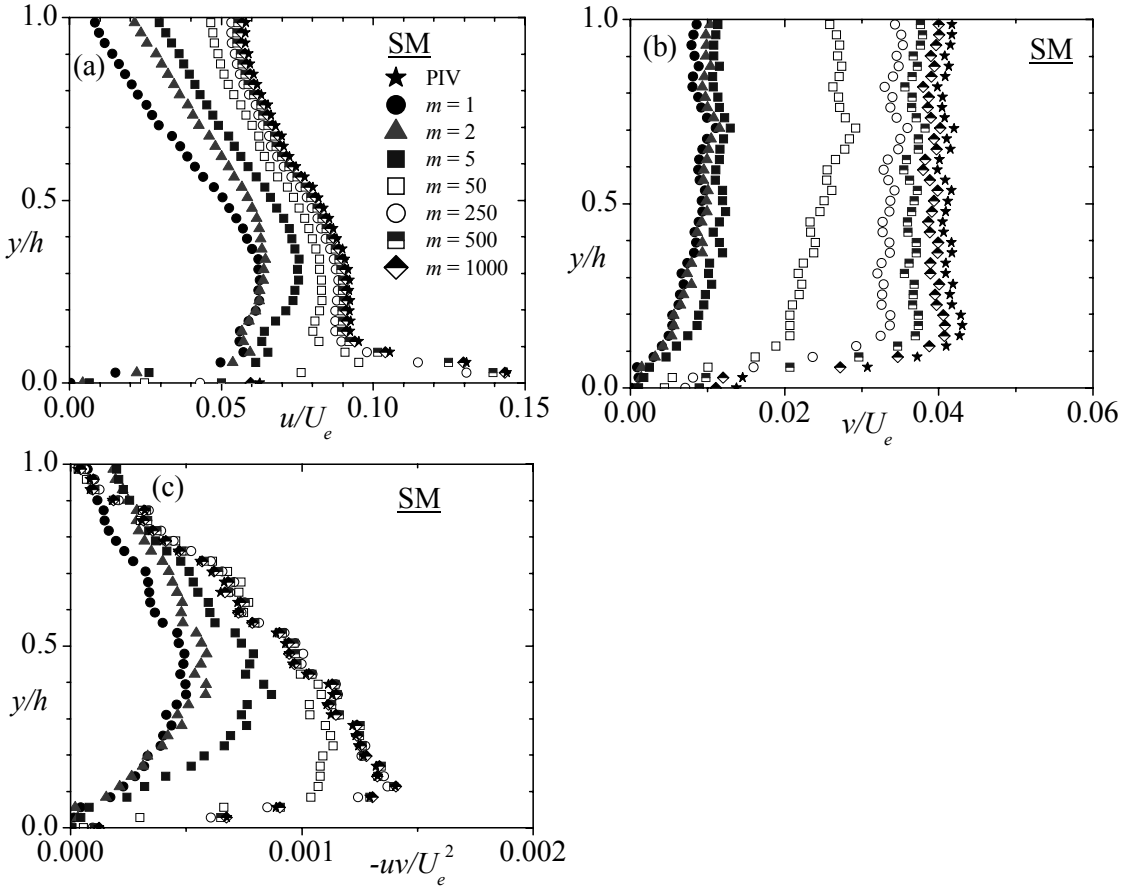

Figure 7.6: Profiles of turbulent quantities for Test SM (a) Streamwise turbulent intensity (b) Transverse turbulent intensity and (c) Reynolds shear stress obtained using various modes in reconstruction. Symbols are: PIV: ξ; m = 1: ,; m = 2: 7; m = 5: !; m = 50: ∀; m = 250: –; m = 500: (; m = 1000: Σ.

corresponding PIV data.

The profiles obtained in the separated shear layer (at x/k = 4 and 9) and plotted in Figure 7.7 show similar trends to that observed at the upstream location. When profiles at the two locations of Test APG in the separated region are compared, it is observed that the reconstructed profiles at x/k = 4 showed a slower tendency to collapse onto the PIV ensemble than profiles at x/k = 9. For example, at x/k = 9, the distinct peak values observed in u, v and -uv from the PIV data are already noticeable by modes 1 and 2. On the other hand, $m \geq 5$ modes are required to clearly reveal the dominant peaks at x/k = 4.

Similar to the observation made at the upstream location, fewer number of POD modes are required to collapse the reconstructed Reynolds shear stress collapsed on the PIV profile in comparison to the turbulent intensities (or Reynolds normal stresses). These results provide additional support to earlier observation that, irrespective of the test condition or location, the large scales contribute more effectively to the Reynolds shear stress than they contribute to the turbulent kinetic energy or Reynolds normal stresses. Unlike the upstream location, however, the POD modes required to collapse the transverse turbulent intensity is not any larger than needed for the streamwise turbulent intensity profiles. The observed differences in the v distributions in the upstream and shear layer are likely due to the large values of V (and $\partial V/\partial y$) in the separated shear layer than at the upstream location. As explained earlier, the large values of $\partial V/\partial y$ would contribute to the production of v^2 in the separated shear layer whereas the negligible values of $\partial V/\partial y$ at the upstream location would imply that v^2 would only benefit from energy redistribution via u^2.

In Figure 7.8, the trends observed in the turbulent intensities and Reynolds shear stress in the redevelopment region are qualitatively similar to those made in the separated shear layer and at the upstream location. In the redevelopment region, however, v also required fewer POD modes to collapse onto the PIV data when compared with the distributions reported for the upstream location. It is expected that as the flow develops further downstream and the magnitude of V (and $\partial V/\partial y$) decrease to a level observed at the upstream location, increasingly more modes would be necessary for v to collapse onto the PIV data.

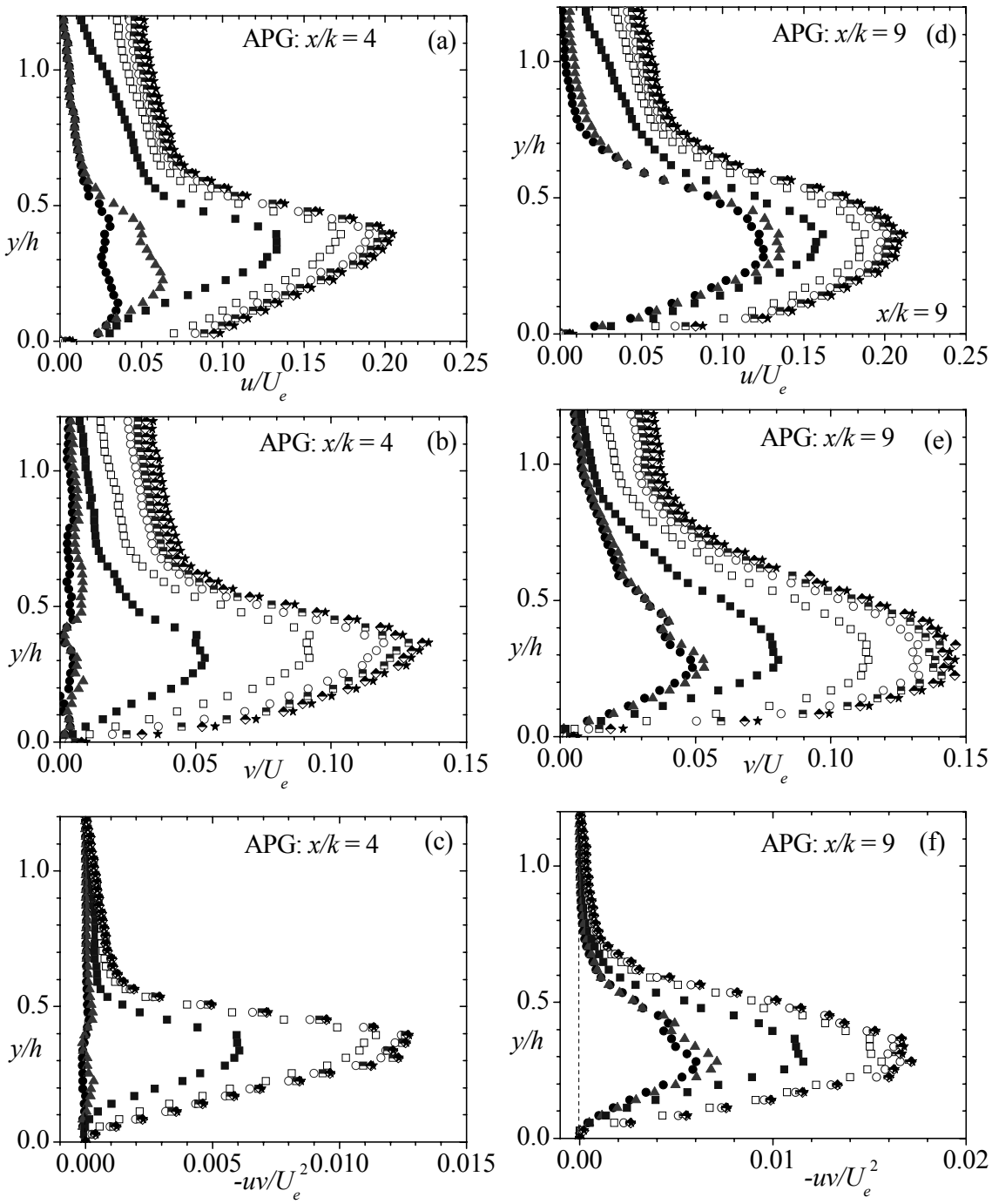

Figure 7.7: Profiles of turbulent quantities for Test APG at x/k = 4 and 9: (a), (d) Streamwise turbulent intensity (b), (e) Transverse turbulent intensity and (c), (f) Reynolds shear stress obtained using various modes in reconstruction. Symbols are: PIV: ξ; m = 1: ,; m = 2: 7; m = 5: !; m = 50: ∀; m = 250: –; m = 500: (; m = 1000: Σ.

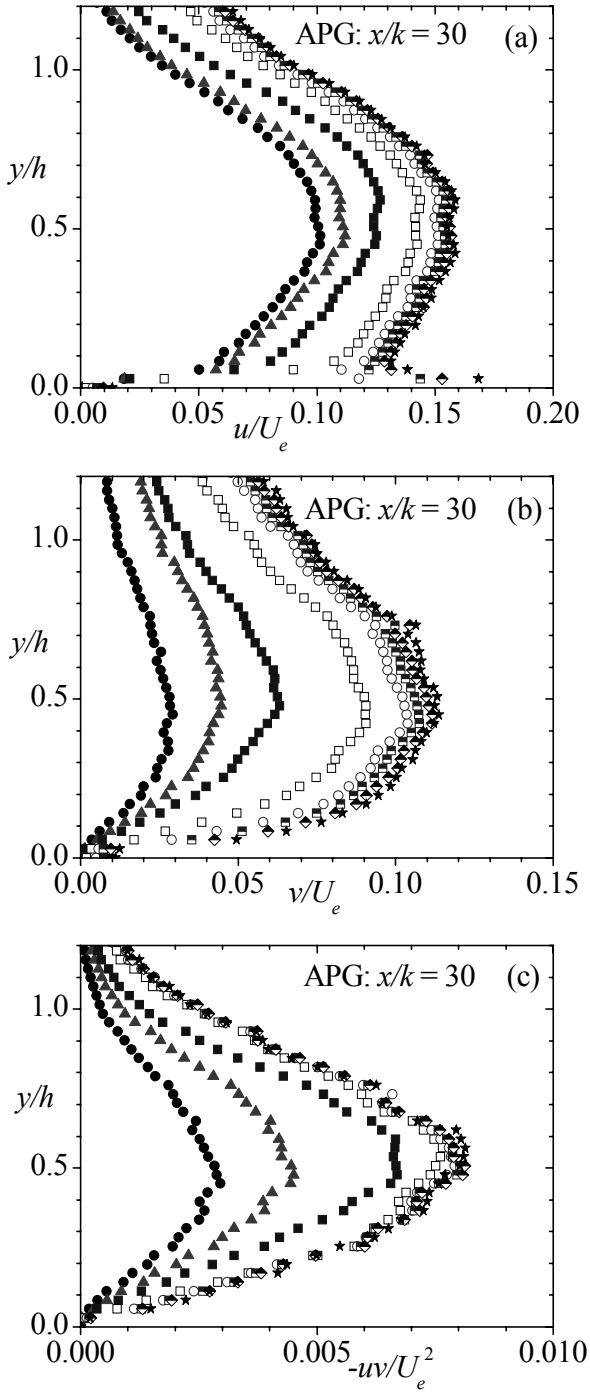

Figure 7.8: Profiles of turbulent quantities for Test APG at x/k = 30 (a) Streamwise turbulent intensity (b) Transverse turbulent intensity and (c) Reynolds shear stress obtained using various modes in reconstruction. Symbols are: PIV: ξ; m = 1: ,; m = 2: 7; m = 5: !; m = 50: ∀; m = 250: –; m = 500: (; m = 1000: Σ.

7.2.6 Reynolds Stress Ratios from Various POD Modes

In the previous section, it was argued that the large scales, in general, contribute most effectively to the Reynolds shear stress and least to the transverse turbulent intensity. Those observations are further quantified in this section by comparing the stress ratios from increasing number of POD modes to those obtained from the PIV data.

Figures 7.9 and 7.10, respectively, show profiles of the Reynolds normal stress ratio (v^2/u^2) and the correlation coefficient ($-\rho_{uv}$) from modes m = 2, 5, 50, 250, 500 and 1000 to the PIV data. As in the previous section, these profiles were obtained at the upstream location, within the separated shear layer and in the redevelopment region.

The largest scales (which correspond to the lower values of m) contribute more significantly to the streamwise component than to the transverse component. This observation is valid for all test conditions and/or locations. At the upstream location and x/k = 4, for example, $v^2/u^2 \approx 0.2$ and 0.5, respectively, in the region $y/h < 0.5$. With increasing number of POD modes, the importance of large scales diminishes and the contribution from the smaller scales increases. The results presented in Figure 7.9 imply that the larger scales are relatively more important to the dynamics of u^2 than for v^2. Conversely, the relatively smaller scales would play a more significant role in the dynamics of v^2 than for u^2.

Figure 7.11 reveals that the large scales are more correlated than the small scales. This observation is based on the premise that the magnitude of the correlation coefficient decreases with increasing POD mode (decreasing size of coherent structure). At mode 1 (not shown), for example, a perfect correlation ($-\rho_{uv} = 1$) was observed across the channel.

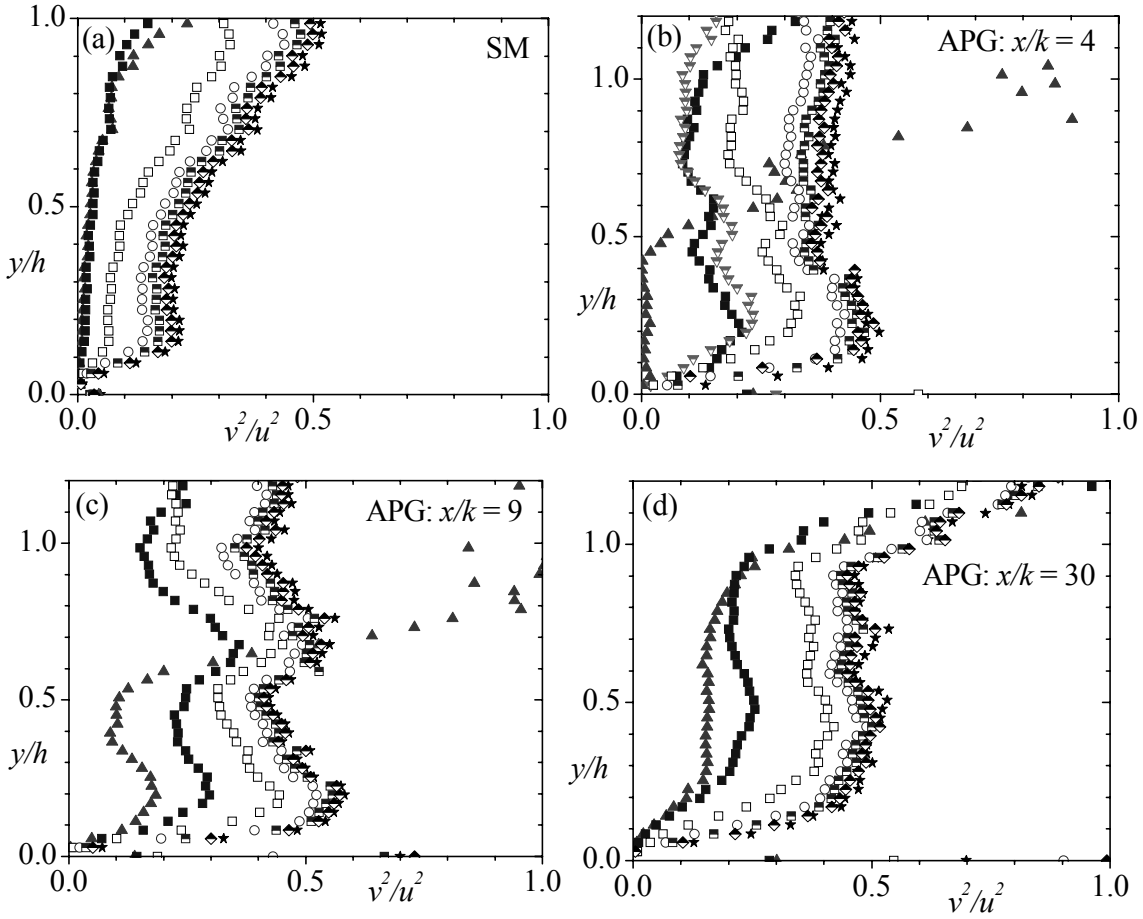

Figure 7.9: Profiles of stress ratios, v^2/u^2: (a) SM (b) APG: x/k = 4, (c) APG: x/k = 9, and (d) APG: x/k = 30, obtained using various modes in reconstruction. Symbols are: PIV: ξ; m = 2: 7; m = 5: !; m = 50: ∀; m = 250: –; m = 500: (; m = 1000: Σ.

The ratios of the Reynolds shear stress to the normal stresses ($-uv/v^2$ and $-uv/u^2$) are shown in Figures 7.12 and 7.13, respectively. When the overall contributions from the small and large scales to the Reynolds stresses are considered, it is observed that $-uv/v^2 <$ 1, as evident from the PIV data at all test locations. On the other hand, the large scales contribute more effectively to the shear stress ($-uv$) than to transverse normal stress (v^2) so that $-uv/v^2$ is generally larger than unity for lower POD modes. In the region $y/h < 0.4$ at the upstream location, for example, $-uv/v^2$ = 7.5 for the first 5 POD modes. The contributions from the lower POD modes to $-uv$ and u^2 are relatively more complex than observed in the prior plots. At the upstream location, for example, the first 10 modes ($m \leq$

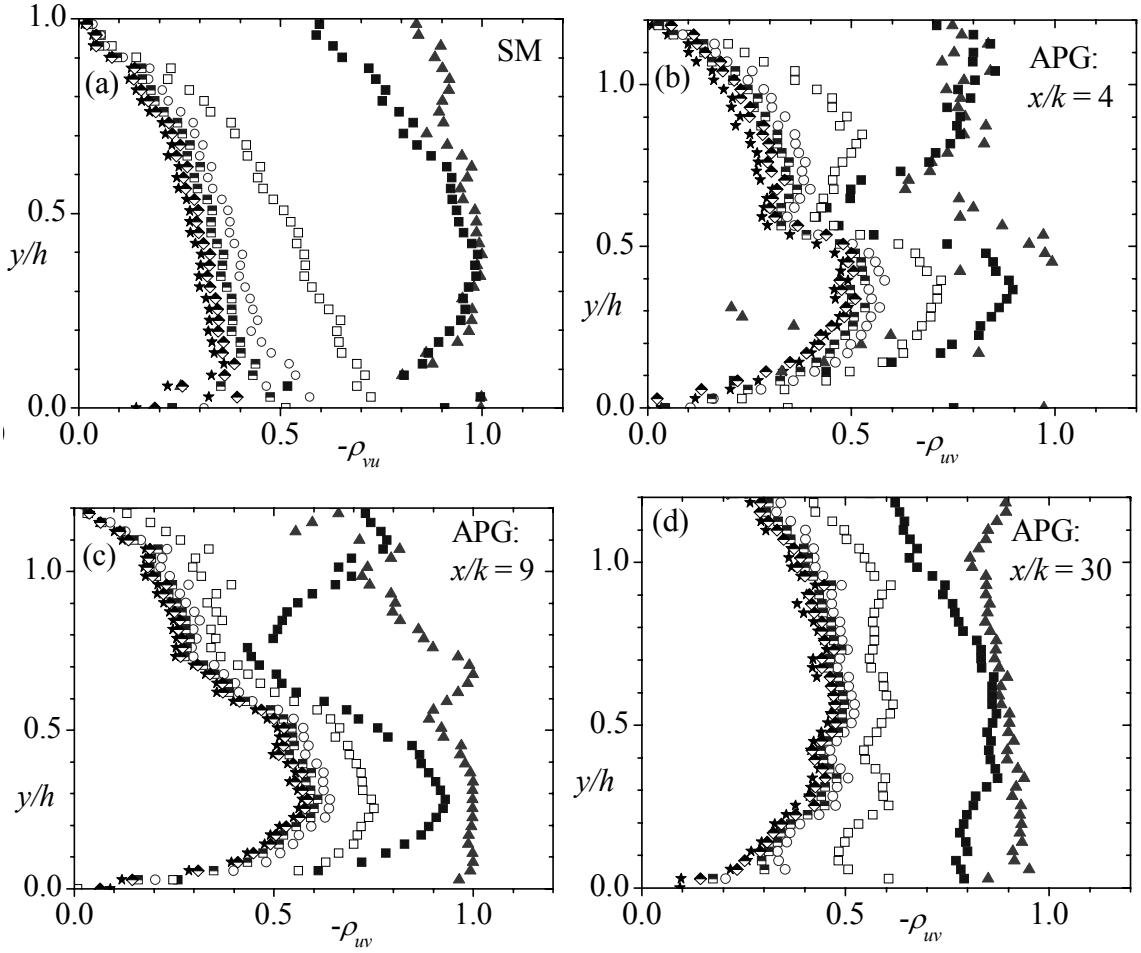

Figure 7.10: Profiles of shear stress correlation coefficient, $-\rho_{uv} = -uv/(v^2u^2)^{0.5}$: (a) SM (b) APG: $x/k = 4$, (c) APG: $x/k = 9$, and (d) APG: $x/k = 30$, obtained using various modes in reconstruction. Symbols are: PIV: ξ; $m = 2$: 7; $m = 5$: !; $m = 50$: ∀; $m = 250$: –; $m = 500$: (; $m = 1000$: Σ.

10) contribute more to u^2 than to $-uv$ in the region $y/h \leq 0.4$. The reverse observation is made in the outer part of the channel ($y/h > 0.4$). A similar observation is also made at for $m = 2$ at $x/k = 5$.

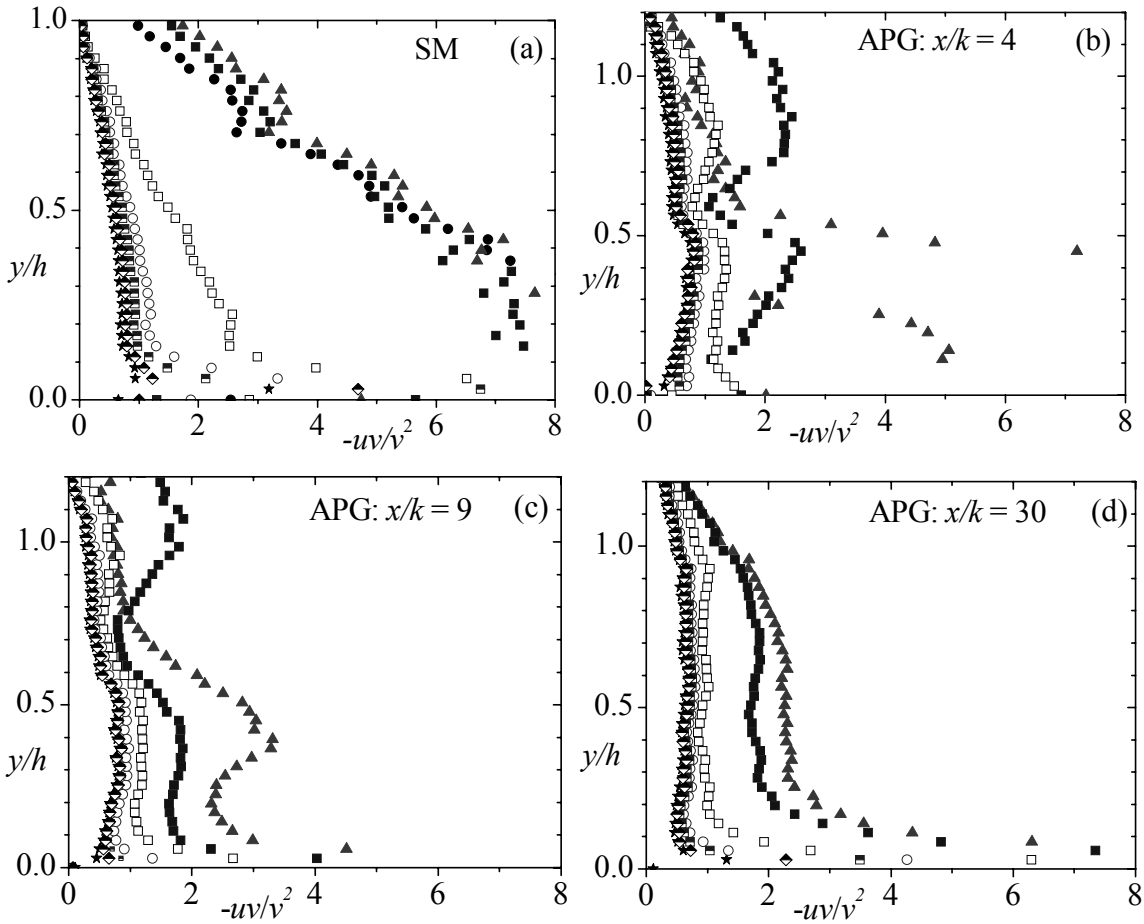

Figure 7.11: Profiles of shear stress correlation coefficient, $-uv/v^2$: (a) SM (b) APG: x/k = 4, (c) APG: x/k = 9, and (d) APG: x/k = 30, obtained using various modes in reconstruction. Symbols are: PIV: ξ; m = 2: 7; m = 5: !; m = 50: ∀; m = 250: –; m = 500: (; m = 1000: Σ.

7.3 Summary of Results

Proper orthogonal technique has been applied to the flow in upstream section of the rib (Test SM), in the separated shear layer (Tests CC-P1, FPG-P1 and APG-P1) and in the redevelopment region (Tests APG-P2 and APG-P3). The contribution from the first dominant mode to the turbulent kinetic energy and Reynolds shear stress is higher at the upstream section than in the separated layer. This was attributed to a more uniform distribution of energy among the POD modes in the relatively more complex separated

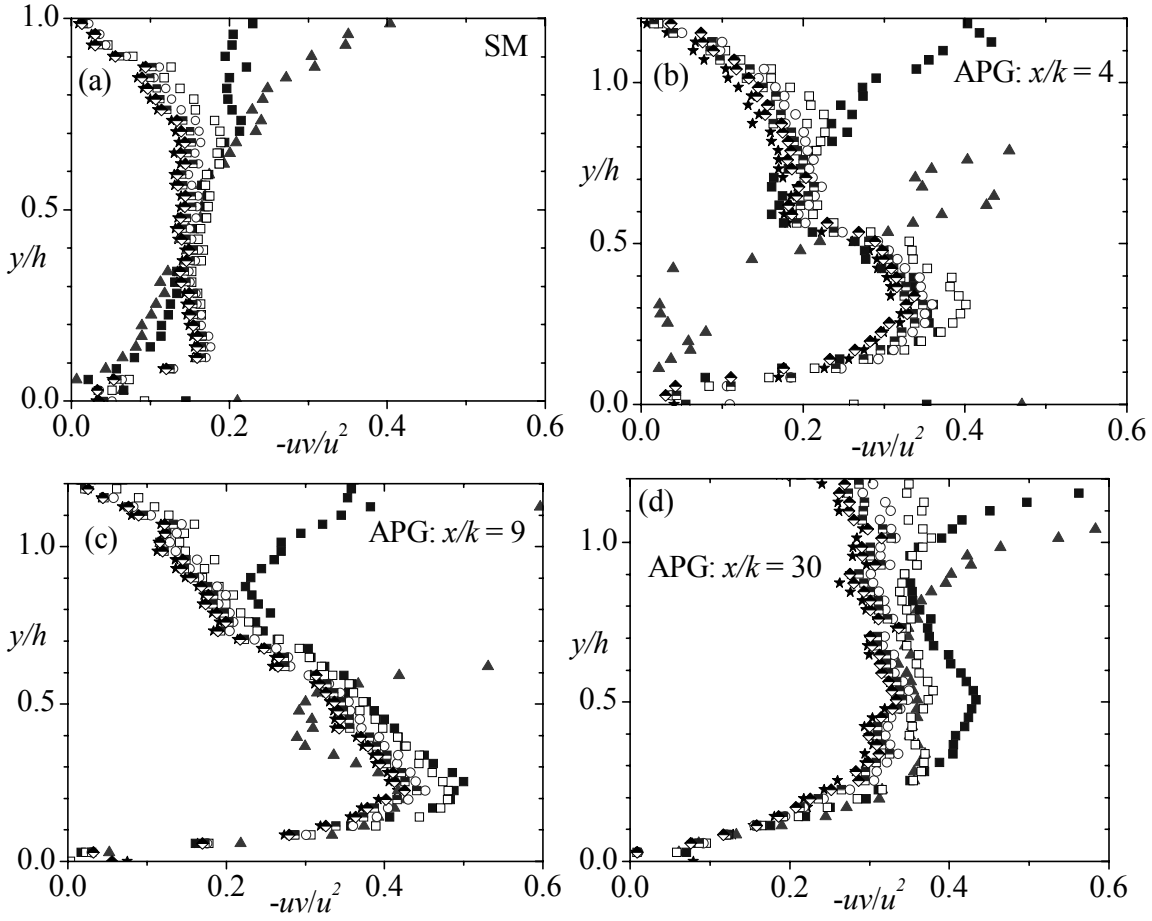

Figure 7.12: Profiles of shear stress correlation coefficient, $-uv/u^2$: (a) SM (b) APG: x/k = 4, (c) APG: x/k = 9, and (d) APG: x/k = 30, obtained using various modes in reconstruction. Symbols are: PIV: ξ; m = 2: 7; m = 5: !; m = 50: ∀; m = 250: –; m = 500: (; m = 1000: Σ.

shear layer than in the upstream section. The results also show that the contribution of the first mode to the Reynolds shear stress was much greater than the contribution to the turbulent kinetic energy. The turbulent intensities, Reynolds shear stress as well the ratios of Reynolds stress show that that the large scale structures contribute most to Reynolds shear stress and least to transverse normal stress.

CHAPTER 8: SUMMARY AND FUTURE WORK

This chapter summarizes the major conclusions of this thesis. The implications of the results for turbulence modeling and recommendations for future work are also presented.

8.1 Summary and Conclusion

A series of detailed experimental investigations are undertaken to the study the characteristics of separated and reattached flows in pressure gradients generated in diverging and converging channels. The pressure gradients were created in channels with a flat lower wall and nonlinearly diverging and converging upper wall. A transverse square rib of height k = 6 mm was used to create separation. A reference parallel-wall channel was also employed to facilitate the interpretation of the pressure gradient flows. A high resolution planar particle image velocimetry technique (PIV) was used to conduct the velocity measurements.

In the first part of this investigation, measurements were made in the generic asymmetric converging and diverging channel without the rib on the channel wall. Measurements were made in the diverging channel at Re_h of 27050 (Test D1) and 12450 (Test D2) and in the converging channel at Re_h = 19280 (Test C). The key findings of this investigation are summarized below:

- In case of APG, the lower boundary layer parameters were significantly higher than the corresponding values in the upper boundary layer. Furthermore, the turbulent intensities, Reynolds shear stress and turbulence production were enhanced more significantly in the lower boundary layer than in the upper

boundary layer. On the other hand, the effect of FPG was found to be similar on both the upper and the lower boundary layers.

- APG enhances production of turbulent kinetic energy and Reynolds shear stress, while these quantities are attenuated by FPG. As a result, the turbulent intensities and Reynolds shear stress are increased in APG and decreased in FPG.
- Different velocity and length scales were used to interpret the mean velocity defect profiles. It was found that the mixed velocity scale proposed by Zagarola and Smits (1998), $U_e\delta^*/\delta$, and the boundary layer thickness are the most successful in collapsing the profiles of both the APG and FPG onto a single curve.

The separated and reattached flows in the converging, diverging and parallel-wall channels downstream of the transverse square rib were then investigated. The Reynolds number based on the approach velocity and rib height was approximately 2700. Preliminary experiments were also conducted to determine if the position of the rib relative to the start of the diverging section had any effect on mean and turbulent quantities. In these preliminary experiments, the rib was placed at x/k = -25, 0 and 25. The principal findings of this investigation are summarized below:

- The preliminary test in the APG channel revealed that when the rib was located at x/k = 25, the reattachment length was about 20% longer than those measured for x/k = -25 and 0. However, no significant effects of different rib locations were observed on the mean and turbulent quantities in the separated and redevelopment region.
- For the measurements conducted in the FPG, APG and parallel-walled channel, the reattachment length was found to be nearly independent of pressure gradient.

- The flow dynamics in the upper boundary layer of the separated region and early stages of flow redevelopment were observed to be insensitive to the pressure gradients. The similarity in profiles within the separated region implies that the flow dynamics is this region is entirely dominated by the separated shear layer.
- On the contrary, the effects of the separated shear layer diminished in the redevelopment region so that the dynamics of the flow in this region is dominated by pressure gradient effects.
- In the separated shear layer, V and $\partial V/\partial y$ increased substantially. This increased the production of v^2 substantially. As a result, v increased three-folds compared with its upstream value. The streamwise turbulent intensity also increased but its maximum value is only 40% higher than the corresponding upstream value.
- Similar to the flow in pressure gradient without the rib, the mean defect profiles at various stages of redevelopment collapsed better when scaled with the mixed scaling $U_e\delta^*/\delta$ than with the friction velocity U_τ.
- The Reynolds stress profiles in nearly zero pressure gradient were observed to collapse onto the upstream profiles at $x/k = 120$. However, at this location the Reynolds stresses in APG and FPG are, respectively, higher and lower than the upstream profile. This indicates a significantly longer distance would be required in APG and FPG flows should ever relax back to the upstream flow.
- The profiles obtained in the present FPG channel at $x/k \approx 120$ and those in the same channel but without the ribs collapsed reasonably well but significant differences exist between the results with and without the rib in the APG channel.

In the last part of this thesis, proper orthogonal technique has been applied to the flow in the upstream section of the rib (Test SM) and in the separated shear layer (Tests CC-P1, FPG-P1 and APG-P1) as well as in the redevelopment region (Tests APG-P2 and APG-P3). The key findings of this investigation are summarized below:

- The contribution of the first mode to turbulent kinetic energy as well as Reynolds shear stress was highest to Test SM and lowest in the region of the separated shear layer.
- POD recovered Reynolds shear stress more efficiently than the turbulent kinetic energy. This implies that the large scale or dominant structures play more substantial role in the Reynolds shear stress than in the turbulent kinetic energy or Reynolds normal stresses.
- The turbulent intensities, Reynolds shear stress as well the ratios of Reynolds stress show that that the large scale structures contribute most to Reynolds shear stress and least to transverse normal stress.

8.2 Implications for Turbulence Modeling

The benchmark experimental data reported in pressure gradients and separated and reattached flows in pressure gradients will be invaluable for validating and/or calibrating advanced turbulence models for fluid engineering applications. Based on the results presented in the present study, the following useful remarks can be made.

- The attached pressure gradient flows are not isotropic. Therefore advanced turbulence models such as Second Moment Closures which solve the transport equations for the Reynolds stresses would be more suitable for predicting

pressure gradient turbulent flows than the standard two-equation turbulence models.

- In the separated region, the distribution of mixing length in the inner region does not follow the well-documented linear profile reported for simple near-wall turbulent flows. This suggests that the primitive mixing length or eddy viscosity models are not suitable for these types of flows.
- In the separated and reattached flows, the production term in the transport equation for v^2 is non-negligible and the flow is not isotropic. This is an indication that turbulence models which cannot distinguish between the various Reynolds stresses would not be suitable for the flow field investigated in this work. More advanced models such as Second Moment Closures would be more appropriate for these flows.
- In the separated region, the turbulence in not in energy equilibrium. In general, only turbulence models that take into account all the transport terms (including diffusion and convective terms) will be able to accurately predict these complex flows.

8.3 Recommendations for Future Work

On the basis of the above conclusions and the current understanding of the separated and reattached flows, the following issues warrant further research.

An effect of wide range of pressure gradients to the separated and reattached flows should be considered and an addition of direct pressure measurements is also recommended. Furthermore, the complex structure of the separated and reattached flows ultimately requires three-dimensional measurements in order to gain complete

understanding of the flow physics. The comprehensive dataset reported is well suited for the validation of turbulence models. So, an investigation should be undertaken to assess the suitability of various turbulence models to the separated and reattached flows. Extension of the POD decomposition to the vorticity field is also suggested to obtain further insight into the coherent structures.

REFERENCES

Abu-Mulaweh, H.I., 2005, "Turbulent Mixed Convection Flow over a Forward-Facing Step - The Effect of Step Height," Int'l J. Thermal Sci., **44**, pp. 155-162.

Adrian, R.J., 1991, "Particle-Imaging Techniques for Experimental Fluid," Ann. Rev. Fluid Mech., **23**, pp. 261-304.

Agelinchaab, M. and Tachie, M.F., 2008, "PIV Study of Separated and Reattached Open Channel Flow over Surface Mounted Blocks", J. Fluids Eng., 130, pp. 061206.

Alfonsi, G. and Primavera, L, 2007, "Dynamics of POD Modes in Wall Bounded Turbulent Flow," Proc. R. Soc. A., **463**, pp. 593-612.

Alving, A.E. and Fernholz, H.H., 1996, "Turbulence Measurements around a Mild Separation Bubble and Downstream of Reattachment," J. Fluid Mech., **322**, pp. 297-328.

Angele, K.P. and Muhammad-Klingmann, B., 2006, "PIV Measurements in a Weakly Separating and Reattaching Turbulent Boundary Layer," Eur. J. Mech. B/Fluids, **25**, pp. 204-222.

Antoniou, J. and Bergeles, G., 1988, "Development of the Reattached Flow Behind Surface-Mounted Two-Dimensional Prisms," J. Fluid Eng., **110**, pp.127-133.

Aubertine, C.D. and Eaton, J.K., 2005, "Turbulence Development in a Non-Equilibrium Turbulent Boundary Layer with Mild Adverse Pressure Gradient," J. Fluid Mech., **532**, pp. 345-364.

Aubertine, C.D. and Eaton, J.K., 2006, "Reynolds Number Scaling in a Non-Equilibrium Turbulent Boundary Layer with Mild Adverse Pressure Gradient," Int. J. Heat and Fluid Flow, **27**, pp. 566-575.

Barenblatt, G.I., 1995, "Scaling for Fully Developed Turbulent Shear Flows. I. Basic Hypothesis and Analysis," J. Fluid Mech., **248**, pp. 513-520.

Bergeles, G. and Athanassiadis, N., 1983, "The Flow Past a Surface-Mounted Obstacle," Journal of Fluids Engineering, **105**, pp. 461-463.

Berkooz, G., Holmes, P. and Lumley, J. L., 1993, "The Proper Orthogonal Decomposition in the Analysis of Turbulent Flows," Ann. Rev. Fluid Mech., **25**, pp. 539 – 575.

Blackwelder, R.F. and Kovasznay, L.S.G., 1970, "Large-Scale Motion of a Turbulent Boundary Layer with a Zero and a Favorable Pressure Gradient," Report No. 2 Dept. of Mechanical Engineering, The Johns Hopkins University, Maryland, USA.

Blackwelder, R.F. and Kovasznay, L.S.G., 1972, "Large-Scale Motion of a Turbulent Boundary Layer during Relaminarization," J. Fluid Mech., **53**, pp. 61-83.

Bourassa, C., Thomas, F.O. and Nelson, R.C., 2000, "Experimental Investigation of Turbulent Boundary Layer Relaminarization with Application to High-Lift Systems: Preliminary Results," AIAA Applied Aerodynamics Conference, 18th, Denver, CO.

Bradshaw, P. and Wong, F.Y.F., 1972, "The Reattachment and Relaxation of a Turbulent Shear Layer," J. Fluid Mech., **52**, pp. 113-135.

Buschmann, M.H. and Gad-el-Hak, M., 2007, "Recent Developments in Scaling of Wall-Bounded Flow," Prog. Aero. Sci., **42**, pp. 419-467.

Castillo, A.L., 2000, "Application of Zagarola/Smits Scaling in Turbulent Boundary Layers with Pressure Gradient," Advances in Fluid Mechanics III, WIT Press, pp. 275-288.

Castro, I.P. and Epik, E., 1998, 1998, "Boundary Layer Development after a Separated Region," J. Fluid Mech., **374**, pp. 91-116.

Cazemier, W., Verstappen, R.W.C.P. and Veldman, A.E.P., 1998, "Proper Orthogonal Decomposition and Low-Dimensional Models for Driven Cavity Flows," Phys. Fluids, **10**, pp. 1685-1699.

Chandrsuda, C. and Bradshaw, P., 1981, "Turbulence Structure of a Reattaching Mixing Layer," J. Fluid Mech., **110**, pp. 171-194.

Ching, C.Y., Djenidi, L., and Antonia, R.A., 1995, "Low-Reynolds-Number Effects in a Turbulent Boundary Layer," Exp. Fluids, **19**(1), pp. 61-68.

Cizmas, P.G., Palacious, A. Brien, T.O. and Syamlal, M., 2003, "Proper Orthogonal Decomposition of Spatio Temporal Patterns in Fluidized Beds," Chem. Eng. Sci., **158**, pp. 4417-4427.

Clauser, F.H., 1954, "Turbulent Boundary Layers in Adverse Pressure Gradients," J. Aero. Sci., **21**, pp. 91-108

Coleman, H.W. and Steele, W.G., 1995, "Engineering Application of Experimental Uncertainty Analysis," AIAA Journal, **33**, pp. 1888-1896.

Cutler, A.D. and Johnston, J.P., 1989, "The Relaxation of a Turbulent Boundary Layer in an Adverse Pressure Gradient," J. Fluid Mech., **200**, pp. 367-387.

Degraaff, B.D., 1999, "Reynolds Number Scaling of the Turbulent Boundary Layer on a Flat Plate and on Swept and Unswept Bumps," Ph.D. Thesis, Stanford.

Djilali, N., Gartshore, I.S., 1991, "Turbulent Flow Around a Bluff Rectangular Plate. Part I: Experimental Investigation," J. Fluids Eng., **113**, pp. 53-59.

Dönch, F., 1926, ”Divergente und Konvergente Turbulente Strömungen mit Kleinen Öffnungs-Winkeln,” Forch. Arb. Geb. Ing. Wes., Helf, **282**, pp. 1-58.

Driver, D.M. and Seegmiller, H.L., 1985, “Features of a Reattaching Turbulent Shear Layer Subject to an Adverse Pressure Gradient,” AIAA Journal, **82**, 1029-1044.

Jović, S. and Driver, D.M., 1994, “Backward-Facing Step Measurements at Low Reynolds Number, Re_h = 5000,” NASA Technical Memorandum 108807.

Durst, F., Fischer, M., Jovanovic, J. and Kikura, H., 1998, “Methods to Set Up and Investigate Low Reynolds Number, Fully Developed Turbulent Plane Channel Flows,” J. Fluids Eng., **120**(3), pp. 496-503.

Eaton, J.K., and Johnston, J.P., 1981, “A Review of Research on Subsonic Turbulent Flow Reattachment,” AIAA Journal, **19**, pp. 1093 – 1100.

Escudier, M.P. and Abdel-Hameed, A., Johnson, M.W. and Sutcliffe, C.J., 1998, “Laminarisation and Re-Transition of a Turbulent Boundary Layer Subjected to Favorable Pressure Gradient,” Exp. Fluids, **25**, pp. 491-502.

Fernholz, H.H. and Warnack, D., 1998, “The Effects of a Favorable Pressure Gradient and of the Reynolds Number on an Incompressible Axisymmetric Turbulent Boundary Layer. Part 1. The Turbulent Boundary Layer,” J. Fluid Mech., **359**, pp. 329-356.

Finnicum, D.S. and Hanratty, T.J., 1998, “Effect of Favorable Pressure Gradients on Turbulent Boundary Layers,” AIChE, **34**, pp. 529-540.

Forliti, D.J., Strykowski, P.J. and Debatin, K., 2000, “Bias and Precision Errors of Digital Particle Image Velocimetry,” Exp. Fluids, **28**, pp. 436-447.

Gad-el-Hak, M. and Bandyopadhyay, P.R., 1994, “Reynolds Number Effects in Wall-Bounded Flows,” App. Mech. Rev., **47**(8), pp. 307-364.

George, W.K. and Castillo, L., 1997, “Zero-Pressure-Gradient Turbulent Boundary Layer,” App. Mech. Rev., **50**(12), pp. 689-729.

Gui, L., Longo, J. and Stern, F., 2001, “Towing Tank PIV Measurement System, Data and Uncertainty Assessment for DTMB Model 5512,” Exp. Fluids, **31**, pp. 336-346.

Harsha, P.T and Lee, S.C., 1970, “Correlation between Turbulent Shear Stress and Turbulent Kinetic Energy,” AIAA Journal, **8**, pp. 1508-1510.

Holmes, P., Lumley, J. L., Berkooz G., 1998, “Turbulence, Coherent Structures, Dynamical Systems and Symmetry,” Cambridge University Press.

Ichimiya, M., Nakamura, I. and Yamashita, S., 1998, "Properties of a Relaminarizing Turbulent Boundary Layer under a Favorable Pressure Gradient," Exp. Thermal and Fluid Sci., **17**, pp. 37-48.

Johnson, D.A. and King, L.S., 1985, "A Mathematical Simple Turbulence Closure Model for Attached and Separated Boundary Layers," AIAA Journal, **23**, pp. 1684-1992.

Jović, S., 1996, "An Experimental Study of a Separated/Reattached Flow Behind a Backward Facing Step, Re_h = 37,000" NASA Technical Memorandum 110384.

Jović, S., 1998, "Recovery of Reattached Turbulent Shear Layers," Exp. Thermal Fluid Sci., **17**, pp. 57-62.

Keane, R.D. and Adrian, R.J., 1990, "Optimization of Particle Image Velocimetry, Part1: Doubled Pulsed System," Measurement Sci. and Tech., **1**(11), pp. 1202-1215.

Keane, R.D. and Adrian, R.J., 1992, "Theory of Cross-Correlation Analysis of PIV images," Applied Scientific Research, **49**, pp. 191-215.

Keuhn, D.M., "Some Effects of Adverse Pressure Gradient on Incompressible Reattaching Flow over a Rearward-Facing Step," AIAA Journal, **18**, pp. 343-344.

Kim, D.S., White, B.R., Ayala, A. and Bagheri, N., 1999, "Higher-Order Turbulence Products of Velocity and Temperature for Adverse Pressure Gradient Boundary Layer Flows," Proceedings of Heat Transfer and Fluid Mechanics Institute, pp. 125-132.

Kim, J., Moin, J., Moser, R., 1987, "Turbulence statistics in fully developed channel flow at low Reynolds number," J. Fluid Mech., **177**, pp. 133-166.

Kiya, M. and Sasaki, K., 1983, "Structure of a Turbulent Separation Bubble," J. Fluid Mech., **137**, pp. 83-113.

Kline, S.J., Reynolds, W.C., Schraub, F.A. and Runstadler, P.W., 1967, "The Structure of Turbulent Boundary Layers," J. Fluid Mech., **30**, pp. 741- 773.

Kostas, J., Soria, J., Chong, M.S., 2002, "Particle Image Velocimetry Measurements of a Backward-Facing Step Flow," Exp. Fluids, **33**, pp. 838-853.

Kostas, J., Soria, J., Chong, M.S., 2005, "A Comparison between Snapshot POD Analysis of PIV Velocity an Vorticity Data," Exp. Fluids, **38**, pp. 146-160.

Krogstad, P. -Å. And Antonia, R.A., 1999, "Surface Roughness Effects in Turbulent Boundary Layers," Exp. Fluids, **27**(5), pp. 450-460.

Krogstad, P.-Å., Andersson, A.I., Bakken, O.M. and Ashrafian, A., 2005, "An Experimental and Numerical Study of Channel Flow with Rough Walls," J. Fluid Mech., **530**, pp. 327-352.

Launder, B.E., Reece, G.J. and Rodi, W., 1975, "Progress in Development of a Reynolds-Stress Turbulence Model Closure," J. Fluid Mech., **68**, pp. 537-566.

Le, H., Moin, P. and Kim, J., 1997, "Direct Numerical Simulation of Turbulent Flow Over a Backward-Facing Step," J. Fluid Mech., **330**, pp. 349-374.

Lumley, J. L., 1967, "The Structure of Inhomogeneous Turbulent Flow," In Atmospheric Turbulence and Radio Wave Propagation (ed. A. M. Yaglon & V. I. Tatarski), pp.167-178, Nauka, Moscow.

Mei, R., Adrian, R. J. Hanratty, T. J., 1991, "Particle Dispersion in Isotropic Turbulence under Stokes Drag and Basset Force with Gravitational Settling," J. Fluid Mech., **225**, pp. 481 – 495.

Meyer, E.K., Pederson, J.M. and Ozcan, O., 2007, "A Turbulent Jet in Crossflow Analysed with Proper Orthogonal Decomposition," J. Fluid Mech., **583**, pp. 199-227.

Millikan, C.B., 1938, "A Critical Discussion of Turbulent Flows in Channels and Circular Tubes," Proceedings of 5th International Congress of Applied Mechanics, Cambridge.

Moin, P., and Moser, R., 1989, "Characteristic-Eddy Decomposition of Turbulence in a Channel," J. Fluid Mech., **200**, pp. 479 – 509.

Nikuradse, J., 1929, "Untersuchungen über die Strömungen des Wassers in Konvergenten un Divergenten Kanälen," Forch. Geb. Ing. Wes., Heft, 289.

Orrelano, A. and Wengle, H., 2001, "POD Analysis of Coherent Structures in Forced Turbulent Flow over a Fence," J. Turbulence, 2, pp. 1-35.

Österlund, J.M., Johansson, A.V., Nagib, H.M. and Hites, M.H., 1999, "Wall Shear Stress Measurements in High Reynolds Number Boundary Layers from Two Facilities," 30th AIAA Fluid Dynamics Conference, 28 June - 1 July, Norfolk, Virginia.

Perry, A, Bell, J.B. and Joubert, P.N., 1966, "Velocity and Temperature Profiles in Adverse Pressure Gradient Turbulent Boundary Layers," J. Fluid Mech, **25**, pp. 299-320.

Piirto, M., Saarenrinne, P., Eloranta, H. and Karvinen, R., 2003, "Measuring Turbulence Energy with PIV in Backward-Facing Step Flow," Exp. Fluids, **35**, pp. 219-236.

Prasad, A.K., 2000 "Particle Image Velocimetry," Current Sci., **79**, pp. 51-57.

Purtell, L.P., and Klebanoff, P.S., and Buckley, F.T., 1981, "Turbulent Boundary Layer at Low Reynolds Number," Phys. Fluids, **24**(5), pp. 802-811.

Ra. S.H., and Chang, P.K., 1990, "Effects of Pressure Gradient on Reattaching Flow Downstream of a Rearward-Facing Step," J. Aircraft, **27**(1), pp. 93-95.

Raffel, M., Willert, C.E. and Kompenhaus, J., 1998, "Particle Image Velocimetry: A Practical Guide," Springer Verlag.

Reichert, R.S, Hatay, F.F., Birigen, S. and Huser, A., 1994, "Proper Orthogonal Decomposition Applied to Turbulent Flow in a Square Duct," Phys. Fluids, **6**, pp. 3086-3092.

Robbins, K., 1998, "Visualization of Scientific Video Data using KL Decomposition," IEEE Transactions on Visualization and Graphics, **4**, pp. 330-343.

Ruderich, R. and Fernholz, H.H., 1986, "An Experimental Investigation of a Turbulent Shear Flow with Separation, Reverse Flow and Reattachment," J. Fluid Mech., **496**, pp. 283-322.

Ruetenik, J.R. and Corrison, S., 1955, "Equilibrium Turbulent Flow in a Slightly Divergent Channel," 50 Jahre Grenzschichtforschung, Friedr. Vieweg and Son. Braunschweig, 446.

Saikrishnan, N., Marusic, I. and Longmire, E.K., 2006, "Assessment of Dual Plane PIV Measurements in Wall Turbulence using DNS Data," Exp. Fluids, **46**, pp. 265-278.

Samuel, A.E. and Joubert, P.N., 1974, "A Boundary Layer Developing in an Increasingly Adverse Pressure Gradient," J. Fluid Mech., **66**, pp. 481-505.

Scarano, F. and Riethmuller, M., 1999, "Iterative multigrid approach in PIV image processing with discrete window offset," Exp. Fluids, 26, pp. 513-523.

Sen, M., Bhaganagar, K. and Juttijudata, V., 2007, "Application of Proper Orthogonal Decomposition (POD) to Investigate a Turbulent Boundary Layer in a Channel with Rough Walls," J. Turbulence, **8**, pp. 1-21.

Shah, M.K., Agelinchaab, M. and Tachie, M.F., 2008, "Influence of PIV Interrogation Area on Turbulent Statistics up to 4^{th} Order Moments in Smooth and Rough Wall Turbulent Flows", Exp. Thermal and Fluid Sci., **32**, pp. 725-747.

Shinneeb, A.-M., 2006, "Confinement Effects in Shallow Water Jets," University of Sasketchewan, Ph.D. Thesis.

Sirovich, L., 1987, "Turbulence and the Dynamics of Coherent Structures, Part 1: Coherent Structures," Quarterly J. of Applied Math., **45**, pp. 561 - 571.

Skåre, P.E., and Krogstad, P.-Å., 1994, "A Turbulent Equilibrium Boundary Layer Near Separation," J. Fluid Mech., **272**, pp. 319-348.

Smits, A.J. and Wood, D.H., 1985, "The Response of Turbulent Boundary Layers to Sudden Perturbations," Ann. Rev. Fluid Mech., **17**, pp. 321-358.

Spalart, P.R. and Watmuff, J.H., 1993, "Experimental and Numerical Study of a Turbulent Boundary Layer with Pressure Gradients," J. Fluid Mech., **249**, pp. 337-371.

Spalart, P.R., 1988, "Direct simulation of a turbulent boundary layer up to Re_θ=1410," J. Fluid Mech., **187**, pp. 61-98.

Sreenivasan, K.R., 1989, "The turbulent boundary layer, Frontiers in Experimental Fluid Mechanics," edited by M. Gad-el-Hak, Springer Verlag, Berlin, pp. 159-209.

Stern, F., Muste, M., Berninati, L. M. and Eichinnger, W.E., 1999, "Summary of experimental Uncertainty Assessment Methodology with Example," IIHR Technical Report no. 406, The University of Iowa, Iowa City, I.A.

Sutardi and Ching, C.Y., 2003, "The Response of a Turbulent Boundary Layer to Different Shaped Transverse Grooves," Exp. Fluids, **35**, pp. 325-337.

Tachie, M.F., Agelinchaab, M. and Shah, M.K., 2007, "Turbulent Flow over Transverse Ribs in Open Channel with Converging Side Walls," Int'l. J. Heat Fluid Flow, **28**, pp. 683 – 707.

Tachie, M.F., James D.F., and Currie, I.G., 2003, "Velocity Measurements of Shear Flow Penetrating a Porous Media," J. Fluid Mech, **493**, pp. 319-343.

Tachie, M.F., Balachandar, R. and Bergstrom, D.J., 2001, "Open Channel Boundary Layer Relaxation Behind a Forward Facing Step at Low Reynolds Numbers," J. Fluids Eng., **123**, pp. 539-544.

Tennekes, H. and Lumley, J.L.,1972, "A First Course in Turbulence," MIT Press.

Tilmann, W. 1945, "Investigation of some particulars of turbulent boundary layers on plates," British Ministry of Aircraft Production. Volkonrodo. Translation MAP-VG. 34-45T.

Townsend, A.A., 1961, "Equilibrium Layers and Wall Turbulence," J. Fluid Mech., **11**, pp. 97-120.

Wahidi, R., Chakroun, W. and Al-Fahed, S., 2005, "The Behaviour of the Skin-Friction Coefficient of a Turbulent Boundary Layer Flow over a Flat Plate with Differently Configured Transverse Square Grooves," Exp. Sci. Fluid Flow, **30**, pp. 141-152.

Wei, T. and Willmarth, W.W., 1989, "Reynolds-Number Effects on the Structure of a Turbulent Channel Flow," J. Fluid Mech., **204**, pp. 57-95.

Westerweel, J., Draad, A. A., Th. Van der Hoeven, J. G., and Oord van, J., 1996, "Measurement of Fully Developed Turbulent Pipe Flow with Digital Particle Image Velocimetry," Exp. Fluids, **20**, pp. 165 – 177.

White, F.M., 1974. Viscous Fluid Flow. McGraw-Hill, New York.

Wilcox, D.C. 2004, "Turbulence Modeling for CFD, Second Edition" DCW Publishers,.

Willert, C. E. and Gharib, M., 1991, "Digital Particle Image Velocimetry," Exp. Fluids, **10**, pp. 181-193.

Zagarola, M.V. and Smits, A.J., 1998, "Mean-Flow Scaling of Turbulent Pipe Flow," J. Fluid Mech., **373**, pp. 33-79.

APPENDIX A: Two-Dimensionality of the Flow

A.1 Two-Dimensionality of the Flow

In this section, the two-dimensionality of the upstream flow and also the flow field in the separated shear layer and early redevelopment region is quantified. Since PIV is a whole-field measurement technique and allows for the calculation of velocity gradients, the distributions of $\partial U/\partial x$ and $\partial V/\partial y$ at the channel mid-span were calculated. The mean velocity gradients, $\partial U/\partial x$ and $\partial V/\partial y$, at the midspan of the upstream location of Tests D1, D2 and C are plotted in Figure A.1. Notwithstanding the scatter in the data, it is observed that the mean velocity gradients are relatively small (as expected) and $\partial U/\partial x \approx -\partial V/\partial y$ as

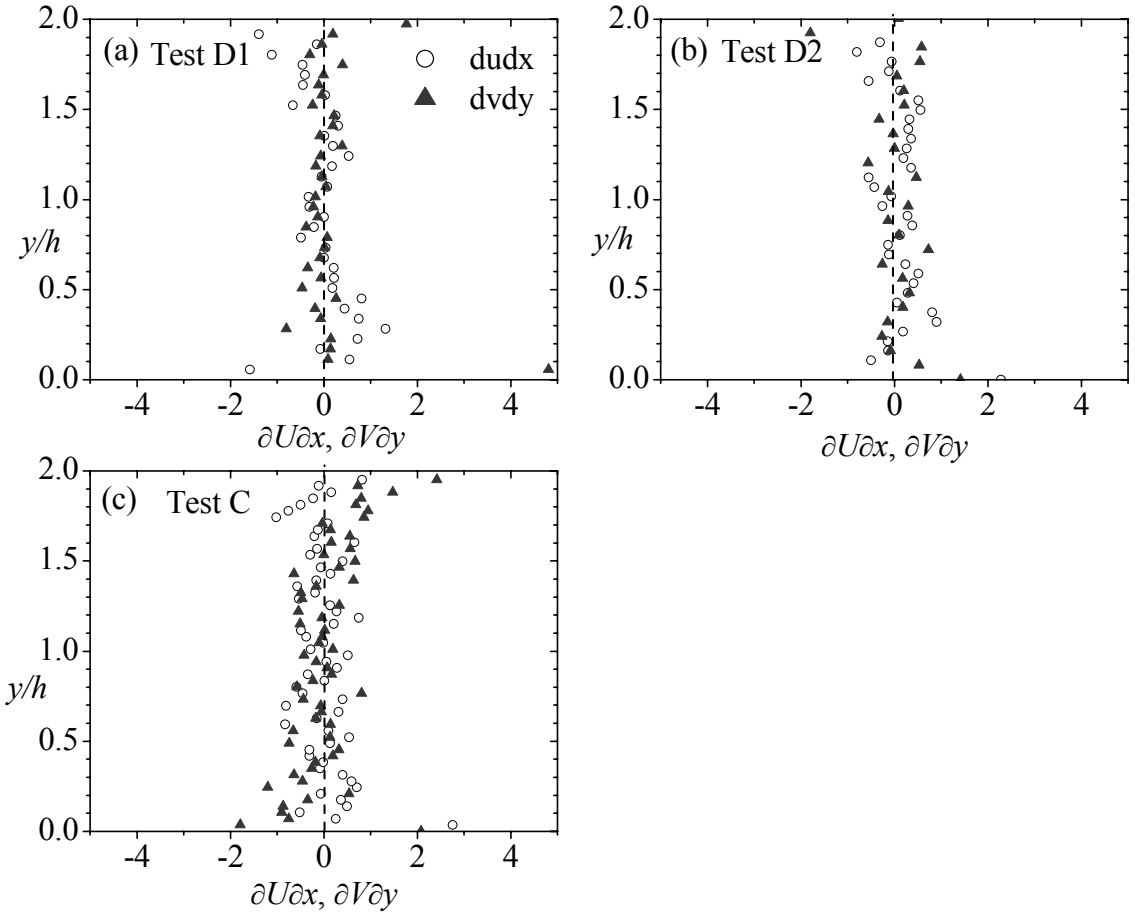

Figure A.1: The mean velocity gradients at upstream locations: (a) Test D1, (b) Test D2 and (c) Test C.

required by continuity equation for two-dimensional flow. Based on these results, it is concluded that departure of the mean flow from two-dimensionality is not severe at the upstream locations of the converging and diverging channels.

The flow in the separated and the early redevelopment region is evolving rapidly. Any departure of the mean flow from two-dimensionality would be more severe in the separated region and immediately downstream of the reattachment than at the upstream locations. To investigate the two-dimensionality of the flow in these regions, typical profiles of the mean velocity gradients are plotted at $x/k = 4$ (centre of the recirculation bubble) and at $x/k = 13$ (immediately downstream of the reattachment). As expected, the mean velocity gradients are significantly higher than those obtained at the upstream locations (Figure A.1). However, in this case as well, $\partial U/\partial x \approx -\partial V/\partial y$ indicating the mean flow is fairly two dimensional.

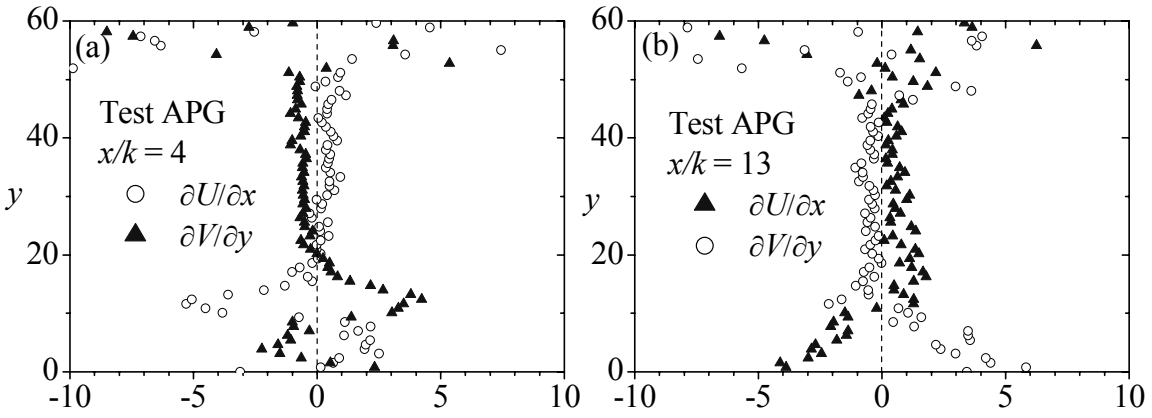

Figure A.2: The mean velocity gradients at selected locations in: (a) separated region and (b) redevelopment region.

In one of our recent experimental study[1], PIV measurements were conducted over an array of transverse triangular ribs furnished at the upper and the lower walls. To assess the two-dimensionality of the mean velocity and turbulent field, measurements were obtained at the midspan location and at z =+45mm and -45mm which correspond to $z/B = \pm 0.25$, where B denotes the spanwise width of the channel. Although the flow over arrays of two-dimensional transverse triangular ribs is not identical to the present study,

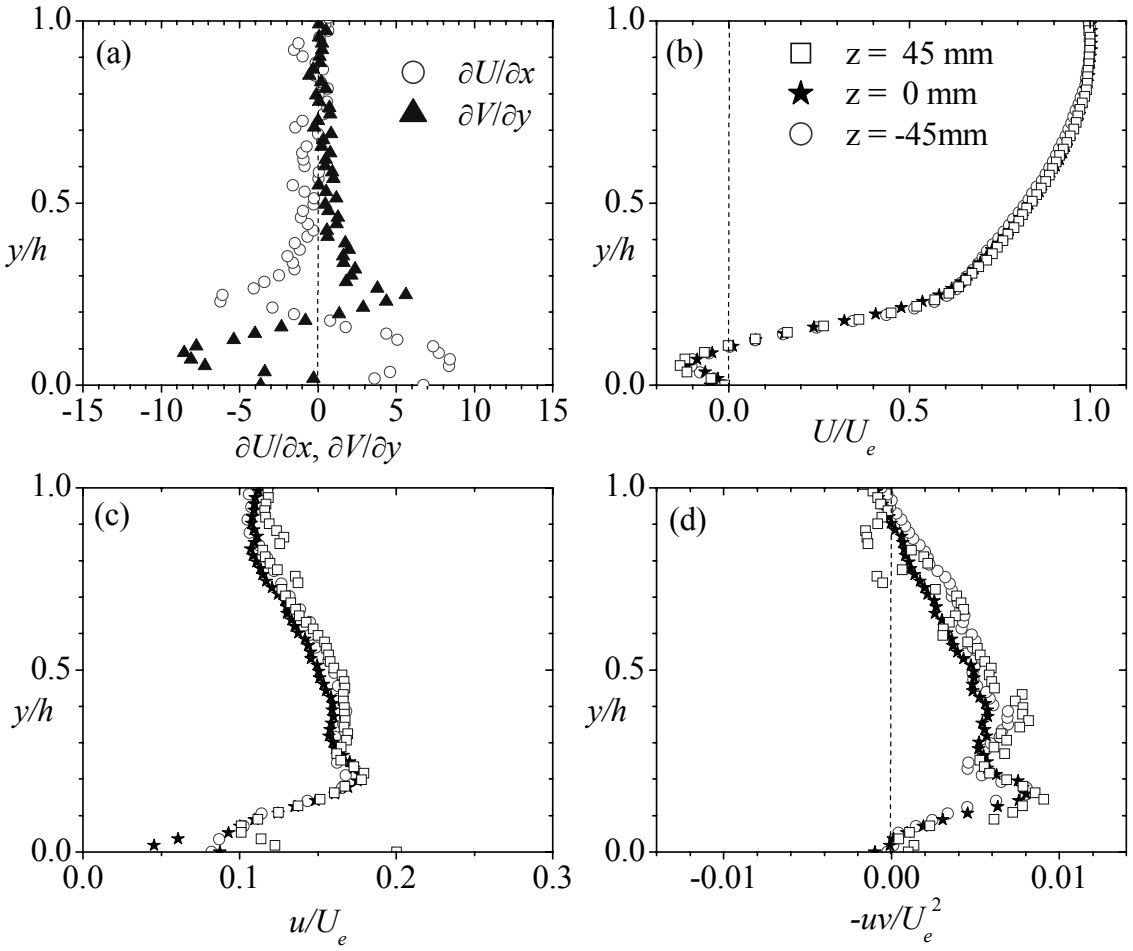

Figure A.3: The profiles of (a) the mean velocity gradients at midspan and (b) the mean velocity profiles, (c) the streamwise turbulent intensity and (d) the Reynolds shear stress at various spanwise locations.

[1] Tachie, M.F. and Shah, M.K., 2008, "Favorable Pressure Gradient Turbulent Flow over Straight and Inclined ribs on Both Channel Walls," Phys. Fluids, **20**, pp. 095103.

the channel height is the same in both studies. The mean velocity gradients at midspan (z = 0) are plotted in Figure A.3a. It is observed that $\partial U/\partial x \approx -\partial V/\partial y$ indicating that the mean flow is reasonably two-dimensional. The two-dimensionality of the flow is further verified by plotting the mean velocity, streamwise turbulent intensity and Reynolds shear stress at the three spanwise locations (Figures A.3b-d). The mean velocity and turbulent quantities are nearly similar at these spanwise locations. This provides further evidence that the mean flow and also the turbulence field are fairly two-dimensional.

APPENDIX B: Measurement Uncertainty

B.1 Measurement Error

Measurement is the act of assigning a value to some physical variables. The relative closeness of agreement between an experimentally determined value of a quantity and its true value indicates the accuracy of a measurement. Error is the difference between the experimentally determined value and the true value. Most often, the true values of measured quantities are unknown. Therefore, estimation of the error must be made and that estimate is called an uncertainty. Coleman and Steele (1995) have presented a detailed uncertainty assessment methodology. Stern *et al.* (1999) provided comprehensive guidelines for the application of uncertainty assessment methodology into the test process and documentation of results. In general, the total error is composed of two components: a precision component, P, and a bias component, B. Coleman and Steele (1995) classified an error as precision if it contributes to the scatter of the data and systematic error is a bias error. Gui *et al.* (2001) quantified the evaluation of bias uncertainty in PIV measurements and its contribution to the total measurement uncertainty. According to studies such as Forliti *et al.* (2000) a Gaussian peak-fitting algorithm is found to have the lowest bias and precision errors. They reported that the evaluation bias and gradient of the evaluation bias can both be minimized effectively by using Gaussian digital masks on the interrogation window, so that the measurement uncertainty can be reduced.

B.1.1 Minimizing Measurement Error

Through careful selection of experimental conditions such as time between image pairs certain errors can be minimized. Peak locking, which is an artifact of sub-pixel particle displacement being biased toward integer values, is a major contributor to the bias error.

In the present study, a number of steps were taken during image acquisition and image processing to reduce peak locking. The particle image diameter was estimated to be d_p = 1.40 μm (1.89 px), 1.40μm (1.89 px) and 1.43 μm (1.93 px) in Tests D1, D2 and C, respectively. Meanwhile, the particle image diameter was estimated to be d_p = 16.8 μm (2.27 px), 16.7μm (2.26 px) and 16.5 μm (2.23 px) in Tests CC, APG and FPG, respectively. These values are close to the value of 2.0 px recommended by Raffel *et al.* (1998) to minimize peak locking. The histogram, Figure A.1, shows no discernible peak locking effects which imply that the contribution to the bias error is minimal. The large sample size (2040 instantaneous images) also reduces the precision error.

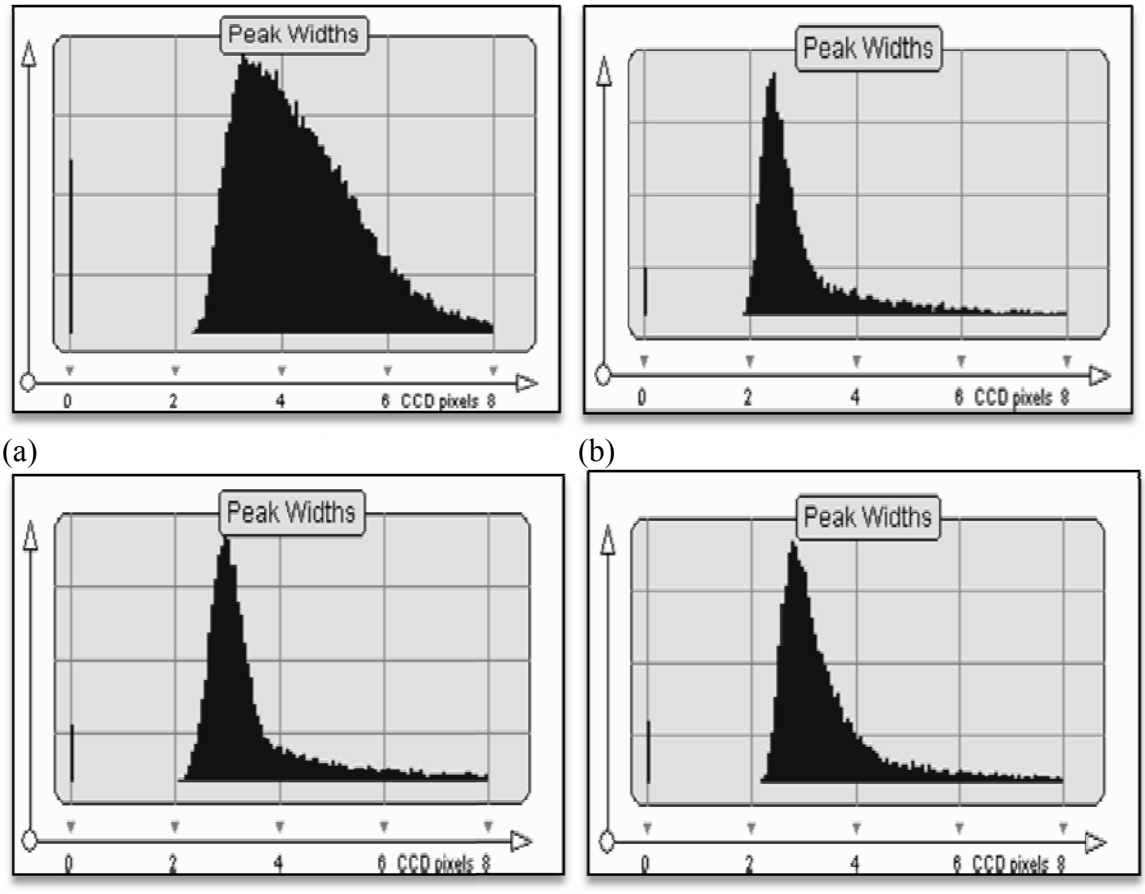

Figure B.1: Sample histogram of plane: (a) *P1* in Test D1, (b) *P1* in Test APG and (c) *P2* in Test APG.

The effect of velocity gradient bias errors that occurs in flows with large mean velocity gradients is also a concern. The velocity gradients tend to broaden the displacement peak and reduce the amplitude. The error associated with the velocity gradient is typical of all boundary layers. Keane and Adrian (1992) suggested that for cross-correlation technique, to achieve an acceptable valid detection probability of 95%, the acceptable gradients should follow the expression

$$\frac{M\Delta U_y \Delta t}{d} < 0.03\,, \qquad (1)$$

where M is the magnification factor, $\Delta U_y = (\partial U/\partial y)(d/2)$, Δt is the time between the two laser pulses and d is the length of the interrogation area size. For Test *D2,* a magnification factor of 6.42^{-1}, $\partial U/\partial y$ of 20 (near wall region) and Δt of $400\mu s$ yields approximately 0.001. For this and other test locations (not shown) the condition expressed in the above equation is easily satisfied.

In near-wall turbulence, it is necessary to keep the interrogation area size as small as possible in order to resolve the smallest spatial scales in the flow. On the other hand, the dynamic range of the measured velocity values increases with larger interrogation area sizes which implies that larger interrogation area sizes are desirable to achieving large dynamic range. The above conflicting interests require that a compromise between spatial resolution and velocity dynamic range has to be made. The dynamic range in a PIV measurement based on a pixel displacement level is the displacement divided by the sub-pixel accuracy. The sub-pixel accuracy is a function of many parameters, for which most are beyond the PIV system itself and therefore often unknown. As a rule-of-thumb 0.1 pixel accuracy is a realistic value (Scarano and Riethmuller, 1999). In our measurements, it was ensured that particle displacement was less than ¼ of the size of the

interrogation area as recommended by many researchers. For a typical PIV recording of 32 × 16 pixels, the maximum displacement is 8 pixels so that the dynamic range is of the order of 8/0.1 = 80.

B.1.2 Measurement Uncertainty

Adrian (1999) proved that random influences can be summed into a single error, and it can be found by repeating the measurement. Prasad (2000) reported that random influences in PIV usually scale with the particle image diameter as

$$\sigma_{random} = cd_e , \tag{2}$$

where d_e, is the effective particle diameter and c is a constant whose value is between 0.05 and 0.10, depending upon experimental conditions.

The uncertainty analysis of the present measurement follows the AIAA standard derived and explained by Coleman and Steele (1995). A complete uncertainty analysis of the PIV measurement involves identifying and quantifying both the bias (the fixed, systematic or constant) and the precision (random) uncertainties in each part of the measurement chain. These uncertainties include particle response to fluid motion, light sheet positioning, light pulse timing, and the error arising from the peak-finding algorithm to determine the average particle displacement, (Tachie *et al.*, 2003).

B.1.2.1 Biased error

In PIV measurement, the instantaneous velocity at any point is the average fluid velocity for an interrogation region and is described by the following data-reduction equation described in Gui *et al.* (2001).

$$u_i = \frac{\Delta s L_0}{\Delta t L_I}, \tag{3}$$

where i equals 1 and 2 for the x and y coordinates, respectively, Δt is the time interval between laser pulses, Δs is the particle displacement from the correlation algorithm, L_0 is the width of the camera view in the object plane, and L_I is the width of the digital image. The bias limit of the measured velocity is determined with a root-sum-square (RSS) of the elementary bias limits based on the sensitivity coefficients given as

$$B_{u_i} = \theta_{L_0}^2 B_{L_0}^2 + \theta_{L_I}^2 B_{L_I}^2 + \theta_{\Delta s}^2 B_{\Delta s}^2 + \theta_{\Delta t}^2 B_{\Delta t}^2, \tag{4}$$

where the sensitivity coefficients, θ_x are defined as

$$\theta_X = \frac{\partial u_i}{\partial X}, \quad X = (L_0,\ L_I, \Delta t, \Delta s) \tag{5}$$

The classification of bias error sources and contribution to the bias limits for U and V are provided in Table A.1 and Table A.2, respectively. Also shown in Tables A.1 and A.2 are the manufacturer's specifications of the elementary bias limits for Δt and Δs. The bias limit for L_0 is obtained from a calibration procedure.

Table B.1: Bias limits of the streamwise mean velocity component at the near wall region.

Variable	Magnitude	B_x	θ_x	$B_x\theta_x$	$B_x\theta_x$ /Σ $B_x\theta_x$	$(B_x\theta_x)^2$
L_o (m)	9.88E-02	5.00E-04	1.08E+00	5.39E-04	2.73E-01	2.91E-07
L_i (pix)	2.048E+03	5.00E-01	-5.20E-05	-2.60E-05	-1.32E-02	6.77E-10
Δt (s)	4.500E-04	1.00E-07	-2.37E+02	-2.37E-05	-1.20E-02	5.61E-10
Δs (pix)	9.940E-01	1.27E-02	1.07E-01	1.36E-03	6.90E-01	1.86E-06
U (m/s)	1.200E-01					
			$\Sigma B_x\theta_x$ =	1.85E-03	$\Sigma(B_x\theta_x)^2$ =	2.15E-06
					Bias Error =	1.47E-03
					%Bias Error =	1.22%

Table B.2: Bias limits of the transverse mean velocity component at the near wall region.

Variable	Magnitude	B_x	θ_x	$B_x\theta_x$	$B_x\theta_x$ /Σ $B_x\theta_x$	$(B_x\theta_x)^2$
L_o (m)	9.88E-02	5.00E-04	5.05E-02	2.53E-05	1.28E-02	6.38E-10
L_i (pix)	2.048E+03	5.00E-01	-2.44E-06	-1.22E-06	-6.18E-04	1.49E-12
Δt (s)	4.000E-04	1.00E-07	-1.25E+01	-1.25E-06	-6.33E-04	1.56E-12
Δs (pix)	4.140E-02	1.27E-02	1.21E-01	1.53E-03	7.77E-01	2.35E-06
V (m/s)	3.000E-02					
			$\Sigma B_x\theta_x$ =	1.56E-03	$\Sigma(B_x\theta_x)^2$ =	2.35E-06
					Bias Error =	1.53E-03
					%Bias Error =	5.11%

B.1.2.2 Precision Error

The precision error, P, of a measured variable, X is given by

$$P_x = \frac{K \cdot \sigma}{\sqrt{N}} \tag{6}$$

where K is the confidence coefficient and has a value of 2 for a 95% confidence level for sample size N images. σ is the standard deviation of the sample of N readings of the variable X, and is defined as

$$\sigma = \sqrt{\frac{1}{N-1}\sum_{n=1}^{N}\left(X_n - \overline{X}\right)^2} \tag{7}$$

where $\overline{X}$ is the mean given by the equation

$$\overline{X} = \frac{1}{N}\sum_{n=1}^{N} X_n \ . \tag{8}$$

B.1.2.3 Total Uncertainty

The total uncertainty, E, in the result u_i is the root-sum-square (RSS) of the bias and precision limits, given by

$$E_X = \sqrt{B_X^2 + P_X^2} \quad (9)$$

The standard deviation of the measured dataset was estimated in the near-wall region and along the center line for Test APG in the separated region at x/k = 4 to be 0.63% and 0.14%, respectively. These regions were specifically chosen due to the presence of wide range of velocities and turbulence intensity distributions. Since the requirement of maximum seeding particle displacement was met and the online validation feature of the PIV system was applied, it can be assumed that the sample standard deviation is not too different from that defined in Eqn. (7). On the basis of this assumption, the standard deviation of the dataset in this study yield precision limits in the near-wall region and along the center of the channel were 0.54% and 0.09%, respectively in the separated region. The measurement uncertainty at 95% confidence level in mean velocities, U and V, was estimated to be 1.33% and 5.13%, respectively, for the near-wall region. Along the center line of the channel these quantities are 0.59% and 5.11% for U and V, respectively. The measurement uncertainty in turbulence intensities and Reynolds stresses was estimated to be ±5% and ±7%, respectively. The uncertainty in Reynolds stresses was estimated to be ±10%. The uncertainty in the triple velocity correlations and energy budget terms is on the order of ±15%. Error bars are used to indicate measurement uncertainty in selected graphs.

APPENDIX C: Comparison with Previous Studies

C.1 Comparison with Previous Studies

In this section, selected locations of Test CC are compared with measurements reported by Antoniou and Bergeles (1988) downstream of transverse square rib obtained in a wind tunnel experiment using hotwire, denoted by Test AB. As is well known, hotwire measurements are unreliable in the regions of high turbulent intensity and flow reversal due to direction ambiguity. For these reasons, no data were reported in the separated region. Comparison is also made with the results of Agelinchaab and Tachie (2008) obtained in an open channel flow downstream of a transverse square rib using PIV, denoted by Test AT. The test conditions for the three test cases are summarized in Table C.1. In Table C.1, U_o is the reference upstream velocity, $\mathrm{Re}_k = U_o k/\nu$ and $\mathrm{Re}_\theta = U_o \theta/\nu$, $k/2h$ is the blockage ratio and k/δ_o is the perturbation strength. The values of the reattachment lengths (x_r/k) in these studies are also presented in the table. The turbulence levels in Test AB and AT are, respectively, 0.5% and 5% compared with 5% in the present study (Test CC). It should be noted that the Re_k and the k/δ_o are highest for Test AB and lowest for Test AT. Even though the two previous studies do not have exactly the same upstream conditions as the present study, the comparison is still meaningful.

Table C.1: The summary of test conditions for Test CC and the reference measurements.

	U_o (m/s)	Re_k	Re_θ	δ_o (mm)	$k/2h$	k/δ_o	x_r/k
Present (Test CC)	0.445	2670	620	19	0.09	0.31	10.4
Antoniou & Bergeles (1988) (Test AB)	15.000	20000	1420	14	--	1.42	11.5
Agelinchaab &Tachie (2008) (Test AT)	0.315	1920	1800	55	0.07	0.11	8.5

The present value of x_r/k = 10.4 for Test CC (k/δ_o = 0.31) is about 10% lower than x_r/k = 11.5 reported by Antoniou and Athanassiadis (1988). However, it should be noted that in their study, the perturbation strength was higher (k/δ_o = 1.43) and the background freestream turbulence was lower (0.5% compared with background turbulence of 5% in the present study). Both effects (higher k/δ_o and lower turbulence level) would increase the reattachment length. Agelinchaab and Tachie (2008) reported a value of x_r/k = 8.5 in their open channel flow over a square rib (k/δ_o = 0.11). The lower value reported by Agelinchaab and Tachie (2008) may be partly attributed to the lower perturbation strength (i.e., k/δ_o = 0.11 in their study compared with k/δ = 0.31 in the present study).

In Figure C.1a, the mean velocity profiles are plotted at the center of the recirculation bubble (x/x_r = 0.5) and at the reattachment location (x/x_r = 1). The mean velocity variation for Tests CC and AT are in good agreement in the separated region. In the present and previous study negative velocities in the separated region are as high as $0.2U_e$. In Figure C.1b, the mean velocity profiles are also compared in the redevelopment region for Test CC at x'/k = 3 and 20 (x' is taken zero at the reattachment location) with Test AB at x'/k = 5 and 25 and Test AT at x'/k = 2 and 20, respectively. In the redevelopment region, the mean velocity profiles tend to recover towards a typical boundary layer or channel flow profile. The recovery rate of the three test cases is different in the redevelopment region. This may partly be attributed to the x'/k locations being slightly different, the difference in upstream conditions as well as flows recovering under different conditions i.e., open channel vs. closed channel or wind tunnel. It should also be noted that at both locations of comparison, Test AB profiles are farther downstream i.e., x'/k = 2 (Test CC) vs. 5 (Test AB) and x'/k = 21 (Test CC) vs. 25 (Test

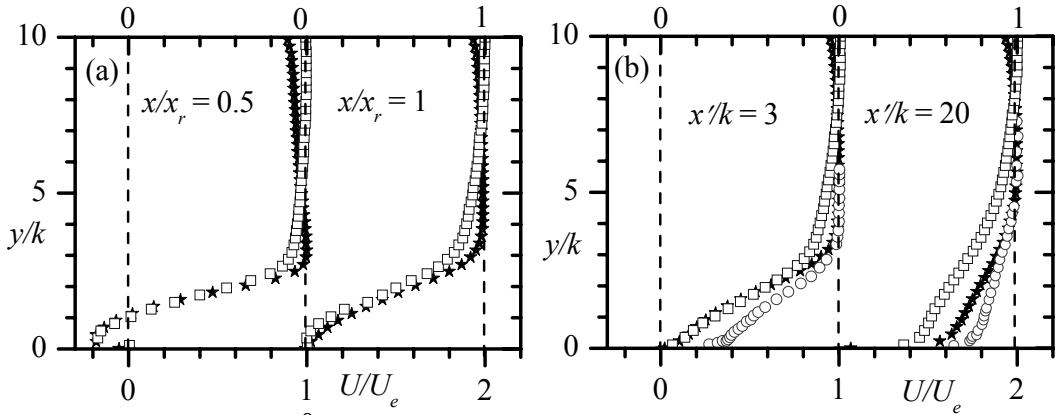

Figure C.1: The mean velocity profiles (a) separated region, (b) redevelopment region. Symbols are Test CC: ξ; Test AT: ∀; Test AB: –.

AB) which might be responsible for some deviation from the present results.

The turbulent intensity profiles, u/U_e and v/U_e, are compared in the separated and the redevelopment region in Figure C.2 and C.3, respectively. The turbulent intensities are significantly enhanced in the separated region. The turbulent intensity peaks are up to 20% higher for Tests CC than AT likely due to the stronger perturbation strength (k/δ_o). The region of the flow perturbed by the rib is also similar for Tests CC and AT i.e., in the region $y/k < 3$. In the separated and redevelopment region, the turbulence levels for Tests CC and AT are similar away from the wall, i.e. in the region $y/k > 3$. However, u/U_e is much smaller in the region $y/k > 3$ for Test AB compared to Test CC in the redevelopment region. This is likely due to the experiment being conducted in wind tunnel at relatively lower turbulence levels and not due to the recovery of the flow. In the redevelopment region, the turbulent intensity profiles decay rapidly. The recovery of u/U_e for three test cases and v/U_e for the two test cases is qualitatively similar. Jović (1998) reported that flow recovery in the early stages of redevelopment is faster for flows with stronger perturbation but diminished downstream of $x/k > 30$ and the profiles with

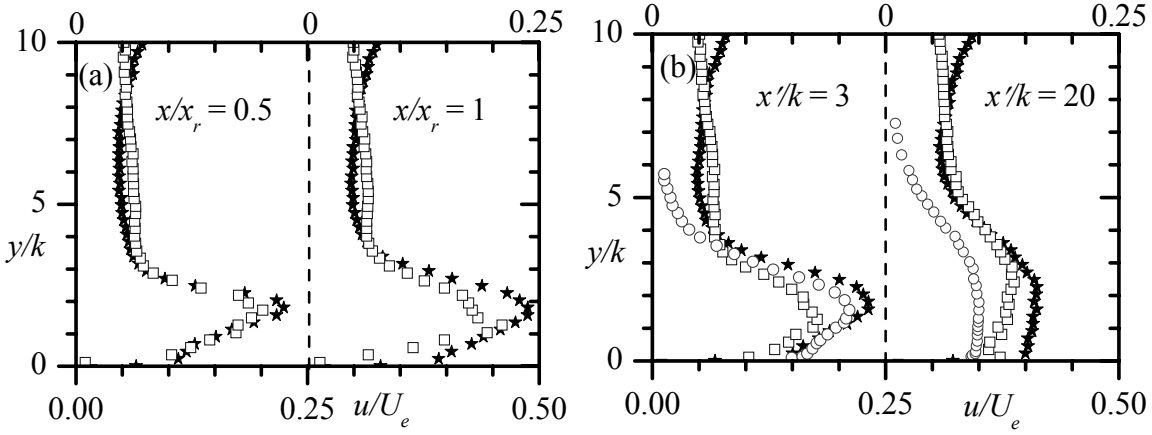

Figure C.2: The profiles of streamwise turbulent intensity in: (a) separated region, (b) redevelopment region. Symbols are Test CC: ξ; Test AT: ∀; Test AB: –.

different perturbations recovered at a similar rate.

The Reynolds shear stress profiles are plotted in Figure C.4. These profiles show a similar trend as the turbulent intensities. The Reynolds shear stress is higher in case of Test CC than Test AT in the separated region. The Reynolds shear stress is also enhanced in the region $y/k < 4$ for both flows. In the redevelopment regions the profiles decay rapidly but away from the wall, the Reynolds shear stress levels are similar.

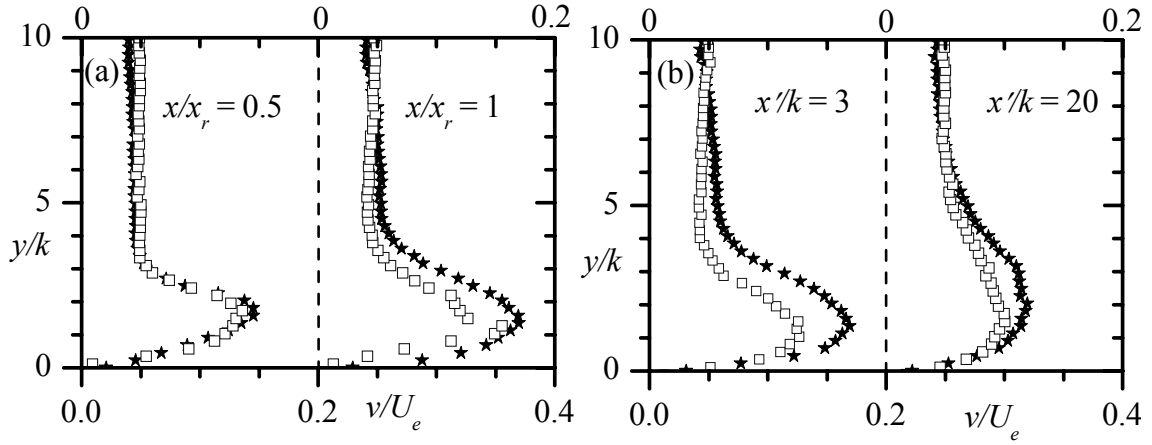

Figure C.3: The profiles of transverse turbulent intensity in: (a) separated region, (b) redevelopment region. Symbols are Test CC: ξ; Test AT: ∀.

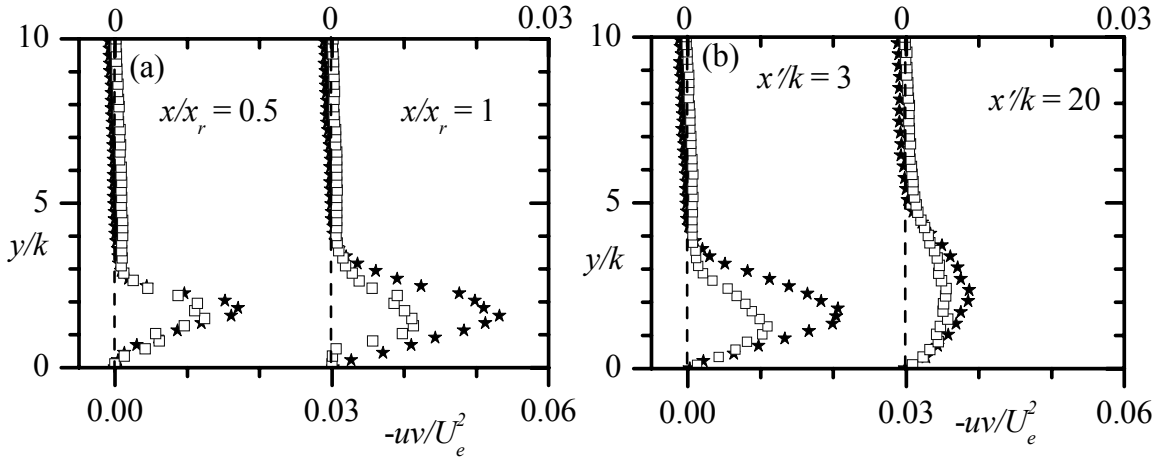

Figure C.4: The profiles of Reynolds shear stress in: (a) separated region, (b) redevelopment region. Symbols are Test CC: ξ; Test AT: ∀.

APPENDIX D: POD Reconstruction

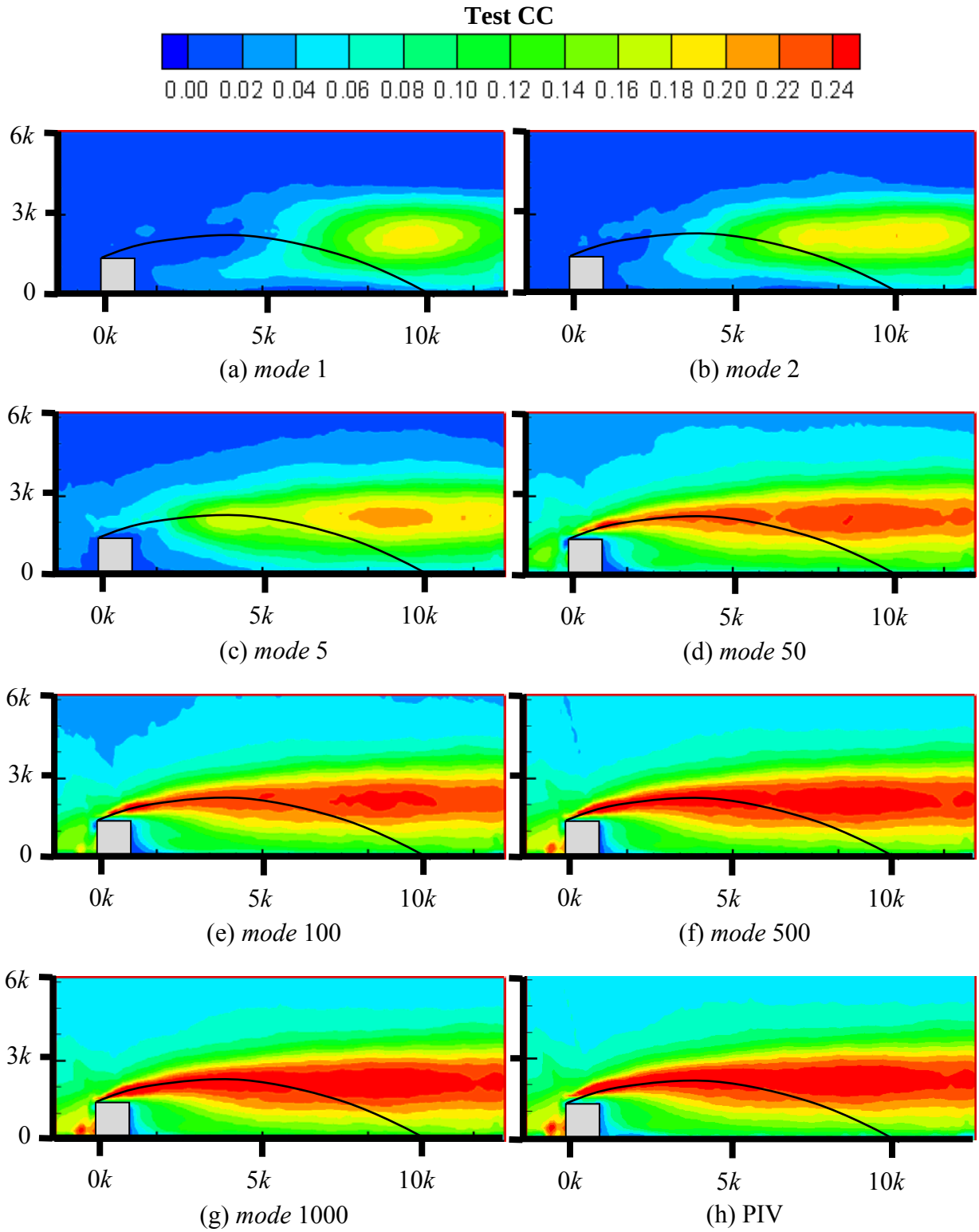

Figure D.1: Iso-contours of streamwise turbulent intensity, u/U_e^2, for Test CC obtained using (a) 1, (b) 2, (c) 5, (d) 50, (e) 100, (f) 500 and (g) 1000 modes in reconstruction and (h) from PIV data. Mean separation line is also shown.

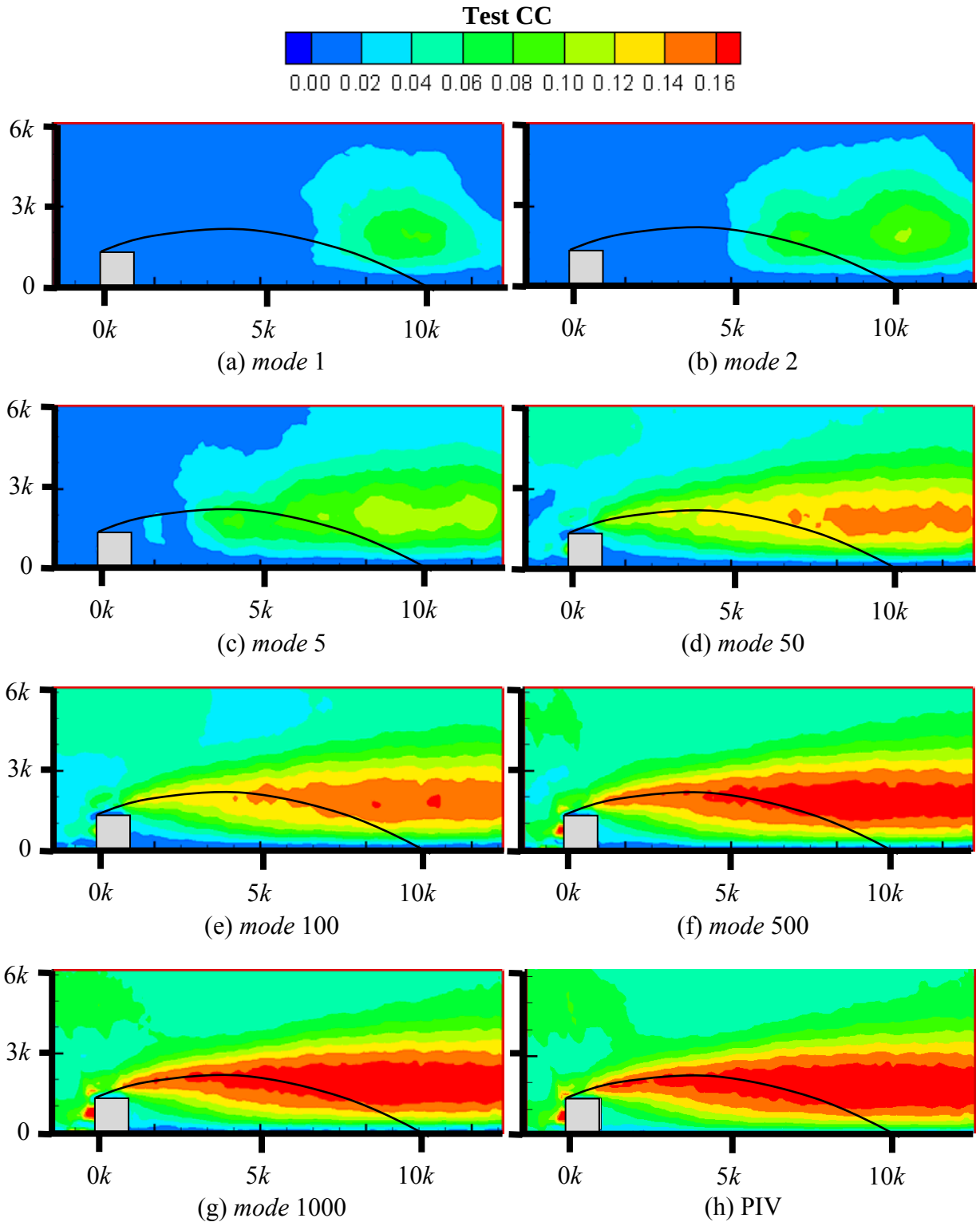

Figure D.2: Iso-contours of transverse turbulent intensity, v/U_e^2, for Test CC obtained using (a) 1, (b) 2, (c) 5, (d) 50, (e) 100, (f) 500 and (g) 1000 modes in reconstruction and (h) from PIV data. Mean separation line is also shown.

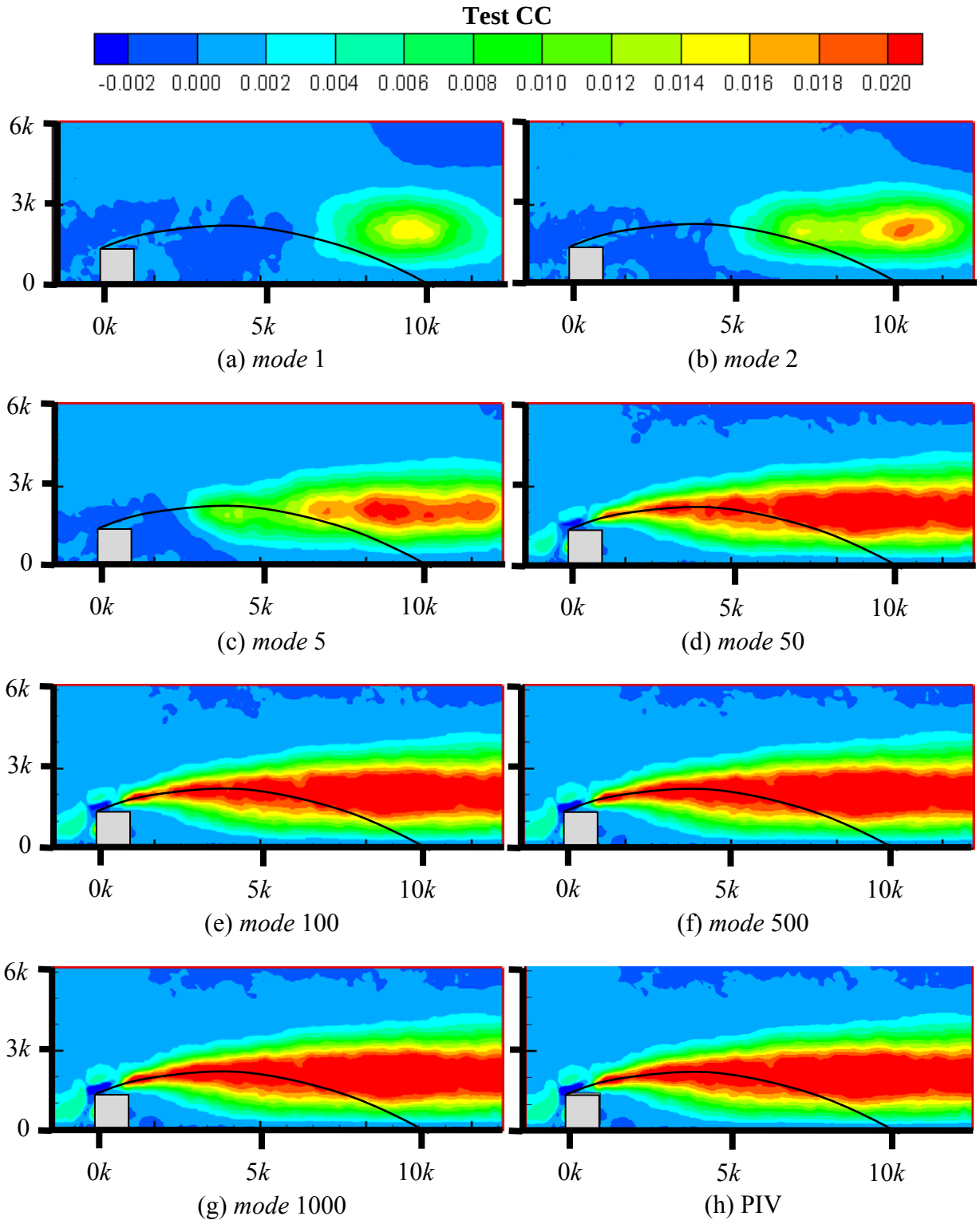

Figure D.3: Iso-contours of Reynolds shear stress, $-uv/U_e^2$, for Test CC obtained using (a) 1, (b) 2, (c) 5, (d) 50, (e) 100, (f) 500 and (g) 1000 modes in reconstruction and (h) from PIV data. Mean separation line is also shown.

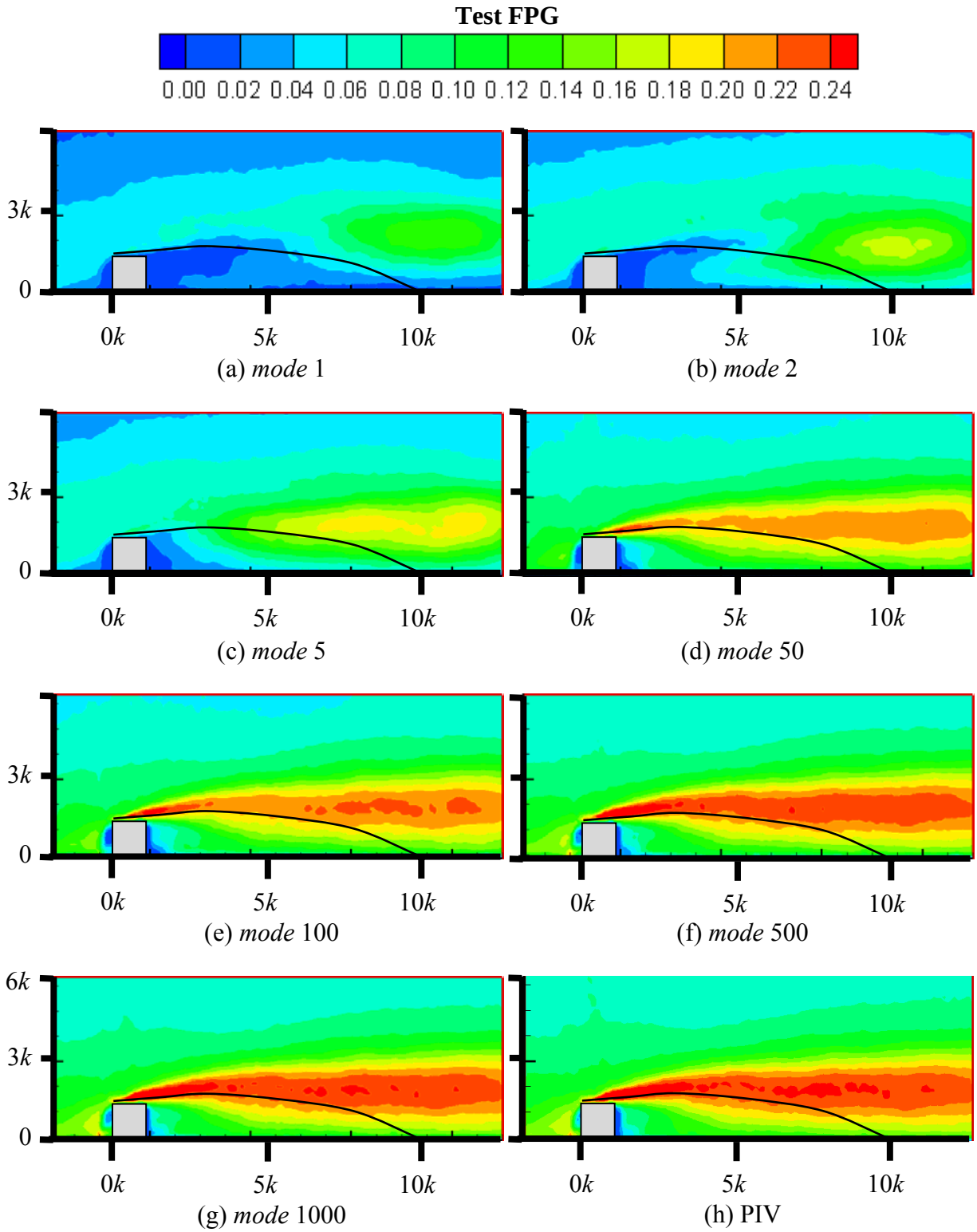

Figure D.4: Iso-contours of streamwise turbulent intensity, u/U_e^2, for Test FPG obtained using (a) 1, (b) 2, (c) 5, (d) 50, (e) 100, (f) 500 and (g) 1000 modes in reconstruction and (h) from PIV data. Mean separation line is also shown.

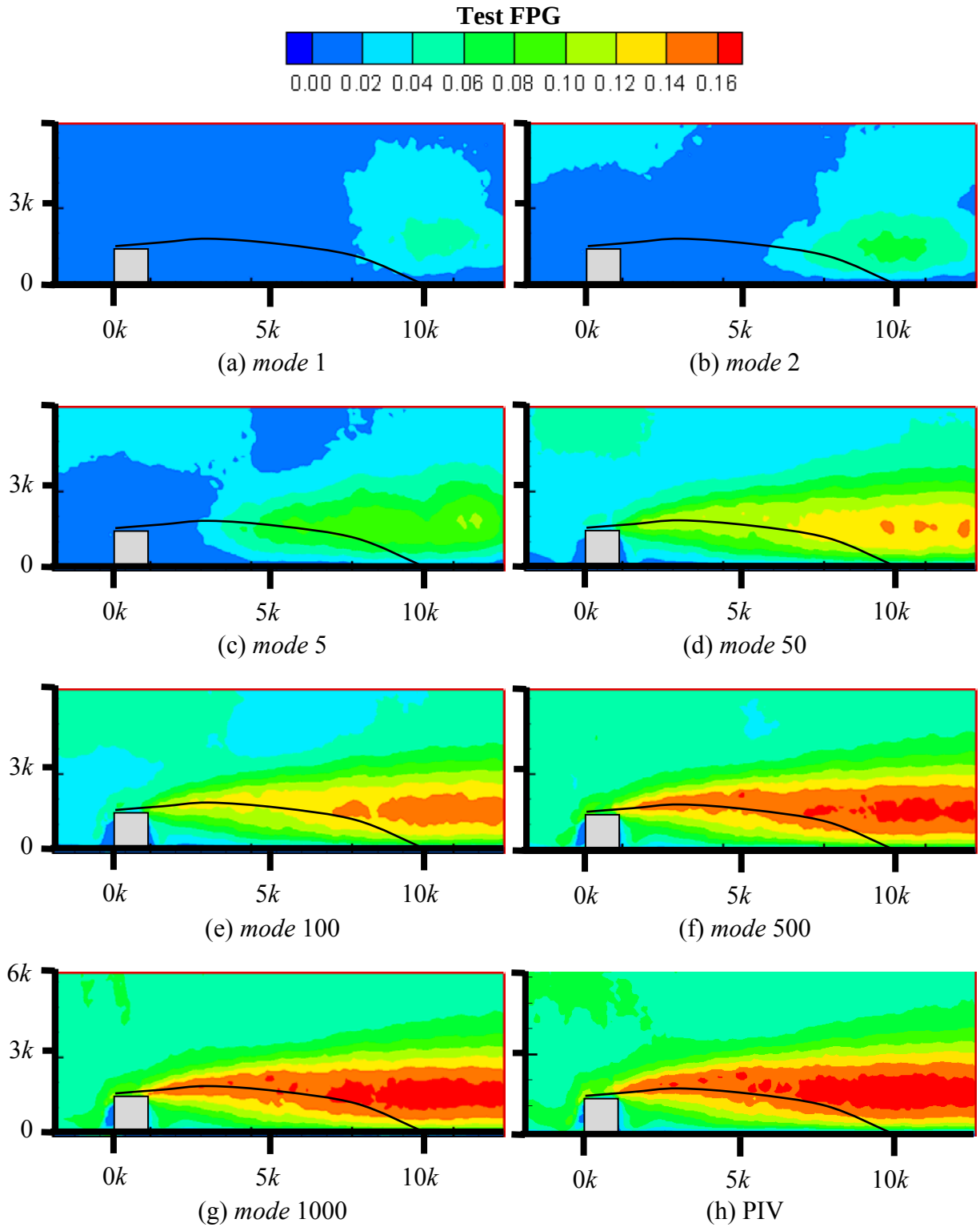

Figure D.5: Iso-contours of transverse turbulent intensity, v/U_e^2, for Test FPG obtained using (a) 1, (b) 2, (c) 5, (d) 50, (e) 100, (f) 500 and (g) 1000 modes in reconstruction and (h) from PIV data. Mean separation line is also shown.

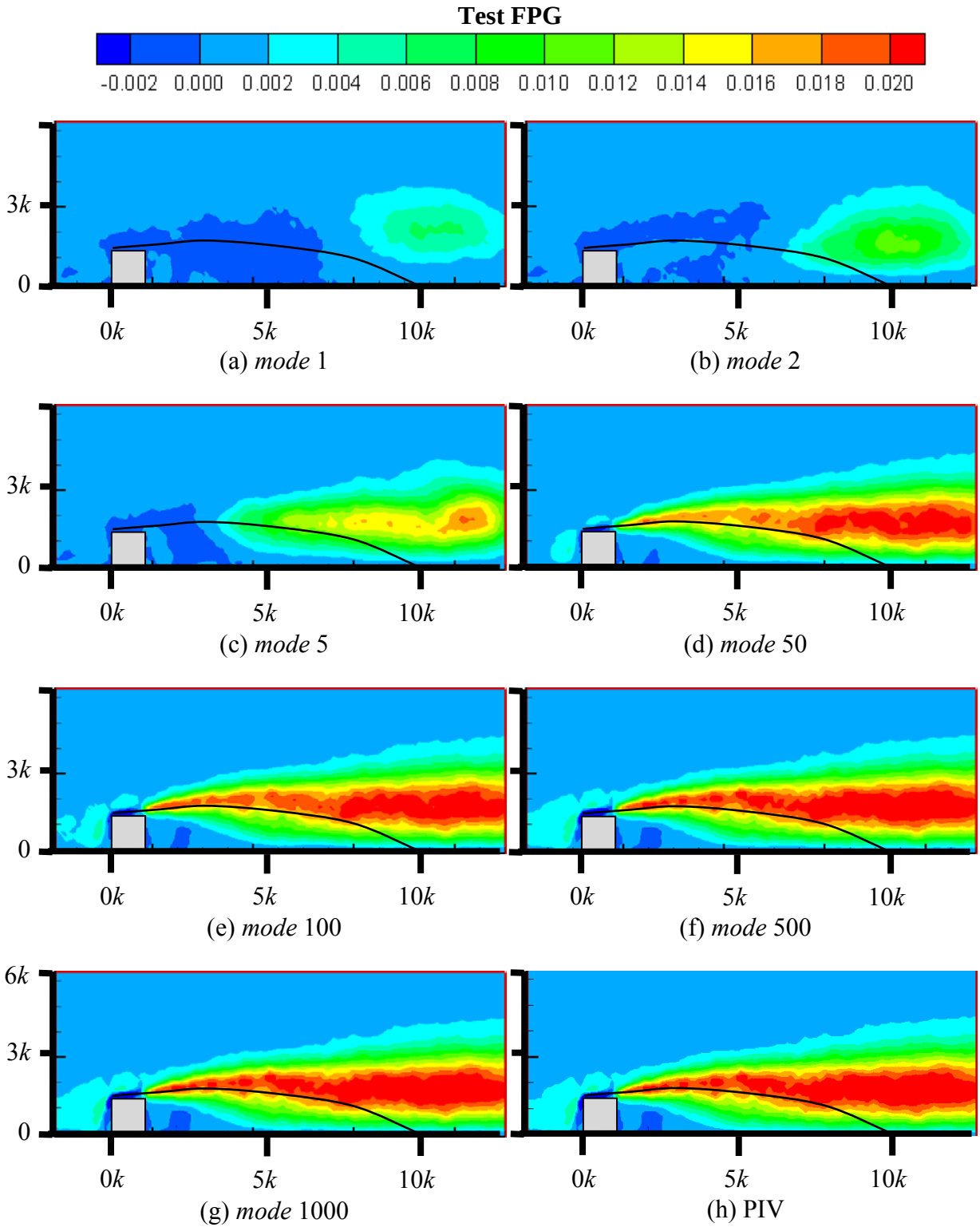

Figure D.6: Iso-contours of Reynolds shear stress, $-uv/U_e^2$, for Test FPG obtained using (a) 1, (b) 2, (c) 5, (d) 50, (e) 100, (f) 500 and (g) 1000 modes in reconstruction and (h) from PIV data. Mean separation line is also shown.